
**LISA Optical Bench development:
Experimental investigation of
Differential-Wavefront Sensing for a
spaceborne Gravitational Wave detector**

Von der Quest-Leibniz-Forschungsschule
der Gottfried Wilhelm Leibniz Universität Hannover
zur Erlangung des akademischen Grades

Doktor der Naturwissenschaften Dr. rer. nat.
von

M. Sci. Alvise Pizzella

geboren am 06.04.1995 in Padova, Italien

2025

Referent: Apl. Prof. Dr. Gerhard Heinzel
Max Planck Institute for Gravitational Physics (AEI)
Callinstraße 38, 30167 Hannover, Germany

Korreferent: Prof. Dr. Karsten Danzmann
Max Planck Institute for Gravitational Physics (AEI)
Callinstraße 38, 30167 Hannover, Germany

Korreferent: Prof. Dr. Oliver Gerberding
Universität Hamburg, Institut für Experimentalphysik
Luruper Chaussee 149, 22761 Hamburg, Germany

Date of Defence: 24th January 2025

Some minor corrections recommended by the referents that do not change the arguments or results have been applied to the version submitted on the 27th November 2024.

*A mio Nonno Guido
che ha spinto questa ricerca prima di me,
mi mancherai*

*A mio Papá Alessandro
che mi ha insegnato come pensare*

measure

etymology: italian *misura*, french *mésure*, latin MENSURA, coming from MENSUS, past participle of the verb METÍRI meaning *to measure*. This verb has its origins in the Indo-European root *MĀ*; as the sanscrit *māti* meaning *measure, to measure*, greek *mātrām* → *mètron*, slavish and serbian *mata*, celtic *mead, meas*, ancient alt german *mëz, māza* and the modern *Maas*, ancient german *mezzan* and modern *messen*, gothic *mitan māta*.

This root can also be found in the words *meter* - the fundamental unit to measure lengths, *imitate, mimic* - the act of 'measuring' someone or something in order to reproduce it, *mathematics* (since this root gained also the metaphorical meaning of "thinking"), *moon* (since the lunar period was the fundamental unit to measure months' duration) and hence *month* [22].

Abstract

The Laser Interferometer Space Antenna (LISA) is a satellite mission led by the European Space Agency (ESA) scheduled to be launched in 2035. It will be the first space-based gravitational wave (GW) observatory, aiming to detect GWs in the $10^{-4} - 10^{-1}$ Hz band. Heterodyne laser interferometry is used to measure changes in distance between two test masses (TMs) shielded by two spacecraft and separated by millions of kilometers. The ambitious sensitivity of $\text{pm}/\sqrt{\text{Hz}}$ presents many technical challenges, such as the weak-light condition and the coupling of the angular jitter of the spacecraft and TMs to the interferometrically-measured longitudinal displacement, or tilt-to-length (TTL).

Addressing this weak-light condition requires careful optimization of the heterodyne detection system, mainly of the quadrant photoreceivers (QPRs) and the phasemeter (PM) electronics. The angular motion of the spacecraft and especially the jitter of the moving optical subassemblies (MOSAs) introduce additional phase noise that is one of the main contributors to the total displacement noise. To mitigate these effects, differential wavefront-sensing (DWS) is employed. DWS serves both in flight for the active control of the position and rotation of the TMs, MOSAs and spacecraft, and on ground, for calibration and subtraction of residual TTL in post-processing. The sensitivity of the DWS technique under weak-light conditions and in the presence of tilts remains uncharacterized. This gap represents a major focus of the current work, aiming to evaluate DWS performance in conditions that closely simulate those expected in LISA during flight.

During this thesis, such performance was demonstrated for the first time using TDOBS, a testbed representative of LISA's optical bench (OB). This is an ultra-stable interferometer testbed that has been developed to validate critical interferometric techniques for the LISA mission. The testbed features a pair of steering mirrors that can induce synthetic tilts between the beams to simulate spacecraft or TM motion. This experiment, which already successfully demonstrated optical reduction of TTL by means of imaging systems (ISs) using kHz beat notes, was upgraded to beat notes in the 5-25 MHz band, becoming fully LISA representative. Furthermore, TDOBS features low-noise QPRs comparable to those of LISA.

The first part of the thesis focuses on understanding the DWS signals, modelling their dependence on the geometrical properties of the optical setup, and their calibration. This section is essential for connecting the measurements performed in TDOBS to their analogue in LISA, and for estimating how to test LISA's requirements on the ground.

The second part focuses on the experimental setup. The DWS noise performance is characterized and broken down into individual noise contributors. Experimental investigations are presented, including first-time measurements of DWS noise under weak-light conditions and in the presence of beam tilts. The working principle of a novel architecture of tracking beat notes from a quadrant photodiode (QPD) is demonstrated for the first time using optically generated beat notes. To conclude, the future improvements and projects of TDOBS together with the takeaways for LISA are discussed.

Keywords: gravitational waves, LISA, heterodyne interferometry, phasemeter, differential wavefront-sensing, low-noise photoreceiver

Contents

1	Introduction	3
1.1	General Relativity and Gravitational Waves	3
1.2	Gravitational Wave Experiments	6
1.3	LISA	7
1.3.1	The Orbit	7
1.3.2	The Payload	8
1.3.3	The Sensitivity	17
2	Interferometric Signals with Quadrant Photodiodes	19
2.1	Gaussian Beams and Interferometry	19
2.1.1	Gaussian Beams	19
2.1.2	Beam Superposition	22
2.1.3	Interferometers	24
2.1.4	Effect of a Gravitational Wave on an Interferometer	29
2.1.5	Noises of interferometric origin	31
2.2	Ray Transfer Matrices and Imaging Systems	35
2.2.1	Ray Transfer Matrices	35
2.2.2	Imaging Systems	37
2.3	The QPD Signals: Differential Power Sensing, Longitudinal Pathlength Signal and Differential Wavefront-Sensing	37
2.3.1	Differential Power Sensing	38
2.3.2	Longitudinal Pathlength Signal	38
2.3.3	Differential Wavefront-Sensing	39
2.4	Conclusion	56
3	The Tilt-to-Length Coupling and Differential Wavefront-Sensing Optical Bench Simulator	59
3.1	Tilt-to-Length Coupling in LISA	59
3.2	The Tilt-to-Length Coupling and Differential Wavefront-Sensing Optical Bench Simulator	62
3.2.1	The LISA-Optical Bench	64
3.2.2	The Telescope Simulator	65
3.2.3	The Imaging Systems	70
3.3	Upgrade of TDOBS	71
3.3.1	The Modulation Bench	71
3.3.2	The Photoreceivers	74
3.3.3	AC-DC Splitter	83
3.3.4	The Phasemeters	85

3.3.5	The Control Software	87
3.3.6	Vacuum System	90
3.3.7	Thermal Isolation	90
3.4	Conclusion	93
4	Calibration	95
4.1	The Auxiliary QPD	95
4.2	Rotation of the RX beam	98
4.3	Secondary DPS calibration of the other QPDs	100
4.4	DWS calibration of the REFQPDs	100
4.4.1	Angle between the REFQPDs	106
4.4.2	Heterodyne efficiency as a function of the tilt angle, REFQPDs	108
4.5	DWS calibration of the SCIQPDs	110
4.5.1	Angle between the SCIQPDs	115
4.5.2	Heterodyne efficiency as a function of the tilt angle, SCIQPDs	116
4.6	Conclusion	117
5	LISA Requirements, Noise Hunting and Characterization	119
5.1	Noise Requirements	119
5.1.1	Noise Requirements for LISA	119
5.1.2	Noise Requirement on the Phasemeter	124
5.1.3	Noise Requirements for TDOBS	125
5.2	TDOBS: DWS and LPS noise budget	126
5.2.1	Carrier-to-Noise density ratio-dependent phase noises	127
5.2.2	Carrier-to-Noise density ratio-independent phase noises	128
5.2.3	Noise Budget	135
5.3	Phasemeter's noise floor	136
5.4	TDOBS: DWS and LPS noise floor	142
5.4.1	The Performance Measurement Setup	142
5.4.2	The Performance Measurement Results	143
5.5	Conclusion	155
6	LISA-like Noise Investigations	157
6.1	DWS performance with low RX beam power	157
6.1.1	Setup Description	158
6.1.2	Beam Power Control	159
6.1.3	LMH6624 Opamp based TIA #1 Results	159
6.1.4	BFP740 Transistor and AD8038 Opamp based TIA #2	163
6.1.5	Conclusion	166
6.2	DWS performance in presence of a beam tilt	167
6.2.1	Expectation	167
6.2.2	Setup Description	168
6.2.3	Results	170
6.2.4	Conclusion	176
7	The New DWS Architecture	177
7.1	The old and new QPD tracking architecture	177
7.1.1	The Simulation	179
7.1.2	Signal-to-Noise Ratio Considerations	179

7.2	Experimental Testing with Optical Signals	184
7.2.1	Setup	184
7.2.2	Results	185
7.3	Conclusion	188
8	Summary, Future Improvements and Conclusions	189
8.1	Summary	189
8.2	Improvements and Future Projects	192
8.3	Takeaways for LISA	193
Appendices		198
A	Small Vector Noise	199
B	Electronics' Schematics	201
C	DPS calibrations from TDOBS	205
D	DWS calibrations from TDOBS	210
E	Imaging System calculations	212
E.1	Propagation of a generic beam through a generic optical system . . .	212
E.2	Propagation through a generic Imaging System	213
E.2.1	AOM double-pass imaging systems	214
E.3	DWS and Imaging Systems	215

Chapter 1

Introduction

After giving a brief introduction to general relativity (GR), gravitational waves (GWs) and the history of GW experiments, this Chapter introduces the main features of the LISA mission. For a more complete argumentation about GR and GWs the Author refers to [51].

1.1 General Relativity and Gravitational Waves

Albert Einstein published the theory of general relativity (GR) in 1915 [26, 27, 24, 25]. The theory was an innovative way of seeing gravity no longer as a distance interaction between bodies but as a mutual interaction between spacetime and bodies, where "matter tells spacetime how to curve, and spacetime tells matter how to move" [79]. Spacetime is described as a Riemannian manifold and its properties are expressed by the *metric tensor* $g_{\mu\nu}$. The energy-mass distribution is described with the energy-momentum tensor $T_{\mu\nu}$. Finally, Einstein's field equations relate the spacetime properties $g_{\mu\nu}$ to the energy-momentum tensor $T_{\mu\nu}$

$$R_{\mu\nu} - \frac{1}{2}Rg_{\mu\nu} = \frac{8\pi G}{c^4}T_{\mu\nu}, \quad (1.1)$$

where G is Newton's constant, c is the speed of light, $R_{\mu\nu}$ is the Ricci tensor and R is the Ricci scalar. The coupling constant on the right side of the equation (1.1) is as small as $\frac{8\pi G}{c^4} \approx 2.071 \times 10^{-43} \text{ s}^2 \text{m}^{-1} \text{kg}^{-1}$, making spacetime very stiff to deform; only extremely massive and energetic events give rise to a significant curvature. In the absence of matter, equation (1.1) is solved by the flat Minkowskian metric $\eta_{\mu\nu} = \text{diag}(-1, 1, 1, 1)$.

GWs emerge when analyzing small perturbations of a metric. This can be shown by taking the flat metric as an example. In a situation where the energy-mass density contribution is very small, the metric $g_{\mu\nu}$ differs only slightly from the flat metric. Mathematically, the metric can be *linearized* as

$$g_{\mu\nu} = \eta_{\mu\nu} + h_{\mu\nu} \quad |h_{\mu\nu}| \ll 1 \quad |\partial_\rho h_{\mu\nu}| \ll 1, \quad (1.2)$$

where the tensor $h_{\mu\nu}$ represents the small deviations from the flat metric. In the *weak field approximation* defined in equation (1.2), the Einstein field equations (1.1) can be shown to become a wave equation for the tensor $\bar{h}_{\mu\nu} = h_{\mu\nu} - \frac{1}{2}\eta_{\mu\nu}h_\rho^\rho$

$$\square \bar{h}_{\mu\nu} = -\frac{16\pi G}{c^4}T_{\mu\nu}, \quad (1.3)$$

where \square is defined as the flat space d'Alambertian operator $\square = \eta_{\mu\nu}\partial^\mu\partial^\nu$. Equation (1.3) is the starting point for calculating the generation of GWs within the linearized theory. To study the propagation of GWs and their interaction with TMs, we fix the energy-momentum tensor to zero ($T_{\mu\nu} = 0$) as we are in a vacuum. Hence, equation (1.3) can be rewritten as

$$\square\bar{h}_{\mu\nu} = 0 \quad (1.4)$$

Such an equation as (1.4) can be solved with the Green function method. The generic solution takes the form

$$h_{\mu\nu} = A_{\mu\nu}e^{ik_\rho x^\rho}, \quad (1.5)$$

with $A_{\mu\nu} \in \mathbb{C}$ and $k \in \mathbb{R}$, $k = (\omega/c, \mathbf{k})$ $\omega/c = |\mathbf{k}|$ (with the usual convention of taking the real part after the computation) along with the transverse condition $k_\rho A^\rho = 0$ and light speed propagation condition $k_\rho k^\rho = 0$. Gauging away the degrees of freedom, one can set the trace to vanish $\bar{h} = 0$. This gauge is called the traceless transverse (TT) gauge. The $A_{\mu\nu}^{TT}$ tensor for a generic GW propagating in the $k = (1, 0, 0, 1)$ direction is

$$\bar{h}_{\mu\nu}^{TT} = \begin{pmatrix} 0 & 0 & 0 & 0 \\ 0 & h_+ & h_\times & 0 \\ 0 & h_\times & -h_+ & 0 \\ 0 & 0 & 0 & 0 \end{pmatrix} e^{i\omega_{gw}(t - \frac{z}{c})}, \quad (1.6)$$

where ω_{gw} is the GW's frequency and $t - \frac{z}{c}$ is the retarded time. Two degrees of freedom are left, as in the case of electromagnetic waves. The resulting wave is, hence, a superposition of two *polarizations* named *plus* (+) and *cross* (\times), respectively. One can define two polarization tensors as

$$\varepsilon_+ = \begin{pmatrix} 0 & 0 & 0 & 0 \\ 0 & 1 & 0 & 0 \\ 0 & 0 & -1 & 0 \\ 0 & 0 & 0 & 0 \end{pmatrix} \quad \varepsilon_\times = \begin{pmatrix} 0 & 0 & 0 & 0 \\ 0 & 0 & 1 & 0 \\ 0 & 1 & 0 & 0 \\ 0 & 0 & 0 & 0 \end{pmatrix}. \quad (1.7)$$

At this point, equation (1.6) can be rewritten as

$$\bar{h}_{\mu\nu}^{TT} = \sum_{i=+,\times} h_i \varepsilon_{\mu\nu}^i e^{i\omega_{gw}(t - \frac{z}{c})}. \quad (1.8)$$

In the TT gauge, the coordinates of a particle at rest are not changed by the arrival of a GW, making it seem that GWs have no physical effect on matter. This effect is instead to be searched in the consequences of a change of the metric, for example in the variation of the *proper distance* between two points at rest. In the presence of a GW, the metric $g_{\mu\nu}$ is

$$g_{\mu\nu} = \eta_{\mu\nu} + \bar{h}_{\mu\nu}^{TT} = \begin{pmatrix} -1 & 0 & 0 & 0 \\ 0 & 1 + h_+ \cos(\omega_{wg}(t - \frac{z}{c})) & h_\times \cos(\omega_{wg}(t - \frac{z}{c})) & 0 \\ 0 & h_\times \cos(\omega_{wg}(t - \frac{z}{c})) & 1 - h_+ \cos(\omega_{wg}(t - \frac{z}{c})) & 0 \\ 0 & 0 & 0 & 1 \end{pmatrix}. \quad (1.9)$$

Taking two simultaneous events $\mathbf{x}_1 = (ct_1, x_1, 0, 0)$ and $\mathbf{x}_2 = (ct_1, x_2, 0, 0)$ and their distance $\Delta\mathbf{x} = \mathbf{x}_2 - \mathbf{x}_1 = (0, L, 0, 0)$, in the presence of only a *plus* polarized GW the proper distance is

$$s^2 = \eta_{\mu\nu}\Delta x^\mu\Delta x^n u + \bar{h}_{\mu\nu}^{TT}\eta_{\mu\nu}\Delta x^\mu\Delta x^n u \rightarrow s \approx L \left(1 + \frac{1}{2}h_+ \cos \left(\omega_{wg} \left(t - \frac{z}{c} \right) \right) \right). \quad (1.10)$$

The proper distance between the two events, which is L in the absence of a GW, is amplitude-modulated with amplitude $\frac{1}{2}h_+L$. As the proper distance variation is proportional to $\Delta\mathbf{x}$, to define the strength of a GW the relative length variation, or *strain*, is introduced as $h = \frac{\Delta L}{L}$.

An example to help visualize the effect of a GW's propagation is to use a ring of matter placed on a plane perpendicular to the wave's propagation. The ring starts at rest position. After one-quarter of the period, in the case of a plus polarized wave, one axis is stretched (y-axis in Figure 1.1), while the perpendicular axis contracts simultaneously. After one-half of the period, the ring returns to its rest position. After three-quarters of the period the two axes switch roles. The cross-polarization has the same effect, but with a $\frac{\pi}{4}$ rotation.

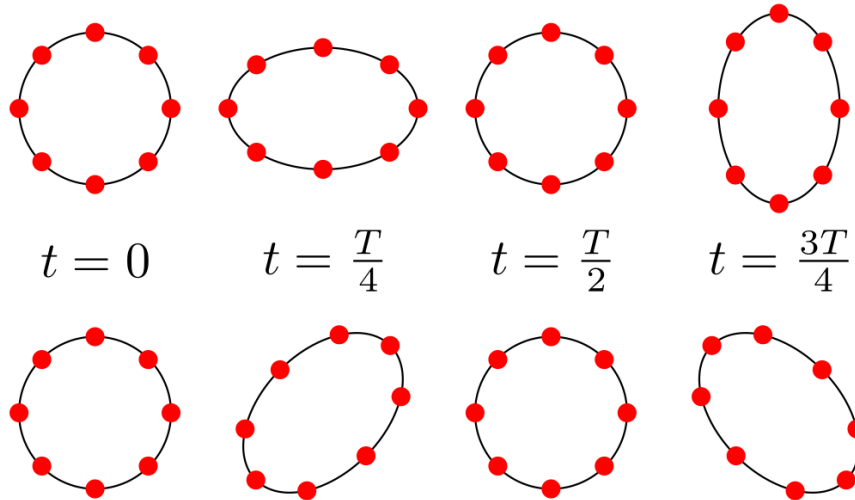


Figure 1.1: Effect of a GW propagating through a ring of matter lying on a plane perpendicular to the GW's propagation axis. Figure from [14].

GWs have characteristically low amplitudes due to the tiny value of GR's coupling constant. We can only hope to measure the effects of the most massive and energetic astronomical objects. Hence, the sources of GWs observed so far were:

- the inspiral and merger of binary black holes (e.g. [2])
- the inspiral and merger of binary neutron stars (e.g. [1])

Still awaited detections are GW from supernovae and spinning neutron stars.

The amplitude of such GWs on Earth is reduced because of the distance to the source: the expected amplitude on Earth is at most of the order of $h \sim 10^{-21}$ [66]. Inflation is also expected to have generated a stochastic background of GWs, which are expected to be smaller than those of astrophysical origin.

The detection of GWs is not only a further confirmation of GR but presents an entirely new way of observing the universe. Astrophysics, up to recently, relied on the observation of the full spectrum of electromagnetic waves and neutrinos. Since the advent of GW detection, the field is enriched with a new type of signal and with sources that were previously unobservable.

1.2 Gravitational Wave Experiments

The technological advances of the 1940s and 1950s made it reasonable to start experiments to detect such small signals as GWs. The pioneer of the field was Joseph Weber, who developed resonant-mass detectors. These relatively simple devices were mostly sensitive at one specific frequency, chosen to be of the order of kHz since that is the expected characteristic frequency of supernovae [62]. A transiting gravitational wave would release some mechanical energy into the bar, and the induced excitation is then detected. A limit of this method is the energy released in the bar itself by the thermal noise. These devices were improved and ran until the first decade of the present century. Since these experiments failed to achieve a clear detection, the effort moved towards GW interferometers (IFMs). These are significantly more complex devices that require the participation of thousands of researchers, on top of more than 30 years of preparation, but they also have a much broader detection band. The detection principle is to monitor the distance between some ideally free-falling TMs¹, which is perturbed by the transit of GWs. Some technical challenges that these experiments have to overcome are the realization of stable laser sources in both power and frequency, seismic isolation systems able to suppress ground motion - due to earth's seismic activity or human activity - by ~ 10 orders of magnitude and the production of large volume high vacuum enclosures for the laser beam propagation. The first large-scale ground-based IFM, LIGO, was completed in 1999 in the US, while VIRGO, in Italy, was completed in 2003. In 2016, LIGO announced the first ever detection of a GW [2].

A significant limitation to the sensitivity of these devices is the earth itself. The microscopic vibrations caused by the earth's seismic activity produce residual motion characterized by a displacement spectral density of [66]

$$x(f) = \begin{cases} 10^{-9} \text{m}/\sqrt{\text{Hz}} & \text{from 1 to 10 Hz} \\ 10^{-9} \left(\frac{10\text{Hz}}{f}\right)^2 \text{m}/\sqrt{\text{Hz}} & \text{for } f > 10\text{Hz}, \end{cases} \quad (1.11)$$

originating a strain noise orders of magnitude above the typical GW strain signal [51]. These can be effectively decoupled from the detector's output by seismic isolation stages. However, the varying gravitational field caused by these microscopic vibrations, which is called Newtonian noise or gravity gradients noise, cannot. This makes the measurement of frequencies lower than ~ 1 Hz impossible. Conversely, the mHz region of the GW spectrum is potentially very rich in GW sources, including fascinating objects as supermassive black holes [51]. Newtonian noise can be avoided only by moving away from its source i.e. the Earth. This leads to space-borne GW IFMs, such as the LISA from ESA and TianQin [50] and Taiji [82] from

¹On earth it is impossible to have real free-fall. It is possible instead to have quasi-free-fall, i.e. an object which is, to a certain extent, characterized by the spectrum of stray acceleration in the relevant degrees of freedom typical of free-fall.

China. Another strategy currently followed in ground-based detectors is the active subtraction of the interferometric signal caused by Newtonian noise [74].

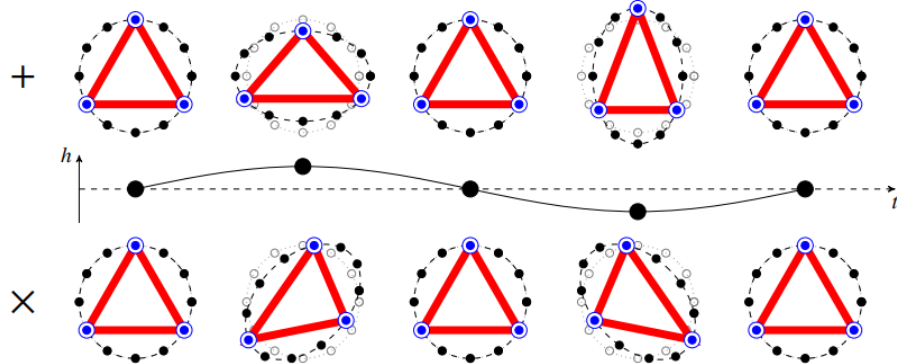


Figure 1.2: Exaggerated representation of the interaction of the LISA constellation with a GW transiting in a perpendicular direction to the plane of the constellation, for both polarizations. Figure from [20].

1.3 LISA

The Laser Interferometer Space Antenna (LISA) is planned to be the first space-based GW observatory and is currently scheduled to be launched in 2035 as of the writing of this thesis (2025) [28]. The LISA mission is led by ESA and is a collaboration of ESA, National Aeronautics and Space Administration (NASA) and an international consortium of scientists and space agencies. LISA consists of three equal spacecraft which, in space and far from sources of Newtonian noise, will be able to detect GWs in the $10^{-4} - 1$ Hz band [19]. This section addresses the main features of this mission.

1.3.1 The Orbit

LISA's three spacecraft form a near equilateral triangular constellation, the so-called *cartwheel* formation, with an armlength of 2.5×10^9 m [53]. As illustrated in Figure 1.3, the constellation is placed on a heliocentric orbit, following the Earth with a $\sim 20^\circ$ separation, meaning approximately 5×10^{10} m distance from the Earth [19]. The plane of the constellation is angled at 60° with respect to the ecliptic. As it orbits, the constellation rotates on its plane, as depicted in Figure 1.3. These particular heliocentric orbits are chosen to maximize the stability of the constellation, i.e. minimizing the variation of armlength and corner angle between the spacecraft - which inevitably happen due to the gravitational interaction with all the planets in the solar system [63] - while keeping the spacecraft close enough to the Earth to allow communications [19]. The stability of these orbits is guaranteed over the mission time of 10 years (4 nominal + 6 extension) [53]. In this configuration, the constellation's plane always faces the sun on the same side, which is essential for the required thermal stability of the spacecraft. The Chinese mission Taiji adopts a similar orbit, albeit orbiting ahead of the Earth [82] in contrast with LISA, while TianQin plans a geocentric orbit [50]. The constellation's stability is shown in Figure 1.4. The armlength variation rate is constrained to be smaller than 10 m/s with

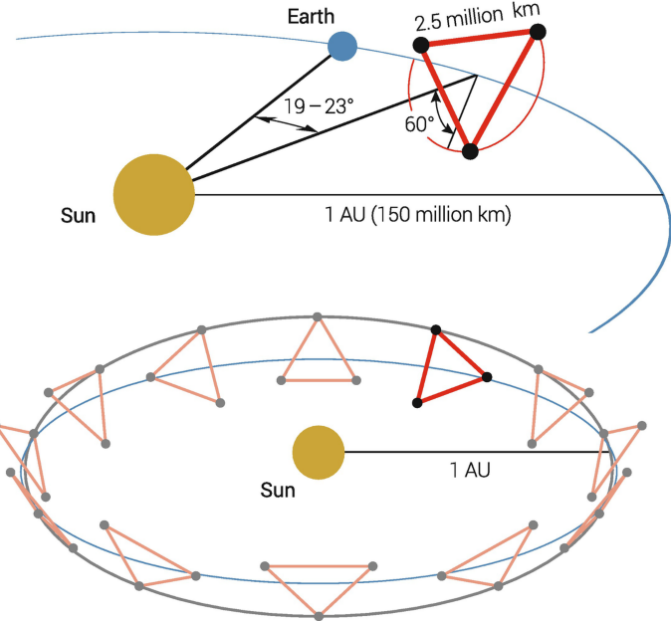


Figure 1.3: Drawing of LISA and its heliocentric orbit. Above: The equilateral triangle follows the Earth with a separation angle of $\sim 20^\circ$ separation, meaning approximately 5×10^{10} m distance from the Earth [19]. The center of the triangle lies on the ecliptic plane, and the triangle itself will form a 60° with the ecliptic plane. Bottom: depiction of the rotation of the constellation during the orbit. Figure from LISA Mission Consortium, adapted from [20].

relative armlength variations up to few percent, while the corner angle always lies within $60^\circ \pm 1^\circ$.

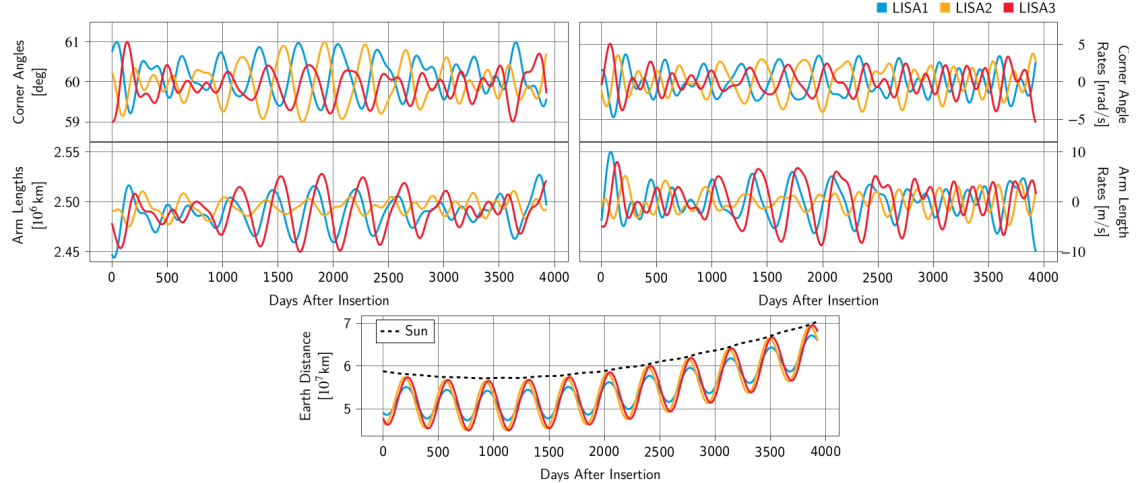


Figure 1.4: Graphs with the orbital parameters of the LISA mission. Figures from [17].

1.3.2 The Payload

The LISA payload faces numerous challenges to achieve its goal of measuring the separation between two TMs that are 2.5×10^9 m apart with \sim pm resolution. This subsection describes the subsystems contributing to reaching this requirement.

The Optical System

The optical system (OS) contains all the components needed for the interferometric measurement (see Figure 1.8). The OS consists of two MOSAs, one per laser link. Each MOSA holds an ensemble of gravity reference sensor (GRS), optical bench (OB) and telescope, and each GRS shields a test mass (TM). The TM-to-TM displacement measurement is split into 3 sub-measurements as depicted in Figure 1.8:

- The test mass interferometer (TMI) measures the displacement of the start TM with respect to its OB in the start spacecraft.
- The Long-Arm IFM, or inter-satellite interferometer (ISI) performs the inter-satellite measure of the displacement between the above mentioned OB in the start spacecraft and the corresponding OB in the end spacecraft.
- In the end spacecraft a second TMI measures again the displacement between the second OB and the end TM.

The TM-to-TM distance is evaluated by combining the three sub-measurements. Each sub-measurement has to reach the \sim pm resolution.

The main component of the OS is the OB, which is a Zerodur[®]² glass-ceramic plate with a diameter of approximately 450 mm [12], where all the needed optical components are attached, including photodiodes (PDs) and laser couplers. The optical components are distributed on both sides of the plate, with side A facing the telescope and side B facing the TM. The technique used for bonding the fused silica mirrors and beam splitters (BSs) onto the OB is hydroxide catalysis bonding [12].

Each OB hosts three beams and three IFMs. The beams are the beam received from the remote spacecraft (RX), the transmitted beam (TX) and the beam received from the other OB in the same spacecraft through the backlink fiber (LO). Side A of the OB hosts exclusively the ISI, which interferes the RX beam with the TX beam; on side B, the TMI interferes the TX beam after a reflection on the TM with the LO beam. A reference interferometer (RFI) is also present; this is placed on side B and interferes LO and TX beam without reflection on the TM. Its readout provides a phase reference in the other IFMs as well as an error signal for phase-locking [20]. A total of four QPDs per IFM are needed to measure each output port of the IFM redundantly (see Figure 1.5). One 4-lens imaging systems (ISs) is placed on each output port of each IFM for TTL mitigation (see Section 3.1) and beam compression. The measurements of both ports of an IFM are combined using *balanced detection*, a technique that uses the fact that the outputs of the two interferometric ports have a π shift to suppress correlated noises as relative intensity noise (RIN) (see 2.1.5) or straylight by subtracting them [33]. In the ISI, all photoreceivers (PRs) are operated continuously and simultaneously (hot-redundant) while in the TMI and RFI only two PRs are operated at any given time (i.e., two are nominal, and the other two are “cold redundant”).

Two additional mechanisms are present in the OB. The point-ahead angle mechanism (PAAM) is a very stable steering mirror that points the transmitted beam to

²Zerodur[®] is a lithium-aluminosilicate glass-ceramic with a very low coefficient of thermal expansion, about $2 \times 10^{-8} K^{-1}$, chosen to give a high thermal stability.

where the receiving spacecraft is going to be in a time $\tau = \frac{L}{c} \sim 8.3$ s. The beam alignment mechanisms (BAMs) uses a couple of rotatable glass slabs to laterally shift the TX and RX beam and correct for misalignments.

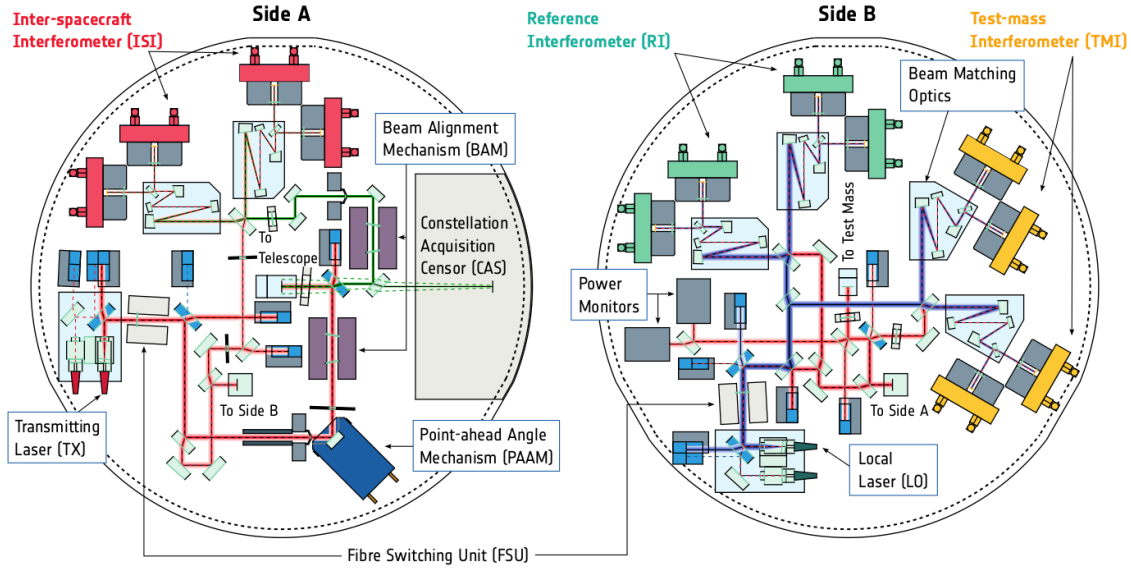


Figure 1.5: Representation of the LISA OB. The labeled beams are: TX - red, RX - green, LO beam - blue. Figure from [17].

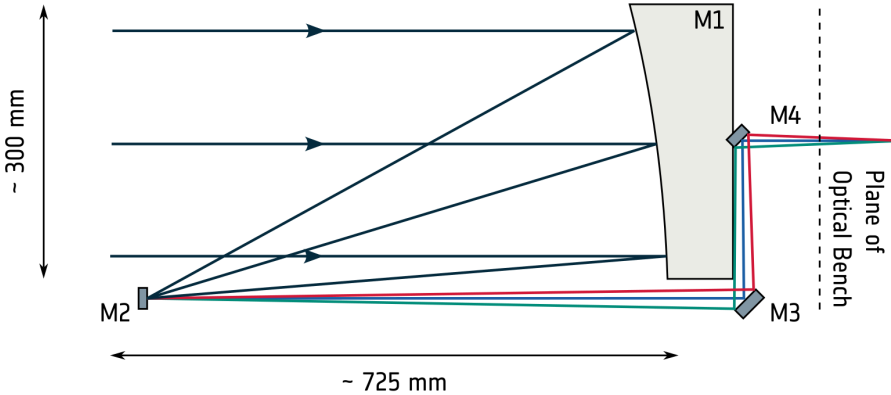


Figure 1.6: Representation of the LISA telescope, depicting also the imaging properties. Figure from [17].

The telescope (in Figure 1.6) collects light from the RX beam and directs it to the OB while simultaneously transmitting the TX beam with an appropriate beam profile. The telescope is an off-axis telescope with a main mirror diameter of 30 cm, a total length of 60 cm [20] and a magnification of ~ 134 [65] (see Subsection 2.2.2). Its design has the properties of an imaging system (IS), as it images the RX beam on an exit pupil, the RX-clip: any spacecraft rotation causes an effective magnified rotation of the RX beam around this pupil [65]. Because of the long inter-satellite baseline and its finite size, the telescope can only gather up to ~ 450 pW of laser power [30]. This makes a direct back reflection of the incoming beam unfeasible, as this would result in receiving about as little as 6.25×10^{-20} W of the sent power in the transmitting spacecraft [19]. In contrast to ground-based IFMs, LISA operates

in transponder mode, i.e. each satellite will return an amplified copy of the weak received RX beam to the transmitting spacecraft. This is achieved by measuring the phase of the RX beam and phase locking to it the TX beam's phase. This results in a total of 6 transponder links (2 per arm) [19].

The long baseline also leads to a main difference between the TMI and ISI: in the first case, the two interfered beams have a limited propagation length, are both fundamental Gaussian modes and have powers of the order of $\sim 100\ldots300\ \mu\text{W}$ [34]; in the latter case the received laser beam is a small portion of a huge and almost flat wavefront which is clipped and focused by the telescope.

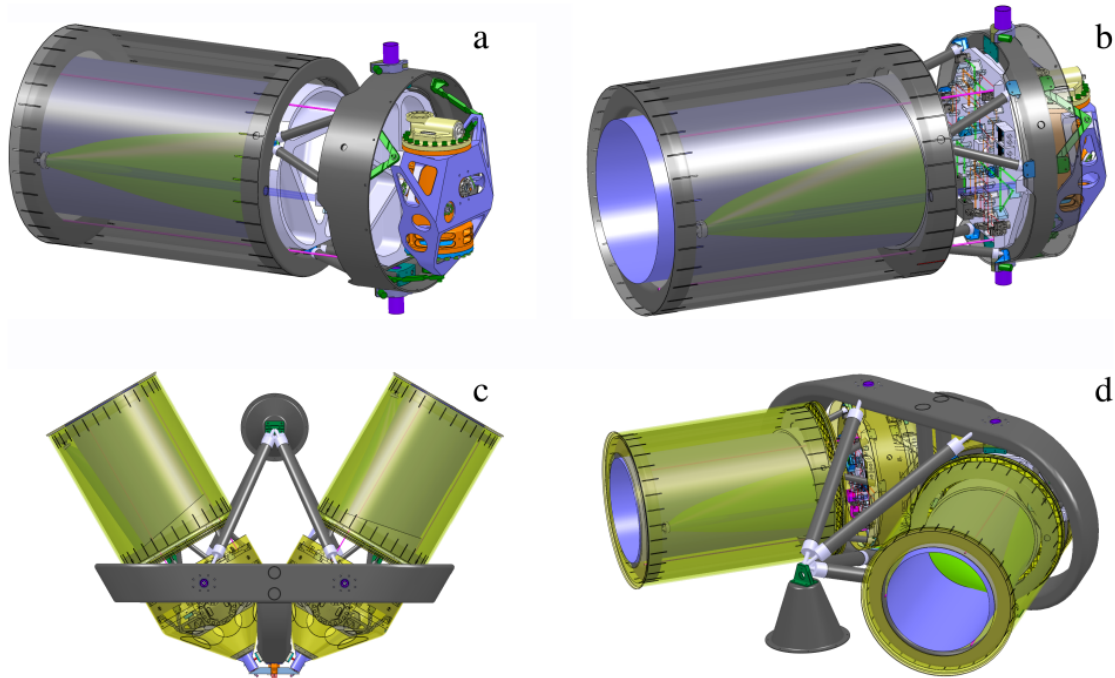


Figure 1.7: Drawing of the optical assembly with the two MOSAs. Each MOSA consists of the telescope, the OB and the GRS. The OB is orthogonal to the telescope's axis. A support ring holds both OB and GRS. The angle between the two telescopes is nominally 60° , but can be varied by $\pm 1.5^\circ$ using the optical assembly tracking mechanism (OATM). Figure from [20]

The relative velocities between the spacecraft cause time-dependent Doppler shifts between the laser beams in the range of $\pm 8\ \text{MHz}$ [42]. This setup does not allow LISA to operate as a homodyne IFM³. Hence a heterodyne interferometric detection system is employed⁴. The heterodyne interferometric detection system (comprising the lasers, PRs and PMs, among other instruments) imposes some limitations on the frequencies of the beat notes, which have to lie in the 5-25 MHz band [42]. To achieve this the laser beams has a controlled and time-dependent frequency offset, explained in detail in [42].

As mentioned in Subsection 1.3.1, the angle between the satellites is subject to variations of $\pm 1^\circ$. To correct for pointing error, each MOSA can be individually rotated about a vertical pivot axis for precision pointing toward their respective

³see Section 2.1.3

⁴see Section 2.1.3

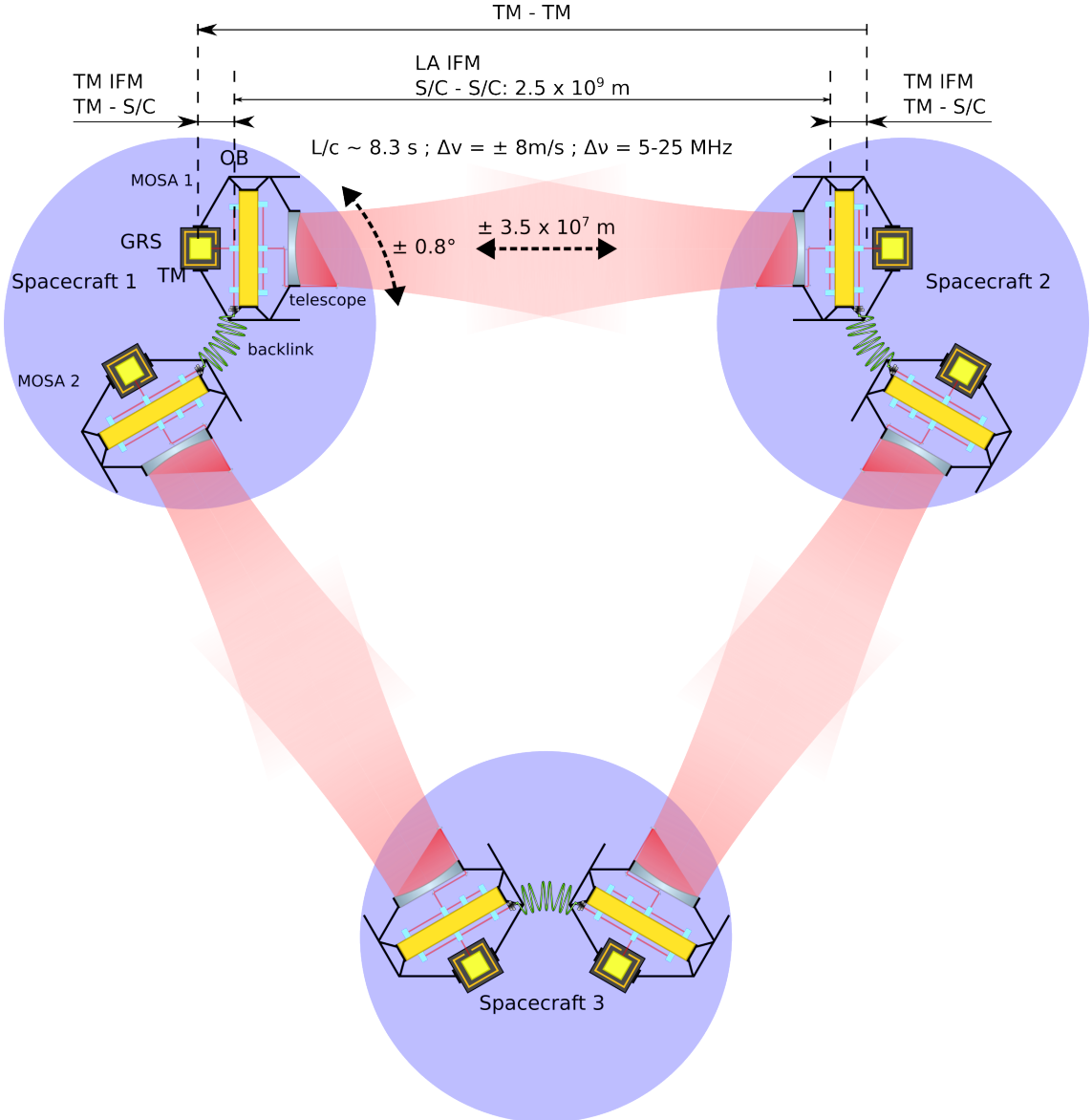


Figure 1.8: Schematic drawing of the OS in LISA’s spacecraft. Each spacecraft hosts 2 MOSAs, consisting of a GRS shielding a TM, an OBs and a telescope. The two OBs of a spacecraft are connected together by the backlink fiber. The TM to TM measurement subdivision is also illustrated on the top.

remote counterpart [3] by the OATM, with an actuation range of $\pm 1.5^\circ$. The optical assembly tracking mechanism (OATM) actuates on the ensemble of GRS, OB and telescope, and its angular jitter contributes to the total spacecraft pointing jitter. The expected spacecraft pointing jitter with respect to inertial space is expected to be $5 \text{ nrad}/\sqrt{\text{Hz}}$ [34].

The Test Masses

The TMs are 46 mm cubes with a weight of $m_{\text{TM}}=1.9282 \text{ kg}$ [34], made from a dense 73% gold and 27% platinum alloy. The mixing ratio of the two metals is chosen to have a high density and minimize magnetic susceptibility [17]. The TMs are shielded by the GRS.

The Laser System

The Laser System of LISA has to deliver sufficiently stable laser light in both frequency and amplitude. Each spacecraft hosts two lasers, one per OB. The planned system uses the master oscillator fiber power amplifier (MOFPA) approach, having as low-power master oscillator a Nd:YAG non-planar ring oscillator (NPRO) emitting 40mW of 1064nm light [20]. A small fraction of the light is used for frequency stabilization purposes. The remaining light is passed through an electro-optical modulator (EOM) which imprints phase sidebands for clock-transfer and ranging. After this a double-clad fiber amplifier brings the final power to 2W. The beam is linearly polarized to be able to separate transmitted and received beam [20].

The frequency stability is crucial for LISA. The above mentioned relative velocities lead to armlength differences up to $\Delta L \approx 3.5 \times 10^7$ m (see Figure 1.4). This leads to a massive coupling of laser frequency noise. To see this, one can compare the phase noise induced by frequency noise $\delta\phi_\nu$ (see equation (2.77)) and the phase shift induced on a beam of wavelength $\lambda = \frac{\nu}{c}$ propagating in an interferometric arm by the transit of a GW⁵.

$$\Delta\phi_{gw} \approx 2\pi\nu h \frac{2L}{c} \quad \delta\phi_\nu = 2\pi \frac{\Delta L}{c} \delta\nu \quad (1.12)$$

In order to detect a GW, the phase shift induced by it must be much larger than that induced from frequency noise, or $\Delta\phi_{gw} \gg \delta\phi_\nu$. This statement can be rearranged using the two equations in (1.12) as

$$\frac{\delta\nu}{\nu} \gg h \frac{2L}{\Delta L}. \quad (1.13)$$

Plugging in LISA's typical values of $h \approx 10^{-20}$ and $\frac{\Delta L}{L} \sim 10^{-2}$, the right-hand side of expression (1.13) is $\sim 10^{-18}$. This fractional frequency stability is orders of magnitude away from what is reachable with current laser technology, making this a main challenge. The solution adopted in LISA uses two steps. First, frequency stabilization: the free-running laser would have a fractional frequency stability of $\sim 10^{-10}$. The stabilization by means of an ultra-stable reference cavity improves this to $\sim 10^{-13}$ in the LISA detection band. The second step takes place in post-processing and aims to remove the phase signal caused by the frequency noise using a technique called time delayed interferometry (TDI) [71]. This technique consists of time shifting and combining the individual IFMs' outputs to synthesize virtual interferometric arms with a much smaller armlength difference of the order of $\Delta L_{TDI} \sim 1$ m [19]. This effectively reduces the required fractional frequency stability to $\sim 10^{-11}$, satisfying expression (1.13). To time-shift the measured phase signals, TDI requires the knowledge of the absolute distance between the spacecraft with a precision of the order of 1 m. This is achieved by a pseudo-ranging measurement, which is realized by imprinting a pseudo-random phase modulation onto the laser beams [34] and a delay-locked loop similarly to the GPS [70].

The fractional power stability of the laser must be

- as low as $10^{-4}/\sqrt{\text{Hz}}$ in the detection band to keep the radiation pressure noise

⁵for simplicity, the case where the GW's frequency much lower than the inverse of the round trip time $\tau_{tr} = \frac{2L}{c}$ of the arm (see equation 2.65) is used.

below $3.4 \times 10^{-16} \text{ m/s}^2/\sqrt{\text{Hz}}$ [34, 13] (see equation (1.14)).

$$\delta a_{\text{TM}} = \frac{2}{c m_{\text{TM}}} \delta P \quad (1.14)$$

where m_{TM} is the mass of the TM, δP is the power variation and δa_{TM} is the variation of the TM's acceleration,

- as low as $10^{-8}/\sqrt{\text{Hz}}$ in the 5-50 MHz bandwidth to limit RIN induced phase noise [13] (see Subsection 2.1.5).

The Drag-Free Attitude Control System

The drag-free attitude control system (DFACS) is the subsystem responsible for making LISA's environment as quiet as possible. The principle of operation is to keep the TMs in a state of nearly free-fall by measuring the position and orientation of the TM with respect to the spacecraft, applying a control law and commands to the micro-newton thrusters such that the relative position of orientation of the spacecraft with respect to the TM is maintained [20]. The spacecraft is affected by external forces such as solar radiation pressure, interaction with solar wind and impacts with micrometeoroids. The TMs situated inside the spacecraft are shielded from these external disturbances, but the spacecraft is actively controlled to follow the TMs's geodetic motion. As each LISA spacecraft hosts two TMs, it is impossible to keep both of them in free-fall condition in all degrees of freedom and simultaneously ensure that the TMs stay at their nominal position with respect to the OB [20]. However, it is sufficient to maintain free fall in the direction of the sensitive axes⁶. This can be achieved by controlling the “non-sensitive” degrees of freedom of the test masses and the position and attitude of the spacecraft. Many other forces have to be mitigated in order to maintain a certain degree of free-fall purity in both TMs:

- gravitational force; this force cannot be shielded, and the mass distribution of the spacecraft itself can cause significant disturbances to the TMs. The spacecraft has to be modelled in detail to allow the analysis of mass imbalances and limit gravity gradients [20].
- magnetic forces; these can cause non-gravitational accelerations of the TM because of its non-zero magnetic susceptibility [20].
- electromagnetic forces due to TM's charge; such charge build-up may arise because of interaction with solar wind and cosmic rays. The GRS features fibers for injection of UV light for photoelectric discharge of the TM [19].
- forces from radiometric effect might arise from temperature fluctuations and residual outgassing [20]. For this reason, temperature variations must not exceed $10^{-5} \text{ K}/\sqrt{\text{Hz}}$ at the TMs. Despite being in space, a vacuum system is needed to keep the pressure at 10^{-8} mbar .

The GRS is the main component of the DFACS. The GRS is the housing enclosing a TM, which ensures the drag-free operation, i.e. the effective free-fall of each TM. The GRS's core consists of electrodes, at several mm separation from the test

⁶The sensitive axis is the axis being probed by the TMI and by the ISI.

mass, used for $\text{nm}/\sqrt{\text{Hz}}$ precision capacitive sensing and nN -level electrostatic force actuation in all "non-sensitive" degrees of freedom[19]. Such electrodes are used for the capacitive measurement of the relative position of TM and spacecraft. The TM's stability inside the GRS is expected to be of $1 \text{ nm}/\sqrt{\text{Hz}}$ translational jitter with respect to the OB, and $10 \text{ nrad}/\sqrt{\text{Hz}}$ angular stability with respect to the OB.

The Phase Measurement

The Phase Measurement is the process of extraction of the phase information from the beat notes. This task is carried out by a dedicated instrument, the phasemeter (PM). The LISA PM is based on the digital phase-locked loop (DPLL) scheme shown in Figure 1.9. This scheme is capable of extracting all three instantaneous amplitude, frequency and phase information from the beat note. The working principle is explained in more detail in [8]. Note that a DPLL acts on the beat note output of one segment of a QPD, and hence 4 DPLLs are needed to track a QPR in the simplest scheme⁷. A scheme of the DPLL is shown in Figure 1.9.

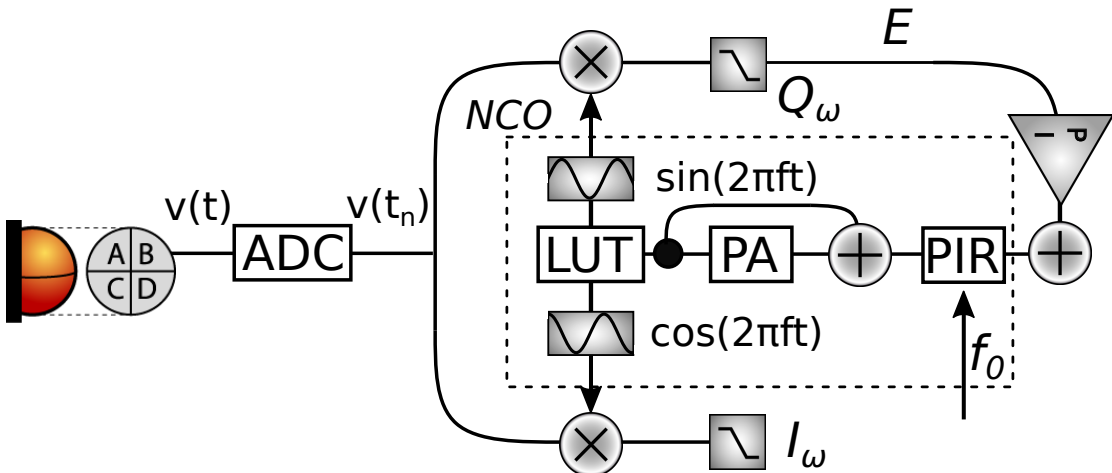


Figure 1.9: Scheme of a digital phase-locked loop (DPLL). The voltage signal from the PD is first digitized by the analog to digital converter (ADC). A mixer and low-pass filter are used to generate the Q and I signals. The Q signal is used as error signal in a proportional-integral (PI)-servo to drive the numerically controller oscillator (NCO). The DPLL outputs the phase increment register (PIR) (instantaneous frequency), phase accumulator (PA) (instantaneous phase), I (instantaneous amplitude) and Q (error signal). Together, these quantities fully describe $v(t)$.

The voltage signal from a photoreceiver (PR)'s channel is a beat note with time-dependent amplitude $A(t)$, frequency $f(t)$ and phase $\varphi(t)$.

$$v(t) = A(t) \sin(2\pi f(t)t + \varphi(t)) \quad (1.15)$$

This signal is digitized by an ADC with sampling frequency f_{samp} , with corresponding sampling period $t_{\text{samp}} = \frac{1}{f_{\text{samp}}}$. The sampling frequency must be high enough such that the Nyquist frequency exceeds the frequency of the highest occurring beat note in the system [20], which is 25 MHz [42]; $f_{\text{samp}} = 80 \text{ MHz}$ has been chosen [17]. Due to limited bandwidth, the DPLL can only track changes of A , f and φ which

⁷More details about this will come in chapter 7

take place on timescales much larger than the sampling period t_{samp} . More in detail, an example of transfer function (TF) of the DPLL is shown in Figure 1.10.

The whole process takes place in the digital domain. The signal is mixed in two quadratures with a digital sine/cosine wave of the same frequency and phase generated by a NCO, resulting in the Q and I signals. The obtained signals have a \sim DC component and a second harmonic ($2f$) component; low pass filtering⁸ eliminates the second harmonic.

$$\text{LPF}[v(t) \cdot \sin(2\pi f + \varphi)] = Q \propto \Delta\varphi \quad (1.16)$$

$$\text{LPF}[v(t) \cdot \cos(2\pi f + \varphi)] = I \propto A \quad (1.17)$$

The PI controller keeps the Q signal very close to zero by actuating on the NCO's frequency; the purpose of this scheme is to make the NCO create a tracking copy of the PR's signal. The NCO consists of a phase increment register (PIR), phase accumulator (PA) and of cosine and sine look up tables (LUTs). The loop needs an initial guess f_0 of the instantaneous frequency to lock. This value is set as the initial value of the PIR. At each iteration the PIR is updated, allowing the calculation of the phase.

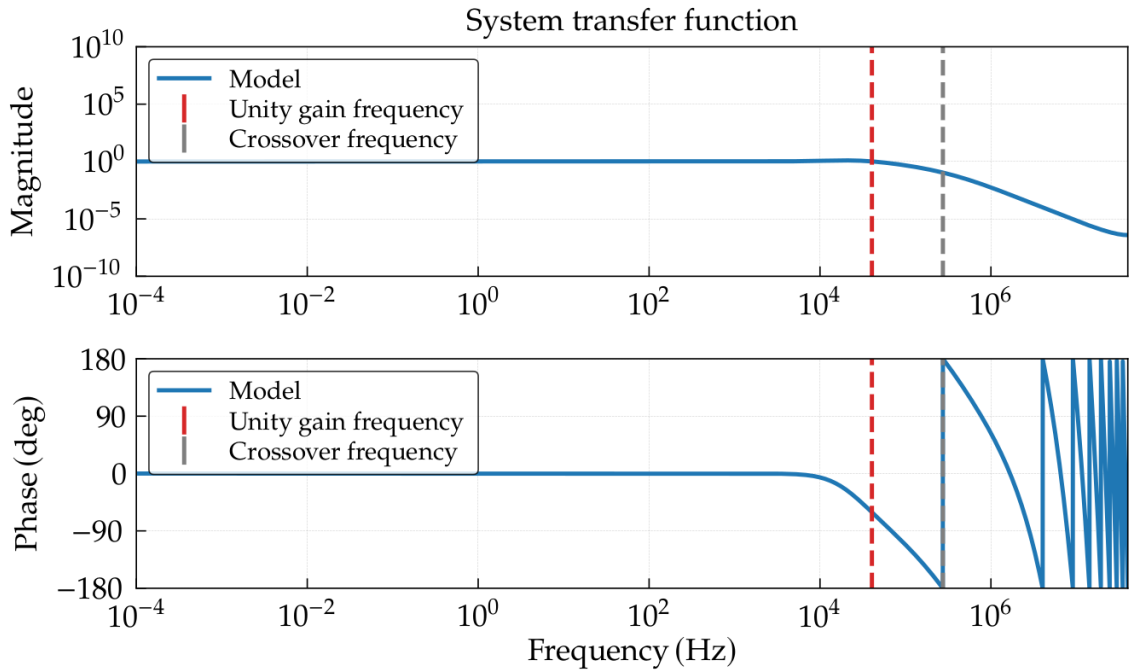


Figure 1.10: Example of TF of the DPLL from [9]. The unity gain frequency of the loop is around 40 kHz and phase margin is $\sim 59^\circ$.

This frequency data are used to reconstruct the signal's phase changes over time $\varphi(t_n)$ as a cumulative sum of the instantaneous frequency values $f(t_i)$.

$$\varphi(t_n) = 2\pi \frac{1}{f_{\text{samp}}} \sum_{i=1}^n f(t_i) \quad (1.18)$$

The PA represents the instantaneous phase of the signal. Finally, the I signal represents the instantaneous amplitude of the signal. For performance reasons,

⁸indicated with the LPF operator in the equation

these operations are implemented in a field-programmable gate array (FPGA) [20]. The required phase reconstruction performance is $2\pi \frac{\text{pm}/\sqrt{\text{Hz}}}{1064\text{nm}} \approx 6\mu\text{rad}/\sqrt{\text{Hz}}$.

A critical point of this scheme is the ADC's sample time jitter: during digitization, the signal is sampled according to the provided ADC clock. A jitter of this clock, combined with time jitter by the ADC itself, causes a phase change in the measured signals. The amplitude spectral density (ASD) of this noise $\tilde{\varphi}_{\text{cj}}(f)$ depends on the signal's frequency f_{signal} and on the ASD of the timing jitter $\tilde{\tau}(f)$.

$$\tilde{\varphi}_{\text{cj}}(f) = 2\pi f_{\text{signal}} \tilde{\tau}(f) \quad (1.19)$$

Unfortunately, all ADCs under test fail this requirement and spoil the system performance [8] for beat notes higher than ~ 5 MHz. This issue can be solved in post-processing by measuring the timing jitter at the ADC. This is done by adding a reference tone to the measured signal; such a tone is called pilot tone (PT). The PT is affected by the same ADC jitter as the main signal. The PT phase correction of the main signal is performed using equation (1.20), where $f_{\text{sig.}}$ is the frequency of the main signal, f_{PT} is the frequency of the PT and φ_{PT} is the measured phase of the PT.

$$\varphi_{\text{sig. cor}} = \varphi_{\text{sig.}} - \varphi_{\text{PT}} \frac{f_{\text{sig.}}}{f_{\text{PT}}} \quad (1.20)$$

1.3.3 The Sensitivity

The expected sensitivity of LISA is shown in Figure 1.11. Since it depends on time, sky location of the source and polarization of the GW, it is conventionally averaged on these parameters. LISA's sensitivity is limited at low frequencies ($< 1\text{mHz}$) by the residual acceleration noise of the TMs, while at higher frequencies ($> 100\text{mHz}$) it is limited by the arm's response. This is due to the fact that the period of the GWs is shorter than the round-trip period of light (see Section 2.1.4). In the "bucket" region, between 1 mHz and 100 mHz, the sensitivity is limited by the interferometric sensing noise, mainly shot noise in the ISI [34], at a level of $10 \text{ pm}/\sqrt{\text{Hz}}$ around 10 mHz, or strain noise of $\sim 10^{-20}/\sqrt{\text{Hz}}$.

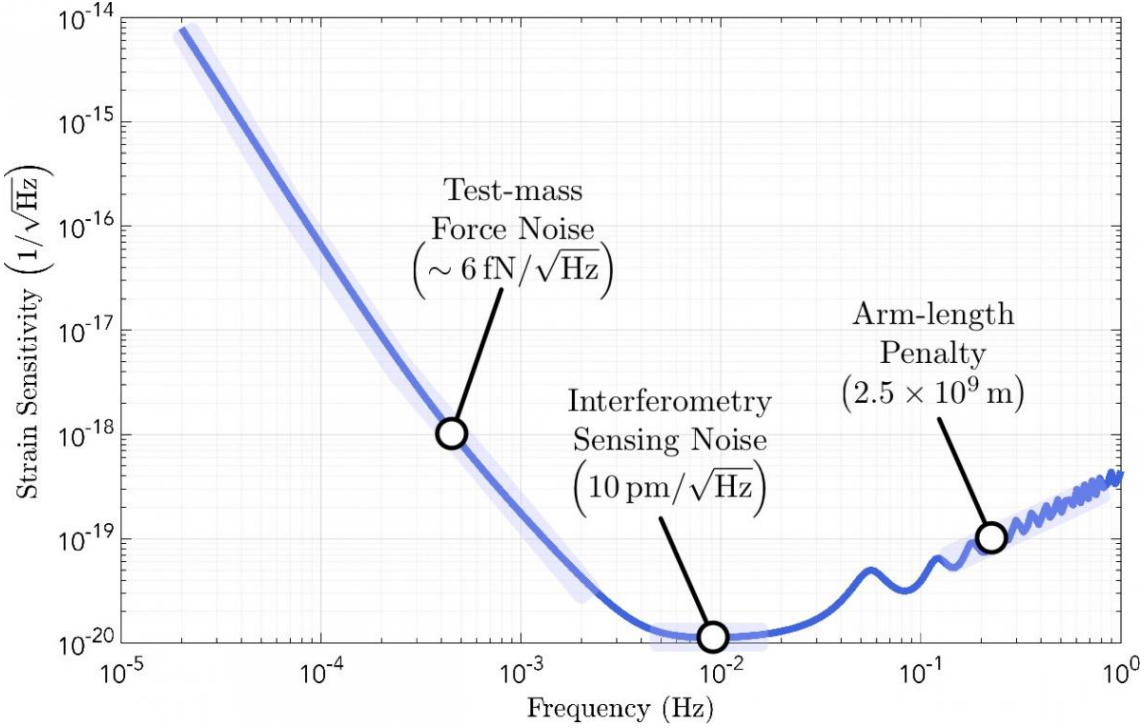


Figure 1.11: ASD of the time, sky and polarization averaged strain sensitivity of LISA. Figure from [19]

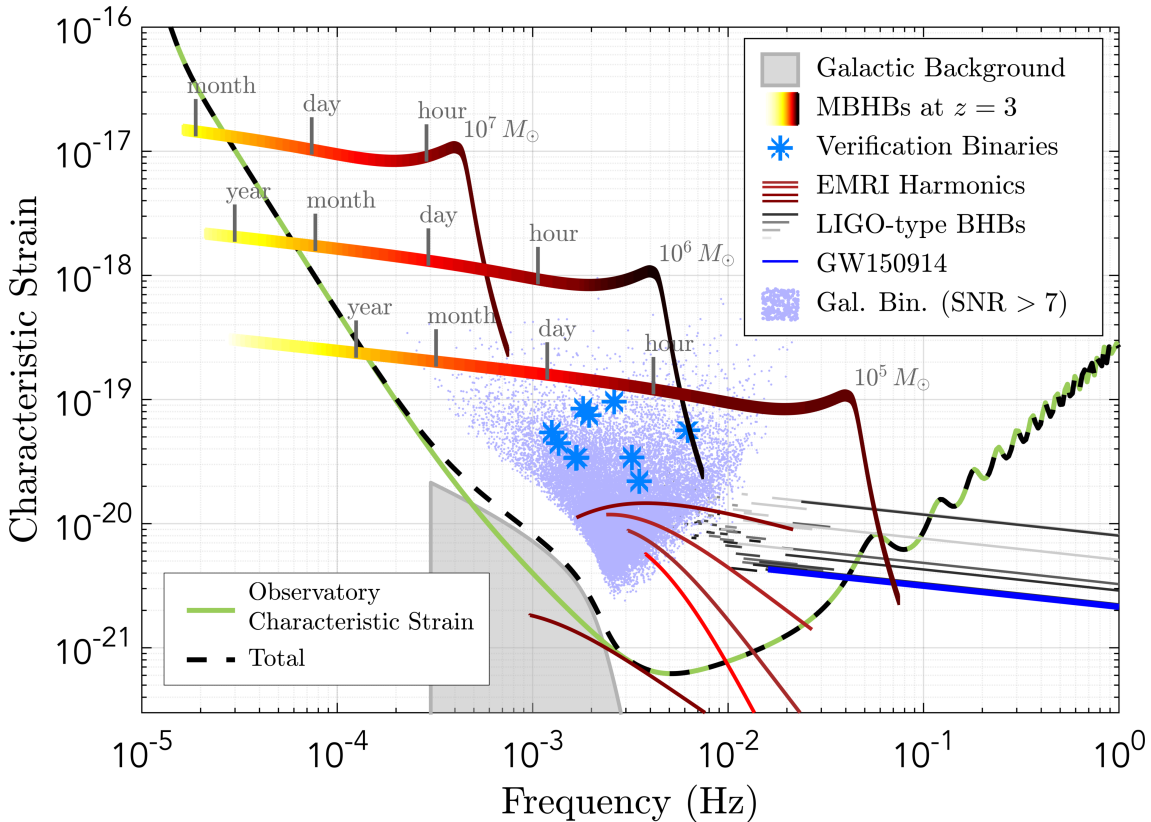


Figure 1.12: Examples of GW sources in the LISA band and LISA's sensitivity in a 3-arm configuration. Figure from [4]

Chapter 2

Interferometric Signals with Quadrant Photodiodes

This chapter introduces the main concepts used in this thesis. The first section introduces a mathematical description of Gaussian beams and beam overlap, followed by interferometers (IFMs), the effect of a gravitational wave (GW) on an interferometer's arm and the noises which affect interferometric measurements. The second section briefly introduces ray transfer matrices, which are used to describe imaging systems (ISs). The last section introduces quadrant photodiodes (QPDs) and the signals which are measured with them, namely differential power sensing (DPS), longitudinal pathlength sensing (LPS), differential wavefront-sensing (DWS). DWS is mathematically modelled in detail as of major relevance throughout the whole thesis.

2.1 Gaussian Beams and Interferometry

2.1.1 Gaussian Beams

For a detailed description of Gaussian laser beams, see [69] or [51]. A laser beam is an electromagnetic field propagating in space. Since the magnetic field mimics the electric field's behaviour, only one of the two needs to be described, and the electric field is traditionally chosen. An electric field $\vec{E}(t, \vec{x})$ propagating in a vacuum obeys the equation

$$\left[-\frac{1}{c^2} \frac{\partial^2}{\partial t^2} + \nabla^2 \right] \vec{E}(t, \vec{x}) = 0. \quad (2.1)$$

Taking a monochromatic component of frequency $\nu = \omega/2\pi$ of $\vec{E}(t, \vec{x})$, this can be factorized as $\vec{E}(t, \vec{x}) = \vec{E}(\vec{x})e^{-i\omega t}$, and replacing this expression in equation (2.1) one gets that $\vec{E}(\vec{x})$ must obey

$$(\nabla^2 + k^2) \vec{E}(\vec{x})e^{-i\omega t} = 0, \quad (2.2)$$

with $k = \frac{2\pi}{\lambda} = \frac{\omega}{c}$, which is called Helmholtz equation. The oscillatory term $e^{-i\omega t}$ is going to be neglected for the remainder of this chapter.

It can be of physical interest to look for solutions of the Helmholtz equation (2.2) where the angle between the vectors normal to the wavefronts¹ and the beam's

¹the 2-dimensional varieties where the phase of the beam is constant.

propagation direction is small. Fixing z to be the electromagnetic field's propagation direction, this can be formalized as

$$\vec{E}(\vec{x}) = \hat{\varepsilon}_p \mathcal{E}(z; x, y) e^{ikz}, \quad (2.3)$$

where $\hat{\varepsilon}_p$ is a generic polarization versor with $|\hat{\varepsilon}_p| = 1$, $|\hat{\varepsilon}_p| \perp \hat{\varepsilon}_z$ and $\mathcal{E}(z; x, y)$ is a slowly varying function of z , such that its dependence on z manifests only for $z \gg k$. This can be summarized in the conditions

$$\left| \frac{\partial^2 \mathcal{E}}{\partial z^2} \right| \ll \left| 2k \frac{\partial \mathcal{E}}{\partial z} \right|, \left| \frac{\partial^2 \mathcal{E}}{\partial x^2} \right|, \left| \frac{\partial^2 \mathcal{E}}{\partial y^2} \right|. \quad (2.4)$$

Applying these conditions to equation (2.2), one obtains the *paraxial approximation*

$$\frac{\partial^2 \mathcal{E}}{\partial x^2} + \frac{\partial^2 \mathcal{E}}{\partial y^2} - 2ki \frac{\partial \mathcal{E}}{\partial z} = 0. \quad (2.5)$$

Equation (2.5) is a partial differential equation which admits infinitely many solutions. The simplest solution is called fundamental mode E_{00} or transverse electromagnetic₀₀ (TEM₀₀) and takes the form

$$\mathcal{E}_{00}(z; x, y) = E_0 \sqrt{\frac{2}{\pi}} \frac{w_0}{w(z)} \exp\left(-\frac{x^2 + y^2}{w(z)^2}\right) \exp\left(i\left(\frac{k(x^2 + y^2)}{2R(z)} + \eta(z) + kz\right)\right), \quad (2.6)$$

where $E_0 \in \mathbb{R}_+$ [V/m] is the amplitude scaling factor, z [m] is the distance from the waist, which is positioned at $z = z_0$ [m], $\varphi = kz$ is the phase that the beam accumulates during propagation, w_0 [m] is the beam radius at the waist and $w(z)$ in equation (2.7) is the local beam radius or spot size.

$$w(z) = w_0 \sqrt{1 + \left(\frac{z}{z_R}\right)^2} \quad (2.7)$$

The geometrical meaning of the spot size is to be the distance from the center for which the intensity decreases by a factor $e^{-2} \sim 13.5\%$ with respect to its maximum value at the beam's center. The parameter z_R [m] is the Rayleigh range which is related to the waist by

$$z_R = \frac{\pi w_0^2}{\lambda} \quad (2.8)$$

and has the geometrical meaning of being the length over which the beam is rather collimated. λ [m] is the wavelength of the beam, and k [1/m] is the wave number

$$k = \frac{2\pi}{\lambda}. \quad (2.9)$$

Far away from the waist, i.e. where $z \gg z_R$, the beam diverges. Equation (2.7) can be approximated to

$$w(z) \approx w_0 \frac{z}{z_R} = \Theta z \text{ with } \Theta = \frac{w_0}{z_R} = \frac{\lambda}{\pi w_0}, \quad (2.10)$$

where Θ is divergence angle. Note that the smaller the waist, the shorter the Rayleigh range and the bigger the divergence angle. $R(z)$ [m] is the curvature radius

$$R(z) = z \left(1 + \left(\frac{z_R}{z}\right)^2\right) \quad (2.11)$$

which is infinite at the waist position, $R(z = 0^\pm) = \pm\infty$, and asymptotically zero at infinity, $R(\pm\infty) = \pm\infty$, and has a minimum of $R(z = \pm z_R) = \pm 2z_R$. Finally, the $\eta(z)$ term is the *guoy phase*

$$\eta(z) = \arctan\left(\frac{z}{z_R}\right), \quad (2.12)$$

which is an extra phase term that a Gaussian beam accumulates with respect to a plane wave. To recover the vectorial nature of the electric field, the polarization vedor has to be added, giving

$$\vec{E}_{00}(z; x, y) = \hat{\varepsilon}_p \mathcal{E}_{00}(z; x, y) e^{-ikz}. \quad (2.13)$$

The intensity $[\frac{W}{m^2}]$ of the beam is proportional to the squared modulus of the electric field

$$I(z; x, y) = \frac{|E(z; x, y)|^2}{2Z}, \quad (2.14)$$

where $Z [\Omega]$ is the wave impedance of the medium in which the beam is propagating. For a fundamental Gaussian beam (2.13) this gives

$$I(z; x, y) = I_0 \frac{2}{\pi} \left(\frac{w_0}{w(z)} \right)^2 \exp\left(-2 \frac{x^2 + y^2}{w(z)^2}\right), \quad (2.15)$$

where $I_0 = \frac{|E_0|^2}{2Z}$. The total power of the beam (2.13) can be found by integrating the intensity in equation (2.15) over an infinite surface on the xy plane.

$$P_0 = \int_{\mathbb{R}} \int_{\mathbb{R}} dx dy I(z; x, y) = I_0 w_0^2 \quad (2.16)$$

The power P_\circ impinging on a circular portion of plane centered around $z = 0$ and of radius r can be derived from equation (2.15) and is

$$P_\circ = P_0 (1 - e^{-\rho^2}) \quad \rho = \frac{\sqrt{2}r}{w(z)}. \quad (2.17)$$

The other possible solutions to equation (2.5) are called higher-order modes. These are an infinite set of solutions that can be collected in a base. The most used bases are the Hermite-Gauss and the Laguerre-Gauss bases, which make use of Hermite polynomials and generalized Laguerre polynomials, respectively. For example, Hermite-Gauss modes are given by

$$H_{ij}(x, y, z) = \frac{1}{\sqrt{2^{i+j-1} \pi i! j!}} \frac{w_0}{w(z)} H_i \left(\frac{x\sqrt{2}}{w(z)} \right) H_j \left(\frac{y\sqrt{2}}{w(z)} \right) \exp\left(-\frac{x^2 + y^2}{w(z)^2}\right) \exp\left(-i \left(\frac{k(x^2 + y^2)}{2R(z)} - (i + j + 1)\eta(z) \right)\right), \quad (2.18)$$

where $i, j \geq 0$. $H_i(x)$ are the Hermite polynomials of order i . Such modes appear with propagation because of misalignments and spurious reflections. Notice that higher order modes accumulate a different guoy phase according to their order.

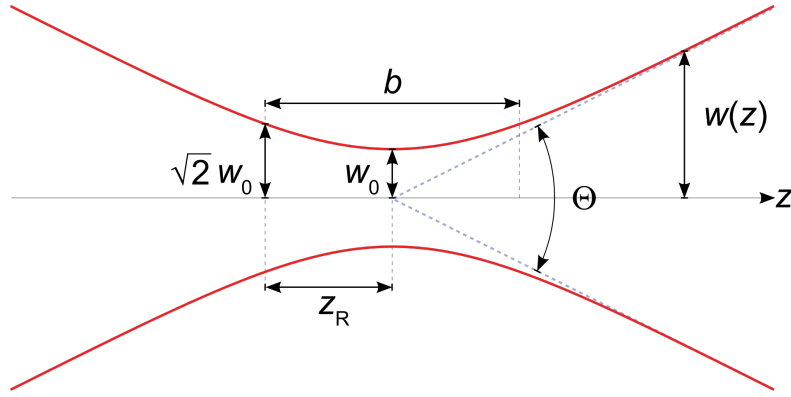


Figure 2.1: Left: Schematic representation of the profile of a fundamental mode Gaussian beam. The waist w_0 is the minimum width of the beam at its center. Departing from the waist position and symmetrically in both directions, the beam width $w(z)$ increases according to equation (2.7). For distances larger than z_R , $w(z)$ can be approximated using (2.10). Source https://en.wikipedia.org/wiki/Gaussian_beam.

Short application to LISA. Assuming a received beam is a $w_0 \approx r = 15$ cm radius beam with waist position situated on the next spacecraft $d \approx 2.5 \times 10^9$ m separation, the fraction of the received beam's power f gathered by the $r = 15$ cm radius telescope is

$$w(d) \approx \Theta d = \frac{\lambda}{\pi w_0} d = \frac{\lambda}{\pi r} d = 5.65 \times 10^3 \text{ m}$$

$$f = \left[1 - \exp \left(-2 \frac{r^2}{w(d)^2} \right) \right] \approx 2 \frac{r^2}{w(d)^2} = \frac{2\pi^2 r^4}{\lambda^2 d^2} = 1.41 \times 10^{-9}.$$

2.1.2 Beam Superposition

When two beams $\vec{E}_1(z; x, y)$ and $\vec{E}_2(z; x, y)$ are interfered, the electric fields have to be summed.

$$\vec{E}_{\text{total}}(z; x, y) = \vec{E}_1(z; x, y) + \vec{E}_2(z; x, y) \quad (2.19)$$

As the intensity of the total electric field is calculated using equation (2.14), the interference term appears.

$$I_{\text{total}}(z; x, y) = \frac{1}{2Z} \left[\underbrace{|E_1(z; x, y)|^2 + |E_2(z; x, y)|^2}_{\text{DC intensity}} + \underbrace{\hat{\varepsilon}_{p, 1} \cdot \hat{\varepsilon}_{p, 2} (E_1(z; x, y) E_2(z; x, y)^* + E_1(z; x, y)^* E_2(z; x, y))}_{\text{interference intensity term}} \right] \quad (2.20)$$

The power measured by a PD located at $z = z_{\text{PD}}$ is the integral of (2.20) over the PD's surface S_{PD} is

$$\begin{aligned} P_{\text{total, PD}} = & \frac{1}{2Z} \left[\int_{S_{\text{PD}}} dS |\vec{E}_1(z_{\text{PD}}; x, y)|^2 + \int_{S_{\text{PD}}} dS |\vec{E}_2(z_{\text{PD}}; x, y)|^2 + \right. \\ & + \hat{\varepsilon}_{p,1} \cdot \hat{\varepsilon}_{p,2} \left(\int_{S_{\text{PD}}} dS \vec{E}_1(z_{\text{PD}}; x, y) \vec{E}_2(z_{\text{PD}}; x, y)^* + \right. \\ & \left. \left. + \int_{S_{\text{PD}}} dS \vec{E}_1(z_{\text{PD}}; x, y)^* \vec{E}_2(z_{\text{PD}}; x, y) \right) \right]. \end{aligned} \quad (2.21)$$

From now on the dependence of \vec{E} on z_{PD} will be omitted. It is convenient to define the overlap integral $I_{\text{overlap}} \in \mathbb{C}$ of the two beams as [80]:

$$I_{\text{overlap}} = \hat{\varepsilon}_{p,1} \cdot \hat{\varepsilon}_{p,2} \frac{\int_{S_{\text{PD}}} dS \vec{E}_1(x, y) \vec{E}_2(x, y)^*}{\sqrt{\int_{S_{\text{PD}}} dS |\vec{E}_1(x, y)|^2} \sqrt{\int_{S_{\text{PD}}} dS |\vec{E}_2(x, y)|^2}} = \sqrt{\eta_{\text{het}}} e^{i\psi}, \quad (2.22)$$

where $0 \leq \sqrt{\eta_{\text{het}}} \leq 1$ is the *heterodyne efficiency*. This parameter depends only on the PD and beams' geometry, which quantifies the spatial overlap of the two beams and hence the 'quality' of the interference. When considering a QPD, the heterodyne efficiency can be calculated for each segment. Then equation (2.21) can then be rewritten as

$$P_{\text{total, PD}} = P_{1,\text{PD}} + P_{2,\text{PD}} + 2\sqrt{\eta_{\text{het}} P_{1,\text{PD}} P_{2,\text{PD}}} \cos(\psi). \quad (2.23)$$

For two generic Gaussian beams with same linear polarization, generic phases $\varphi_i = kz_i$ and detected with an infinite area single element photodiode (SEPD), the overlap integral in equation (2.22) takes the form [78]

$$I_{\text{overlap, GB-GB}} = 2 \frac{1}{w_1(z)} \frac{1}{w_2(z)} \frac{e^{i(\Delta\varphi + \Delta\eta)}}{\sqrt{\frac{1}{w_{\text{eff}}^4} + \frac{k^2}{4R_{\text{rel}}^2}}} e^{i \arctan\left(\frac{kw_{\text{eff}}^2}{2R_{\text{rel}}}\right)}, \quad (2.24)$$

where the used quantities are

$$\frac{1}{w_{\text{eff}}^2} = \frac{1}{w_1^2(z)} + \frac{1}{w_2^2(z)} \quad \frac{1}{R_{\text{rel}}} = \frac{1}{R_1(z)} - \frac{1}{R_2(z)} \quad (2.25)$$

$$\Delta\varphi = k(z_1 - z_2) \quad \Delta\eta = \eta_1(z) - \eta_2(z). \quad (2.26)$$

In the case of a plane wave and a Gaussian beam, describing the plane wave as $\vec{E}_{\text{plane}}(x, y) = \vec{E}_P e^{ikz_P}$ with $\int_{S_{\text{PD}}} dS |\vec{E}_{\text{plane}}(x, y)|^2 = |E_P|^2 S_{\text{PD}}$, assuming that the Gaussian beam is fully detected by the SEPD, and that the SEPD is round hence the area is $S_{\text{PD}} = \pi r_{\text{PD}}^2$, the overlap integral takes the very simple form

$$I_{\text{overlap, GB-PW}} = \frac{\sqrt{2}w_0}{r_{\text{PD}}} e^{i \arctan\left(\frac{kw(z)^2}{2R(z)}\right)} e^{i(\eta(z) + \Delta\varphi)}, \quad (2.27)$$

where $\Delta\varphi = k(z_1 - z_P)$.

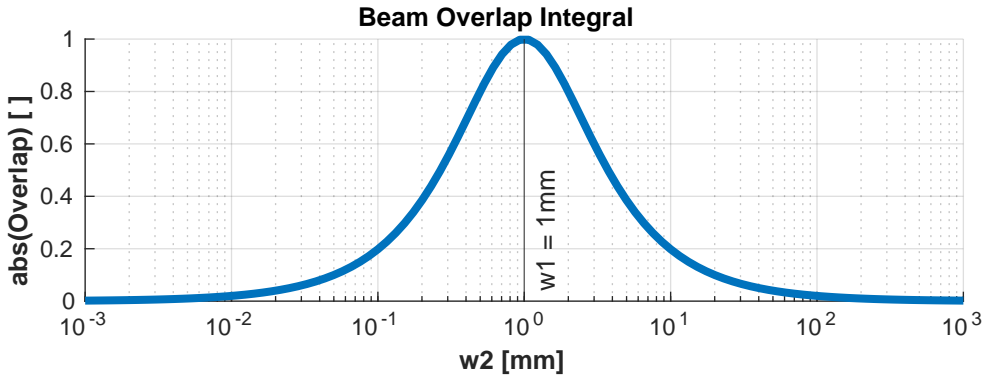


Figure 2.2: Plot of $|I_{\text{overlap, GB-GB}}|$ from equation (2.24) for $R_{\text{rel}} = \infty$. Gaussian beam overlap looks like a resonance curve as the overlap is maximum if the two beam sizes are identical.

2.1.3 Interferometers

Interferometry (from latin *intēr* (= inbetween) + *fēro* (to bring) + *mētior* (= to measure), to be used acronym IFM) is a technique which uses the interference of superimposed waves, such as electromagnetic waves, to extract information. This technique is applied when the used electromagnetic wave's frequency is very high ($> 10^{10}$ Hz), making it impossible to follow both the amplitude and phase of a beam individually, as, for instance, radiotelescopes do. In such case, an additional beam must be interfered, and the phase-difference-dependent power is measured. IFMs are largely used for their high sensitivity to measure microscopic displacements, refractive index changes or irregularities of surfaces. Several interferometric topologies exist, depending on the needs and purposes.

The (Homodyne) Michelson Interferometer

This Sub-subsection briefly explains how a Michelson IFM works in its most straightforward conceptual scheme, as it is the current standard for ground-based GW detectors. Michelson and Morley used a similar device to prove the non-existence of ether [51].

The layout described here is shown in Figure 2.3. The beam source is a monochromatic laser light source, which generates a single laser beam. This beam is sent to a 50-50 ratio beam splitter (BS). The beam is split into two equal power and equal phase beams, with perpendicular propagation directions, x and y . At the end of both arms, two mirrors, M_x and M_y reflect each beam backwards. The two beams recombine at the BS. Recombination at the BS generates two beams, one of which is heading back to the laser source while the other one is heading to the PD. The PD measures the intensity of this beam. Since only one monochromatic beam is used, such an IFM is called a *homodyne* IFM.

To describe the main features of an IFM mathematically, it is sufficient to describe the beam as a plane wave

$$a_i = a_0 e^{i(kz - \omega t)}, \quad (2.28)$$

where a_0 is the complex amplitude a_0 ($\Re[a_0] = [\text{V/m}]$) which carries the information

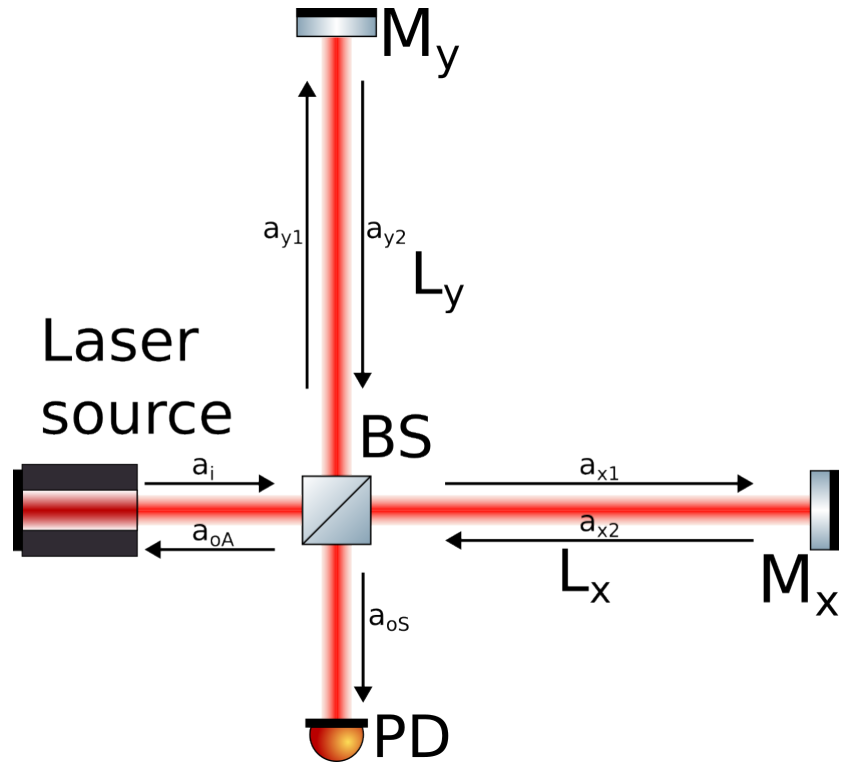


Figure 2.3: Topology of a simple Michelson IFM.

of the amplitude E_0 and phase φ_0 of the beam.

$$a_0 = E_0 e^{i\phi_0} \quad (2.29)$$

$$\Re[a_0] = E_0 \text{ (beam's amplitude)} \quad (2.30)$$

$$\arg(a_0) = \varphi_0 \text{ (beam's initial phase)} \quad (2.31)$$

All optics are assumed to be ideal, i.e. lossless and perfectly reflecting in the case of the mirrors. The BS can be represented with the unitary matrix

$$\begin{pmatrix} a_{\text{out}, 1} \\ a_{\text{out}, 2} \end{pmatrix} = \begin{pmatrix} \rho & i\tau \\ i\tau & \rho \end{pmatrix} \begin{pmatrix} a_{\text{in}, 1} \\ a_{\text{in}, 2} \end{pmatrix}, \quad (2.32)$$

where ρ and τ are respectively the reflectivity and transmittance of the BS. For a lossless 50-50 BS, $\rho = \tau = \frac{1}{\sqrt{2}}$. After the BS the initial beam splits and becomes

$$a_{x1} = i\tau a_i = i\tau a_o e^{i(kz - \omega t)} \quad (2.33)$$

$$a_{y1} = \rho a_i = \rho a_o e^{i(kz - \omega t)}. \quad (2.34)$$

The beams are then reflected on the mirrors $M_{x,y}$, which in this example have an ideal reflectivity of 1. By propagating along different arms, the beams accumulate different phases. Just before the recombination at the BS the respective plane waves are

$$a_{x2} = e^{i2kL_x} a_{x1} = i\tau a_o e^{i2kL_x} e^{i(kz - \omega t)} \quad (2.35)$$

$$a_{y2} = e^{i2kL_y} a_{y1} = \rho a_o e^{i2kL_y} e^{i(kz - \omega t)}. \quad (2.36)$$

After recombination, there are two outputs from the BS. One is called *symmetric port*, since the beams out of it have been once reflected and once transmitted by the

BS. The other one is called *antisymmetric port* since the beams were either twice reflected or twice transmitted.

$$a_{o,S} = \rho a_{x2} + i\tau a_{y2} = \rho i\tau a_o e^{i(kz-\omega t)} (e^{i2kL_x} + e^{i2kL_y}) \quad (2.37)$$

$$a_{o,A} = i\tau a_{x2} + \rho a_{y2} = a_0 e^{i(kz-\omega t)} (-\tau^2 e^{i2kL_x} + \rho^2 e^{i2kL_y}) \quad (2.38)$$

The intensity can be obtained using equation (2.14): $I = \frac{|E|^2}{2Z} = \frac{EE^*}{2Z}$. The overlap integral of plane waves is always one. From here on, I define $I_0 = \frac{|a_0|^2}{2Z}$.

$$I_{o,S} = I_0 2\rho^2 \tau^2 (1 + \cos(2k(L_x - L_y))) \quad (2.39)$$

$$I_{o,A} = I_0 (\tau^2 + \rho^4 - 2\rho^2 \tau^2 \cos(2k(L_x - L_y))) \quad (2.40)$$

As a result, the output intensity is the sum of a DC term, resulting from the individual beam's intensities, and an interference term due to the interference between the two beams. One can check that the energy is conserved at every moment as $I_{o,S} + I_{o,A} = I_0$ as the two interference terms are opposite. This means that the pathlength difference $L_x - L_y = \Delta L$ just determines which port the intensity is directed towards. Plugging in the reflectance and transmittance values for an ideal IFM, one obtains the intensity heading out of each port.

$$I_{o,S} = \frac{I_0}{2} (1 + \cos(2k\Delta L)) = I_0 \cos^2(k\Delta L) \quad (2.41)$$

$$I_{o,A} = \frac{I_0}{2} (1 - \cos(2k\Delta L)) = I_0 \sin^2(k\Delta L) \quad (2.42)$$

A displacement of the order of one wavelength in one arm diverts all the power from one port to the other. The measured displacement on the symmetric port is for example

$$\Delta L = \frac{\lambda}{2\pi} \arccos \left(2 \frac{I_{oS}}{I_0} - 1 \right). \quad (2.43)$$

Note that an IFM, unlike many other measurement techniques, is *self-calibrated*, as the wavelength of the beam is the only needed conversion factor from detector output (the integrated intensity on a PD) to length. Unfortunately, such an IFM has some *blind spots*: this is when the sensitivity vanishes, or $\frac{\partial I}{\partial \Delta L} = 0$. This means that if the measured power crosses that spot, one can no longer tell from the IFM's output if ΔL has increased or decreased. This is shown in Figure 2.4.

The IFM's output signal is converted into a voltage output by the photoreceiver (PR). This, for the symmetric port, is equal to

$$V_{o,S} = R A \int_{S_{PD}} dS I(x, y, z_{PD}). \quad (2.44)$$

Where $R[\Omega]$ is the gain of the trans-impedance amplifier (TIA) of the PR, $A[\frac{A}{W}]$ is the responsivity of the PD, z_{PD} is the position of the PD along the beam path, S_{PD} is the PD's surface and (x, y) are the transverse beam's coordinates.

A crucial parameter in IFMs is the contrast $0 \leq C \leq 1$, which indicates the ratio of the interference term's amplitude over the DC beam powers, defined as

$$C = \left| \frac{I_{\max} - I_{\min}}{I_{\max} + I_{\min}} \right| = \left| \frac{V_{\max} - V_{\min}}{V_{\max} + V_{\min}} \right|, \quad (2.45)$$

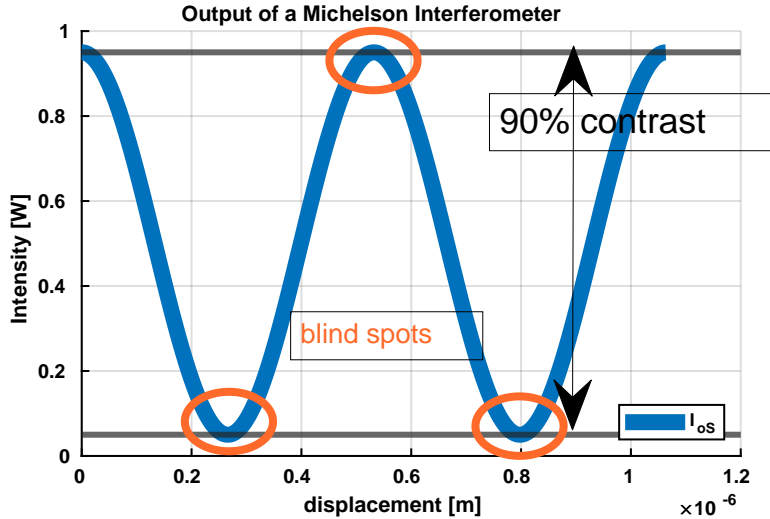


Figure 2.4: Schematic graph of the intensity of the $I_{o,S}$ port of the Michelson IFM in Figure 2.3 in case of using a wavelength of 1064 nm. In this example, the contrast is 90%, and the total intensity of 1 W. The output's blind spots are highlighted in orange.

where the right side of equation (2.45) holds only if the TIA introduces a negligible offset. The contrast is related to the heterodyne efficiency in equation (2.22) by

$$C = \frac{2\sqrt{\eta_{\text{het}} P_1 P_2}}{P_1 + P_2}. \quad (2.46)$$

One can easily see from equations (2.39) and (2.40) that in the case of a plane-wave IFM this is

$$C_{o,S} = \frac{4\rho^2\tau^2}{4\rho^2\tau^2} = 1 \quad (2.47)$$

$$C_{o,A} = \frac{4\rho^2\tau^2}{2(\rho^4 + \tau^4)}. \quad (2.48)$$

The contrast of the symmetric port is always one, while the asymmetric port varies according to the reflectance and transmittance of the BS. This is an idealized example, as plane waves have a perfect overlap; in the realistic case, other factors such as losses, reflectance and transmittance mismatches at the BS, and the use of Gaussian beams having imperfect beam overlap lower, in general, the contrast.

The (Heterodyne) Mach-Zender Interferometer

Heterodyne interferometry is the case in which beams at different frequencies are interfered. The advantage of this is it removes the unavoidable blind spots of homodyne interferometry. A possible implementation of a heterodyne IFM setup is shown in Figure 2.5. The beam from one laser source is split and then propagated through two acousto-optical modulators (AOMs). These are devices that use photon-phonon interaction to shift the frequency of a laser beam by a value typically around 80MHz²

²This frequency shift is very small in comparison to the laser beam's frequency, which is, for a $\lambda = 1064\text{nm}$ beam, $\nu \approx 2.82 \times 10^{14}$ Hz: therefore, the two beams can still be considered to have the same wavelength λ

[60]. By using two of these, one can achieve even smaller frequency differences. An alternative could be to have two laser sources and lock their frequencies with a constant offset. The initial laser beam is again equation (2.28), and both BSs are treated with equation (2.32). The output beams of this setup are

$$a_{o,1} = a_0 i \rho \tau (e^{i\omega_1 t + kL_1} + e^{i\omega_2 t + kL_2}) \quad (2.49)$$

$$a_{o,2} = a_0 (\rho^2 e^{i\omega_1 t + kL_1} - \tau^2 e^{i\omega_2 t + kL_2}) \quad (2.50)$$

and the respective powers are

$$I_{o,1} = I_0 2 \rho^2 \tau^2 (1 + \cos(\Delta\omega_{\text{het}} t + k\Delta L)) \quad (2.51)$$

$$I_{o,2} = I_0 (\rho^4 + \tau^4 - 2 \cos(\Delta\omega_{\text{het}} t + k\Delta L)), \quad (2.52)$$

where $\Delta\omega_{\text{het}} = \omega_1 - \omega_2$ takes the name of *heterodyne frequency* and $\Delta L = L_1 - L_2$ is the usual pathlength difference. In heterodyne interferometry, the output is a beat note at the frequency difference between the two beams, and wanted phase information is the phase of this beat note.

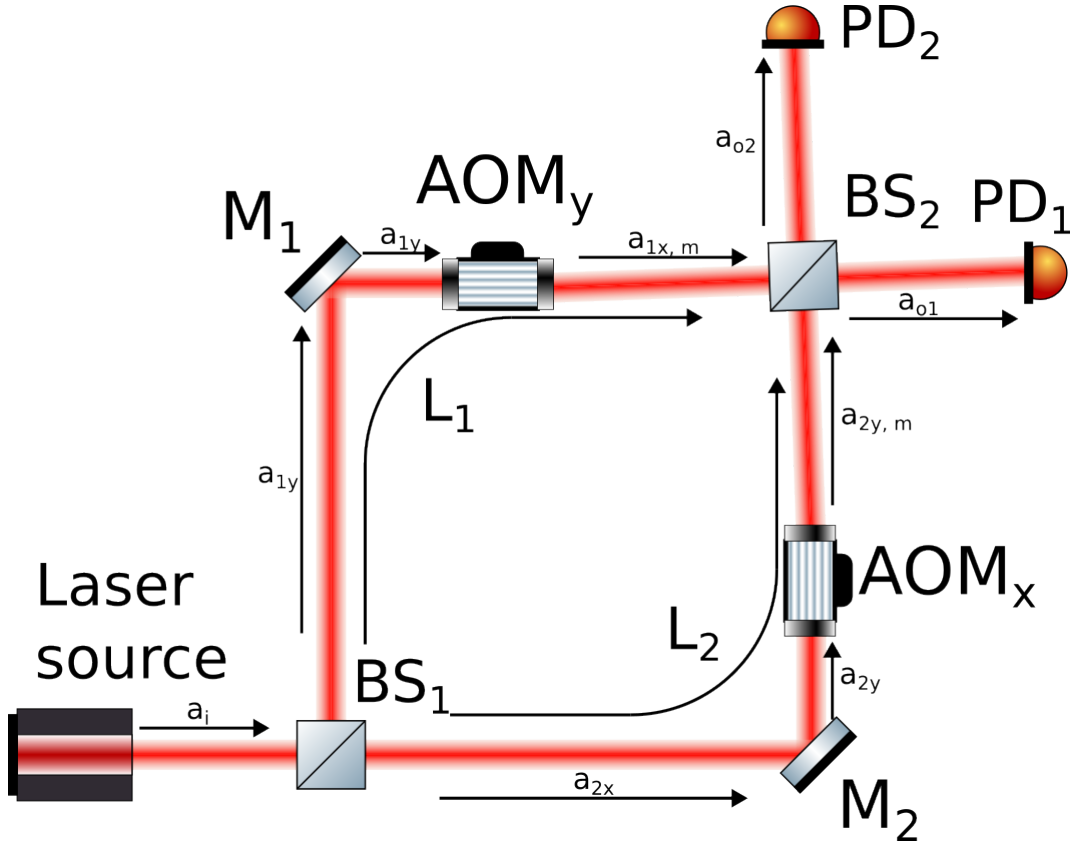


Figure 2.5: Layout of a simple Mach-Zender heterodyne interferometer.

The extraction of the phase information from a heterodyne IFM is more complex than in the case of a Michelson IFM. To demodulate this a dedicated device is needed, the phasemeter (PM). In the case of a fixed frequency beat note, this demodulation can be simplified as following (this subsection is adapted from [67]). The beat note in equation (2.51) can be rewritten for a real IFM's output to be

$$P(t) = \bar{P} [1 + C \cos(\Delta\omega t + \Delta\phi)], \quad (2.53)$$

where \bar{P} is the average power measured by the PD, C is the contrast and $\Delta\phi$ is the phase difference between the beams. If the phase changes are sufficiently slow compared to the beat note oscillation, the phase can be treated as constant ($\frac{d(\Delta\phi)}{dt} \ll \omega$) during one cycle of the demodulation process. The beat note is multiplied by two time series in quadrature represented by $\sin(\Delta\omega t)$ and $\cos(\Delta\omega t)$ at the same frequency and integrated over one (or multiple) period(s). This results in the two quantities int_s and int_c .

$$\begin{aligned}
 \text{int}_s &= \int_0^{2\pi} d(\Delta\omega t) \sin(\Delta\omega t) P(t) \\
 &= \bar{P} \int_0^{2\pi} d(\Delta\omega t) \sin(\Delta\omega t) + \bar{P}C \int_0^{2\pi} d(\Delta\omega t) \sin(\Delta\omega t) \cos(\Delta\omega t + \Delta\phi) \\
 &= \frac{1}{2} \bar{P}C \left[\int_0^{2\pi} d(\Delta\omega t) \sin(2\Delta\omega t + \Delta\phi) + \int_0^{2\pi} d(\Delta\omega t) \sin(-\Delta\phi) \right] \\
 &= \bar{P}C\pi \sin(-\Delta\phi)
 \end{aligned} \tag{2.54}$$

In the first line the first Werner formula has been used, $\sin \alpha \cos \beta = \frac{1}{2}[\sin(\alpha + \beta) + \sin(\alpha - \beta)]$. Similarly, for the cosine integral

$$\begin{aligned}
 \text{int}_c &= \int_0^{2\pi} d(\Delta\omega t) \cos(\Delta\omega t) P(t) \\
 &= \bar{P} \int_0^{2\pi} d(\Delta\omega t) \cos(\Delta\omega t) + \bar{P}C \int_0^{2\pi} d(\Delta\omega t) \cos(\Delta\omega t) \cos(\Delta\omega t + \Delta\phi) \\
 &= \frac{1}{2} \bar{P}C \left[\int_0^{2\pi} d(\Delta\omega t) \cos(2\Delta\omega t + \Delta\phi) + \int_0^{2\pi} d(\Delta\omega t) \cos(-\Delta\phi) \right] \\
 &= \bar{P}C\pi \cos(-\Delta\phi)
 \end{aligned} \tag{2.55}$$

In the second line the first Werner formula has been used, $\cos \alpha \cos \beta = \frac{1}{2}[\cos(\alpha + \beta) + \cos(\alpha - \beta)]$. Hence one can obtain the phase of the beat note as

$$\Delta\phi = -\arctan\left(\frac{\text{int}_s}{\text{int}_c}\right). \tag{2.56}$$

The advantage of such a system is that there are no more blind spots, and pathlength variations longer than one wavelength can be measured. What is shown here is the phase extraction for a heterodyne IFM with a fixed heterodyne frequency; such a demodulation scheme takes the name of single bin fast fourier transform (FFT) PM. This is not the case of LISA, where the heterodyne frequencies vary in a range of 5-25 MHz. For this application a DPLL PM is used.

2.1.4 Effect of a Gravitational Wave on an Interferometer

Michelson interferometers (IFMs) are naturally suited to measure the effect of a GW since they are able to measure the length difference of two perpendicular pathlengths.

With a general relativistic computation, [51] calculates the phase shift induced in an arm of a Michelson IFM by the transit of a monochromatic GW. In LISA, the beam propagating along the arm is not reflected backwards by an end mirror but an amplified beam with a well defined frequency offset it is sent back by the receiver spacecraft; this introduces no difference in the calculation.

Let the IFM's arm be parallel to the x -axis and have a length L . The GW is *plus* polarized in the used reference frame (RF) and propagates along the z -axis. The GW in the TT gauge takes the form

$$h_+(t) = \hat{\varepsilon}_+ h_0 \cos(\omega_{gw} t). \quad (2.57)$$

The spacetime interval in the TT gauge is

$$ds^2 = -c^2 dt^2 + [1 + h_+(t)] dx^2 + [1 - h_+(t)] dy^2 + dz^2. \quad (2.58)$$

The photons in an IFM travel along null geodesics³, hence for a photon propagating along the arm it holds

$$dx = \pm c dt \sqrt{1 + h_+(t)} \approx \pm c dt \left[1 + \frac{1}{2} h_+(t) \right], \quad (2.59)$$

where the plus-minus sign indicates the direction of propagation and the square root has been approximated to the first-order Taylor expansion as $h \sim 10^{-21}$. The photons in the IFM arm first propagate from $x = 0$ to $x = L$ ⁴, and then backwards from $x = L$ to $x = 0$. Let's name the starting time t_0 , the arrival time at the end mirror t_1 and the time of return to the BS t_2 . The time interval experienced by the photon can be calculated by integrating equation (2.59) with proper signs for the travelling directions in the arm.

$$L = \int_0^L dx = c \int_{t_0}^{t_1} dt' \left[1 + \frac{1}{2} h_+(t') \right] = c(t_1 - t_0) + \frac{c}{2} \int_{t_0}^{t_1} dt' h_+(t') \quad (2.60)$$

$$-L = \int_L^0 dx = -c \int_{t_1}^{t_2} dt' \left[1 + \frac{1}{2} h_+(t') \right] = c(t_2 - t_1) + \frac{c}{2} \int_{t_1}^{t_2} dt' h_+(t') \quad (2.61)$$

Summing the two equations (2.60) and (2.61) together one gets

$$t_2 - t_0 = \frac{2L}{c} - \frac{1}{2} \int_{t_0}^{t_2} dt' h_+(t'). \quad (2.62)$$

To first-order approximation $t_2 = t_0 + \frac{2L}{c}$, and this can be replaced on the upper limit of the integral. Plugging in the explicit expression of the GW in equation (2.57) in equation (2.62) one gets

$$\begin{aligned} t_2 - t_0 &= \frac{2L}{c} - \frac{1}{2} \int_{t_0}^{t_0 + \frac{2L}{c}} dt' h_0 \cos(\omega_{gw} t') \\ &= \frac{2L}{c} - \frac{h_0}{2\omega_{gw}} \left[\sin\left(\omega_{gw} \left(t_0 + \frac{2L}{c}\right)\right) - \sin(\omega_{gw} t_0) \right] \\ &= \frac{2L}{c} - \frac{h_0 L}{c} \frac{\sin(\frac{\omega_{gw} L}{c})}{\frac{\omega_{gw} L}{c}} \cos\left(\omega_{gw} \left(t_0 + \frac{L}{c}\right)\right) \\ &= \frac{2L}{c} - h_+ \left(\omega_{gw} \left(t_0 + \frac{L}{c}\right) \right) \text{sinc}\left(\frac{\omega_{gw} L}{c}\right), \end{aligned} \quad (2.63)$$

³Null geodesics are defined as paths characterized by $ds^2 = 0$.

⁴In the TT gauge the coordinates of test masses are not changed by the transit of a GW

where in the third line the identity $\sin(\alpha + 2\beta) - \sin \alpha = 2 \sin \beta \cos(\alpha + \beta)$ has been used and in the fourth line the function $\text{sinc}(x) = \frac{\sin x}{x}$ has been introduced. This means that the transit of a gravitational wave along an arm placed on the x -axis causes a time-dependent time difference in the light's propagation time of

$$\Delta t_{gw}(t) = h_0 \frac{L}{c} \text{sinc}\left(\frac{\omega_{gw} L}{c}\right) \cos\left[\omega_{gw}\left(t - \frac{L}{c}\right)\right]. \quad (2.64)$$

The quantity $\frac{c}{L}$ can be defined to be the *corner frequency* of the IFM, as $\omega_{gw,*} = \frac{c}{L}$. The corresponding phase shift on a laser beam can be obtained by multiplying the time shift in equation (2.64) with the light's pulsation $\omega_l = 2\pi\nu_l$.

$$\Delta\phi_{gw}(t) = h_0 \frac{\omega_l L}{c} \text{sinc}\left(\frac{\omega_{gw}}{\omega_{gw,*}}\right) \cos\left[\omega_{gw}\left(t - \frac{L}{c}\right)\right] \quad (2.65)$$

The physical meaning of the sinc function is that if $\frac{\omega_{gw}}{\omega_{gw,*}} \geq 1$, i.e. the period of the GW is comparable or smaller to the round trip time of a photon in the arm, then the GW changes sign during the propagation along the arm, and partially cancels. This is the case in LISA, where this *armlength-penalty* is reducing the sensitivity on the high frequency end ⁵. In the opposite case $\frac{\omega_{gw}}{\omega_{gw,*}} \ll 1$ the GW has a constant sign along the arm and $\text{sinc}(0) \sim 1$, which is the case in ground-based IFMs. This mechanism also introduces a comb of blind frequencies $\sin\left(\frac{\omega_{gw}}{\omega_{gw,*}}\right) = 0 \rightarrow \frac{\omega_{gw}}{\omega_{gw,*}} = (2n+1)\frac{\pi}{2}$, $n \in \mathbb{N}$ to which an IFM arm of length L is not sensitive at all as the GWs completely cancel.

In a Michelson GW IFM the phase shift at the BS's output is twice that in equation (2.65) as the same effect happens in both arms with opposite signs. In LISA, it is a bit more complicated, as the arms have a 60° angle.

Short application to LISA. Plugging in some typical numbers for LISA ($L = 2.5 \times 10^9$ m, $\omega_{gw} = 1$ mHz, $h_+(t) = 10^{-20} \forall t$) the time shift and phase shift are

$$\omega_{gw,*} = \frac{c}{L} = 0.12 \text{Hz} \quad (2.66)$$

$$\Delta t_{gw} = \frac{2.5 \times 10^9 \text{ m}}{3 \times 10^8 \text{ m/s}} 10^{-20} \sim 10^{-19} \text{ s} \quad (2.67)$$

$$\Delta\phi_{gw} = 2\pi 2.8 \times 10^{14} \text{ Hz} 10^{-19} \text{ s} \sim 10^{-4} \text{ rad} \quad (2.68)$$

$$\Delta L_{gw, eq} = \frac{\lambda}{4\pi} \Delta\phi_{gw} \sim 10^{-11} \text{ m.} \quad (2.69)$$

2.1.5 Noises of interferometric origin

As with any existing measurement setup, the explained interferometric schemes in Section 2.1.3 are also affected by noise. This subsection is a brief overview of the noises linked to the nature of the interferometric measurement itself.

⁵see Figure 1.11

Relative Intensity Noise

An ideal laser emits a constant laser power, which can be formalized as a Gaussian beam (see equation (2.6)) with constant amplitude. Unfortunately, this is not the case, and real lasers suffer power oscillations. Such power oscillations are misinterpreted as pathlength variations by the interferometric measurement. The phase error due to this is called *intensity noise*. As soon explained, the phase noise due to these power oscillations is independent of the mean power of the beam; therefore, this phase noise is called relative intensity noise (RIN). RIN can be described as follows [81]: a laser beam of ideal power P has instead a power $P(t) = \bar{P} + \delta P(t)$ with $\delta P(t) \ll \bar{P} \forall t$. This can be rewritten as $P(t) = \bar{P}(1 + r(t))$ with $r(t) = \frac{\delta P}{P} \ll 1 \forall t$. Given two interfering beams of average powers \bar{P}_1 and \bar{P}_2 , beam overlap $\sqrt{\eta_{\text{het}}}$, frequency difference ω_{het} and phase difference φ , the power impinging on a PD is (from equation (2.23))

$$\begin{aligned}
 P_{\text{out}} &= \bar{P}_1(1 + r_1) + \bar{P}_2(1 + r_2) + 2\sqrt{\eta_{\text{het}}\bar{P}_1(1 + r_1)\bar{P}_2(1 + r_2)}\cos(\omega_{\text{het}}t + \varphi) \\
 &\approx (\bar{P}_1 + \bar{P}_2 + \bar{P}_1r_1 + \bar{P}_2r_2) + 2\left(1 + \frac{r_1 + r_2}{2}\right)\sqrt{\eta_{\text{het}}\bar{P}_1\bar{P}_2}\cos(\omega_{\text{het}}t + \varphi) \\
 &= \underbrace{\bar{P}_1 + \bar{P}_2}_{\text{DC}} + \underbrace{\bar{P}_1r_1 + \bar{P}_2r_2}_{1f\text{-RIN}} + \underbrace{(r_1 + r_2)\sqrt{\eta_{\text{het}}\bar{P}_1\bar{P}_2}\cos(\omega_{\text{het}}t + \varphi)}_{2f\text{-RIN}} + \\
 &\quad + \underbrace{2\sqrt{\eta_{\text{het}}\bar{P}_1\bar{P}_2}\cos(\omega_{\text{het}}t + \varphi)}_{\text{signal}}, \\
 \end{aligned} \tag{2.70}$$

where $\sqrt{1+x} \approx 1 + x/2$ was used, and the term r_1r_2 was neglected. The term $\bar{P}_1 + \bar{P}_2$ is a constant DC term, the term $\bar{P}_1r_1 + \bar{P}_2r_2$ is known as $1f$ -RIN and is an additive noise, while the term $(r_1 + r_2)\sqrt{\eta_{\text{het}}\bar{P}_1\bar{P}_2}\cos(\omega_{\text{het}}t + \varphi)$ is known as $2f$ -RIN and is a multiplicative noise. The induced phase noise can be characterized by calculating the inverse carrier-to-noise (C/N) density ratio (C/N_0) as

$$\tilde{\varphi}_{\text{noise}} = \frac{\text{Noise ASD}}{\text{Signal RMS}}, \tag{2.71}$$

where the noise is evaluated near f_{het} and the root mean square (RMS) of a signal $s(t)$ over a period T is defined as

$$\mathcal{RMS}\{s(t)\} = \sqrt{\frac{1}{T} \int_0^T [s(t)]^2 dt}. \tag{2.72}$$

For the signal (underbraced in equation (2.70)), the RMS operator in equation (2.72) gives $\mathcal{RMS}\{2\sqrt{\eta_{\text{het}}\bar{P}_1\bar{P}_2}\cos(\omega_{\text{het}}t + \varphi)\} = \sqrt{2\eta_{\text{het}}\bar{P}_1\bar{P}_2}$. The phase noise due

to $1f$ -RIN is hence

$$\begin{aligned}
 \tilde{\varphi}_{1f} &= \frac{\bar{P}_1 \tilde{r}_1 + / \boxplus \bar{P}_2 \tilde{r}_2}{\sqrt{2\eta_{\text{het}} \bar{P}_1 \bar{P}_2}} \\
 &\approx \frac{\tilde{r}_1 + / \boxplus \tilde{r}_2}{2\sqrt{\eta_{\text{het}}}} \text{ if } \bar{P}_1 \sim \bar{P}_2 \\
 &\approx \tilde{r}_1 \sqrt{\frac{\bar{P}_1}{2\eta_{\text{het}} \bar{P}_2}} \text{ if } \bar{P}_1 \gg \bar{P}_2
 \end{aligned} \tag{2.73}$$

,

where $\tilde{r}_{1,2}$ is the ASD of the $1f$ -RIN coupling $r_{1,2}$ evaluated at the beat note frequency and $+/ \boxplus$ indicates that a simple sum has to be used in case \tilde{r}_1 and \tilde{r}_2 are correlated (e.g. they come from the same laser) or the squared sum has to be used if they are uncorrelated (e.g. they come from the separate lasers). This coupling is power-dependent and is enhanced in the case of power mismatches.

The coupling of $2f$ -RIN arises as $\tilde{r}_{1,2}$ are multiplied by the beat note. The only frequency band at which RIN can couple into the PM's readout is that around $2f_{\text{het}}$. After multiplication, this causes a third and a first harmonic, of which only the latter one is processed by the PM.

$$\tilde{\varphi}_{2f} = \frac{\tilde{r}_1 + / \boxplus \tilde{r}_2}{2\sqrt{2}} \tag{2.74}$$

In this relation $\tilde{r}_{1,2}$ are evaluated at twice the heterodyne frequency. Note that equation (2.74) is both power- and contrast-independent.

As two detectors measuring the same beams experience the same RIN, a strategy for RIN mitigation is that of using a reference IFM to measure the phase φ_R . This has the same RIN content but does not experience the measurement-related phase variations of the measurement IFM. In post-processing, the phase difference $\varphi - \varphi_R$ is calculated. The performance of this process is limited by the correlation of the subtracted phasors, which depends on the phase of the involved signals. This gives rise to an phase-difference-dependence of the RIN subtraction level [81], which for similar RIN levels $\tilde{r}_1 \sim \tilde{r}_2 = \tilde{r}$ is

$$\widetilde{\varphi - \varphi_{R1f}} = \frac{\sqrt{2}(P_1 \tilde{r}_1(1f_{\text{het}}) + / \boxplus P_2 \tilde{r}_2(1f_{\text{het}}))}{\sqrt{\eta_{\text{het}} \bar{P}_1 \bar{P}_2}} \left| \sin \left(\frac{\varphi - \varphi_R}{2} \right) \right| \tag{2.75}$$

$$\widetilde{\varphi - \varphi_{R2f}} = \frac{\tilde{r}_1(2f_{\text{het}}) + / \boxplus \tilde{r}_2(2f_{\text{het}})}{\sqrt{2}} |\sin(\varphi - \varphi_R)|. \tag{2.76}$$

The quantity $\varphi - \varphi_R$ is the phase difference measured by the PM, which also includes eventual due to the phase TF of the involved electronics. Note also that this calculations assumes the same power ratio in both the measurement anf the reference IFM.

Frequency Noise

Laser frequency noise arises because of variations in the frequency ν , or wavelength λ , of the laser carrier. If in an IFM a beam is first split, propagated along two different arms and then recombined, this frequency noise would cancel out as long

as the propagation pathlengths along the two arms are equal, as the two phase fluctuations would be the same. If not, the phase noise $\delta\varphi_{\text{freq}}$ due to laser frequency variations is proportional to the armlength mismatch Δs because they are delayed with respect to each other. This can be seen in the following equation (2.77) [59].

$$\begin{aligned}\varphi &= \frac{2\pi}{\lambda} \Delta s = \frac{2\pi \Delta s}{c} \nu \\ \tilde{\varphi}_{\text{freq}} &= 2\pi \frac{\Delta s}{c} \tilde{\nu}.\end{aligned}\quad (2.77)$$

The fundamental limit of low power interferometers: Shot Noise

Shot noise is one of the limiting noises in IFMs. It is caused by the quantum nature of light and the consequent random arrival time of individual photons on a PD. A beam consists of a flux of photons in time; let $N_\gamma(t)$ be the function describing the photon flux through an open surface at the time t . This quantity can be derived from the beam's instantaneous power $P(t)$ by dividing it by the energy carried by a single photon $N_\gamma(t) = P(t)/E_\gamma$, with $E_\gamma = h\nu_l = \hbar\omega_l = h\frac{c}{\lambda_l}$. The average number of photons which have gone through the surface in a time τ is $\bar{N}_\gamma = \frac{1}{\tau} \int_0^\tau N(t)dt$. This amount is not stable but is subject to a Poissonian statistic. The average power measured during τ is $\bar{P} = \frac{\bar{N}_\gamma h\nu}{\tau}$. The variance of the average power is

$$\text{Var}(\bar{P})_{\text{shot}} = \Delta P_{\text{shot}}^2 = \frac{\Delta E^2}{\tau^2} = \frac{\Delta N_\gamma^2 h^2 \nu_l^2}{\tau^2} = \frac{\bar{N}_\gamma h^2 \nu_l^2}{\tau^2} = \frac{\bar{P} h \nu_l}{\tau}. \quad (2.78)$$

As there is no correlation between the fluctuations in the number of photons arriving at different times $N_\gamma(t)$ and $N_\gamma(t')$, the auto-correlation function of $N_\gamma(t)$ is a delta function.

$$\langle N_\gamma(t) N_\gamma(t') \rangle = N_0 \delta(t - t') \quad (2.79)$$

This implies that the spectrum of $\tilde{N}_\gamma^2(f)$ is white, i.e. independent of the frequency. [51] demonstrates that one can obtain the one-sided spectrum of a white noise by multiplying its variance (in equation (2.78)) by 2τ . The one-sided power spectral density (PSD) of shot noise is hence

$$\tilde{P}_{\text{shot}}^2(f) = 2\bar{P} h \nu_l. \quad (2.80)$$

The above equation equation (2.80) was derived considering the power flux through an open surface and describes an intrinsic noise of the beam. In an experiment, this surface would be the active area of a PD. In a PD, only a fraction of photons is converted into photocurrent. To account for this, the average power has to be multiplied by the efficiency of this process, $\bar{P} \rightarrow \eta_{\text{PD}} \bar{P}$ where $\eta_{\text{PD}} = \frac{h\nu_l}{q} A \leq 1$ is the quantum efficiency of the PD, h is Planck's constant, q is the fundamental charge, and A [A/W] is the responsivity of the PD. This substitution is done directly in equation (2.82) after the calculation of the phase noise associated to power shot noise.

As in the case of RIN, the power fluctuations caused by the shot noise on the photodiode are fundamentally indistinguishable from those caused by a phase variation. The coupling to phase noise can be calculated using equation (2.71) on output power (2.23)

$$P_{\text{out}}(\varphi) = \bar{P}_1 + \bar{P}_2 + 2\sqrt{\eta_{\text{het}} \bar{P}_1 \bar{P}_2} \cos(\omega_{\text{het}} t + \varphi), \quad (2.81)$$

Where $P_{1,2}$ are the powers of the two interfering beams. Accounting for η_{PD} this gives

$$\begin{aligned}\tilde{\varphi}_{\text{shot}}(f) &= \sqrt{\frac{(\bar{P}_1 + \bar{P}_2)h\nu_l}{\eta_{\text{PD}}\eta_{\text{het}}\bar{P}_1\bar{P}_2}} \\ &\approx \sqrt{\frac{2h\nu_l}{\eta_{\text{PD}}\eta_{\text{het}}\bar{P}}} \text{ if } \bar{P}_1 \sim \bar{P}_2 \\ &\approx \sqrt{\frac{h\nu_l}{\eta_{\text{PD}}\eta_{\text{het}}\bar{P}_2}} \text{ if } \bar{P}_1 \gg \bar{P}_2.\end{aligned}\quad (2.82)$$

Note that, in the case where $\bar{P}_1 \gg \bar{P}_2$, the phase noise depends only on the power of the weakest beam. Equation 2.82 is often written in terms of current shot noise since what has been discussed above for photons and laser powers applies dually to currents and electrons when the electrons are generated in the PD. The two formulations are perfectly equivalent.

$$\tilde{\varphi}_{\text{shot}}(f) = \sqrt{\frac{(\bar{P}_1 + \bar{P}_2)h\nu_l}{\eta_{\text{PD}}\eta_{\text{het}}\bar{P}_1\bar{P}_2}} = \sqrt{\frac{q(i_1 + i_2)}{\eta_{\text{het}}i_1i_2}}, \quad (2.83)$$

where $i_{1,2} = AP_{1,2}$ is the photocurrent induced on the PD by the laser beam. The case where one beam is much less powerful than the other one is relevant for LISA, as shot noise is the largest noise source in the ISI. The resulting ASDs of phase and pathlength noise due to shot noise for $P_1 \gg P_2$ and $\eta_{\text{PD}} = \eta_{\text{het}} = 1$ are

$$\tilde{\varphi}(f) = \sqrt{\frac{h\nu_l}{\bar{P}}} = 4.32 \times 10^{-10} (P[\text{W}])^{-\frac{1}{2}} \text{ rad}/\sqrt{\text{Hz}} \quad (2.84)$$

$$\widetilde{\Delta L}(f) = \frac{1}{2\pi} \sqrt{\frac{hc\lambda_l}{\bar{P}}} = 7.32 \times 10^{-17} (P[\text{W}])^{-\frac{1}{2}} \text{ m}/\sqrt{\text{Hz}}. \quad (2.85)$$

Short application to LISA. Plugging in the RX beam power for LISA $\bar{P}_{\text{RX}} = 92 \text{ pW}$ [30] in equations (2.84, 2.85) gives

$$\tilde{\varphi}(f) = 4.50 \times 10^{-5} \text{ rad}/\sqrt{\text{Hz}} \quad (2.86)$$

$$\widetilde{\Delta L}(f) = 7.63 \times 10^{-12} \text{ m}/\sqrt{\text{Hz}} \quad (2.87)$$

These values are just one order of magnitude smaller than those in equations (2.68, 2.69).

2.2 Ray Transfer Matrices and Imaging Systems

2.2.1 Ray Transfer Matrices

This subsection introduces the aspects of ray transfer matrices used in this thesis. For a more detailed description, see [69]. Ray transfer matrices (also known as ABCD matrices) describe the propagation of geometrical optical rays through

paraxial optical elements, such as lenses and curved mirrors[69]. They describe a ray propagating along an axis z by using its transverse position x and angle $\theta = \frac{\partial x}{\partial z}$. These two parameters are made into a 2-vector $\vec{r} = (x, \theta)^T$, and every propagation medium can be described with a 2×2 matrix describing how the optical element changes the vector \vec{r} .

$$\begin{pmatrix} x_2 \\ \theta_2 \end{pmatrix} = \begin{pmatrix} A & B \\ C & D \end{pmatrix} \begin{pmatrix} x_1 \\ \theta_1 \end{pmatrix} \quad \begin{pmatrix} A & B \\ C & D \end{pmatrix} = \begin{pmatrix} \frac{\partial x_2}{\partial x_1} & \frac{\partial x_2}{\partial \theta_1} \\ \frac{\partial \theta_2}{\partial x_1} & \frac{\partial \theta_2}{\partial \theta_1} \end{pmatrix} \quad (2.88)$$

Such matrices can be calculated for simple optical elements such as free space propagation, thin lenses, and refraction through curved interfaces. Elements of further complexity such as thick lenses can be described by combining such matrices backwards.

$$M_{\text{free space}}(d) = \begin{pmatrix} 1 & d \\ 0 & 1 \end{pmatrix} \quad (2.89)$$

$$\hat{M}_{\text{curved interface}}(n_1, n_2, R) = \begin{pmatrix} 1 & 0 \\ \frac{n_1 - n_2}{Rn_2} & \frac{n_1}{n_2} \end{pmatrix} \quad (2.90)$$

$$\hat{M}_{\text{curved mirror}}(R) = \begin{pmatrix} 1 & 0 \\ -\frac{2}{R} & 1 \end{pmatrix} \quad (2.91)$$

$$\hat{M}_{\text{thin lens}}(f) = \begin{pmatrix} 1 & 0 \\ -\frac{1}{f} & 1 \end{pmatrix} \quad (2.92)$$

Where the d is the free space propagation distance, n_1 and n_2 are, respectively, the initial and final refraction index, f is the focal length, and R is the radius of curvature (RoC) of the interface, defined to be $R > 0$ for convex curvatures i.e. center of curvature is after interface. The determinant of the above matrices (2.89, 2.90, 2.91, 2.92) is $\frac{n_1}{n_2}$, which is one if there is no refraction index change. A thick lens can be modelled by combining the refraction at curved interfaces of RoC R_1 and R_2 and the propagation through the lens's thickness t .

$$M_{\text{thick lens}} = \hat{M}_{\text{curved interface}}(n_2, n_1, R_2) \cdot M_{\text{free space}}(t) \cdot \hat{M}_{\text{curved interface}}(n_1, n_2, R_1) \quad (2.93)$$

$$= \begin{pmatrix} 1 & 0 \\ \frac{n_2 - n_1}{R_2 n_1} & \frac{n_2}{n_1} \end{pmatrix} \begin{pmatrix} 1 & t \\ 0 & 1 \end{pmatrix} \begin{pmatrix} 1 & 0 \\ \frac{n_1 - n_2}{R_1 n_2} & \frac{n_1}{n_2} \end{pmatrix} \quad (2.94)$$

Note that $\det[M_{\text{thick lens}}] = 1$. Ray transfer matrices can be used not only to model the propagation of a light ray through a system but also to determine how a system changes the mode of a Gaussian beam [69]. This is done by replacing the $\vec{r} = (x, \theta)^T$ vector with $\vec{r}_{\text{GB}} = (q, 1)^T$ where q is the so-called q-parameter of a Gaussian beam.

$$q = z + iz_R \quad (2.95)$$

In this context, the ray transfer equation becomes

$$\begin{pmatrix} q_2 \\ 1 \end{pmatrix} = k \begin{pmatrix} A & B \\ C & D \end{pmatrix} \begin{pmatrix} q_1 \\ 1 \end{pmatrix}, \quad (2.96)$$

and the second component of the equation just serves as a normalization. The final form for equation (2.96) is

$$q_2 = \frac{Aq_1 + B}{Cq_1 + D} \quad (2.97)$$

2.2.2 Imaging Systems

In classical optics, pupil-to-pupil imaging systems (ISs) image a specific point along the beam's propagation z_1 into a second one z_2 . This means all rays leaving from z_1 at a specific x_1 position, independently on the angle θ_1 , cross in z_2 at a certain x_2 position. In terms of ray transfer matrix formalism, the condition for this is that the B element of the matrix describing the system is zero; therefore $x_2 = A \cdot x_1$. As the determinant of the matrix describing an imaging system (IS) is one, this implies $D = A^{-1}$, hence a generic IS ray transfer matrix is

$$M_{\text{IS}} = \begin{pmatrix} m^{-1} & 0 \\ C & m \end{pmatrix}. \quad (2.98)$$

At the simplest level, such systems can be realized by one lens or a curved mirror at the proper spatial separation. An IS is characterized by having an input and output object plane [69], and a magnified image of the input object plane forms at the output object plane. The *image demagnification* of the IS is m^{-1} , while m is the *angular magnification* or *beam compression*. For simplicity, during the rest of this thesis I will refer to m simply as *magnification*.

Appendix E reports some calculations performed using this formalism, which have been used to realize the experiment.

2.3 The QPD Signals: Differential Power Sensing, Longitudinal Pathlength Signal and Differential Wavefront-Sensing

In LISA, and therefore in this thesis, quadrant photodiodes (QPDs) are widely used. A QPD is a PD where the sensitive area is divided into four segments, called quadrants, and each quadrant gives an independent measurement of power and phase. The gap between the segments is called *slit* and is insensitive. This Section is a brief description of the QPD-based techniques and signals that are largely used in this experiment. These recover the position, relative phase and angle of the impinging beams.

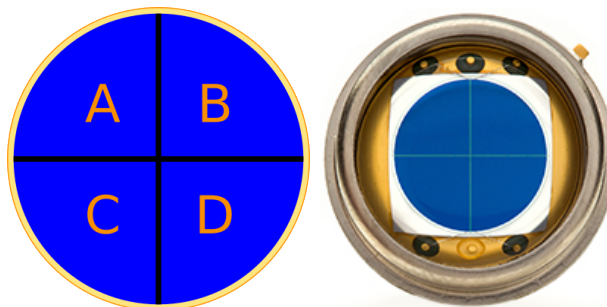


Figure 2.6: left: Schematic drawing of a QPD, with the used segment naming convention used throughout this thesis. Right: picture of a QPD from first sensor (<https://www.first-sensor.com/de/produkte/optische-sensoren/detektoren/quadranten-pin-photodioden-qp/>)

2.3.1 Differential Power Sensing

DPS is a technique that uses a QPD to measure the position of an impinging beam. Information on the beam position is achieved by comparing the power P_i with $i \in (A, B, C, D)$ that is impinging in each segment, more specifically calculating the dimensionless quantities DPS_v (vertical DPS) and DPS_h (horizontal DPS)

$$DPS_v = \frac{P_{\text{top}} - P_{\text{bottom}}}{P_{\text{top}} + P_{\text{bottom}}} = \frac{P_A + P_B - P_C - P_D}{P_A + P_B + P_C + P_D} \quad (2.99)$$

$$DPS_h = \frac{P_{\text{left}} - P_{\text{right}}}{P_{\text{left}} + P_{\text{right}}} = \frac{P_A - P_B + P_C - P_D}{P_A + P_B + P_C + P_D}. \quad (2.100)$$

The quantities DPS_v and DPS_h are related, respectively, to the vertical and horizontal beam displacement from the center of the QPD. The relation between displacement and DPS is called DPS calibration. In the ideal case of a TEM_{00} beam (see equation (2.6)) impinging on a QPD with vanishing slit width and infinite radius, the relation can be derived analytically (see equation (2.101))

$$DPS_v(\Delta y) = -\text{erf}\left(\frac{\sqrt{2}\Delta y}{w(z)}\right) \quad DPS_h(\Delta x) = -\text{erf}\left(\frac{\sqrt{2}\Delta x}{w(z)}\right), \quad (2.101)$$

where $w(z)$ is the beam's spot size at the QPD (see equation (2.7)) and Δy , Δx are the vertical and horizontal displacements of the beam's position. Depending on the laser beam and QPD used, this technique can reach an alignment precision up to fractions of micrometers. By using amplitude modulation and consequent demodulation, it is possible to track the position of more than one beam on the same QPD.

2.3.2 Longitudinal Pathlength Signal

The longitudinal pathlength sensing (LPS) signal combines the four phase measurements from the individual segments of a QPD to calculate a QPD phase signal, which is then calibrated into pathlength Δs , defined as

$$\Delta s = \frac{\lambda}{2\pi} \Delta \varphi. \quad (2.102)$$

Two different formulae are most commonly found in the literature to calculate pathlength, the mean phase and the LISA Pathfinder longitudinal signal. The average phase LPS simply calculates the arithmetic average of the phase measured by each segment

$$s_{\text{AP}} = \frac{1}{k} \frac{\varphi_A + \varphi_B + \varphi_C + \varphi_D}{4}. \quad (2.103)$$

This is the most straightforward way of calculating the phase, but it does not take into account how much power is impinging in each segment. The LISA Pathfinder longitudinal signal⁶ weights the four measured phases by the correspondingly measured power

$$s_{\text{LPF}} = \frac{1}{k} \arg(A_A e^{i\varphi_A} + A_B e^{i\varphi_B} + A_C e^{i\varphi_C} + A_D e^{i\varphi_D}). \quad (2.104)$$

⁶This formula takes the name from the fact that it was implemented in the PM in LISA Pathfinder [5].

This formula, in the ideal case of a QPD with vanishing slits, coincides with the pathlength that a SEPD would measure. These two formulae coincide if the powers per segment are the same.

For this thesis, the average phase is used, but the difference with respect to the LISA Pathfinder would be negligible as the beams are always very well centered on the measuring QPDs and hence the powers very similar.

2.3.3 Differential Wavefront-Sensing

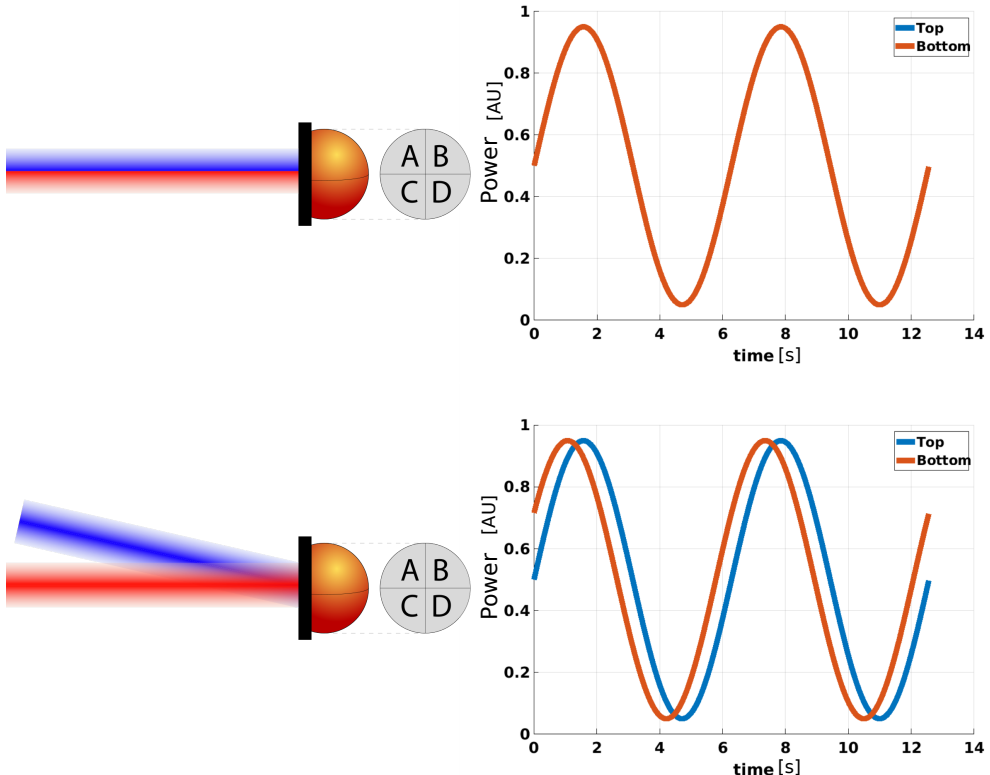


Figure 2.7: Representation of two beams impinging on a PD. The red beam is the reference beam, while the blue beam is the measurement beam, which can be subject to tilt (in this case around the center of the QPD). If the measurement beam is aligned as in the upper case, the phases of the four beat notes on the four segments of the QPD is in-phase, and hence the DWS values vanish. In case of a tilt of the measurement beam, as in the lower case, an offset between the phases measured on the top and bottom quadrants of the QPD occurs because the wavefronts of the measurement beam reach them at different times. This phase offset can be calibrated versus the measurement beam's physical tilt angle.

DWS [55, 56] is a technique that uses a QPD to measure the angle of an impinging beam. It can be thought of as the analogue of DPS, but using interference rather than DC power measurement and measuring tilt between wavefronts rather than beam position on a QPD. The setup requires one more aligned (i.e. centered and perpendicular to the QPD) reference beam, but the outcome has interferometric-level precision. In this subsection DWS is explained as implemented in LISA, with heterodyne interferometry. The relative phase of the beat note between the reference

beam and the measurement beam is separately measured in the four segments of the QPD, giving φ_i with $i \in (A, B, C, D)$. These are then compared by calculating the quantities DWS_v (vertical DWS) and DWS_h (horizontal DWS) [dimension = rad]

$$DWS_h := \varphi_{\text{left}} - \varphi_{\text{right}} = \frac{\varphi_A + \varphi_B - \varphi_C - \varphi_D}{2} \quad (2.105)$$

$$DWS_v := \varphi_{\text{top}} - \varphi_{\text{bottom}} = \frac{\varphi_A - \varphi_B + \varphi_C - \varphi_D}{2}. \quad (2.106)$$

An additional quantity with expected null output which can be computed is the ellipticity, or *cross DWS signal* DWS_c ⁷

$$DWS_c = \frac{\varphi_A - \varphi_B + \varphi_C - \varphi_D}{2}. \quad (2.107)$$

The geometrical meaning of DWS is that of measuring the different time of arrival of the wavefronts of the measurement beam on the segments of the QPD. This difference in time of arrival causes - among other effects - the beat notes generated at the QPD's segments to have a phase offset between them, as depicted in Figure 2.7. The bigger the tilt, the bigger the offset; the exact relation between offset and angle is the DWS calibration and is derived during this Section. For small tilts, this relationship is linear:

$$DWS_i \approx \kappa_1 \theta_i, \quad (2.108)$$

where θ is the tilt angle and $i \in (v, h)$ indicates the tilt axis. The quantity κ_1 [rad/rad] is called DWS gain (or *gain at null angle*) and depends on the wavelength, beam parameters and size of the QPD. Its order of magnitude is roughly $\kappa_1 \approx \frac{r_{\text{QPD}}}{\lambda}$, where r_{QPD} is the QPD radius and λ is the beam's wavelength. As the typical size of a QPD is 1 mm and $\lambda \sim 1 \mu\text{m}$, this gives $\kappa_1 \sim 10^3$ [rad/rad], meaning that a 1 rad DWS phase offset in the electrical beat notes corresponds to 1 mrad tilt angle between optical wavefronts.

Analytical DWS model

In this subsection, an analytical model is derived to determine the calibration function and other features involving DWS in case of tilts around the center of the QPD. This work was started and carried out mostly by myself before finding out that it was already elegantly published by [41] in case of an infinite radius QPD. Also included in [41] is the more general case of tilts not happening at the center of the QPD, which generally gives a lower DWS gain. Therefore I used the same formalism as in [41] and further expanded the model to describe DWS in the case of a finite-size QPDs, the non-linearity of DWS for large tilts and the heterodyne efficiency loss as a function of the tilt.

The electric field of a tilted beam Let $\vec{x} = (x, y, z)^T$ be the laboratory's RF. In this RF the QPD is a surface defined by $z = 0$, and the reference beam propagates along the z -axis. The electric field of the reference beam in the lab's RF is

⁷cross DWS is not related to any physical quantity other than the ellipticity of the beam. Any beam tilt angle don't show up in it as it will be explained further in this Section. This signal can be used as noise floor benchmark for a the DWS measurement.

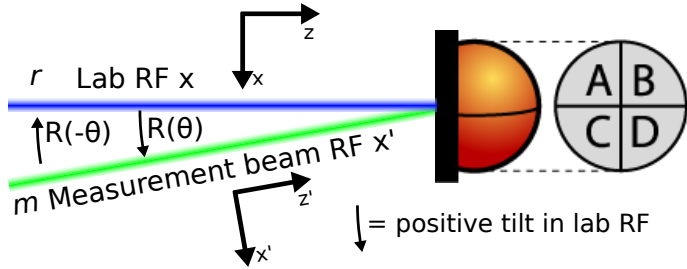


Figure 2.8: Scheme of the used reference frames in the calculation and angular orientation of the measurement beam's tilt at the QPD. The reference beam is here depicted in blue color as the LO beam and the measurement beam in green as the RX beam.

$$\vec{E}(\vec{x})_r = \hat{\varepsilon}_r \mathcal{E}_r(\vec{x}), \quad (2.109)$$

where $\hat{\varepsilon}_r = (\epsilon_x, \epsilon_y, 0)^T$ is a generic polarization vector an electromagnetic wave propagating along the z -axis and

$$\mathcal{E}_r(\vec{x}) = \sqrt{\frac{2}{\pi}} \frac{E_r}{w_r(z_r)} \exp \left(-\frac{x^2 + y^2}{w_r(z_r)^2} + i \left(k \frac{x^2 + y^2}{2R_r(z_r)} + kz_r + \eta(z_r) \right) \right), \quad (2.110)$$

where $z_r = z - z_{0,r}$ is the waist position adjusted z-coordinate and $w_{0,r}$ is the beam's waist. The constant $\sqrt{\frac{2}{\pi}} \frac{E_r}{w_r(z_r)}$ plays no role in the beam's phase and will be omitted. The measurement beam propagates on a generic, slightly rotated axis with respect to the z -axis called z' . This axis is used to define a the measurement beam's RF, which uses the primed coordinates $\vec{x}' = (x', y', z')^T$. Without loss of generality, this rotation is assumed to be a yaw rotation with pivot on the QPD's center $(x, y, z)^T = (0, 0, 0)^T$. Therefore, lab RF and measurement beam's RF are related by a rotation matrix (2.111)

$$\begin{pmatrix} x \\ y \\ z \end{pmatrix} = \begin{pmatrix} \cos(\theta) & 0 & \sin(\theta) \\ 0 & 1 & 0 \\ -\sin(\theta) & 0 & \cos(\theta) \end{pmatrix} \begin{pmatrix} x' \\ y' \\ z' \end{pmatrix} \quad \text{or } \vec{x} = R(\theta) \vec{x}'. \quad (2.111)$$

The electric field of the measurement beam is expressed by the same equations 2.109 and 2.110 in the measurement beam's RF. As the electric field is a vector field and transforms as

$$\vec{E}(\vec{x}) = R(-\theta) \vec{E}'(\vec{x}') = R(-\theta) \vec{E}'(R(\theta) \vec{x}), \quad (2.112)$$

where in the second step equation (2.111) has been used. The measurement beam's propagation axis in the lab RF is $(x = -\tan(\theta)z, y = 0)$. The expression for the measurement beam in the lab's RF is hence

$$\begin{aligned} \mathcal{E}_m(\vec{x}) &= \mathcal{E}'_m(R(\theta) \vec{x}) \\ &= \sqrt{\frac{2}{\pi}} \frac{E_m w_{m,0}}{w_m(z_m)} \exp \left(-\frac{\cos(\theta)^2 x^2 + y^2}{w_m(z_m)^2} + i \left(k \frac{\cos(\theta)^2 x^2 + y^2}{2R_r(z_m)} + \right. \right. \\ &\quad \left. \left. + k(\sin(\theta)x + z_m) + \eta(z_m) \right) \right), \end{aligned} \quad (2.113)$$

where $z_m = \cos(\theta)(z - z_{0,m})$ being the waist position adjusted z-coordinate in the lab RF. The polarization verson is rotated with $R(-\theta)$

$$\hat{\varepsilon}'_m = \begin{pmatrix} \epsilon_x \\ \epsilon_y \\ 0 \end{pmatrix} \rightarrow \hat{\varepsilon}_m = R(-\theta) \hat{\varepsilon}'_m = \begin{pmatrix} \cos(\theta) \epsilon_x \\ \epsilon_y \\ \sin(\theta) \epsilon_x \end{pmatrix}. \quad (2.114)$$

As the effective tilts are very small (\lesssim mrad), the θ dependent terms can be expanded to the 1st order in θ . Relative variations of the Guoy phase, curvature radius and of $w_m(-z_{0,m})$ along the z -axis can be shown to be of the order of 10^{-6} and can be neglected. The new resulting term is simply $e^{ikx\theta}$:

$$\vec{E}_m(\vec{x}) = \hat{\varepsilon}_m \sqrt{\frac{2}{\pi}} \frac{E_m w_{m,0}}{w_m(z_m)} \exp \left(-\frac{x^2 + y^2}{w_m(z_m)^2} + i \left(k \frac{x^2 + y^2}{2R_r(z_m)} + \underbrace{kx\theta}_{\text{tilt}} + kz_m + \eta(z_m) \right) \right). \quad (2.115)$$

The intensity of the superimposed beams is

$$I_{\text{ifm}} = \frac{1}{2Z} \left[|\vec{E}_r + \vec{E}_m|^2 = |E_r|^2 + |E_m|^2 + \vec{E}_r \cdot \vec{E}_m^* + \vec{E}_r^* \cdot \vec{E}_m \right]. \quad (2.116)$$

As any multiplicative or additive constant does not contribute to the phase variation, the terms $|E_r|^2$ and $|E_m|^2$ will be omitted and factors as $\frac{1}{2Z}$, $\sqrt{\frac{2}{\pi}} \frac{E_{m,r} w_{m,r,0}}{w_{m,r}(z_{m,r})}$, $e^{i(kz_{m,r} + \eta(z_{m,r}))}$ set to one. The term $\vec{E}_r^* \cdot \vec{E}_m$ carries the same phase information as $\vec{E}_r \cdot \vec{E}_m^*$ and will also be omitted⁸. Let's suppose that the reference and measurement beams share the same linear polarization, either vertical or horizontal. If they are vertically polarized, then $\hat{\varepsilon}_r \cdot \hat{\varepsilon}_m = 1$; if they are horizontally polarized, $\hat{\varepsilon}_r \cdot \hat{\varepsilon}_m = \cos(\theta)$. The resulting interference intensity term (see equation (2.20)), omitting the multiplicative constants, is:

$$I_{\text{ifm,v}}(x, y, \theta) = \exp \left(-\frac{x^2 + y^2}{w_{\text{eff}}^2} + ik \frac{x^2 + y^2}{2R_{\text{rel}}} + ikx\theta \right) \quad (2.117)$$

$$I_{\text{ifm,h}}(x, y, \theta) = \cos(\theta) \exp \left(-\frac{x^2 + y^2}{w_{\text{eff}}^2} + ik \frac{x^2 + y^2}{2R_{\text{rel}}} + ikx\theta \right). \quad (2.118)$$

where the quantities w_{eff} and R_{rel} are introduced, *mutatis mutandis*, in equation (2.25). Defining the parameter

$$\rho = \frac{w_{\text{eff}}^2 k}{2R_{\text{rel}}} \quad (2.119)$$

allows to greatly simply equations (2.117, 2.118) as

$$I_{\text{ifm,v}}(x, y, \theta) = \exp \left(-\frac{x^2 + y^2}{w_{\text{eff}}^2} (1 - i\rho) + ikx\theta \right) \quad (2.120)$$

$$I_{\text{ifm,h}}(x, y, \theta) = \cos(\theta) \exp \left(-\frac{x^2 + y^2}{w_{\text{eff}}^2} (1 - i\rho) + ikx\theta \right). \quad (2.121)$$

The parameter ρ has the geometrical meaning of effective-waist-normalized wavefront mismatch, or relative wavefront-mismatch. ρ is zero if the two radii of curvature are identical. Note that the values of ρ are typically smaller than 1. For instance, for two interfering beams having the same spot size $w_r = w_m = w$, and supposing $R_r = -R_m = R$ to maximize $\frac{1}{R_{\text{rel}}}$, as the smallest possible value of $|R|$ is

⁸This step corresponds to omitting the complex conjugate of $\vec{E}_r \cdot \vec{E}_m^*$ and causes the presence of an immaginary term in the resulting intensity. This apparent issue is not relevant, as this derivation aims to recover the phase of the interference intensity term.

$|R_{\min}| = 2z_R$, the largest value of $\frac{1}{R_{\text{rel}}}$ is $\frac{1}{R_{\text{rel},\min}} = \frac{1}{z_R}$. The maximum value that ρ can have is

$$\rho = \frac{w_{\text{eff}}^2 k}{2R_{\text{rel}}} \rightarrow \rho_{\max} = \frac{w^2 k}{2R} = \frac{w^2 k}{2z_R} = \frac{w^2 k}{k w^2} = 1. \quad (2.122)$$

For simplicity, equation (2.120) will from here on be used.

The Beat note A PD integrates the intensity of the beam (2.117) over its active surface S_{PD} , obtaining a power. This *de facto* is a weighted average of the local phase, where the weights are the local intensity values. The obtained expression P_{SEPD} in (2.123) represents the a beat note, of which the PM can extract phase and amplitude. Mathematically, these operations are represented by $\arg(P_{\text{SEPD}})$ and $|P_{\text{SEPD}}|$ respectively.

$$P_{\text{SEPD}} = \int \int_{S_{\text{QPD}}} dx dy \exp \left(-\frac{x^2 + y^2}{w_{\text{eff}}^2} (1 - i\rho) + ikx\theta \right) \quad (2.123)$$

In case of a limited size PD or round PD, the integrals are analytically challenging (unless $\theta = 0$). I will describe the finite QPD case later in the Section; therefore an infinite QPD radius is at first assumed. This assumption allows us to obtain analytic results which are valid in the case where the beam spot size at the QPD is much smaller than the QPD's size. A numerical solution to the limited PD size case is in Sub-subsection 2.3.3.

The Infinite PhotoDiode case In case of a SEPD of infinite radius equation (2.123) becomes

$$P_{\text{SEPD}} = \int_{-\infty}^{+\infty} dx \int_{-\infty}^{+\infty} dy \exp \left(-\frac{x^2 + y^2}{w_{\text{eff}}^2} (1 - i\rho) + ikx\theta \right). \quad (2.124)$$

A QPD instead integrates separately the intensity on each quadrant; for instance, for quadrant A of the QPD in Figure 2.6 and assuming an infinite radius and no slits one obtains

$$P_{\text{QPD},A} = \int_{-\infty}^0 dx \int_0^{+\infty} dy \exp \left(-\frac{x^2 + y^2}{w_{\text{eff}}^2} (1 - i\rho) + ikx\theta \right). \quad (2.125)$$

And similarly for the other segments, with the proper integration boundaries. For symmetry reasons, $P_{\text{QPD},C} = \int_{-\infty}^0 dx \int_{-\infty}^0 dy E_{\text{ifm}} = P_{\text{QPD},A}$ and $P_{\text{QPD},B} = P_{\text{QPD},D}$. Also $\varphi_{\text{left}} = P_{\text{QPD},A \cup C} = \int_{-\infty}^0 dx \int_{-\infty}^{+\infty} dy E_{\text{ifm}} = \arg(P_{\text{QPD},A}) = \varphi_A$, hence the left phase $\varphi_{\text{left}} = \arg(P_{\text{QPD},A \cup C}) = \frac{1}{2}(\varphi_A + \varphi_C)$, and similarly for the right phase. Using the properties of the $\arg()$ function, the DWS signals then take the form

$$\text{DWS}_v = \frac{\varphi_A + \varphi_B - \varphi_C - \varphi_D}{2} = \arg \left(\frac{\int_{-\infty}^{+\infty} dx \int_0^{+\infty} dy I_{\text{ifm}}}{\int_{-\infty}^{+\infty} dx \int_{-\infty}^0 dy I_{\text{ifm}}} \right) \quad (2.126)$$

$$\text{DWS}_h = \frac{\varphi_A - \varphi_B + \varphi_C - \varphi_D}{2} = \arg \left(\frac{\int_{-\infty}^0 dx \int_{-\infty}^{+\infty} dy I_{\text{ifm}}}{\int_0^{+\infty} dx \int_{-\infty}^{+\infty} dy I_{\text{ifm}}} \right). \quad (2.127)$$

These integrals are a double integral of the types

$$\int_{-\infty}^{+\infty} \exp(-(ax^2 + bx + c)) dx = \frac{\sqrt{\pi}}{\sqrt{a}} e^{\frac{b^2}{4a} - c} \quad (2.128)$$

$$\int_{-\infty}^0 \exp(-(ax^2 + bx + c)) dx = \frac{\sqrt{\pi}}{2\sqrt{a}} e^{\frac{b^2}{4a} - c} \left(1 + \operatorname{erf} \left(\frac{b}{2\sqrt{a}} \right) \right), \quad (2.129)$$

which is valid for $\Re(a) \geq 0$. In equation (2.129), if the integral is evaluated in $x \in [0, +\infty]$, the $\operatorname{erf} \left(\frac{b}{2\sqrt{a}} \right)$ term changes sign. The above used constants are

$$a_x = a_y = \frac{1}{w_{\text{eff}}^2} (1 - i\rho) \quad b_x = +ik\theta \quad b_y = 0 \quad c = 0,$$

where as required $\Re(a_x), \Re(a_y) \geq 0$. The explicit result for (2.124) and (2.125) are

$$P_{\text{SEPD}} = \frac{\pi w_{\text{eff}}^2}{1 - i\rho} \exp \left(\frac{-k^2 w_{\text{eff}}^2 \theta^2}{4(1 - i\rho)} \right) \quad (2.130)$$

$$P_{\text{QPD}, A \cup C} = \frac{\pi w_{\text{eff}}^2}{2(1 - i\rho)} \exp \left(\frac{-k^2 w_{\text{eff}}^2 \theta^2}{4(1 - i\rho)} \right) \left(1 + i \operatorname{erfi} \left(\frac{kw_{\text{eff}}\theta}{2\sqrt{1 - i\rho}} \right) \right) \quad (2.131)$$

$$P_{\text{QPD}, B \cup D} = \frac{\pi w_{\text{eff}}^2}{2(1 - i\rho)} \exp \left(\frac{-k^2 w_{\text{eff}}^2 \theta^2}{4(1 - i\rho)} \right) \left(1 - i \operatorname{erfi} \left(\frac{kw_{\text{eff}}\theta}{2\sqrt{1 - i\rho}} \right) \right), \quad (2.132)$$

where $\operatorname{erf}(iz) = i \operatorname{erfi}(z)$.

The DWS signals on an Infinite QPD For an infinite radius QPD by substituting integrals (2.131) and (2.132) into (2.126) and (2.127), one gets

$$\text{DWS}_v(\theta) = 0 \quad \text{DWS}_h(\theta) = \arg \left(\frac{1 + i\alpha}{1 - i\alpha} \right) \quad [\text{DWS}_c(\theta) \equiv 0] \quad (2.133)$$

with

$$\alpha = \operatorname{erfi} \left(\frac{kw_{\text{eff}}\theta}{2\sqrt{1 - i\rho}} \right) = \operatorname{erfi} \left(\frac{w_{\text{eff}}k\theta}{2} \sqrt{\frac{1 + i\rho}{1 + \rho^2}} \right). \quad (2.134)$$

For simplicity $\beta = \frac{w_{\text{eff}}k\theta}{2} \sqrt{\frac{1 + i\rho}{1 + \rho^2}}$ is defined, and $\alpha = \operatorname{erfi}(\beta)$. As expected, DWS is an odd function of the tilt angle, as if θ is transformed as $\theta \rightarrow -\theta$, then $\alpha \rightarrow -\alpha$ and $\text{DWS}(-\theta) = \arg \left(\frac{1 - i\alpha}{1 + i\alpha} \right) = -\text{DWS}(\theta)$. As the beam tilts to be measured are usually very small, it makes sense to linearize the expression for $\text{DWS}_h(\theta)$ from equations (2.133, 2.134) around $\theta = 0$. This procedure leads to the coefficient κ_1 defined in (2.108). Assuming $\theta \ll 1 \rightarrow \alpha \ll 1$, the first-order approximation is relatively intuitive, following the steps

$$\begin{aligned} \arg \left(\frac{1 + i\alpha}{1 - i\alpha} \right) &\approx \arg(1 + 2i\alpha) = \arctan \left(\frac{2\Re[\alpha]}{1 - 2\Im[\alpha]} \right) \approx \arctan(2\Re[\alpha]) \approx 2\Re[\alpha] \\ \operatorname{erfi}(x) &\approx \frac{2}{\sqrt{\pi}} x \\ \Re[\beta] &= \frac{w_{\text{eff}}k\theta}{2} \frac{1}{\sqrt[4]{1 + \rho^2}} \cos \left(\frac{1}{2} \arctan(\rho) \right) = \frac{w_{\text{eff}}k\theta}{2} F(\rho) \\ \Im[\beta] &= \frac{w_{\text{eff}}k\theta}{2} \frac{1}{\sqrt[4]{1 + \rho^2}} \sin \left(\frac{1}{2} \arctan(\rho) \right) = \frac{w_{\text{eff}}k\theta}{2} G(\rho), \end{aligned}$$

with the explicit expression of the $F(\rho)$ and $G(\rho)$ being

$$F(\rho) = \sqrt{\frac{1 + \sqrt{1 + \rho^2}}{2(1 + \rho^2)}} \quad (2.135)$$

$$G(\rho) = \frac{\rho}{\sqrt{1 + \rho^2} \sqrt{2(1 + \sqrt{1 + \rho^2})}}. \quad (2.136)$$

This results in

$$\text{DWS}_h(\theta) \approx \frac{2}{\sqrt{\pi}} k w_{\text{eff}} F(\rho) \theta + \mathcal{O}(\theta^3), \quad (2.137)$$

from which it is clear that

$$\kappa_1 = \frac{\partial}{\partial \theta} \text{DWS}_h(\theta) |_{\theta=0} \quad (2.138)$$

as in [41]. The parameter κ_1 has the physical meaning of being the DWS gain when the tilt angle is zero. The linearization (2.137) is useful since it gives an easy way to compare the DWS signals induced for small angles by different beam geometries. Hence, $F(\rho)$ is usually close to one (see Figure 2.9). This makes w_{eff} the dominant parameter in determining κ_1 . For a given w_{eff} , κ_1 is maximum for $\rho = 0$, that is $\frac{1}{R_{\text{rel}}} \rightarrow 0$ and hence when the two radii of curvature are the same $R_m = R_r$.

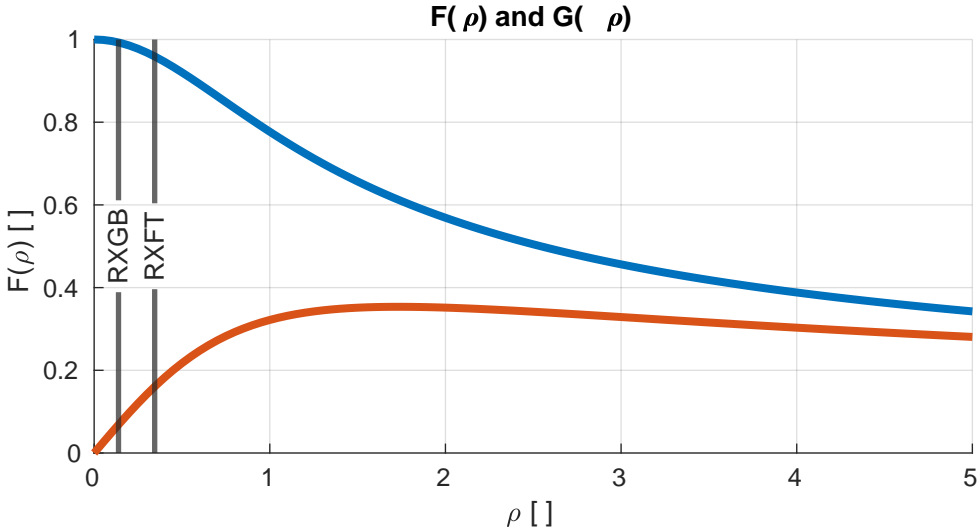


Figure 2.9: Plot of $F(\rho)$ and $G(\rho)$. $G(\rho)$ is relevant only for expansion terms from the third order onwards, where it appears only squared. The values of ρ for the RX-GB & LO and RX-FT & LO beams are indicated, being $\rho_{\text{RX-GB} \& \text{LO}} = 0.1387$ and $\rho_{\text{RX-FT} \& \text{LO}} = 0.3446$ respectively. These specific beams are part of the TDOBS experiment, which is introduced in Section 3.2.2.

Further expanding DWS_h from equations (2.133, 2.134) shows also for the non linear nature of DWS. As DWS is an odd function, this procedure gives only odd

non-zero coefficients. The first three terms are

$$\text{DWS}_h(\theta) = \kappa_1\theta + \kappa_3\theta^3 + \kappa_5\theta^5 + \mathcal{O}(\theta^7) \quad (2.139)$$

$$\kappa_1 = \frac{2}{\pi^{\frac{1}{2}}} F(\rho) w_{\text{eff}} k \quad (2.140)$$

$$\kappa_3 = \frac{F(\rho)(F(\rho)^2 - 3G(\rho)^2)(\pi - 4)(w_{\text{eff}} k)^3}{6\pi^{\frac{3}{2}}} \quad (2.141)$$

$$\kappa_5 = \frac{F(\rho)(F(\rho)^4 - 10F(\rho)^2G(\rho)^2 + 5G(\rho)^4)(96 + \pi(3\pi - 40))(w_{\text{eff}} k)^5}{240\pi^{\frac{5}{2}}} \quad (2.142)$$

Typical order of magnitudes are $\kappa_1 \sim 10^3$ rad/rad, $\kappa_3 \sim 10^9$ rad/rad³ and $\kappa_5 \sim 10^{13}$ rad/rad⁵. Practically, κ_5 is always negligible, while κ_3 defines at which angle the non-linearity starts being relevant. κ_3 is always negative, meaning that the DWS gain is maximum if $\theta = 0$ and decreases in case of a tilt.

The Finite PhotoDiode case The results shown above are valid for a QPD or infinite radius, or more generally in cases where $r_{\text{QPD}} \gg w_{\text{eff}}$. In order to treat cases where the two values are comparable, the integrals (2.124, 2.125) have to be limited to the QPD's effective area. The typical shapes for a QPD are either square or circular, with small slits separating the quadrants. The only case which can be treated analytically is a square QPD. Equation 2.143 calculates the beat note in case of a square QPD without slits.

$$\begin{aligned} P_{\text{square QPD}} &= \int_{-r}^{+r} \int_{-r}^{+r} \exp(-(a_x x^2 + a_y y^2 + b_x x + b_y y + c)) dx dy = \\ &= \frac{\pi}{\sqrt{a_x a_y}} \operatorname{erf}\left(\sqrt{\frac{r}{a_y}}\right) e^{\frac{b_x^2}{4a_x}} e^{\frac{b_y^2}{4a_y}} e^{-c} \left[\operatorname{erf}\left(\frac{b_x + 2a_x r}{2\sqrt{a_x}}\right) - \operatorname{erf}\left(\frac{b_x - 2a_x r}{2\sqrt{a_x}}\right) \right] \end{aligned} \quad (2.143)$$

In case of a round QPD without slits the most one can do is to solve just one of the two integrals, as in (2.144). Results for this are in the numerical DWS Subsection 2.3.3.

$$\begin{aligned} P_{\text{round QPD}} &= \int_{-r}^{+r} \int_{-\sqrt{r^2 - x^2}}^{+\sqrt{r^2 - x^2}} \exp(-(a_x x^2 + a_y y^2 + b_x x + b_y y + c)) dx dy = \\ &= e^{\frac{b_x^2}{4a_x}} e^{-c} \int_{-r}^{+r} dx \sqrt{\frac{\pi}{a_y}} \exp(-(a_x x^2 + b_x x)) \operatorname{erf}\left(\sqrt{(r^2 - x^2)a_x}\right) \end{aligned} \quad (2.144)$$

Heterodyne efficiency decrease Besides the DWS signals, equation (2.130) also predicts a decrease of the beat note's amplitude due to the tilt. The overlap integral of two parallel Gaussian beams was already calculated in equation (2.24) in the case of an infinite SEPDI, and is re-written here in terms of ρ .

$$I_{\text{overlap, GB-GB}} = 2 \frac{1}{w_1(z)} \frac{1}{w_2(z)} \frac{w_{\text{eff}}^2 e^{i(\Delta\varphi + \Delta\eta)}}{\sqrt{1 + \rho^2}} e^{i \arctan(\rho)}, \quad (2.145)$$

With $\sqrt{\eta_{\text{het}, 0}} = \Re[I_{\text{overlap, GB-GB}}]$. As visible in equation 2.145, the heterodyne efficiency depends on ρ and is maximum if the relative wavefront mismatch is $\rho = 0$.

This is physically interpretable as the two wavefronts being in-phase in the whole transverse space. The interference of the two beams is converted into an electrical beat note at every point of the surface of the PD. All of these beat notes are in-phase, hence are summed up constructively. As soon as ρ departs from zero, in the sum a destructive component appears.

A similar effect can be caused by the tilt, which introduces a further mismatch between the wavefronts. The heterodyne efficiency on an infinite SEPD then varies as

$$\sqrt{\eta_{\text{het}}}(\theta) = \sqrt{\eta_{\text{het}, 0}} e^{-\xi^2 \theta^2} \quad \xi = \frac{kw_{\text{eff}}^2}{4\sqrt{1+\rho^2}}. \quad (2.146)$$

Hence the presence of a wavefront mismatch reduces $\sqrt{\eta_{\text{het}, 0}}$, but also reduces the constant ξ . The term $e^{-\xi^2 \theta^2}$ always dominates the $\cos(\theta)$ effect caused by the beam's rotation which occurs if the polarization plane is the same as the rotation plane. A typical value is $\xi \sim 10^3 \text{ rad}^{-1}$ which is a huge effect, causing a contrast decrease by a factor of 10 for a tilt of only 1.5 mrad on a SEPD. It is to be noted that, when calculating the amplitude of the beat note on a QPD, this works differently, as the interference signal is integrated separately on the four segments. Mathematically, this can be described as $P_{\text{SEPD}}(E_{\text{ifm}}) \neq P_{\text{QPD}}(E_{\text{ifm}})$, where the operators SEPD-power $P_{\text{SEPD}}(E_{\text{ifm}})$ and QPD-power $P_{\text{QPD}}(E_{\text{ifm}})$, together with the QPD-segment-power, were for convenience defined.

$$P_{\text{SEPD}}(I_{\text{ifm}}) = \left| \int_{-\infty}^{+\infty} \int_{-\infty}^{+\infty} dx dy I_{\text{ifm}} \right| \quad (2.147)$$

$$P_{\text{QPD, A}}(I_{\text{ifm}}) = \left| \int_{-\infty}^0 \int_0^{+\infty} dx dy I_{\text{ifm}} \right| \quad (2.148)$$

$$P_{\text{QPD, B}}(I_{\text{ifm}}) = \left| \int_0^{+\infty} \int_0^{+\infty} dx dy I_{\text{ifm}} \right| \quad (2.149)$$

$$P_{\text{QPD, C}}(I_{\text{ifm}}) = \left| \int_{-\infty}^0 \int_{-\infty}^0 dx dy I_{\text{ifm}} \right| \quad (2.150)$$

$$P_{\text{QPD, D}}(I_{\text{ifm}}) = \left| \int_0^{+\infty} \int_{-\infty}^0 dx dy I_{\text{ifm}} \right| \quad (2.151)$$

$$P_{\text{QPD}}(I_{\text{ifm}}) = P_{\text{QPD, A}}(I_{\text{ifm}}) + P_{\text{QPD, B}}(I_{\text{ifm}}) + P_{\text{QPD, C}}(I_{\text{ifm}}) + P_{\text{QPD, D}}(I_{\text{ifm}}) \quad (2.152)$$

It turns out that the loss of contrast on QPD segments occurs roughly half as rapid as on a SEPD. In order to analytically calculate this effect for the QPD amplitude the absolute value of equation (2.132) must be calculated. This includes calculating the absolute value of a complex error function term, which is not present in the SEPD intensity in equation (2.130). As separating real and imaginary part of a complex error function is analytically impossible, this calculation is analytically not possible. Results for this are in the numerical DWS Subsection 2.3.3.

Numerical DWS model

This Subsection shows the used numerical integration method and characterization and lists all the numerical answers to the unsolved questions from above which required the integration of equations (2.124) and (2.125).

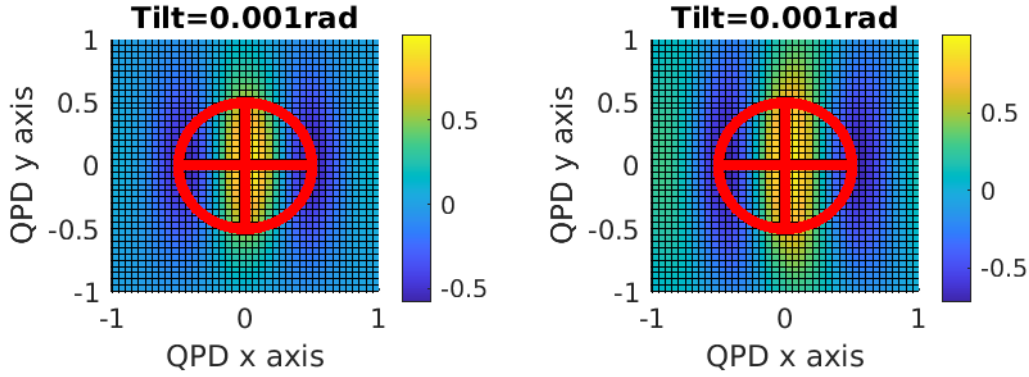


Figure 2.10: Plot of the numerical integration of the interference intensity term in equation (2.117) in arbitrary units. The used beam parameters are $w_{\text{eff}} = 0.6686$ mm, $\rho = -0.13865$ on the left and $w_{\text{eff}} = 0.8740$ mm, $\rho = -0.34461$ on the right. The used photodiode geometry is that of the reference QPDs (REFQPDs) (see section 3.2). These specific beams and QPDs are part of the TDOBS experiment, which is introduced in Section 3.2.2. The plot shows the resulting intensity of the interference term (2.117) for a tilt of $\theta = 1$ mrad together with the contour of a GAP1000Q QPD. The plots are downsampled by a factor 10 for plotting clearness.

The numerical integration method The continuous space (x, y) has been discretized to a point-grid (x_i, y_j) of spatial separation Δs . All integrals are approximated to discrete sums, and the integrand function is evaluated in the center of each square bin, as

$$P(I_{\text{ifm}}) = \int \int_{S_{\text{QPD}}} dx dy I_{\text{ifm}}(x, y) \approx \sum_{i, x_i \in S_{\text{QPD}}} \sum_{j, y_j \in S_{\text{QPD}}} I_{\text{ifm}}(x_i, y_j) \Delta s^2 = P(I_{\text{ifm, num}}). \quad (2.153)$$

Using the resulting power $P(I_{\text{ifm, num}})$, amplitude and phase can be calculated as usual. It can be shown that this method causes an error of $\mathcal{O}(\Delta s^2)$. In a calculation using the science QPDs (SCIQPDs) beam parameters and a spatial grid of $\Delta s = 5$ μm ⁹, this method has shown an error in the DWS signal estimation of at most 5×10^{-5} rad and a maximum DWS gain error of 4×10^{-2} rad/rad. Given that the DWS signal is $\mathcal{O}(1)$ rad and that the DWS gain is $\mathcal{O}(10^3)$ rad/rad, the results of this method are trustable up to 10^{-5} in terms of predicted DWS gain, which is well within the target for this analysis. Figure 2.10 shows, as an example, some intensity fields calculated during this process.

Finite QPD size The first investigation which was carried out was how the finite QPD size affects the resulting DWS signals in the case of a round QPD. The resulting electric field of a given interfering configuration was integrated on QPDs of different sizes. The resulting DWS signal was fit with a third-order polynomial to derive the first two coefficients of the polynomial expansion κ_1 and κ_3 . Slits are neglected to make the result scalable in terms of $r_{\text{QPD}}/w_{\text{eff}}$. This was feasible upon numerically checking that slits as small as $s = 20$ μm have a negligible effect, as this value is much smaller than both the QPD and beam radii. Figures 2.11 and 2.12 show the relation between κ_1 and κ_3 , respectively, and the QPD's radius.

⁹this value was chosen as it is one quarter of the GAP1000Q's slit width

κ_1 strongly decreases as the QPD's radius shrinks. This relationship can be decently approximated with an exponential function $f(r) = \kappa_{1,\text{th}}(1 - a \exp(-b * r))$, where $\kappa_{1,\text{th}}$ is the expected κ_1 value from equation (2.140). The visible discrepancy between the simulated values at large QPD radii and the theoretical value is likely due to a systematic error in the fitting procedure.

κ_3 also strongly decreases as the QPD's radius shrinks. This relationship can also be roughly approximated with the function $f(r) = \kappa_{3,\text{th}} \exp(b \exp(-c * r))$, where $\kappa_{3,\text{th}}$ is the expected κ_3 value from equation (2.141). Also here the visible discrepancy between the simulated values at large QPD radii and the theoretical value is likely due to a systematic error in the fitting procedure.

Figure 2.13 plots the measured values from Figures (2.140) and (2.141) together. Note that κ_3 decreases much quicker than κ_1 , resulting in the fact that a smaller QPD gives a less steep but more linear DWS signal.

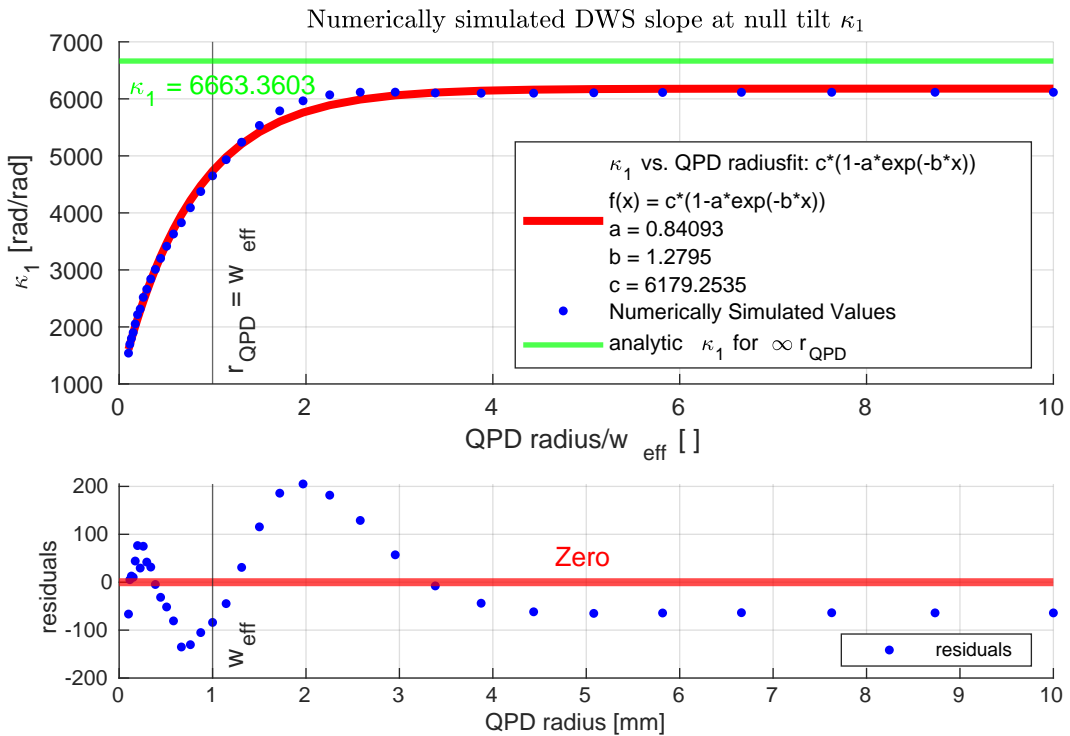


Figure 2.11: DWS slope at null tilt κ_1 computed as a function of the relative radius of the QPD $r_{\text{QPD}}/w_{\text{eff}}$.

DWS models for TDOBS I calculated some DWS calibrations for TDOBS, the experiment introduced in Section 3.2. Figures 2.14, 2.15 and 2.16 show the results of the numerical modelling of the DWS signals for some TDOBS specific cases, where the used PD is a GAP1000Q, alongside an analytical calibration valid if the QPD has an infinite radius. As the QPD's size is reduced, the DWS signals have a lower slope and look more linear as discussed in the previous paragraph.

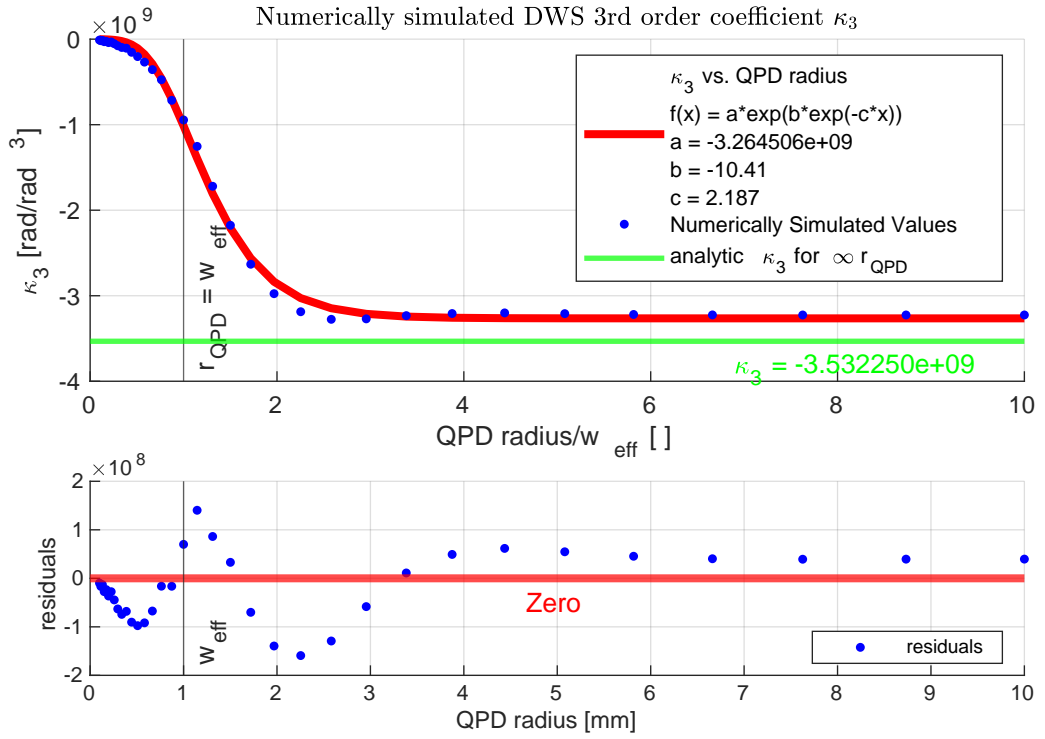


Figure 2.12: DWS third-order fit parameter κ_3 computed as a function of the relative radius of the QPD r_{QPD}/w_{eff} .

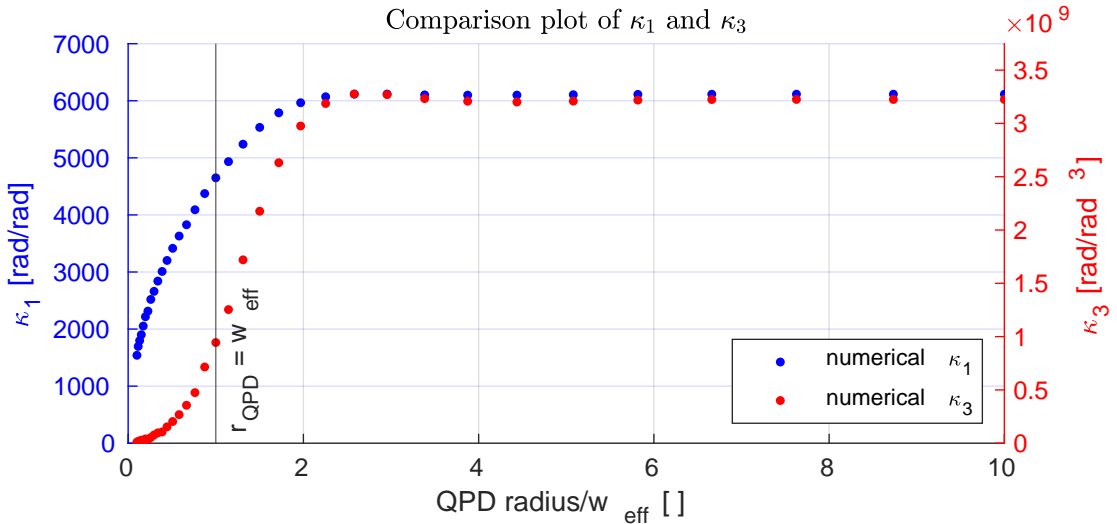


Figure 2.13: DWS first- and third-order fit parameter κ_1 & κ_3 plotted together, normalized to their asymptotic value.

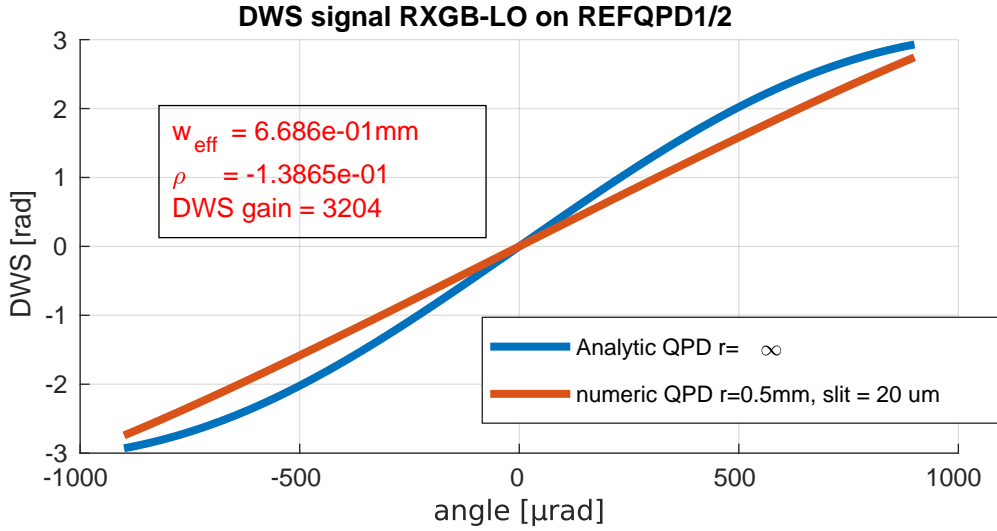


Figure 2.14: DWS curves computed for the RX-GB & LO beams (the beam parameters are shown in the textbox in the plot) at the REFQPDs. The analytic curve is calculated for an infinite size QPD, while the numerical curve is calculated for the specific GAP1000Q size.

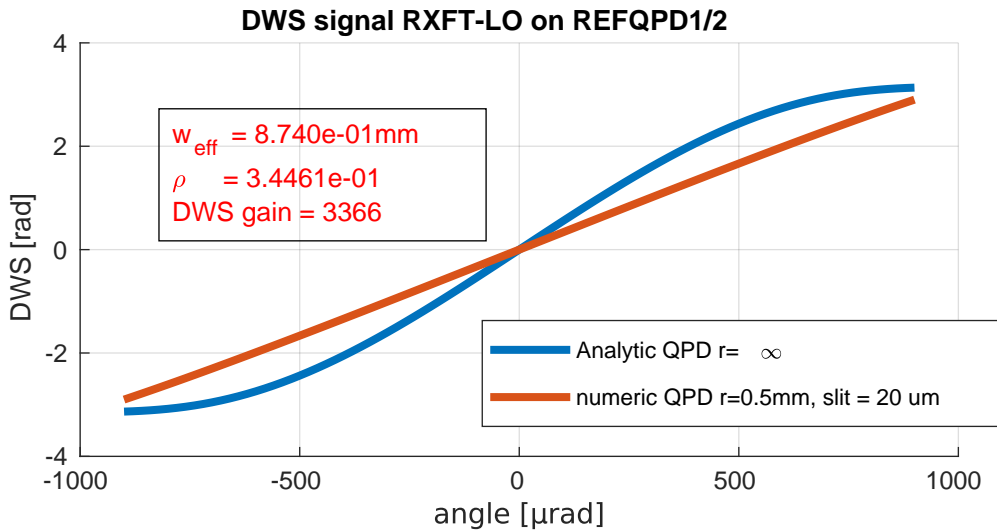


Figure 2.15: DWS curves computed for the RX-FT & LO beams (the beam parameters are shown in the textbox in the plot) at the REFQPDs. The analytic curve is calculated for an infinite size QPD, while the numerical curve is calculated for the specific GAP1000Q size. Note that in this case the limited size of the QPD completely suppresses κ_3 .

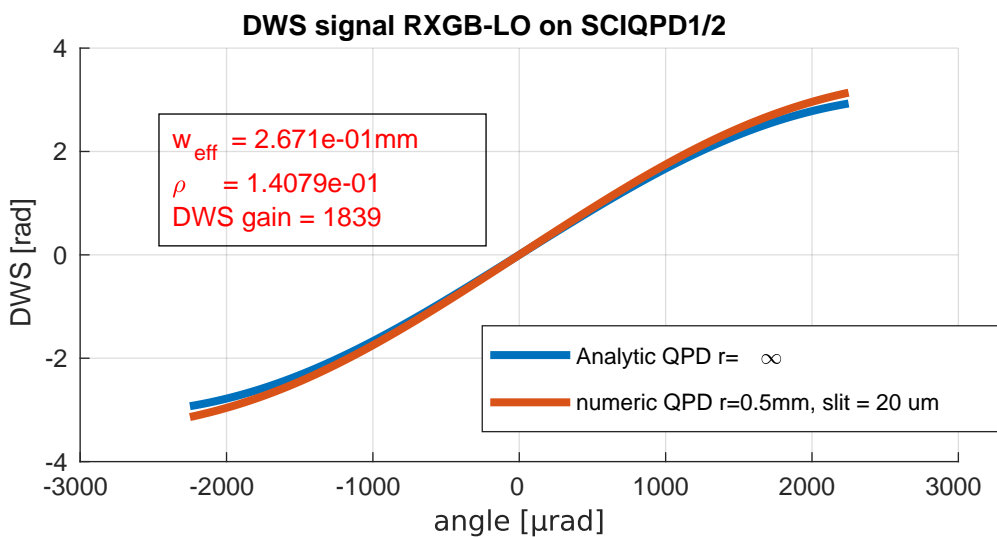


Figure 2.16: DWS curves computed for the RX-GB & LO beams (the beam parameters are shown in the textbox in the plot) at the SCIQPDs. The analytic curve treats the QPD as infinite size, while the numerical curve is calculated for the specific GAP1000Q size. The DWS gain is calculated at the QPD, excluding any magnification from the IS. The x -axis range has been extended as in the experiment the angle would be magnified by the IS.

Heterodyne efficiency as a function of the tilt angle As already addressed in paragraph 2.3.3, the heterodyne efficiency decreases as one beam is tilted. This phenomenon is driven by the fact that, in the presence of e.g. a horizontal tilt, the interfering beams are not anymore in-phase. As the phase offset between the beat notes at two points of the PD is proportional to their separation¹⁰ (see tilt term in equation (2.115)), this effect is expected to be mitigated in the case of a finite size PD. Therefore, taking as an example an infinite SEPD, a finite SEPD and a finite QPD, the decrease of the heterodyne efficiency is strongest in the first case and further mitigated on the finite SEPD and finite QPD.

Figures 2.17 and 2.18 plot the numerically simulated decrease of the heterodyne efficiency as a function of the measurement beam's tilt angle for the specific parameters of the RX-GB & LO beams (see Section 3.2). The calculated configurations are the heterodyne efficiency decrease on a) a finite size SEPD with a radius of 0.5 mm, b) a finite size QPD of the same radius, and c) a single segment of a QPD of the same radius. The simulated curves were fitted with a Gaussian function, and the obtained coefficients are reported in Table 2.1.

For the finite SEPD amplitude, the simulated curve can still be approximated to a Gaussian curve as described for an infinite SEPD, but the constant ξ has a different, in particular smaller, value. The same holds for the QPD amplitude, with a further smaller ξ value. The single segment of the QPD gives a very similar ξ value to that of the QPD amplitude, but the angle of maximum heterodyne efficiency is not anymore zero (see Table 2.1). The next simulation shows more details on this.

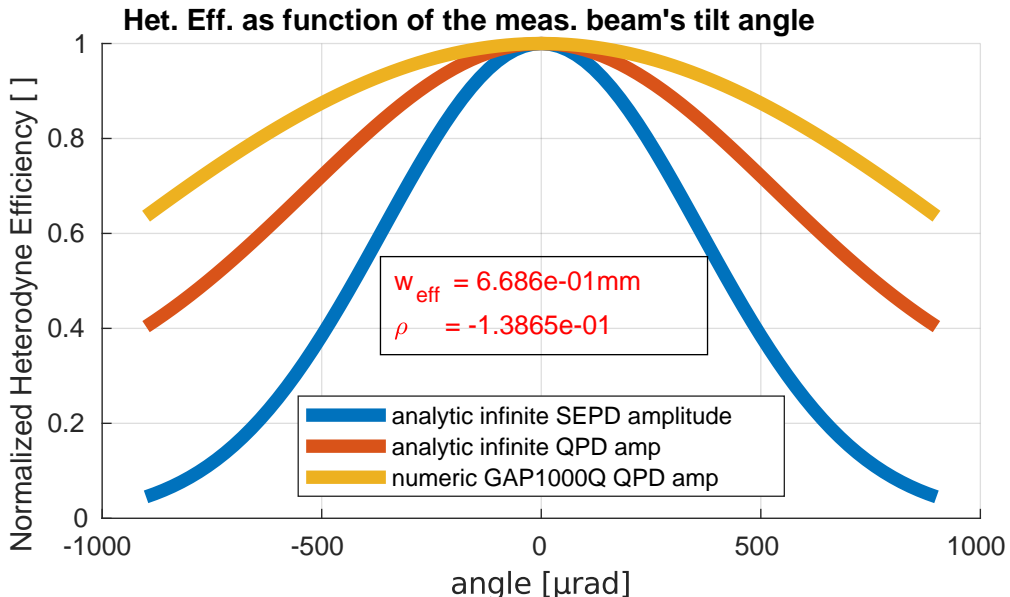


Figure 2.17: Heterodyne efficiency decrease as a function of beam the tilt angle in the case of an infinite SEPD, a finite SEPD and a finite QPD for a horizontal beam tilt around the center of the QPD. Used beam parameters are those of RX-GB & LO beams impinging on the REFQPDs. The curves for a finite SEPD and finite QPD were fit with a Gaussian function, and the obtained coefficients are reported in Table 2.1. The fit is not shown for simplicity.

¹⁰To be more precise, it is proportional to the projection of their separation onto the axis of the tilt.

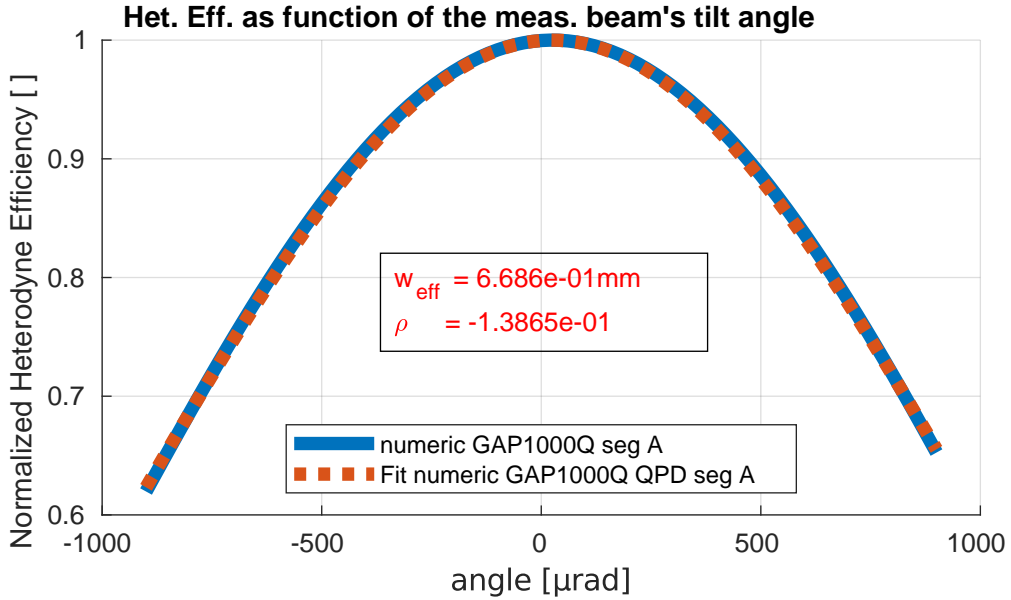


Figure 2.18: Heterodyne efficiency decrease as a function of beam the tilt angle in the case of a segment of a finite QPD for a horizontal beam tilt around the center of the QPD. Used beam parameters are those of RX-GB & LO beams impinging on the REFQPDs. The curve was fit with a Gaussian function, and the obtained coefficients are reported in Table 2.1.

Parameter	SEPD amplitude	QPD amplitude	Segment A amplitude
a []	1.018 ± 0.004	1.002 ± 0.0003	1.002 ± 0.0003
s [μrad]	218 ± 38	951.6 ± 0.8	951.3 ± 0.8
x_0 [μrad]	0 \pm 2	0 \pm 0.39	-0.25 \pm 0.39

Table 2.1: Fit parameters from Figures 2.17 and 2.18. The used fit function is $f(x) = a \exp\left(-\frac{1}{2} \left(\frac{x-x_0}{s}\right)^2\right)$. The parameter ξ can be derived as $\xi = \frac{1}{\sqrt{2}s}$.

Heterodyne efficiency as a function of ρ For symmetry reasons, if the beams are centered, the tilt angle at which the heterodyne efficiency is maximum in a SEPD and a QPD is always zero. On the other hand, the tilt angle at which the heterodyne efficiency is maximum in a QPD segment is a function of the parameter ρ . This can be naively understood as ρ states how mismatched the wavefronts are, with the mismatch being zero if $\rho = 0$. In the case of $\rho \neq 0$, a tilt of the beam can, in general, reduce the mismatch hence increasing the heterodyne efficiency.

This is shown in the following simulations (Figures 2.19 and 2.20), which use the beam parameters for the TMI in LISA reported in Section 5.1.1 together with an exaggerated range for ρ of $\rho \in [-1, 1]$, while the beam spot size was set to be 0.46 mm, which is approximately the largest possible value.

Figure 2.19 shows the normalized heterodyne efficiency of a QPD (see equation (2.152)) as a function as a function of the beam tilt angle for various values of ρ . The normalization is useful to suppress the dependency of the curve's maximum value on ρ . As ρ departs from 0, the heterodyne efficiency curve broadens. Simultaneously, the curve's shape departs from Gaussianity. This process depends only on $|\rho|$.

Figure 2.20 shows the normalized heterodyne efficiency of a segment of a QPD (see equations (2.148, 2.149, 2.150, 2.151)) as a function as a function of the beam tilt

angle for various values of ρ . For this plot, segment A was chosen. The normalization is useful to suppress the dependency of the curve's maximum value on ρ . As ρ departs from 1, the angle at which the heterodyne efficiency is maximum shifts either to positive or negative tilt angles. Simultaneously, the curve's shape departs from Gaussianity. This fact is relevant when combining the beat notes from a QPD to calculate the DWS or LPS signals.

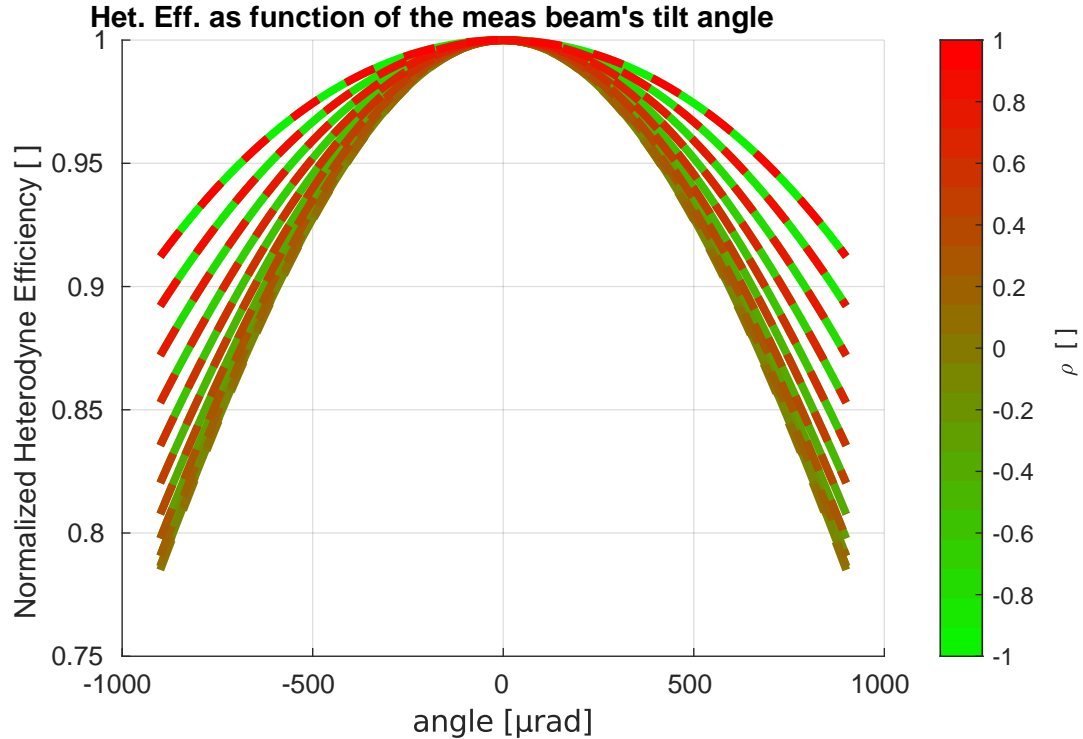


Figure 2.19: Heterodyne efficiency of the combined four segments of a QPD in the TMI, based on equation (2.152) numerically calculated for a finite QPD and plotted for various values of ρ . The curves depend only on $|\rho|$ and not on the sign of ρ , hence the curves for values of $\rho > 0$ are plotted with dashed lines to avoid overlap.

The numerically calculated curves in Figures 2.19 and 2.20 were fitted using Gaussian curves $f(x) = a \exp\left(-\frac{1}{2} \left(\frac{x-x_0}{s}\right)^2\right)$ to obtain the relationship between the fit parameter and ρ . The resulting fit parameters are reported in Figure 2.21.

The plot of the a parameter states that the heterodyne efficiency for both QPD and QPD segment is maximum at $\rho = 0$, while it decreases symmetrically as $|\rho|$ increases. This behaviour of the QPD matches equation (2.146), as for $|\rho| = 1$ the parameter a decreases by a factor of $\sqrt{2}$. The single QPD channel experiences a mitigated decrease of a .

The plot of the parameter s states that the amplitude of the Gaussian curve increases symmetrically as ρ increases, meaning that the decrease of the heterodyne efficiency as a function of the beam tilt angle is mitigated for higher values of ρ . This effect is stronger for the QPD-heterodyne efficiency. The error bars on s increase as a function of $|\rho|$, as the approximation of the numerically calculated curves to a Gaussian function worsens.

The plot of the parameter x_0 shows that the tilt angle at which the heterodyne efficiency of a QPD is maximum is always 0 rad. This is expected due to symmetry

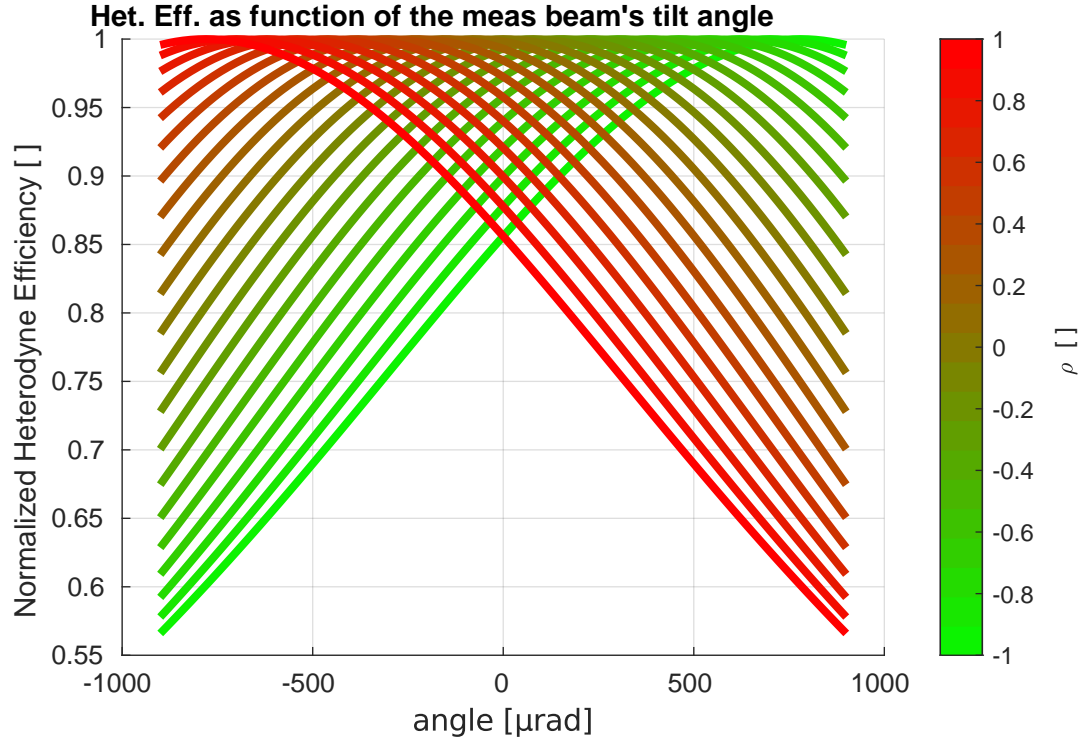


Figure 2.20: Heterodyne efficiency of segment A of a QPD in the TMI, based on equation (2.125) numerically calculated for a finite QPD and plotted for various values of ρ .

reasons. On the other hand, the angle at which the heterodyne efficiency of a QPD-segment is maximum is an odd function of ρ . This means that, in any situation where ρ is different than zero, the maximum of the heterodyne efficiency is not at a tilt angle of 0 rad.

These considerations are relevant in any context where the signals from a misaligned IFM using a QPD are used. In the case of centered beams, a wavefront mismatch breaks the symmetry between LPF and AP LPS (see Section 2.3.2). Furthermore, there are non-trivial implications on LPS and DWS noise calculations, as these depend on the heterodyne efficiency. Note that values the maximum $|\rho|$ in LISA is 0.469 for both the TMI and ISI, hence these effects could be also very pronounced.

2.4 Conclusion

In the first part of this chapter, the main concepts of Gaussian beams, interferometry and ray transfer matrices were introduced. The second part of this chapter introduces the main signals derived from the use of QPDs, in specific differential power sensing (DPS), longitudinal pathlength sensing (LPS) and differential wavefront-sensing (DWS). A detailed model is derived for DWS, to describe the signal depending on the geometrical properties of the used setup. This model calculates the DWS signals a) analytically under the assumption of infinite QPD size and no slits, b) semi-analytically and numerically for a general case. The reduction of the heterodyne efficiency as a function of the beam tilt, which is a relevant parameter in the noise performance models, is also discussed.

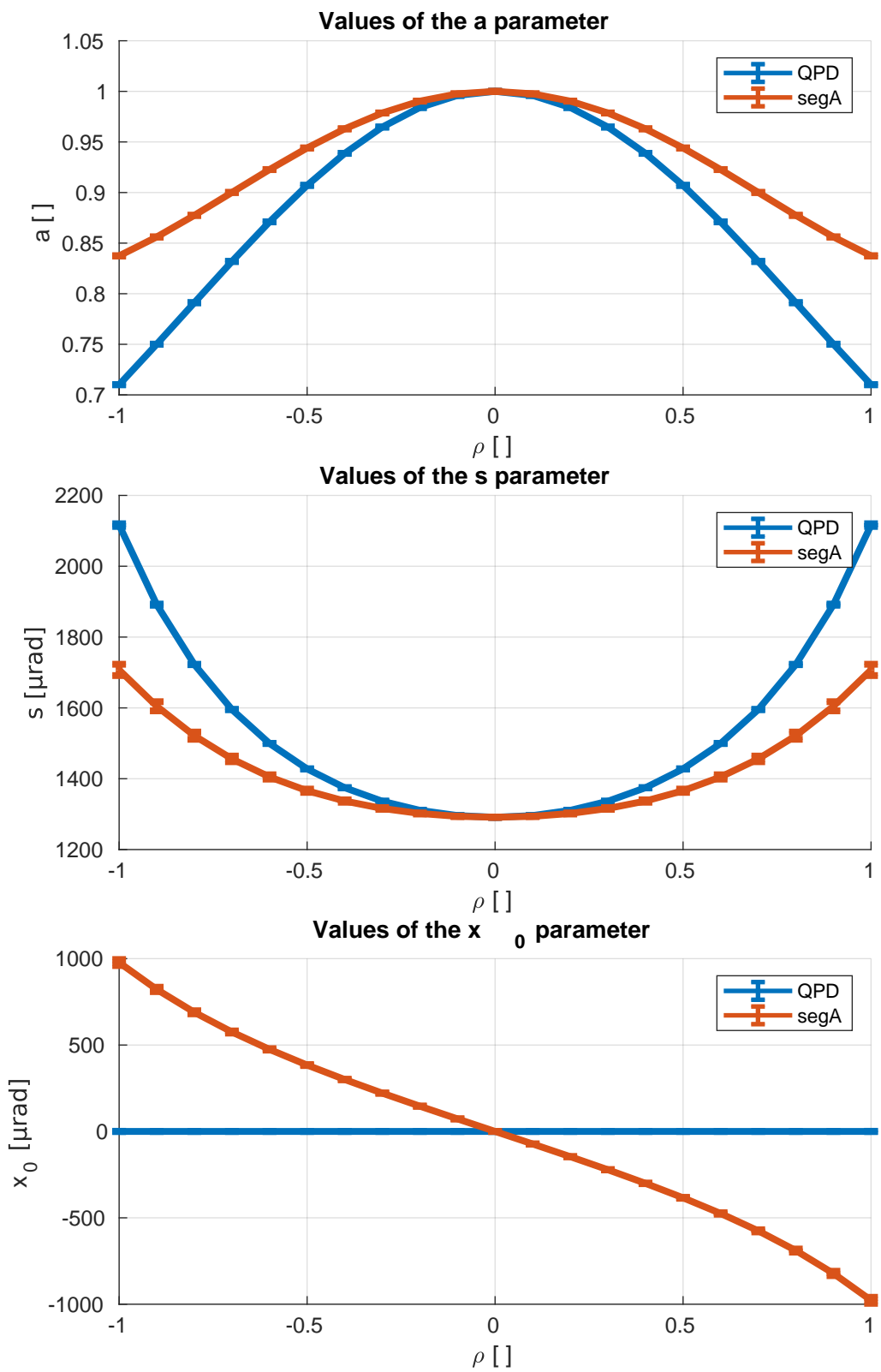


Figure 2.21: Plot of the fit parameters from the Gaussian fit of Figures 2.19 and 2.20.

Chapter 3

The Tilt-to-Length Coupling and Differential Wavefront-Sensing Optical Bench Simulator

In Section 2.1.3 interferometry was introduced as an *transducer* capable of converting optical pathlength, related to the target of the measurement, into a voltage signal. This is an ideal picture, as the measured voltage variations can have many other causes, which are indistinguishable from pathlength variations of the same magnitude; some causes related to the laser’s properties were described in Subsection 2.1.5. Another possible issue is the coupling of pathlength variations which are *not* the target of the measurement. This is caused, for instance, by tilts of a test mass (TM), which alter the optical path of a laser beam reflecting on the TM, even if the center of mass of the TM has not moved. Such issue currently affects the sensitivity of ground-based interferometers (IFMs) at low frequencies [52], and is estimated to be the second-largest noise entry in LISA’s TMI [34].

3.1 Tilt-to-Length Coupling in LISA

Figure 3.1, above shows an example of how tilt couples into the pathlength measurement. The target of the measurement is the displacement of the center of mass of the TM, indicated with the coordinate x . If the TM shifts along the x -axis, the optical pathlength changes, and this is measured by the IFM as a change of power due to interference. A free floating TM is also likely to rotate around its center of mass; such rotations are indicated by the coordinate θ . The beam reflecting on the TM tilts by 2θ and travel a longer optical pathlength. The IFM cannot distinguish a variation of θ from a variation of x . The mentioned example is called *lever-arm* TTL and gives an additional pathlength of $\Delta s_{\text{lever}} = d_{\text{pivot}}\theta^2$, where d_{pivot} is the TM to PD distance [67, 40] and belongs to the category of geometrical TTL, together with the piston effect [67, 40]. Sources of non-geometrical TTL also exist, as variations of beam offset and parameters as well as wavefront errors, can couple into the interferometric measurement [67, 40].

All of these TTL couplings would be of little consequence if the interferometric topology was stable, but in reality this is never the case. In LISA the angular stability is at most $1 \text{ nrad}/\sqrt{\text{Hz}}$ [34, page 19], as a result of active control of the spacecraft’s attitude and of the TM’s degrees of freedom. In such condition and

despite further mitigation, TTL is foreseen to be one of the main noise sources in the TMI [34, Figure 18].

TTL mitigation in LISA is achieved through three main channels:

1. *Active*: control of the spacecraft's attitude and MOSA's angle and TM's position and angle with respect to the MOSA to the order of few $\text{nrad}/\sqrt{\text{Hz}}$ and $\text{nm}/\sqrt{\text{Hz}}$.
2. *Offline*: post-processing subtraction of the additional pathlength caused by TTL. This procedure requires a model of the extra pathlength caused by the tilt $\Delta s = \Delta s(\eta, \varphi)$ ¹ [58]. Such models have already been developed for LISA-Pathfinder [40] and a 24-parameter TTL model has been developed for LISA in [58]; these parameters can be recovered either by calibration manoeuvres [49] or by measuring the naturally occurring MOSA's jitter via DWS and fitting to the readout signals [17].
3. *Passive*: suppression of geometrical TTL by using imaging systems (ISs) [77, 67, 3] (see Subsection 2.2.2).

Active Control The active control of the spacecraft by means of the micro-newton thrusters keeps the angular jitter at a level of few $\text{nrad}/\sqrt{\text{Hz}}$. In order to achieve this, a readout with at least this sensitivity is needed. This is provided in LISA by DWS (see Section 2.3.3). DWS has demonstrated its effectiveness in the GRACE Follow-On mission, where it was key for achieving the precise laser-beam pointing required between the two spacecraft in low Earth orbit [21]. This successful deployment validated DWS as a critical tool for inter-satellite laser interferometry, offering a foundation for its extended application in the LISA mission, where the technology needs to operate in the more challenging condition of weak-light heterodyne detection.

Post-processing TTL corrections in post-processing have been demonstrated to reach the LISA's required performance only if the DWS noise floor is lower than $1.5 \text{ nrad}/\sqrt{\text{Hz}}$ (see Figure 3.2) [58]. To the knowledge of the author, such sensitivity - which is also required for the active control - has not been proven yet on ground in LISA-like conditions and in the whole LISA detection band. This gives motivation for the investigations of the thesis.

Imaging Systems Imaging systems (ISs) are optical instruments that can help to mitigate TTL in IFMs [77, 67, 3]. The working principle is shown in Figure 3.1, bottom. By definition, an IS in this context propagates a light ray transiting through the intersection point of its input pupil plane and the optical axis through the intersection of the optical axis and output pupil plane, independently of the light ray's input angle. Since Fermat's principle states that light always takes the shortest path between two points, this implies that all these possible paths have the same length. This principle is illustrated in Figure 3.1. The condition for this solution to be useful is that the beam undergoing tilt must have a well-defined rotation pivot. This is the case in LISA, as

¹Conventionally φ denotes the yaw angle i.e. horizontal rotations and η denotes the pitch angle i.e. vertical rotations of the measurement beam

3.1 TTL Coupling in LISA

- In the inter-satellite interferometer (ISI), the telescope acts as an IS. It images its entrance pupil on the RX-clip on the OB, which becomes the entrance pupil of the ISs of the ISI.
- In the test mass interferometer (TMI) the tilt of the TX beam originates at the surface of the TM, as in Figure 3.1.

Therefore, ISs can be used to image the RX-clip and the TM’s surface onto the QPDs. There is more to this, as actually the ISs in LISA have a three-fold goal [37]:

- Suppress TTL by imaging the point of rotation of the beam into the center of the QPR.
- Compress the beams to adjust their size at the QPR’s active area. Some considerations about this can be found in Appendix E.
- Suppress the diffraction rings caused by beam clipping. The RX beam is clipped both at the telescope and at the RX-clip, causing a concentric diffraction pattern [67]. ISs have the property of imaging their entrance pupil on their exit pupil, suppressing diffraction. This imaging process happens twice along the RX beam path: at the telescope and at the ISs.

In the previous years research has been carried out at Albert Einstein Institute (AEI) showing that IS are an effective technology in suppressing TTL for both the TMI and ISI [72, 16]. Imaging systems with 2 and 4 lenses have been tested. The 4-lens IS’s performance was proven to be less dependent on the beams’ parameters, and hence is the baseline for LISA, which employs 4-lenses refractive folded imaging systems (see Figure 1.5) [12].

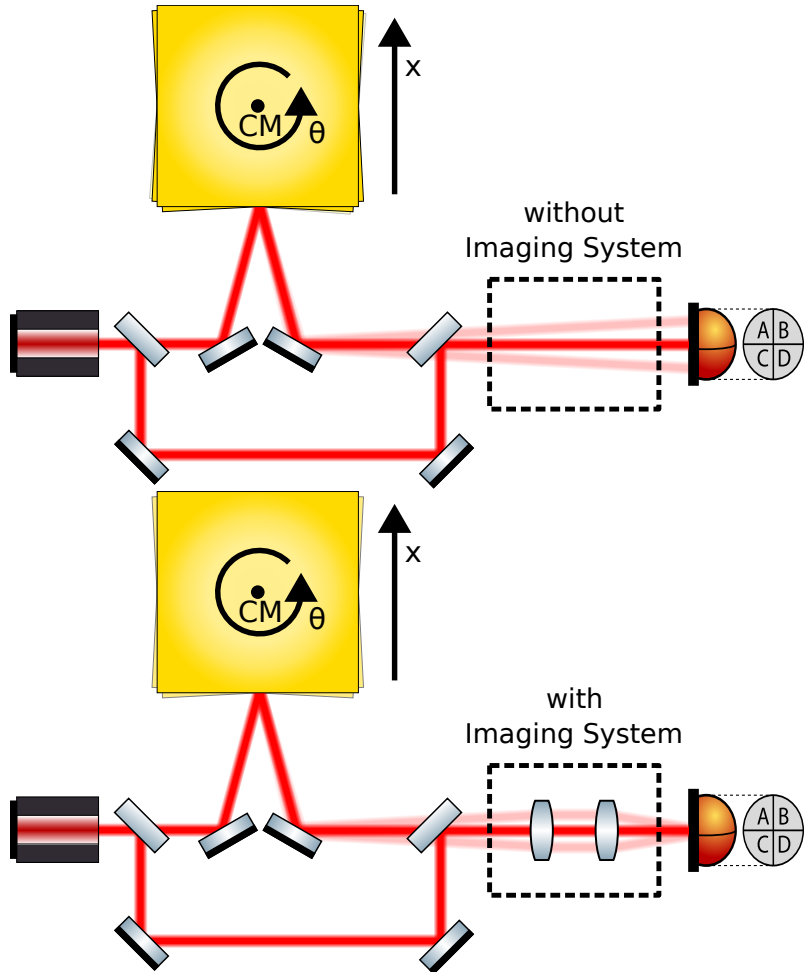


Figure 3.1: Example of an interferometer where the reference beam is reflected on a floating cubic TMs. The longitudinal and angular degrees of freedom of the TM are indicated by the coordinates x and θ . The top IFM features no IS, and in case of TM tilts, the measurement beam is laterally shifted on the QPD. This causes the beam's pathlength to depend not only on x but also on θ due to the lever-arm effect. The bottom IFM features a 2-lens IS, which images the point of rotation of the beam onto the QPD so that beam walk is suppressed. The IS reduces the coupling between the IFM's pathlength difference and θ . Figure inspired by [67].

3.2 The Tilt-to-Length Coupling and Differential Wavefront-Sensing Optical Bench Simulator

The TDOBS experiment was built to investigate interferometric readout noise in a LISA-like environment. Its design procedure and final construction parameters are reported in [15] and the successful results of TTL mitigation by the use of lens ISs in TMI and ISI in case of only vertical beam tilts are published in respectively [72, 16]. During this thesis TDOBS was operated as testbed for some of LISA's key technologies, as testing precision DWS in weak-light conditions and in the presence of tilts, and testing the pre-developments of the LISA PM while using optically generated beat notes as input.

The core of the experiment is a testbed consisting of two baseplates made of ultra-stable Zerodur® glass-ceramic, shown in Figure 3.3 and 3.4. The main baseplate is

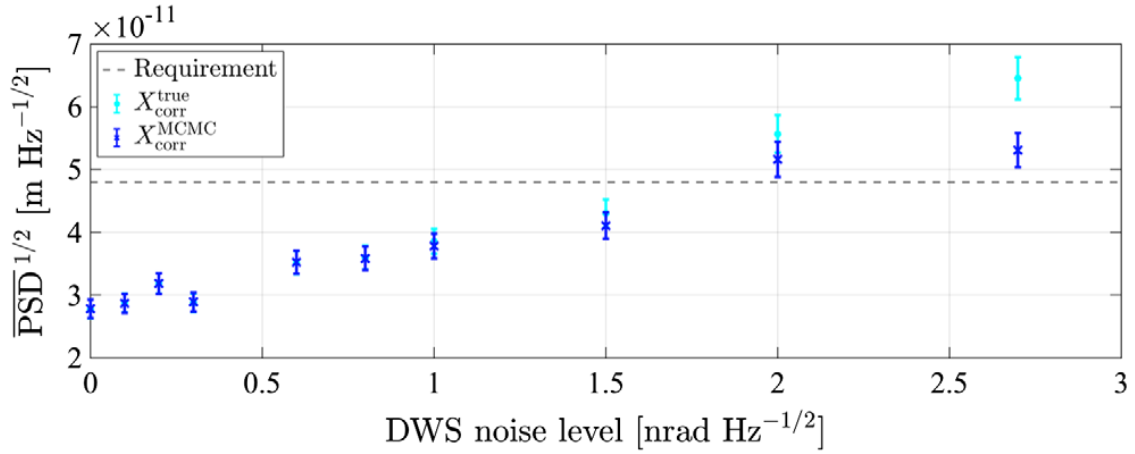


Figure 3.2: PSD of the pathlength noise after post-processing TTL subtraction as a function of the DWS angular noise. The requirement is reached only if the DWS performance is better than $1.5 \text{ nrad}/\sqrt{\text{Hz}}$. Figure from [58].

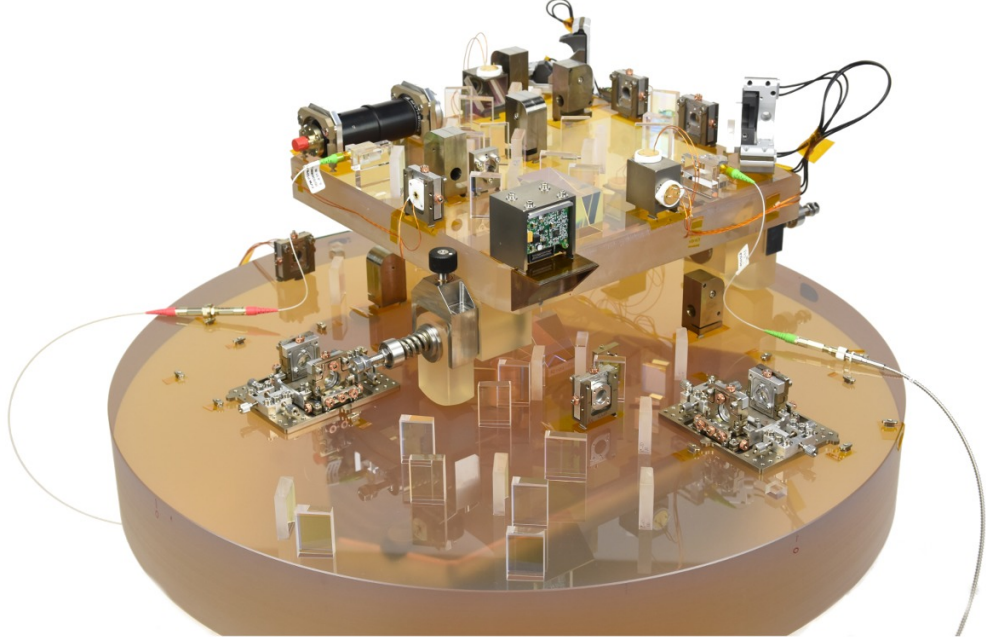


Figure 3.3: Photo of the two baseplates of tilt-to-length coupling and DWS Optical Bench Simulator (TDOBS). The telescope simulator (TS) sits on top of the LISA-Optical Bench (LISA-OB) in its nominal position.

the LISA-OB, which is a simplified version of the OB that is planned for LISA. The second baseplate is the TS, which is an optical ground support equipment (OGSE) used to simulate the beams that the OB receives from the telescope or TM. The testbed is encapsulated in a thermal shield and placed inside a vacuum chamber. All beams used in TDOBS are generated externally from a single laser on a modulation bench (MB) and are fed into the vacuum chamber (VC) and testbed via feed-through optical fibers. Further details on the setup are provided in the remainder of this Section. Figure 3.5 shows a simplified optical layout of the baseplates placed inside the VC and Figure 3.28 shows a simplified optical layout of the whole setup. Table

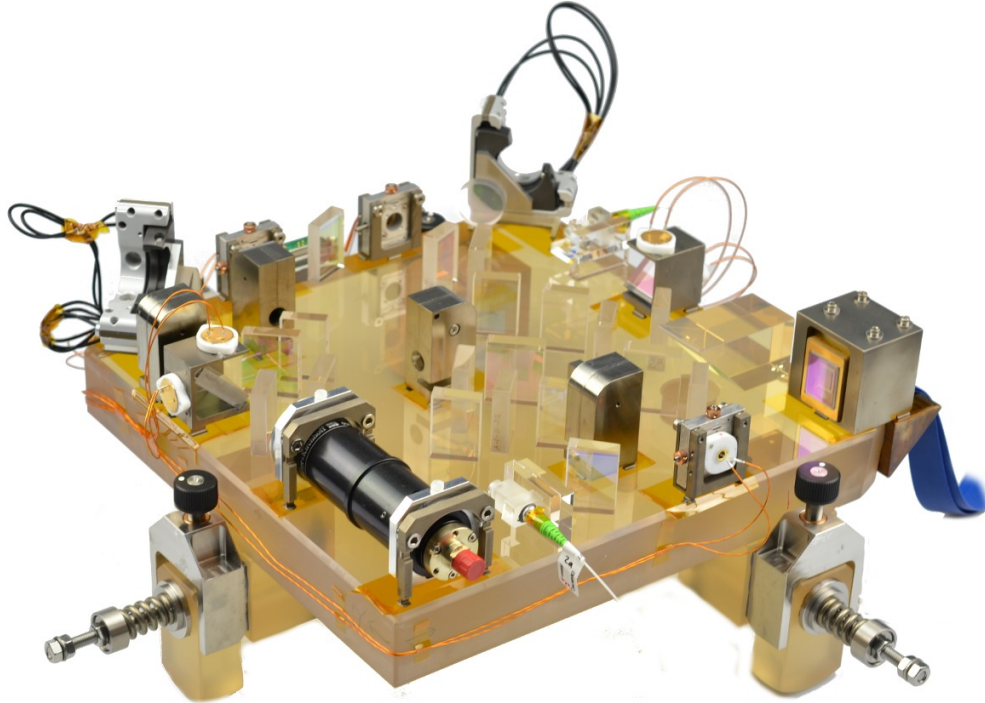


Figure 3.4: Photo of the telescope simulator (TS).

3.1 lists all the used beams, their main features and the color code used to distinguish them through the thesis.

Beam	Injection baseplate	Present in LISA	Fixed/Tilttable	Color
RX	TS	yes	tiltable	green
TX	LISA-OB	yes	fixed	red
LO	TS	no	fixed	blue

Table 3.1: List of the beams and main details used in TDOBS. The indicated beam colors scheme is valid through the whole document.

3.2.1 The LISA-Optical Bench

The LISA-Optical Bench (LISA-OB) consists of a Zerodur® glass-ceramic baseplate of diameter 580 mm, thickness 80 mm and mass 55 kg [15]. The baseplate thickness was chosen to minimize bending, to ensure satisfactory positional stability of all mounted components throughout the build and also measurement accuracy during testing [15]. It simulates the interferometry that happens in one of the IFMs in an OB in a LISA spacecraft while lacking mechanisms such as the PAAM or BAM for simplicity. Mirrors, BS and fiber injector optical sub-assemblies (FIOSs) are hydroxide-catalysis bonded as in LISA and made partially in Glasgow. Other optical components, such as PDs, are glued onto a layer of Kapton tape stuck to the baseplate. This method allows the removal of the glued components should it be required [15].

On the LISA-OB, the TX beam is injected via a FIOS [10]. This is a customized ultra-stable fiber injector attached to the LISA-OB by monolithic joints [10] provid-

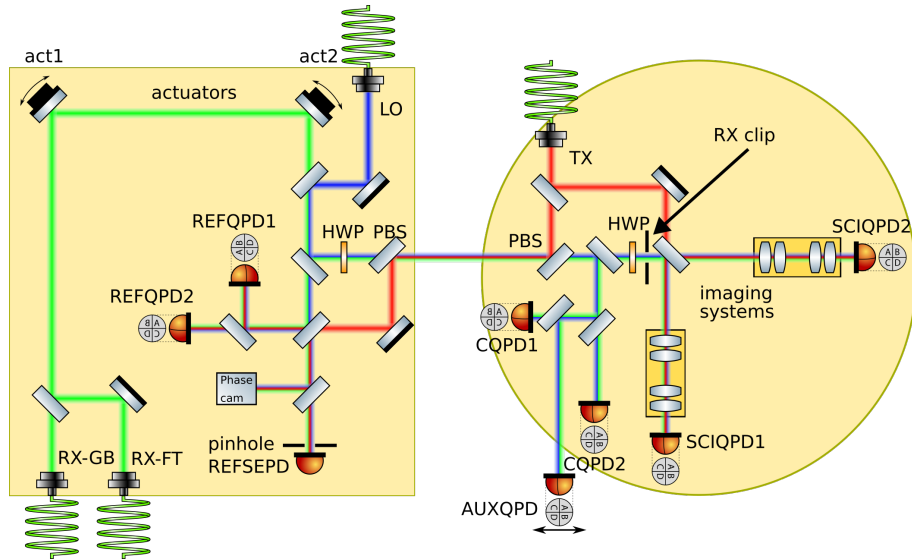


Figure 3.5: Simplified optical layout of TDOBS, with the TS on the left and the LISA-OB on the right.

ing a ~ 2 mm diameter beam². A polarizing beam splitter (PBS) is placed in front of the TX FIOS, cleaning the polarization and setting it to linear vertical. The TX beam simulates the local beam on a spacecraft, and interferes at BS21 with the RX and LO beams, which are injected on the TS and propagated to the LISA-OB via periscope optics. This interference can simulate either the test mass interferometers (TMIs) or the inter-satellite interferometers (ISIs), depending on the used beams. The two output ports of the IFM host two identical 4-lenses imaging systems (see Subsection 3.2.3) and two science QPDs, short SCIQPDs. The LISA-OB also hosts the RX-clip. In TDOBS the RX-clip has a double function. It simulates both the RX-clip on LISA’s OB (see Figure 1.5), i.e. the point in space along the RX’s beam path around which the RX beam is rotated due to the imaging provided by the telescope, and also the point of rotation of the RX beam for the TMI, which is the surface of the TM. In this position, the LISA-OB hosts a magnetic mount which allows the installation of an aperture, such that clipping would take place as in the ISI, while no clipping is required when simulating the TMI.

On the left side of the LISA-OB is a couple of spatially separated QPDs, short calibrated quadrant photodiode pair (CQP), which help to align the beams coming from the telescope simulator (TS) on the LISA-OB [36]. These are large PDs which are suited for DPS measurements. The CQP was fixed and aligned during the baseplate’s manufacture such that any beam from the TS arriving at the center of both QPDs would optimally interfere with the TX beam in both the TS and the LISA-OB.

3.2.2 The Telescope Simulator

The telescope simulator (TS) is a 280 mm \times 280 mm Zerodur® baseplate of thickness 35 mm and mass 7 kg [15]. This sits on top of the LISA-OB as shown in Figure 3.3. It has no rigid connection to the LISA-OB and is free to rotate and translate with respect to it. The layout of the optics on the TS is shown in Figure 3.4. On this

²for further detail on the beam mode see Figure 3.9 and Table 3.1

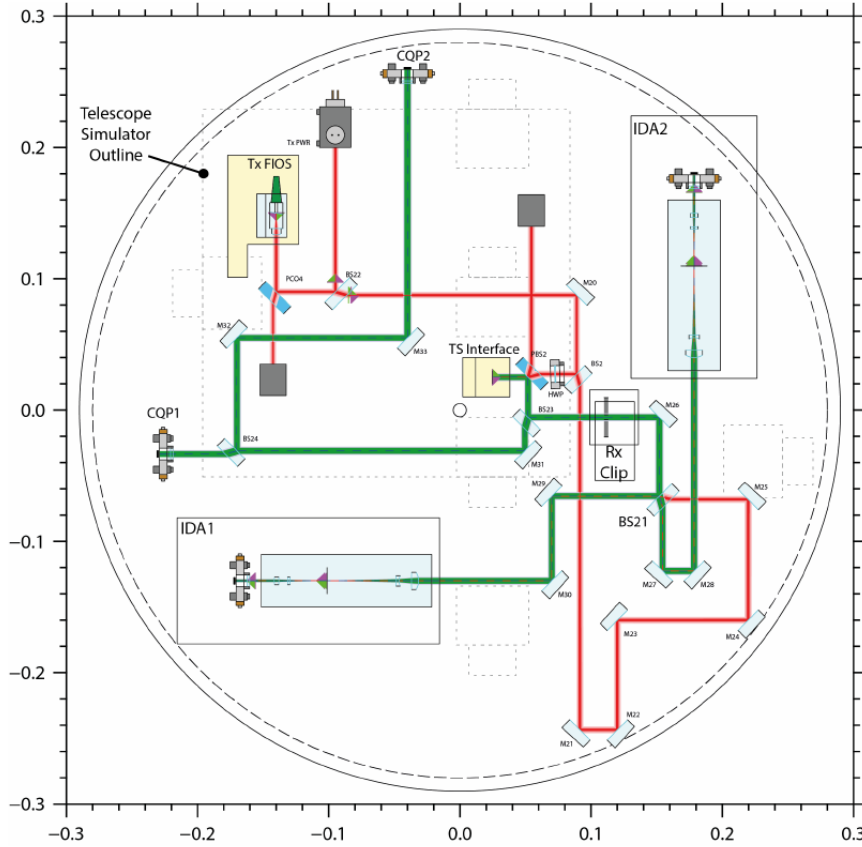


Figure 3.6: Optical layout of the LISA-OB featuring two 4-lenses ISs.

baseplate, the RX and the LO beams are generated. The RX beam simulates the measurement beam, which is either the beam reflected on the TM in the TMI or the received beam from the next spacecraft in the ISI. The LO beam is an auxiliary beam which is not present in LISA, which is used as a phase reference and as an alignment aid. The LO is injected as the TX beam by a FIOS with a polarization cleaning PBS and is a ~ 2 mm diameter Gaussian beam.

The key feature of this baseplate is that it can generate two kinds of RX beams: one is again a FIOS injected, polarization cleaned ~ 2 mm diameter Gaussian beam, named RX-GB; this beam simulates the measurement beam in the TMI. The second is a flat-top beam, called RX-FT beam. This beam simulates the RX beam in LISA, i.e. the measurement beam in the ISI. The RX beam in LISA is a small portion of a Gaussian beam which, after 2.5×10^9 m propagation, has a huge \sim km wavefront. This beam is clipped at the telescope and results in a weak beam with uniform intensity and phase profile. Such a beam is generated in the TS by the Flat-Top beam generator, consisting of a large fiber coupler producing a 9 mm-radius Gaussian beam that is clipped by an apodized aperture [15] (Figure 3.7, bottom left). This is an aperture optimized to generate a beam with a flat profile in both phase and intensity at an optimal working distance of ~ 80 cm. Figure 3.8 shows the intensity profile of the beam at this position. Via BS12 both the RX-GB and the RX-FT are made to propagate along the same axis, and either the RX-GB or the RX-FT beams can be used. Their propagation axis is not exactly the same, but this can be corrected using the actuators (see actuator 1 and actuator 2 in Figure

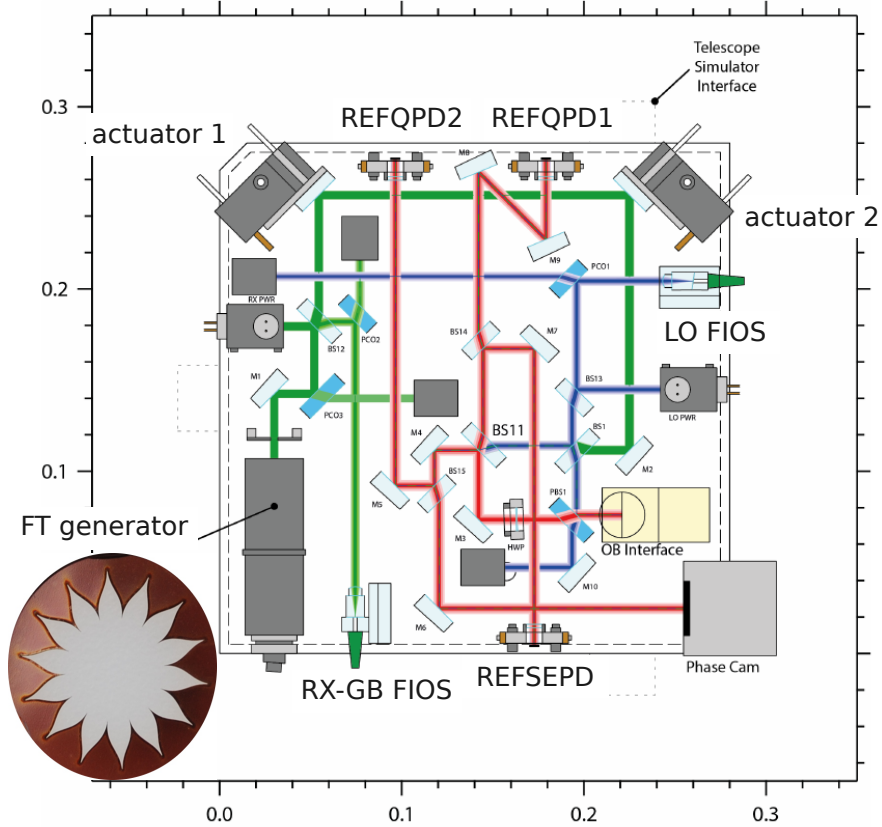


Figure 3.7: Optical layout of the TS. Next to the Flat-Top beam generator is a picture of the apodized aperture placed inside it.

3.7). This operation is quite tedious as the REFQPDs, due to their diameter being much smaller than that of the RX-FT beam, are not sensitive at all to the DPS signal of the RX-FT beam.

The baseplate features a hole through which the periscope optics direct the beams to and from the LISA-OB. The LO and RX beams are propagated to the LISA-OB for the interferometry and the TX beam is propagated from LISA-OB to TS for phase referencing.

Beam	w_0 , radius [mm]	z_0 , waist position [mm]	χ^2/DoF	Prob. worse
RX-GB	0.802 ± 0.007	-635 ± 14	65.98/59	0.248
RX-FT	$\infty \pm -$	$- \pm -$	-/-	-
LO	0.826 ± 0.005	230 ± 17	10.55/53	1
TX	0.788 ± 0.005	100 ± 24	34.06/16	0.005

Table 3.2: Fit parameters from Figure 3.9. The fitting function is $\text{Radius}(z) = w_0 \sqrt{1 + \left(\frac{\lambda(z-z_0)}{\pi w_0^2}\right)^2}$.

To simulate the RX beam tilts the TS, features a pair of mirrors glued on piezo step actuators AG-M100 from AgilisTM. These actuators are capable of performing stable step tilts, with each step being roughly $\sim 5 \mu\text{rad}$.

The RX and LO beams interfere at BS1. A nominal position for the actuators is defined when the RX and LO beams propagate in parallel. The beams leaving BS1

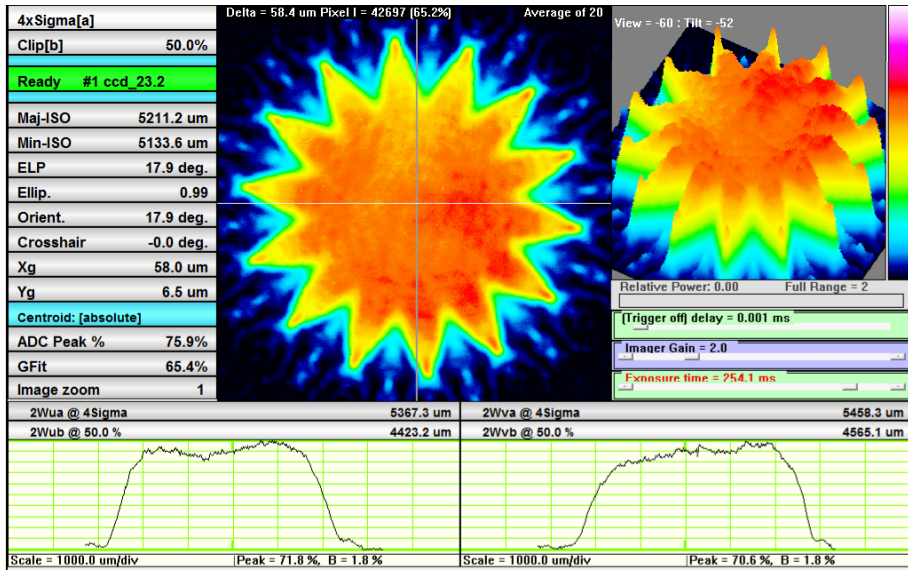


Figure 3.8: Beam profile of the RX-FT beam taken at an 80 cm distance from the FT beam generator. The beam conserves the 'star' shape of the aperture, but one can see that the central intensity profile is approximately flat. On the TS, the RX-clip is placed at 110 cm from the Flat-Top beam generator, so \sim 30 cm further than the nominal position. This is not a problem as the flatness of the RX-FT beam degrades very slowly.

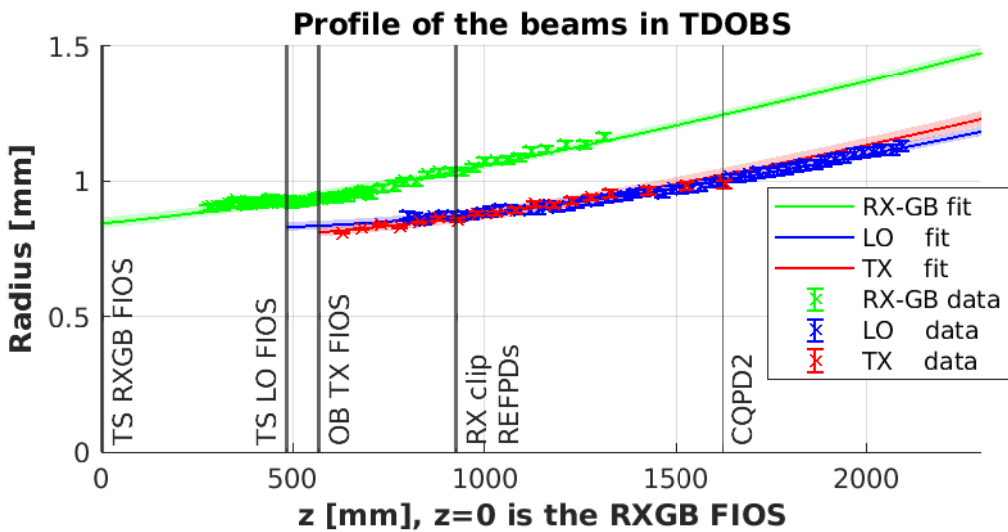


Figure 3.9: Profile of the beams from the two FIOSs on the TS together with the TX beam from the OB. The z -axis is set to be 0 at the RX-GB FIOS, and the beams's propagation axes are referred together at the RX clip. Resulting fit parameters are in Table 3.2. The radius of the RX and LO beams at the RX-clip is respectively 1.038 ± 0.008 mm and 0.874 ± 0.006 mm. The size of the RX beam at the AUXQPD and CQPD2 is 1.19 ± 0.01 mm.

on the left port (see Figure 3.7) stay on the TS, while the beams leaving BS1 from the bottom port are propagated to the LISA-OB via the periscope optics. The TS-bounded port is used to create a copy of the beams entering the LISA-OB, allowing to monitor the beams without having to stop them. This 'copy' is further split at BS11, BS4 and BS15 to create a total of 4 copies. The distance between BS1 and the detectors used for the copies is the same as the geometrical distance between BS1 and the RX-clip, making them *optical* copies of the RX-clip. Monitoring means e.g. to measure DPS and DWS of the RX beam to know its position and angle, or measuring the relative phase between two beams. In the *optical copy* positions several detectors are placed:

- Two of the four copies are occupied by a QPD. These are labelled REFQPD1 and REFQPD2, short REFQPDs. They are positioned such that the LO beam impinges in the center of them, and are used to measure the RX beam's position and angle at the RX-clip using DPS and DWS. In the original version of the TS, the REFQPD2 was a large area SEPD labelled as REF AUX [67, Figure 4.6]. I replaced this in order to have two QPDs placed in optical copies.
- One copy is occupied by a pinhole SEPD. The small size of this PD makes it TTL-insensitive. This SEPD is used as an in-loop detector for two optical pathlength difference (OPD) stabilization loops³.
- One copy is occupied by a phase camera and a trigger-detector for diagnostics, as spatially resolved intensity and phase measurements [67]. This device was not used during this thesis.

An additional large area QPD was developed by me to be gravity-mounted in front of the phase camera. Its goal is to measure the DPS signal of the RX-FT beam in one of the optical copy positions. This QPD has not yet been installed.

The overlap integral of the RX and LO beams was characterized at the REFQPDs by inducing a ~ 10 Hz beat note using the AOMs (see Section 3.3.1 for the beat note generation scheme). This beat note could be tracked with DC electronics while keeping the RX beam in the nominal position. The overlap between RX-GB and LO beams on REFQPD1 and REFQPD2 is $\sqrt{\eta_{\text{het, RX-GB LO}}} \sim 86 \pm 1\%$. This is significantly different from the expected value for an infinite size QPD given by equation (2.24), which predicts a value of 94.5% for the RX-GB & LO beams; this difference is due to the limited size of the REFQPDs. The overlap between RX-FT and LO beams on REFQPD1 and REFQPD2 is $\sqrt{\eta_{\text{het, RX-FT LO}}} \sim 92 \pm 1\%$.

As the TS is free to rotate and translate with respect to the LISA-OB, a reference is needed to define a nominal position. This is given by the CQP and by the LO beam (which is fixed on the TS); the nominal position is when the LO beam is impinging on the center of the CQP.

To achieve $\sim \text{pm}/\sqrt{\text{Hz}}$ stability between TS and LISA-OB, an all Zerodur[®] adjustable mount was designed [67]. This is visible in Figure 3.4. This consists of two pieces of Zerodur[®] - a foot and a mounting block - clamped together by a spring [67]. The clamping force can be increased or decreased by tightening a bolt. When tightened, the clamping force provided by the spring causes enough friction between the two Zerodur[®] blocks to sustain the whole weight of the TS. When the bolt is

³further explained in 3.3.1.

loose, the feet can move relatively to the mounting block, allowing to lift or lower the TS. The length of each mount can be adjusted with such procedure. A micrometer screw placed on the top of each foot helps in the fine-tuning. When the desired position is reached, the bolt has to be tightened and the adjustment screw backed off in order to make the mount a continuous connection of only Zerodur® parts. A total of three mounts is used to hold the TS, and these need to be correctly regulated to center the LO beam on the CQP.

3.2.3 The Imaging Systems

The IS that have been used during the TTL mitigation campaign [72, 16] were removed after testing. They were re-installed by me in front of the SCIQPDs. These image the RX clip onto the center of the SCIQPDs, suppressing the beam walk which occurs while rotating the RX beam. The development details can be found in [73]. A total of four ISs, two featuring two and two featuring four lenses, were built (see Figure 3.10), and we had to the pair to be used. Both ISs have a magnification of ~ 2.5 and very similar ray transfer matrices. The 4-lens IS features a C element very close to zero, outputting a collimated beam. As this one was proven to be better as being more robust against beam parameter variation, this was chosen for installation in TDOBS in front of the SCIQPDs.

$$M_{4L} = \begin{pmatrix} -0.399627 & 0 \\ 8.518 \times 10^{-5} & -2.50233 \end{pmatrix} \quad m_{4L, \text{ th}} = 2.50233 \quad (3.1)$$

$$M_{2L} = \begin{pmatrix} -0.400052 & 0 \\ -0.01346 & -2.50233 \end{pmatrix} \quad m_{2L, \text{ th}} = 2.49967 \quad (3.2)$$

The ISs were aligned by checking that the LO beam impinges in the SCIQPDs in the same position - the center of the QPD - as if the ISs were not present. Following, it was checked that a beam tilt around the RX-clip produces no beam walk. Thanks to the beam compression, the overlap integral of the RX-GB and LO beams at the SCIQPDs is ~ 1 .

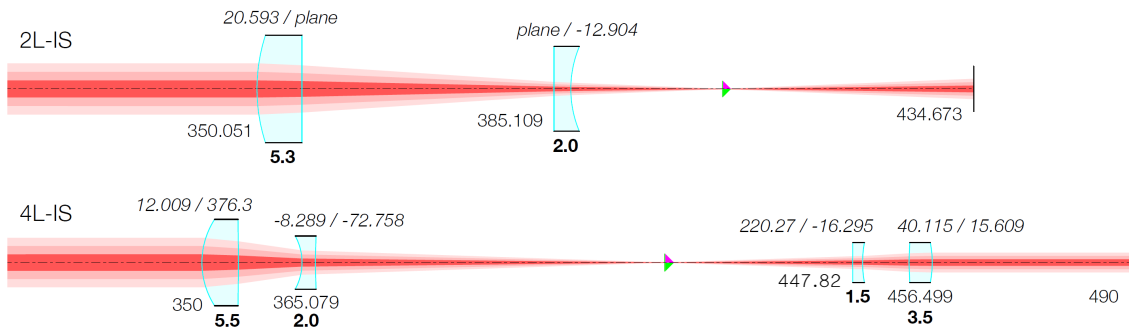


Figure 3.10: Scheme of the 2- and 4-lenses ISs, with positions and RoCs of the lenses in mm. The lenses' positions are measured from the RX-clip, and the final pupil plane represents the QPD's position. The shown beam profile is that of the RX-GB. Figure from [16]; the position value of the third lens in the 4-lens imaging system corrected from a value of 419.745 mm to 447.82 mm.

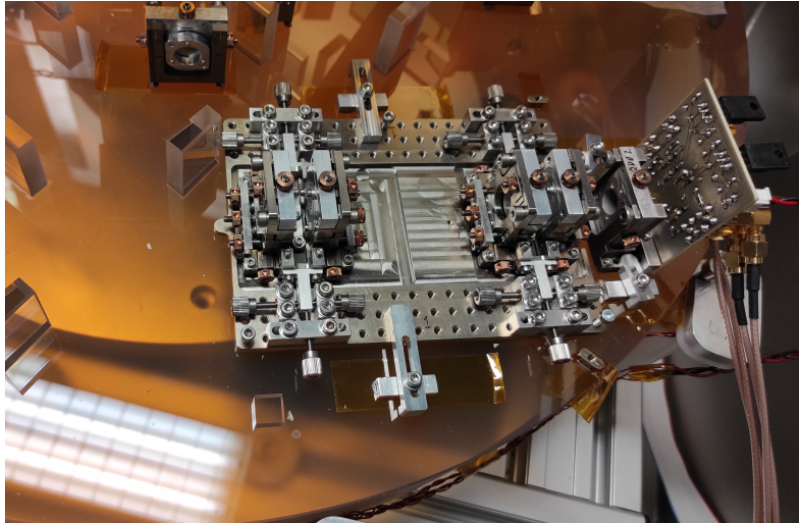


Figure 3.11: Picture of one 4-lense IS positioned in front of SCIQPD2.

3.3 Upgrade of TDOBS

As mentioned in Section 3.2, TDOBS had already been operated to prove the effectiveness of ISs in the reduction of TTL coupling [72, 16] before the start of this work. As the properties of these don't depend on the specific used heterodyne frequency, the experiment was operated with stable heterodyne frequencies of the order of a few kHz. One of the main tasks during the PhD was to upgrade the experiment to the use of MHz heterodyne beat notes, which is closer to LISA. This required redesigning the the MB and upgrading the front-end Electronics (FEE) of the photodiodes (PDs). An additional second-stage amplifier was designed to separate the AC and DC components of the beat notes. A new DPLL-based phasemeter (PM), capable of extracting the phase from MHz beat notes with low noise, was installed in addition to the previously used FFT PM. Further improvements were also made to the vacuum system, and a thermal shield was installed around the TDOBS base-plates.

3.3.1 The Modulation Bench

The modulation bench (MB) is the subsystem which prepares and delivers three beams with a tunable frequency difference lying in the LISA heterodyne band (3-30 MHz).

The used laser source is NPRO-type Nd:YAG laser (laser system 'Prometheus' provided by InnoLight GmbH). The laser beam's frequency can be stabilized by means of an iodine cell to achieve a frequency stability as good as $1000 \text{ Hz}/\sqrt{\text{Hz}}$ at 100 Hz [44]. The laser light is fiber-coupled and injected into the MB.

A simplified version of this setup is shown in Figure 3.28. A scaled version of the MB is shown in Figure E.2. The laser beam is collimated and split into three separate beams (RX, LO, TX). One of the secondary reflections of a BS is detected by a photodiode for input power monitoring. To generate the \sim MHz beat notes the MB uses three AOMs, each in double-pass configuration (see Figure 3.28). This setup allows suppression of the first-order beam's propagation axis dependence on the applied modulation frequency to the AOM f_{AOM} , as the deflection angle of a

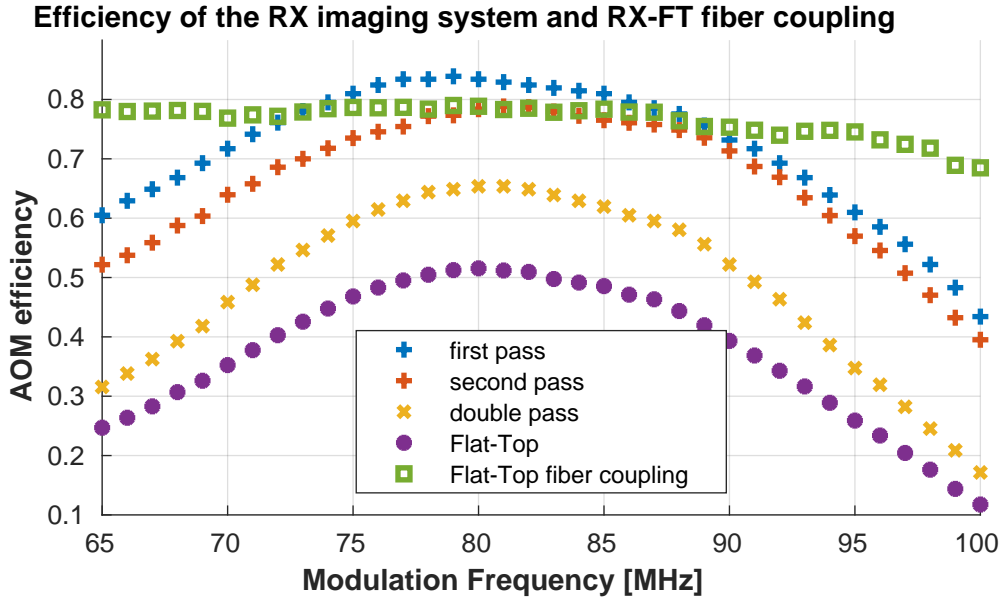


Figure 3.12: Efficiency as a function of the AOM modulation frequency of the RX AOM double-pass system, defined as output power over input power for every stage. Note that the efficiency of the second pass is worse than that of the first pass as the beam does not propagate anymore through the AOM at its waist position. The final fiber coupling efficiency only has a slight dependence on the modulation frequency, and is almost always above $\sim 70\%$.

beam through an AOM due to Bragg's law is

$$\sin(\theta)[f_{\text{AOM}}] = m \frac{\lambda}{c_s} f_{\text{AOM}}, \quad (3.3)$$

where m is the order of the mode, λ is the beam's wavelength, and c_s is the speed of sound in the AOM's crystal. For TDOBS the first-order mode is used, and the AOM's material is PbMoO_4 , which has a $c_s = 3630 \text{ m/s}$. In order to achieve a 20 MHz frequency band as in LISA, the variation of the output angle is $\Delta\theta = 5.9 \mu\text{rad} = 0.34 \text{ deg}$. A beam with such a propagation axis variability cannot be fiber coupled. By applying a second pass through the AOM, the double-passed first-order beam is affected again by the same effect, with reversed angle but additive frequency shift, canceling this dependency out. The double-pass is achieved by using a curved mirror as retro-reflector, reflecting back into the AOM the first-order beam independently of its exit angle. Such system is by definition an imaging system (IS). More details about the realization of this configuration are in Appendix E.2.1. The used nominal frequency is $f_{\text{AOM}} = 80 \text{ MHz}$ for the LO beam, while the RX and TX can be operated at any value within 75-90 MHz without a significant fiber coupling loss; an overall power loss is inevitable since the AOM's efficiency decreases if the modulation frequency departs from the value it is optimized for, which is 80 MHz. A further advantage of the double-pass topology is that the output beam is twice frequency-shifted thus the required bandwidth is halved. This system has proven to be easy to repair even in case of AOM failure, as it has happened twice during the time of this thesis. The performance of this system in terms of output power efficiency is reported in Figure 3.12. All three AOM double-pass systems were found to introduce strong astigmatism to the beams, which had way different vertical (y)

and horizontal (x) modes (see Figure 3.13, above). This caused major loss in the fiber coupling, as fiber couplers are designed for non-astigmatic beams. A solution was found by implementing cylindrical lens telescopes to reduce the mode mismatch between the two axes. The details about this are shown in Figure 3.13.

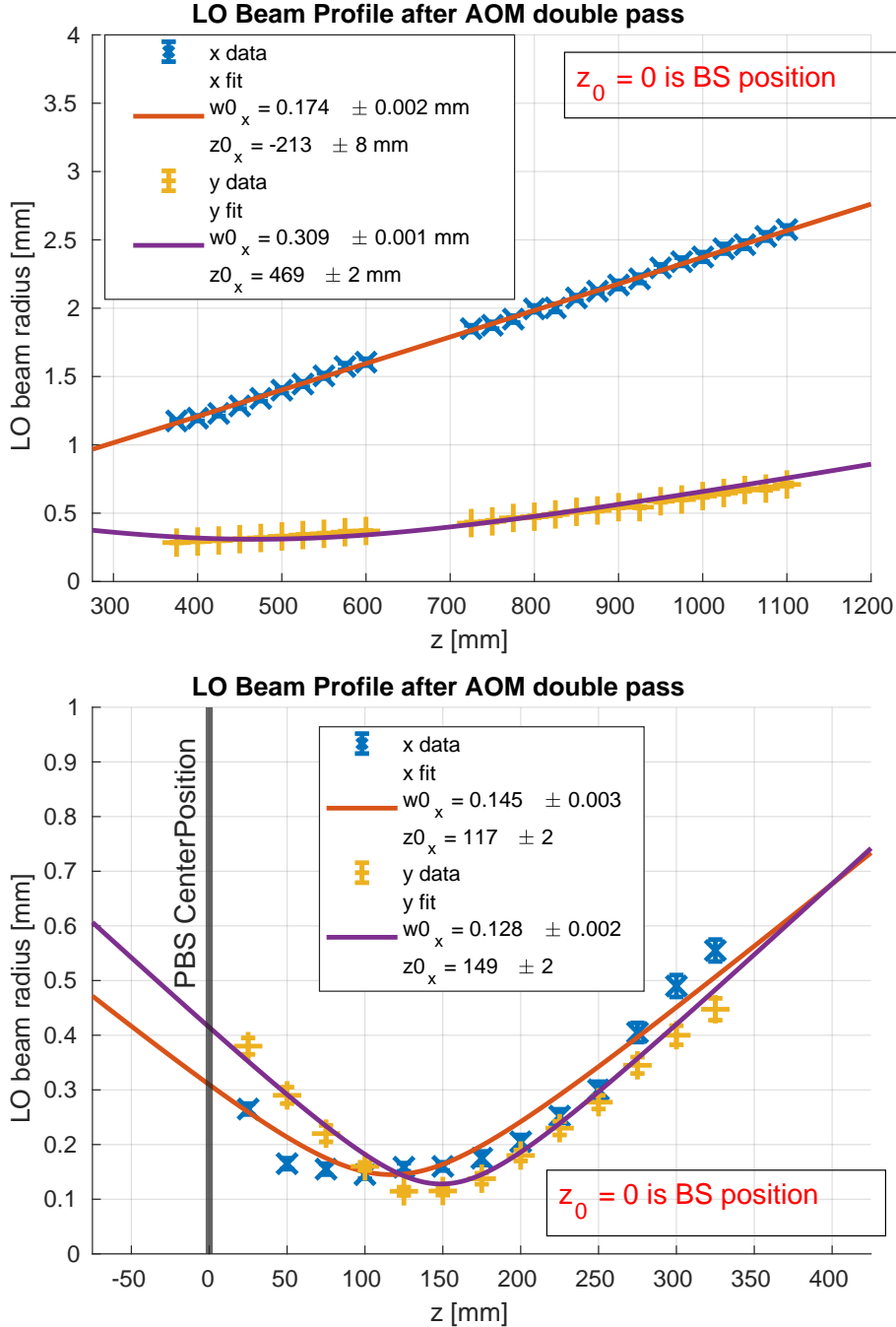


Figure 3.13: Example of the beam astigmatism caused by the AOM double-pass for the LO beam. Above: x and y beam modes measured after the AOM double-pass, showing evidently different modes. Below: x and y beam modes after the cylindrical lens telescope. The initial waist ratio was $w_{0,x}/w_{0,y} = 0.56$ and the average waist position mismatch $\frac{z_{0,x}+z_{0,y}}{\frac{1}{2}(z_{R,x}+z_{R,y})} = -3.67$. After the telescope this was reduced to $w_{0,x}/w_{0,y} = 1.13$ and the average waist position mismatch $\frac{z_{0,x}+z_{0,y}}{\frac{1}{2}(z_{R,x}+z_{R,y})} = -0.58$.

After the AOM double-pass system, the TX and RX beams are phase-locked to the LO beam by piezo actuators in feedback loops. The used sensor for these loops is the reference SEPD (REFSEPD) in the TS. This phase-locking is a historical inheritance from the TTL measurements, when it was used to suppress additional phase contributions prior to the RX-clip. The REFSEPD is a 300 μm diameter SEPD used since the small diameter active area reduces its sensitivity to TTL coupling [67].

The RX beam is further split by means of a half waveplate (HWP) and a PBS, to direct the laser power either to the RX-GB or to the RX-FT beam fiber couplers. All beams are fiber-coupled and propagated to TDOBS via polarization-maintaining optical fibers.

3.3.2 The Photoreceivers

With the term *photoreceiver*, I refer to the ensemble of photodiode (PD) and trans-impedance amplifier (TIA). The characteristics of both PD and TIA are crucial to limiting electronic noise and achieving the phase noise requirement in weak-light conditions, such as in the inter-satellite interferometer (ISI). Based on [32], custom QPRs were developed for TDOBS in order to achieve the cutting-edge performance needed to simulate LISA.

LISA's QPDs

The baseline for LISA's QPRs is to use indium gallium arsenide (InGaAs) for the absorption layer, to have an active area diameter of 1.5mm and 20 μm wide slits [54]. The use of such a large active area is motivated by the beam parameters but has the drawback of causing the QPD to have a large capacitance.

$$C_{\text{PD}} = \frac{\varepsilon A_{\text{PD}}}{d} = \frac{\varepsilon \pi r_{\text{PD}}^2}{d} \quad (3.4)$$

Where A_{PD} is the active area of the PD, r_{PD} is the radius of the PD, ε is the permittivity of the material, and d is the depletion region width of the PD (see Figure 3.14). A high PD capacitance is a problem as this increases the QPR electronic noise at high frequencies. Electronic noise is usually expressed in terms of *equivalent input current noise density* \tilde{i}_{en} in units of $\text{pA}/\sqrt{\text{Hz}}$ [32]. For LISA it is required to be lower than $2 \text{ pA}/\sqrt{\text{Hz}}$ in the LISA heterodyne band [54]. The contributions to \tilde{i}_{en} for a TIA are the Johnson noise of the feedback resistor R_F and the electronic noise of the used active circuit element used to amplify the beat note. Neglecting minor terms, this is

$$\tilde{i}_{\text{en}}(f) \approx \sqrt{\frac{4k_B T}{R_F} + \tilde{i}_{\text{ACE}}^2 + (2\pi f(C_{\text{PD}} + C_{\text{ACE}})\tilde{e}_{\text{ACE}})^2}, \quad (3.5)$$

where k_B is Boltzmann's constant and T is the absolute temperature in Kelvin, usually approximated to 300K for room conditions, C_{ACE} , \tilde{i}_{ACE} and \tilde{e}_{ACE} are, respectively, the capacitance, input current noise and input voltage noise of the used active circuit element, e.g. an operational amplifier (OpAmp) or a transistor. These have typical values of few $\text{pA}/\sqrt{\text{Hz}}$ and $\text{nV}/\sqrt{\text{Hz}}$ [32]. The first term of expression (3.5) would give a value of $1\text{pA}/\sqrt{\text{Hz}}$ for $R_F = 16.6 \text{ k}\Omega$, meaning that a feedback resistance of the order of several $\text{k}\Omega$ is needed. The last term of expression (3.5)

3.3 Upgrade of TDOBS

is frequency dependent and usually dominates for frequencies higher than 20 MHz, and for this reason, QPDs with low capacitance PDs are desired.

As the area is constrained and the permittivity allows little tuning, the only option to lower the capacitance in LISA's photodiodes is to increase the depletion region width by applying a high bias voltage [54]. The PD's capacitance C_{PD} is roughly inversely proportional to the applied bias voltage V_b [54].

$$C_{\text{PD}} = \sqrt{\frac{qN\varepsilon A_{\text{PD}}^2}{2(V_b + V_i)}} + C_0 \quad (3.6)$$

where q is the elementary charge, N is the doping concentration of the diode, V_i is the built-in voltage and C_0 is some additional spurious capacitance. LISA's QPDs are planned to use a 24 V bias voltage. They are currently under development at Nationaal Instituut voor subatomaire fysica (Nikhef)⁴ and Netherlands Institute for Space Research (SRON)⁵.

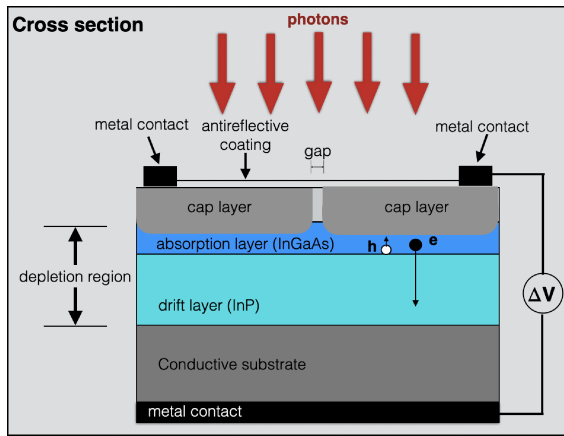


Figure 3.14: Scheme of the cross-section of a LISA QPD. Figure from [54, slide 3].

TDOBS's QPDs

The Photodiodes As of 2025, LISA's QPDs are not available for testing, and other PDs with similar parameters are also not commercially available. Furthermore, at the time of experimental design, a final LISA PRs baseline was not yet ready. With this in mind, we opted to use the QPD model GAP1000Q by [18] as representative of LISA's PDs. This was thought as a tradeoff between area and capacitance, in order to have a large enough active area for high enough DWS gain and a low enough capacitance to not limit the sensitivity at the higher heterodyne frequencies. Note that the needed voltage bias for the GAP1000Q is much lower than 24 V. Hence, we operate it at 5 V bias. A comparison between the parameters of the two PDs and other similar QPD models is shown in Table 3.3:

TDOBS uses a total of four GAP1000Q, two as REFQPDs on the TS and two SCIQPDs. REFQPD2 is also part of the upgrade, as that position was previously occupied by a large silicon SEPD. TDOBS also features some non-LISA-representative PDs, which are not used for DWS. These are:

⁴Dutch institue for subatomic physics, <https://www.nikhef.nl/en/>.

⁵Neatherlands institue for space research, <https://www.sron.nl/>.

3.3 Upgrade of TDOBS

	LISA QPDs	GAP500Q	GAP1000Q	GAP1500Q
Wavelength	1064 nm	1064 nm	1064 nm	1064 nm
Diameter	1.5 mm	0.5 mm	1 mm	1.5 mm
Absorption layer material	InGaAs	InGaAs	InGaAs	InGaAs
Reverse bias voltage	24 V	5 V	5 V	5 V
Responsivity	0.8 A/W	0.6 A/W	0.6 A/W	0.6 A/W
Quantum Efficiency η_{QPD}	0.93	0.70	0.70	0.70
Dark current (@bias)	$\leq 1 \mu\text{A}^*$	0.1 nA	0.6 nA	1 nA
Capacitance (@bias)	$\leq 5 \text{ pF}$	5 pF	9 pF	20 pF

Table 3.3: Comparison table with the parameters of the QPD model planned for LISA (data taken from [54]) and the commercial InGaAs QPD models of various diameters from OEC [18]. Model GAP1000Q (in bold) was chosen for TDOBS. The dark current and capacitance values are per segment. * for the LISA QPD, the 1 μA is a post-irradiation requirement. The value of the LISA QPD is unexpectedly higher, but dark noise is not a limiting noise source. This is discussed in Figure 5.12.

- The calibrated quadrant photodiode pair (CQP), a couple of large silicon QPDs placed on the LISA-OB at different pathlengths along the RX and LO beam paths, which serve as reference for aligning the TS to the LISA-OB. I will refer to these QPDs as CQPD1 and CQPD2.
- The AUXQPD, an additional 8 mm diameter silicon QPD mounted on an external translation stage, which serves as calibration reference for the whole experiment. This QPD size allows us to measure the DPS calibration of the RX-FT beam.
- the REFSEPD, a small area InGaAs SEPD, which acts as an in-loop detector for the optical pathlength difference stabilization loops between the RX & LO and TX & LO beams. This was upgraded from a large silicon photodiode with a small aperture glued in front of it to an OEC GAP300.

Table 3.4 summarizes the main characteristics of the eight PDs used in TDOBS.

Photodiode	Baseplate	Model	Material	Diameter
REFQPD1	TS	OEC GAP1000Q	InGaAs	1mm
REFQPD2	TS	OEC GAP1000Q	InGaAs	1mm
REFSEPD	TS	OEC GQP300	InGaAs	300 μm
SCIQPD1	LISA-OB	OEC GAP1000Q	InGaAs	1mm
SCIQPD2	LISA-OB	OEC GAP1000Q	InGaAs	1mm
CQPD 1	LISA-OB	First Sensor QP22	Silicon	4mm
CQPD 2	LISA-OB	First Sensor QP22	Silicon	4mm
AUXQPD	LISA-OB	Pacific Silicon Sensor PC50-7-TO8	Silicon	8mm

Table 3.4: Table with all used PDs in TDOBS. For a detailed positioning see Figures 3.7 and 3.6.

The Mount All PDs except for the AUXQPD are glued on a PEEK plastic support, which is itself screwed on aluminum flexure mounts. This is adjustable in 2

3.3 Upgrade of TDOBS

degrees of freedom for vertical and horizontal alignment within a ~ 0.15 mm displacement range and < 3 μm precision and is designed to minimize the coupling of temperature variations and minimize thermally induced stress transferred to the baseplate [61, 15, 64]. The mount is shown in Figure 3.15.

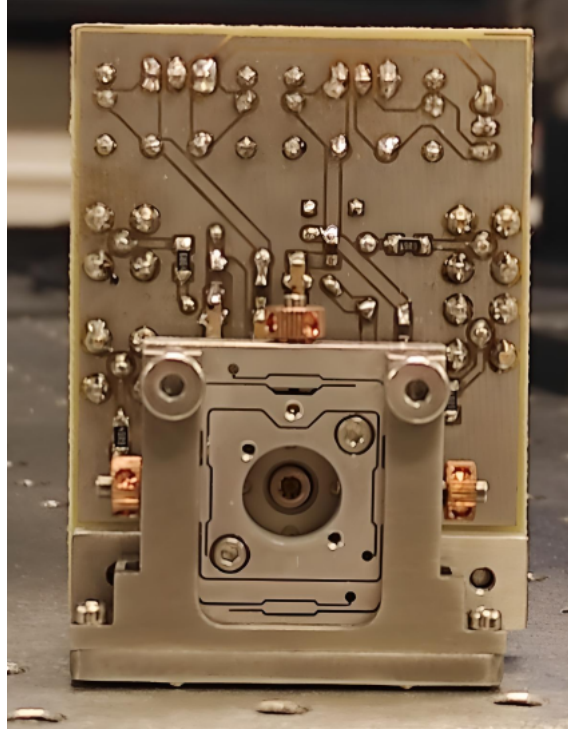


Figure 3.15: Photo of a SCIQPD on the flexure mount with the TIA printed circuit board (PCB) behind it.

The Trans-Impedance Amplifiers Custom TIAs were developed for each QPD, with more than one iteration for the LISA-representative QPDs (REFQPDs and SCIQPDs). As TDOBS was initially built to operate with kHz beat notes, the TIAs of all PD were placed in a single PCB several meters away from the PDs. For the required MHz-beat notes upgrades, the TIA has to be placed very close to the PD (~ 5 mm) to avoid electromagnetic pickup⁶ and to minimize parasitic capacitance. Non-LISA-representative PDs were also upgraded, as it is convenient to completely replace the previous TIA circuit. Dedicated TIA models were manufactured during for each PD, featuring electronical and mechanical adaptations to obtain the needed TF, noise performance and fit the stringent spatial constraints. The PCB's size was critical for the stringent spatial constraints of the TS and LISA-OB.

For the non-LISA-representative QPDs, we designed an OpAmp-based TIA using the AD8038, reported in Table 3.5. For the LISA-representative QPDs, two different TIAs were developed. The first (#1) is a simple OpAmp-based TIA, which was optimized until converging to a configuration based on the LMH6624 OpAmp, $R_F = 40$ $\text{k}\Omega$ and $C_F = 0$ pF. This TIA model was used for the REFQPDs and is currently used for the SCIQPDs. A second lower noise TIA was designed following the current baseline for the LISA TIA (described in [32]) by using commercial counterparts of the

⁶Electromagnetic pickups are especially critical because of the high power MHz signals driving the AOMs.

3.3 Upgrade of TDOBS

flight components. This model is based on the BFP740 transistor and the AD8038 OpAmp and uses a feedback resistance of $R_F = 30.1 \text{ k}\Omega$ (#2). The schematics of the LISA-representative QPDs are reported in Appendix B, and the main features are summarized in Table 3.6. All TIAs are designed to have cutoff frequencies a little higher than 25MHz. The obtained TF for REFQPD2 and CQPD1 is shown in Figure 3.17. The TFs of equivalent QPRs are similar.

Photodiode	OpAmp	R_F [k Ω]	C_F [pF]
CQPD1	AD8038	2	1.5
CQPD2	AD8038	2	1.5
AUXQPD	AD8038	12	1.0
REFSEPD	AD8038	1	3.3

Table 3.5: TIA parameters of the non-LISA-representative PRs.

Photodiode	Transistor	OpAmp	R_F [k Ω]	C_F [pF]
SCIQPDs	-	LMH6624	40	0
REFQPDs #1	-	LMH6624	40	0
REFQPDs #2	BFP740	AD8038	30.1	0

Table 3.6: TIA parameters of the LISA-representative PRs.



Figure 3.16: Photo of the REFQPD1 and REFQPD2 PDs featuring TIA #2, mounted on the flexure mounts and with the TIA PCBs attached right on the back.

The diameter of the used PD is smaller than or comparable to that of the beam impinging on it. The estimated fraction of beam power impinging on each PD's active area is reported in Table 3.7.

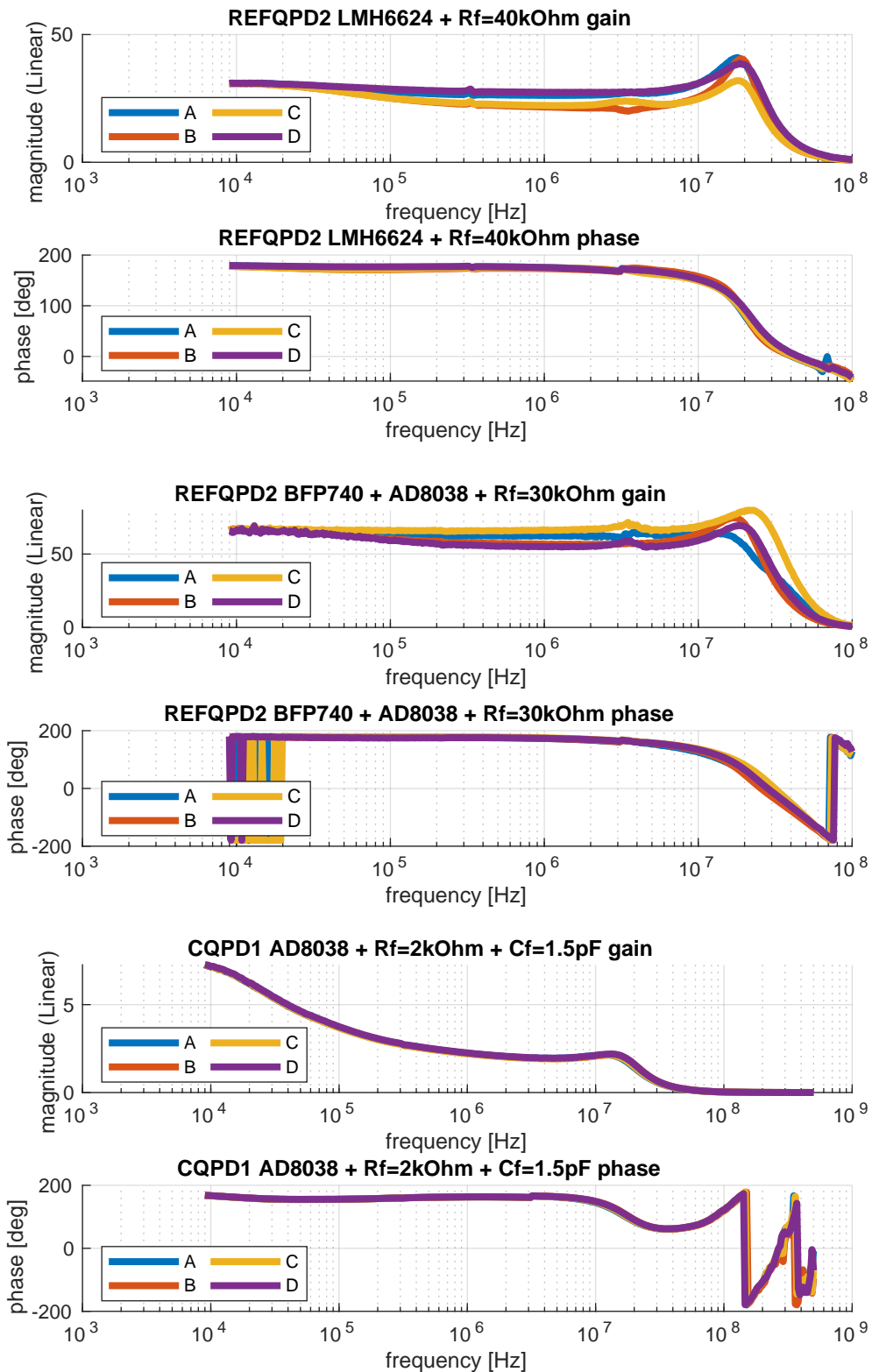


Figure 3.17: From top to bottom: TF of the TIA of REFQPD2 in configuration #1 and #2 and CQPD1. REFQPD2 #1 is representative of the current SCIQPDs' TF. In all plots the B, C, D magnitude is normalized to that of A in the lowest frequency bin.

3.3 Upgrade of TDOBS

Photodiode	RX-GB	RX-FT	LO
REFQPDs	$\sigma_{\text{RX-GB, REF}}=0.371$	$\sigma_{\text{RX-FT, REF}}=0.015$	$\sigma_{\text{LO, REF}}=0.488$
SCIQPDs	$\sigma_{\text{RX-GB, SCI}}=0.980$	-	$\sigma_{\text{LO, SCI}}=0.987$
REFSEPD	$\sigma_{\text{RX-GB, SEP}}=0.041$	-	$\sigma_{\text{LO, SEP}}=0.057$

Table 3.7: Fraction of incident beam power detected by each PD in TDOBS. This amount is estimated using equation (2.17), assuming a centered beam and neglecting slits. For the QPDs, this fraction has to be divided by 4 to obtain the optical power per segment.

3.3 Upgrade of TDOBS

The phase TFs of the four segments of a QPD $\varphi_{\text{TF}, i}$ with $i \in (A, B, C, D)$ cause a *phase bias* on all phase related measurements, as the optical phase is shifted by the electronics. The propagation of such bias to LPS and DWS can be calculated from the measured TFs of each QPD segment by applying the same equations (2.103) and (2.106). The bias for the LISA pathfinder longitudinal signal is excluded from this example.

$$\varphi_{\text{LPS AP, bias}} = \frac{1}{4}(\varphi_{\text{TF}, A} + \varphi_{\text{TF}, B} + \varphi_{\text{TF}, C} + \varphi_{\text{TF}, D}) \quad (3.7)$$

$$\varphi_{\text{DWSv, bias}} = \frac{1}{2}(\varphi_{\text{TF}, A} + \varphi_{\text{TF}, B} - \varphi_{\text{TF}, C} - \varphi_{\text{TF}, D}) \quad (3.8)$$

$$\varphi_{\text{DWSH, bias}} = \frac{1}{2}(\varphi_{\text{TF}, A} - \varphi_{\text{TF}, B} + \varphi_{\text{TF}, C} - \varphi_{\text{TF}, D}). \quad (3.9)$$

This effect has been characterized, as an example, using the data for REFQPD2 in Figure 3.17, obtaining Figure 3.18. Such offset in the case of the LPS signal and of a static beat note frequency is no harm, as only the optical phase variations have a physical meaning. If the beat note frequency is varied, as it happens in LISA due to the Doppler shift, an extra phase contribution appears. Such effect is much more relevant in the case of the DWS signals, as the DWS signals are supposed to be zero if the angle between the beams is zero. Thus this effect must be characterized, as not characterizing the DWS bias as a function of the heterodyne frequency introduces a heterodyne-frequency-dependent offset in the estimation of the angles between the beams.

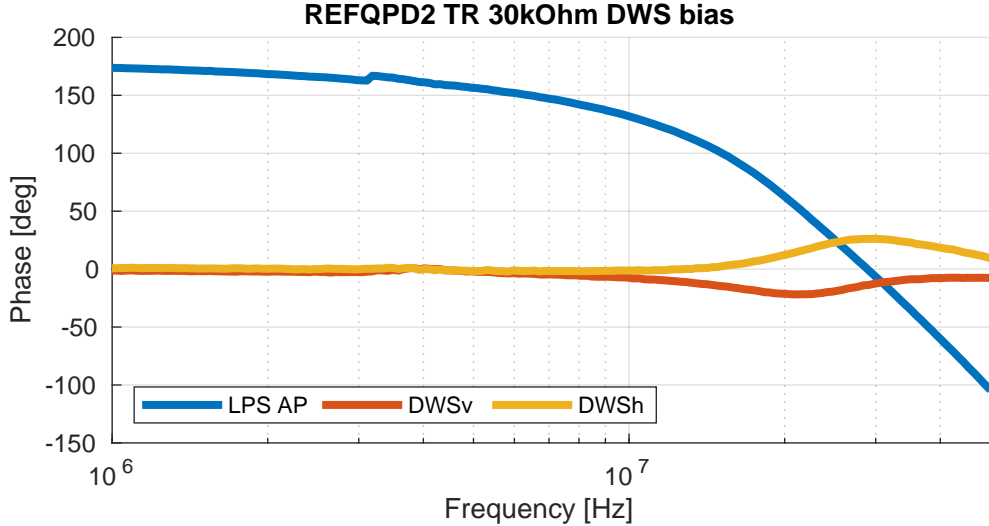


Figure 3.18: LPS and DWS bias calculated measured on REFQPD2.

The electronic noise from the two TIA models was characterized using the white light method [32, Section 3.3], which consists of measuring the output noise of the TIA first without shining any light on the QPD and then by shining a shot noise limited light source, e.g. an incandescence lamp. The output of the first measurement, in equation (3.10), gives the electronic noise of the TIA \tilde{i}_{en} times the TIA's gain G_{TIA} (3.10). The second measurement, in equation (3.11), measures the

3.3 Upgrade of TDOBS

voltage noise in the presence of additional shot noise \tilde{v}_n .

$$\tilde{v}_{\text{en}} = G_{\text{TIA}} \tilde{i}_{\text{en}} \quad (3.10)$$

$$\tilde{v}_n = G_{\text{TIA}} \sqrt{\tilde{i}_{\text{en}}^2 + \tilde{i}_{\text{shot}}^2} \quad (3.11)$$

The amount of shot noise can be estimated from the generated DC photocurrent as $\tilde{i}_{\text{shot}}(2qI_{\text{DC}})^{\frac{1}{2}}$, with $I_{\text{DC}} = V_{\text{DC}}R_{\text{F}}^{-1}$ and R_{F} is the feedback resistor of the TIA. The combination of the two measurements leads to isolating the TIA electronic noise contribution and the gain of the TIA.

$$\tilde{i}_{\text{en}} = \frac{(2qI_{\text{DC}})^{\frac{1}{2}}}{\left(\left(\frac{\tilde{v}_n}{\tilde{v}_{\text{en}}}\right) - 1\right)^{\frac{1}{2}}} \quad G_{\text{TIA}} = \frac{\tilde{v}_{\text{en}}}{\tilde{i}_{\text{en}}} \quad (3.12)$$

Note that this method does not require the *a priori* knowledge the TIA's gain, which is an output of this measurement method. Beyond that, the gain of any second-stage amplifier is factored out in equation (3.12).

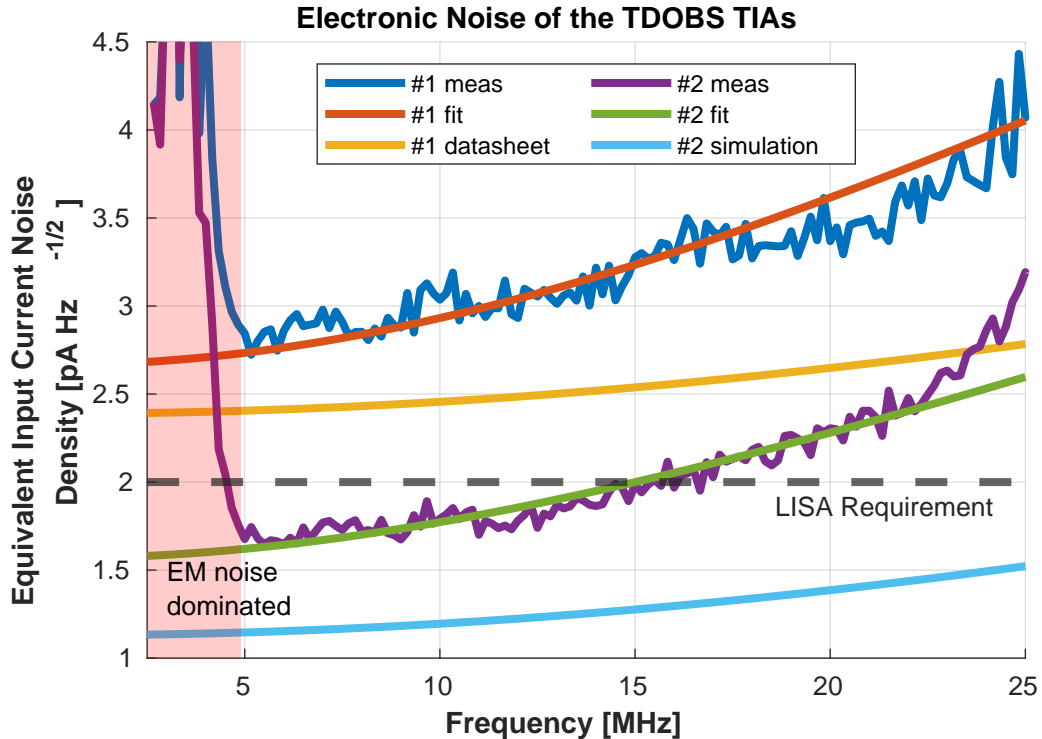


Figure 3.19: Measurements, model and SPICE simulation of the equivalent input current noise density of the two used TIA models. The measurements are carried out using the white-light method [32, Section 3.3]. The fitted noise model relies on equation (3.5). The fitted model values for TIA #1 and #2 are respectively in Tables 3.8 and 3.9. For TIA #1 the measured equivalent input current noise density at 5 MHz is $\tilde{i}_{\text{en}, \#1, 5 \text{ MHz}} = 2.73 \pm 0.04 \text{ pA}/\sqrt{\text{Hz}}$, which is 14% higher than the modeled value of $2.4 \text{ pA}/\sqrt{\text{Hz}}$. For TIA #2 the measured equivalent input current noise density at 5 MHz is $\tilde{i}_{\text{en}, \#2, 5 \text{ MHz}} = 1.6208 \pm 0.0015 \text{ pA}/\sqrt{\text{Hz}}$, which is 41% higher than the modeled value of $1.15 \text{ pA}/\sqrt{\text{Hz}}$. The EM noise peak observed in the white-light measurement disappears if the FFT PM is switched off. Only TIA #2 is able to satisfy the requirement, but just below $\sim 15 \text{ MHz}$.

3.3 Upgrade of TDOBS

Parameter	Expression	Unit	Expected value	Measured value
a	$\sqrt{\frac{4k_B T}{R_F} + \tilde{i}_n^2}$	pA/ $\sqrt{\text{Hz}}$	2.388	2.66 ± 0.04
b	$2\pi(C_{\text{PD}} + C_{\text{OpAmp}})\tilde{e}_n$	$\frac{\text{pA}}{\text{MHz}}/\sqrt{\text{Hz}}$	0.057	0.122 ± 0.002

Table 3.8: Table with the expected values and resulting fit parameters for the equivalent input current noise density of TIA #1 in Figure 3.19. The used feedback resistor has a value of $R_F = 40 \text{ k}\Omega$. The values of i_n , e_n and C_{OpAmp} of the LMH6624 OpAmp can be found in [47]. The fit function is $f(x) = \sqrt{a^2 + b^2 x^2}$.

Parameter	Expression	Unit	Expected value	Measured value
a	$\sqrt{\frac{4k_B T}{R_F} + \tilde{i}_n^2}$	pA/ $\sqrt{\text{Hz}}$	1.064	1.567 ± 0.013
b	$2\pi(C_{\text{PD}} + C_{\text{Tr, EB}})\tilde{e}_n$	$\frac{\text{pA}}{\text{MHz}}/\sqrt{\text{Hz}}$	0.0423	0.0828 ± 0.0011

Table 3.9: Table with the expected values and resulting fit parameters for the equivalent input current noise density of TIA #2 in Figure 3.19. The used feedback resistor has a value of $R_F = 30.1 \text{ k}\Omega$. The values of $C_{\text{Tr, EB}}$ of the BFP740 Transistor OpAmp can be found in [45]. The values of i_n , e_n of the BFP740 can theoretically be calculated using equations (2.17, 2.18) in [32, Page 63]; as [45] does not provide all the required parameters, a SPICE simulation was used. The fit function is $f(x) = \sqrt{a^2 + b^2 x^2}$. The measured value of b is twice that expected, likely due to parasitic capacitance of the PCB.

3.3.3 AC-DC Splitter

The device described here can be considered a custom realized replacement of the variable gain controller in the back-end electronics (BEE) of the LISA PM. The output signals from the QPR in LISA have a nominal amplitude of 1.4 mV in the ISI, 50 mV in the TMI and 87 mV in the RFI [30]. This is the signal is delivered to the phase measurement sub-system (PMS). In order to better exploit the range of the ADC (2 V_{pp}), in LISA the BEE of the PM performs AC and DC signal preconditioning. This step makes use of a variable gain as the beat note changes amplitude during the mission.

The voltage values of the beat notes from the TIAs in TDOBS are similar, depending on the specific used beam powers. As the PM used in TDOBS features no variable gain amplifier, the AC-DC splitters were realized to perform the signal pre-conditioning, with the difference of using a limited comb of set gains. These separate the TIA's output into a DC and AC component. The AC component (the beat note) can optionally be further amplified by extra amplification stages in order to best match the FPGA mezzanine card (FMC) PM's input range of 0.5 V_{pp}. This circuit consists of a PCB with four channels and is able to process the four outputs of one QPR. The AC output features an additional second-stage amplification. The possible gain values are 2.86 V/V, 28.6 V/V and 56.7 V/V.

A total of nine copies of this circuit were realized. The TF of the AC-DC splitters were characterized and are shown in Figure 3.20. Due to space constraints, the AC-DC splitters are placed outside the vacuum chamber (VC). The schematic of one channel of an AC-DC splitter is shown in Figure B.3.

A similar characterization regarding the phase bias of the AC-DC splitters is could, in principle, be done as for the QPRs in Figure 3.18. Practically, these biases are characterized all together by the DWS calibration in Chapter 4.

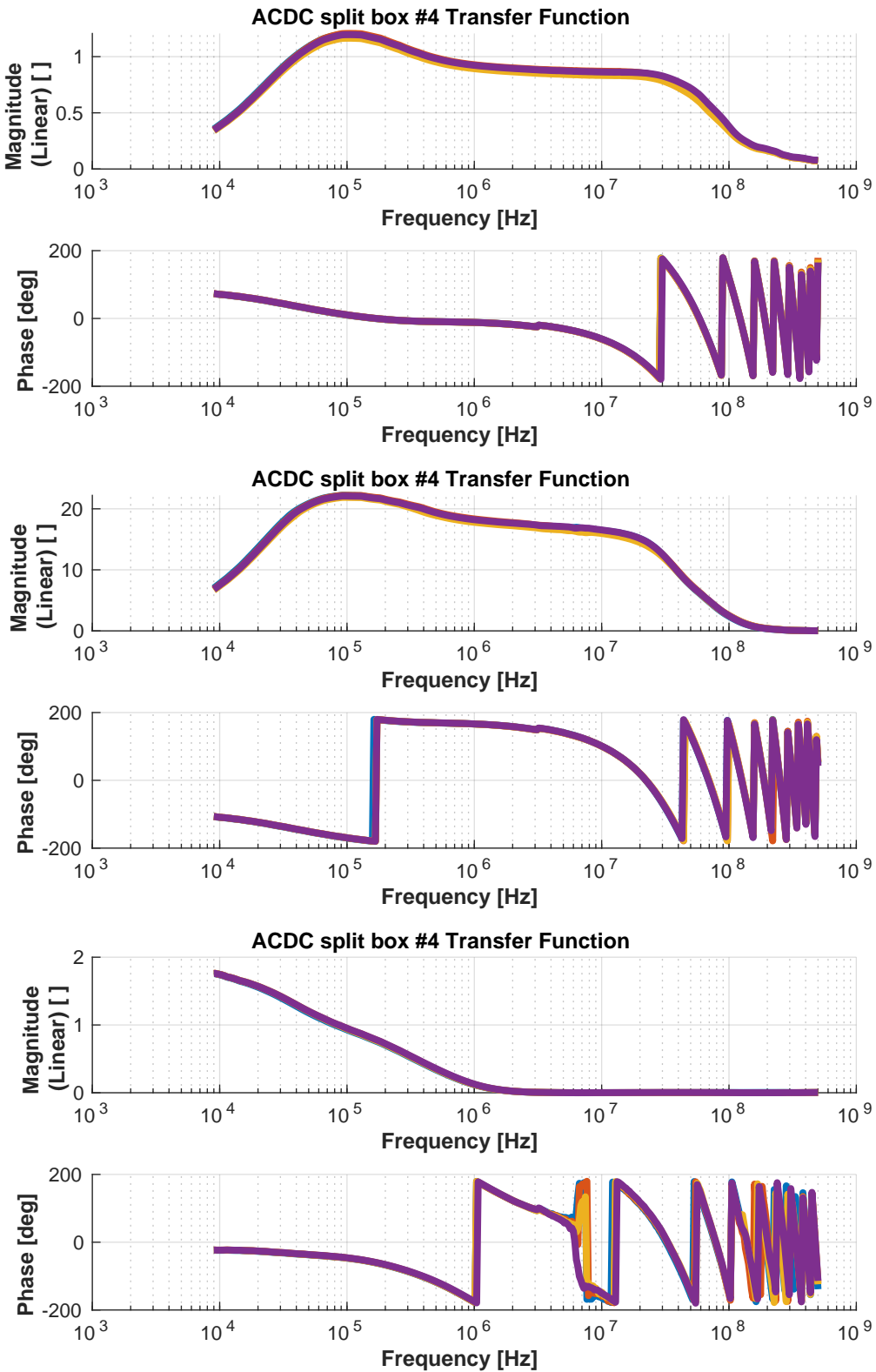


Figure 3.20: TF of the AC-DC Splitter circuits. Above, left: AC output with no further amplification. Above, right: AC output with second-stage amplification, below: DC output.

3.3.4 The Phasemeters

TDOBS uses two different PMs (see Figure 3.21). The master PM is a single bin FFT PM. This is the same PM used for the TTL mitigation measurements in [72, 16]; its control software also controls the actuators and handles the OPDs. A second slave PM featuring the LISA-like DPLL architecture is used for the precision phase measurements, this PM is named FMC PM.

The FFT phasemeter

This PM implements the demodulation scheme explained in Appendix 2.1.3. It can handle up to three beat notes, which must have a fixed and known frequency. It features 16 input channels, for which the PM returns the DC value, the amplitude and phase of the three beat notes and a demodulated signal at $f_{AM} \sim 267$ Hz. This channel is used to measure the DPS⁷ signal of the RX beam only on the QPDs. This PM also generates a $f_{AM} \sim 267$ Hz signal, which is used as a modulation source in the signal generators (SGs) to modulate the power of the RX beam. Last, the FFT also provides an error signal for the two OPDs (see Figure 3.28). The clock output of the master PM is used to time the 3 SGs used to generate the modulation signals for the AOMs, and the clock signal and PT signal for the slave PM.

The sampling frequency is $f_s = 80$ MHz as in LISA. The data output rate is $f_{fund} = 80$ MHz/2²² = 19.0734863281 Hz. This precise value is important, because due to the design of the filters in this PM, the input beat note frequencies must be a multiple of this fundamental frequency; the amplitude modulation frequency is itself $f_{AM} = 14 f_{fund}$. This limits the usable heterodyne frequencies in the experiment to a comb of multiples of f_{fund} , even if the precision phase measurements are conducted with the FMC PM. This is due to the OPD loops, for which the use of a different frequency would cause in the FFT PM's measurement an accumulating 'apparent' phase lag which is compensated by an increasing 'real' phase lag by the actuation on the piezo. This phenomenon keeps increasing the DC component of the error signal until it saturates, and the OPD loop resets. Consequently, a phase jump takes place as the piezo is brought back to its initial setpoint, and this feature is undesired during the measurement. Therefore, the allowed heterodyne frequencies must be $f_{het} = n \cdot f_{fund}$ with $n \in \mathbb{N}$. Due to the limited input digits of the SGs, the simplest solution is to use heterodyne frequencies of the form $f_{het} = f_s 2^{-n}$ with $n \in N$, hence 20 MHz, 10 MHz, 5 MHz or any sum of these.

The performance of this PM model reaches the LISA picometer requirement only for heterodyne frequencies up to a few MHz, and is therefore not compatible with reaching this requirement at 25 MHz. Its performance is still good enough to run the OPD stabilization loop as the reached phase stabilization, due to actuation limitations, is three orders of magnitude worse than the LISA requirement. As no other PM has been programmed to output an error signal for an OPD loop, this task must be performed via the FFT PM.

The FMC PM

This PM is an instrument pre-development toward the final LISA PM. It is structured as one module of the engineering model of the LISA-PM, featuring eight input

⁷see 2.3.1

3.3 Upgrade of TDOBS

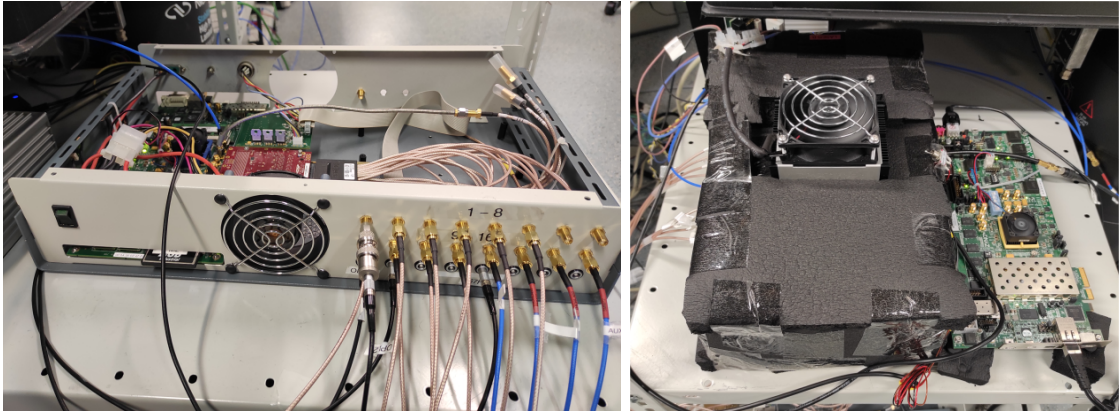


Figure 3.21: PMs of TDOBS. Left: the single bin FFT PM. Right: the FMC PM: on the left is the aluminum enclosure surrounded by the nitrile rubber casing, where the signal pre-conditioning electronics and the ADC are situated. On the right is the FPGA where the PM is implemented. The temperature inside the enclosure needs a stability of at least $10^{-2} \text{ K}/\sqrt{\text{Hz}}$ in the LISA measurement band to achieve the required phase performance.

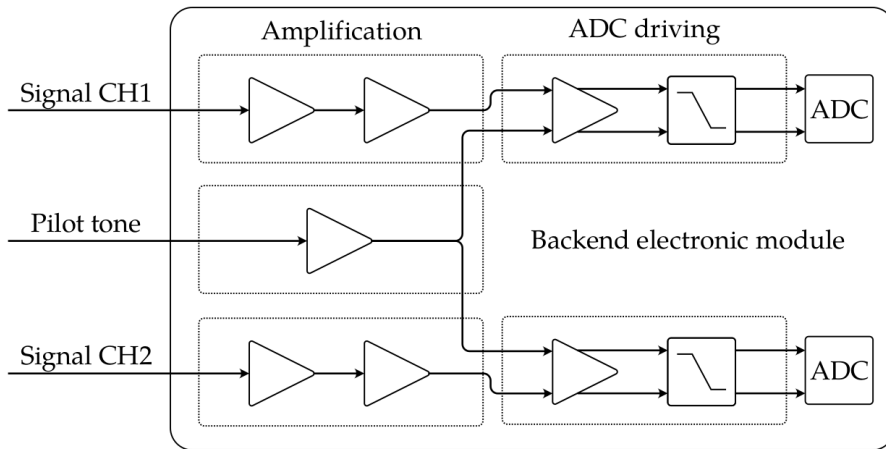


Figure 3.22: Simplified schematic of a BEE module. Figure from [9, page 56]. The module hosts an amplification stage to match the input signals to the ADC's range and the ADCs. The insertion of the PT into each channel is also shown. The real module features instead four input channels per ADC.

channels, but is only AC-coupled. A simplified schematic of the module is shown in Figure 3.22. The used ADC is the ADS6445-EP from Texas Instruments [46]. The working principle is the DPLL explained in Subsection 1.3.2. The sampling frequency is 80 MHz, and the output sampling rate is $80 \text{ MHz}/2^{19}3^25 \sim 3.39 \text{ Hz}$. To operate, the DPLL architecture needs an initial guess of the beat note's frequency, which, in comparison to the FFT PM, does not need to be exact but rather within a $\sim 10 \text{ kHz}$ difference. The signal's frequency can vary during the measurement. The proportional and integral gains of the DPLL have to be set by the user and are crucial for the stability of the DPLL [9]. As a rule of thumb, the proportional gain g_P has to be much larger than the integral gain g_I ; in [9] it was found that a factor of 2^{10} should be kept between proportional and integral gain. The gain values have to be specified in the configuration file of the FMC PM prior to running, as $P = \log_2(g_P)$ and $I = \log_2(g_I)$. A PT is introduced to measure and remove ADC timing jitter in

3.3 Upgrade of TDOBS

post-processing. For all the optical measurements, the used PT frequency is ~ 72 MHz.

The thermal environment of the signal pre-conditioning electronics and of the ADC is critical for the outcome of the phase measurement. This needs to be as stable as 1×10^{-2} K/ $\sqrt{\text{Hz}}$ in the LISA measurement band to reach the desired performance [9]; therefore, the FMC PM's PCB is shielded by a massive aluminum enclosure, which is then surrounded by a layer of nitrile rubber. The whole structure is further actively thermally stabilized by a PID controlled Peltier cell.

In TDOBS, as stated above, the FMC PM is timed by the FFT PM via an external clock signal. The same holds for the SG generating the PT.

PM structure in TDOBS

The FFT PM is used to measure the DC component of the optical signals, obtained from the DC output of the AC-DC splitters. The 16 channels are used to acquire data from three QPDs plus the AC output of the SEPD, which is necessary for the OPD stabilization loop. The FMC PM is used to measure the beat notes from of 2 QPDs using the AC output of the AC-DC splitters. The operation of each PMs is controlled via dedicated clients.

Parameter	FFT PM	FMC PM
# channels	16	8
DC/AC coupled	DC	AC
f_s	19.0734863281 Hz	3.390842013888889 Hz
max performing frequency	~ 5 MHz	40 MHz (Nyquist limit)
PT correction	no	yes

Table 3.10: Summary table of the characteristics of the PMs used in TDOBS.

3.3.5 The Control Software

Each PM is controlled by a dedicated client running on a PC located next to the experiment. Both were developed in C and serve as real-time monitors of the PMs' outputs and data storers.

The FFT PM's client

This client, named `tdobs-control`, is a mixed C and C++ code that retrieves the outputs of the 16 measured channels, each consisting of DC, three beat notes outputs (phase and amplitude) and the $f_{\text{AM}} \sim 267$ Hz amplitude demodulated signal per channel. This is shown in Figure 3.23. It also controls the actuators and is capable of moving them using the PM's measurement output as input, allowing the execution of feedback loops. Several actuator moving functions were developed during this thesis in order to perform calibrations for the experiment (see Chapter 4). The most relevant are an auto-alignment function for the RX beam and a function which rotates the RX beam around the center of REFQPD1.

3.3 Upgrade of TDOBS

The FMC PM's client

This client shows the real-time outputs of the eight measured channels, and is shown in Figure 3.24. The output consists of instantaneous frequency (PIR), amplitude (I) and error signal (Q) of the beat notes of each channel; this is shown in rows 1-4. As a PT is also being injected, its real-time tracking is also shown in rows 5-8. The new architecture for DWS tracking (see Chapter 7) was implemented by Pascal Grafe, and the real-time output is shown in rows 15-25. The last row shows the output of the temperature sensors.

The real-time plotter

This python script was developed to facilitate the visualization of the beam alignment procedures. A screenshot of this is shown in Figure 3.25. This program plots the real-time data from the FFT PM at the same update rate. It is structured to be very versatile, such that one can easily change the plotted elements according to the executed measurement. To input the real-time data into this script, we implemented a last-line reading of the files stored by the FFT PM's client.

As the clients are separate, they have inevitably different starting times; on top of that the two PMs have different sampling frequencies; a direct comparison between the two PM's output is not straightforward.

```
lisauser@lisauser-X105AE:~/Work/tdogs-control

lob_khz_pn Freq A: 5000000.000000 | Freq B: 29296.875000 | Freq C: 48828.125000 |
Package counter: 4378 | Missing packages: 1

Signals CH01: CH02: CH03: CH04: CH05: CH06: CH07: CH08:
DC : +0.021201 -0.066506 -0.000060 -0.015365 -0.502649 -0.513646 -0.515817 -0.501479
A: Amp : +0.000100 +0.125822 +0.000010 +0.000006 +0.000302 +0.000269 +0.000257 +0.000212
A:Phase: +0.715513 -0.431277 +1.264683 +0.787461 +7.426323 +7.064549 +7.138338 +19.815922
B:Ampl: +0.000000 +0.000000 +0.000000 +0.000000 +0.000000 +0.000000 +0.000000 +0.000000
B:Phase: +2.05767605 +32.3320471 +31.232005 +32.511172 +34.4650093 +34.4650093 +34.4650093 +30.000000
C:Ampl: +0.000000 +0.000000 +0.000000 +0.000000 +0.000000 +0.000000 +0.000000 +0.000000
C:Phase: +0.74.331091 -193.637133 +62.952149 -44.655388 +53.503233 +4.901837 +51.006253 +95.584833
Alt:Ampl: +0.000003 -0.014816 -0.000001 +0.000000 +0.031218 +0.03706 +0.033451 +0.033528

Signals CH09: CH10: CH11: CH12: CH13: CH14: CH15: CH16:
DC : +0.405908 -0.492131 -0.499916 -0.488605 +0.113123 +0.115868 +0.118330 +0.116528
A:Ampl: +0.000089 +0.000015 +0.000023 +0.000063 +0.000064 +0.000097 +0.000078 +0.000096
A:Phase: +7.306530 +6.998429 +7.057370 +5.338095 +2.945795 +3.239792 +4.293494 +2.980571
B:Ampl: +0.000001 +0.000001 +0.000001 +0.000001 +0.000000 +0.000000 +0.000000 +0.000000
B:Phase: +54.850002 +24.207634 +17.131466 +105.757913 -37.384118 -105.711809 -155.000533 -148.855967
C:Ampl: +0.000000 +0.000000 +0.000000 +0.000001 +0.000000 +0.000000 +0.000000 +0.000000
C:Phase: +55.960665 -158.708866 +31.363343 +310.845867 -63.880246 +165.209640 +24.867393 -203.802294
Alt:Ampl: +0.032172 +0.632172 +0.032406 +0.032092 +0.067497 +0.067571 +0.067568 +0.067475

OPD1: OPD2:
ERR : -0.0000813 ERR : +0.000813
ACT : +0.482 ACT : -1.753
CH|FREQ: 02 | a CH|FREQ: 02 | a

---- Ref QPD ----
---- Scl QPD 1 - term_out ---- Scl QPD 2 - term_out----
DPS V: -0.970098 DPS V dc: -0.001271 DPS V dc: -0.012629
DPS H: -0.025493 DPS H dc: -0.006679 DPS H dc: +0.002017
DPS W: +1.849593 DPS V AM: -0.001186 DPS V AM: +0.000862
DPS H: +1.985478 DPS H AM: -0.002440 DPS H AM: -0.000639
PHASE1_OFF: +0.316203
PHASE2_OFF: +0.246200
PHASE3_OFF: +0.246200
PHASE4_OFF: +0.1917536

----- Scl QPD 1 - main_pm ----- Scl QPD 2 - main_pm -----
DPS V dc: -0.001277 DPS V dc: 0.012635
DPS H dc: -0.006680 DPS H dc: +0.002041
DPS V AM: -0.001206 DPS V AM: +0.001049
DPS H AM: -0.002502 DPS H AM: -0.000495
data_gate 1

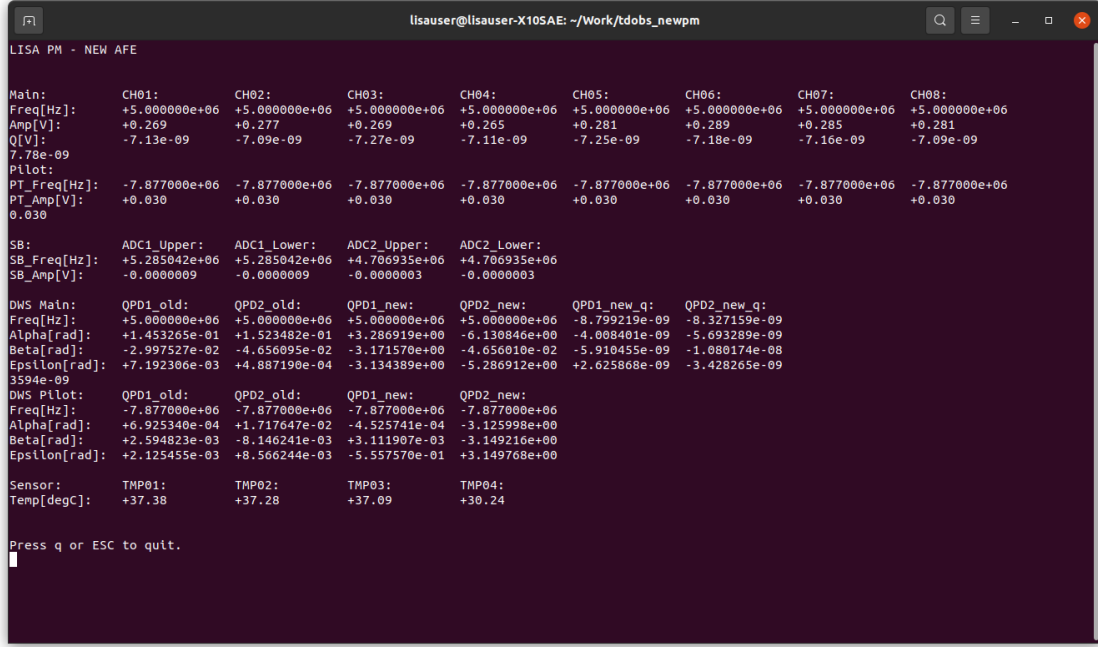
PREDEFINED CONTROL
phase a, freq_a = 'num2str(file_info.freq(1)/1000)' 'kHz
Choose between a set of predefined actuator motions (1: constant velocity line, 2: square, 3: circle, 4: rotate
e RX beam around REFOPD1, 5: align RX beam on CQPs, 6: slow aligned motion, 7: go to nominal position, 8: perf
orm DC offset calibration

5
alignment tolerance (2...1000)/1000:
2
DC or AM calibration( 1(DC) or 2(AM) ):
2
GB or FT beam used( 1(GB) or 2(FT) ):
0
_n_steps for alignment (higher -> quicker and less precise
1
What now? (1: start again, 2: go to manualControlSession, 3: extl)

```

Figure 3.23: Screenshot of the FFT PM's control software.

3.3 Upgrade of TDOBS



```

lisauser@lisauser-X105AE: ~/Work/tobs_newpm
LIISA PM - NEW AFE

Main:      CH01:      CH02:      CH03:      CH04:      CH05:      CH06:      CH07:      CH08:
Freq[Hz]: +5.000000e+06 +5.000000e+06 +5.000000e+06 +5.000000e+06 +5.000000e+06 +5.000000e+06 +5.000000e+06 +5.000000e+06
Amp[V]:   +0.269     +0.277     +0.269     +0.265     +0.281     +0.289     +0.285     +0.281
Q[V]:    -7.13e-09   -7.09e-09   -7.27e-09   -7.11e-09   -7.25e-09   -7.18e-09   -7.16e-09   -7.09e-09
7.78e-09
Pilot:
PT_Freq[Hz]: -7.877000e+06 -7.877000e+06 -7.877000e+06 -7.877000e+06 -7.877000e+06 -7.877000e+06 -7.877000e+06 -7.877000e+06
PT_Amp[V]:  +0.030     +0.030     +0.030     +0.030     +0.030     +0.030     +0.030     +0.030
0.030

SB:        ADC1_Upper:  ADC1_Lower:  ADC2_Upper:  ADC2_Lower:
SB_Freq[Hz]: +5.285042e+06 +5.285042e+06 +4.706935e+06 +4.706935e+06
SB_Amp[V]:  -0.0000009   -0.0000009   -0.0000003   -0.0000003

DWS Main:  QPD1_old:   QPD2_old:   QPD1_new:   QPD2_new:   QPD1_new_q:  QPD2_new_q:
Freq[Hz]:  +5.000000e+06 +5.000000e+06 +5.000000e+06 +5.000000e+06 -8.799219e-09 -8.327159e-09
Alpha[rad]: +1.453265e-01 +1.523482e-01 +3.286919e+00 -6.130846e+00 -4.068401e-09 -5.693289e-09
Beta[rad]:  -2.997527e-02 -4.456095e-02 -3.171570e+00 -4.056010e-02 -5.910455e-09 -1.080174e-08
Epsilon[rad]: +7.192306e-03 +4.887190e-04 -3.134389e+00 -5.286912e+00 +2.625868e-09 -3.428265e-09
3594e-09
DWS Plot:  QPD1_old:   QPD2_old:   QPD1_new:   QPD2_new:
Freq[Hz]:  -7.877000e+06 -7.877000e+06 -7.877000e+06 -7.877000e+06
Alpha[rad]: +6.925340e-04 +1.717647e-02 -4.525741e-04 -3.125998e+00
Beta[rad]:  +2.594823e-03 -8.146241e-03 +3.111907e-03 -3.149216e+00
Epsilon[rad]: +2.125455e-03 +8.566244e-03 -5.557570e-01 +3.149768e+00

Sensor:    TMP01:      TMP02:      TMP03:      TMP04:
Temp[degC]: +37.38      +37.28      +37.09      +30.24

Press q or ESC to quit.

```

Figure 3.24: Screenshot of the FMC PM's control software.

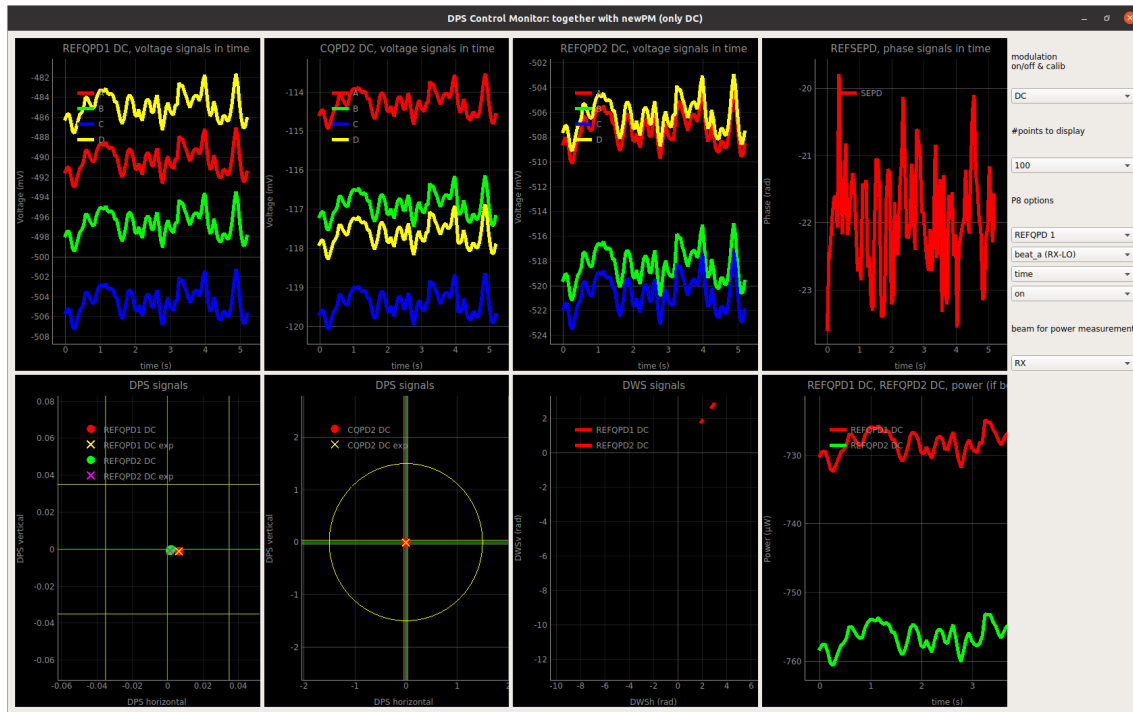


Figure 3.25: Screenshot of the FFT PM's real-time plotter

3.3.6 Vacuum System

TDOBS is placed in a vacuum chamber to be isolated from external disturbances such as acoustic noise, refractive index variations and ambient lights. Additionally, the experiment is expected to benefit from the vacuum also because of the increased thermal stability.

The used VC is of rectangular shape with inner dimensions of $98 \times 80 \text{ cm} \times 48.5 \text{ cm}$ and a total volume of ~ 380 liters. The main port opens on the top. Vacuum is realized by a combination of one scroll pump and one turbo pump connected in series. The system is able to reach a vacuum of $\sim 10^{-5} \text{ mbar}$ when both pumps are active. As the vibration noise from the scroll pump does not allow any precision measurement, the experiment is typically operated in a static vacuum, i.e. with the pumps turned off and the vacuum tank sealed. A leak finder was used to map the main leakages, which were solved in order to improve the duration of the static vacuum. This was achieved through custom designed clamps used to seal the corners of the main port of the VC; these, due to geometric reasons, are pressed less by the atmospheric pressure on the VC. When in static vacuum, the pressure rise is of the order of $\sim 0.3 \text{ mbar}$ per day. The VC itself is positioned on a pneumatic suspension system, used as a passive vibration isolator. Unfortunately, this is broken and cannot easily be repaired, as the manufacturer company ceased to exist. Efforts to repair it stopped as it was estimated that a working suspension would not improve the low frequency performance of the experiment.

The four laser beams are delivered to the TS and LISA-OB by monolithic single-feed-through optical fibers, which extend from the modulation bench (MB) to inside the VC. These fibers are connected to the respective FIOS-fibers inside the vacuum chamber with the additional use of an intermediate fiber to protect the FIOS-fibers.

The output signals from the PRs are propagated through SMA cables and SMA feed-throughs until the AC-DC splitter boards.

3.3.7 Thermal Isolation

A thermal shield has was installed around the baseplates inside the VC to improve TDOBS's thermal stability (see Figure 3.27). This consists of a thin aluminum plate box structure covered with a multilayer insulation blanket. The plate positioned below the experiment was already part of a previously used thermal shield, while the remaining five plates were designed newly by the Author. These were designed in such a way that the opening of the thermal shield does not require to disconnect any of the many cables inside the VC. An array of eight temperature sensors monitors the temperature in several positions, both inside and outside the thermal shield. The vacuum chamber was also covered with a thick layer of armafex[®] to improve the passive thermal isolation. An active temperature control system is planned to be operated on the TDOBS VC. The actuators for this control system are already installed, but the control was not operated yet.

Note that because of the very good passive thermal isolation and due to the power dissipated by the electronics heating inside the thermal shield, everytime the tank is evacuated at least one day has to pass in order to reach a temperature steady state.

3.3 Upgrade of TDOBS

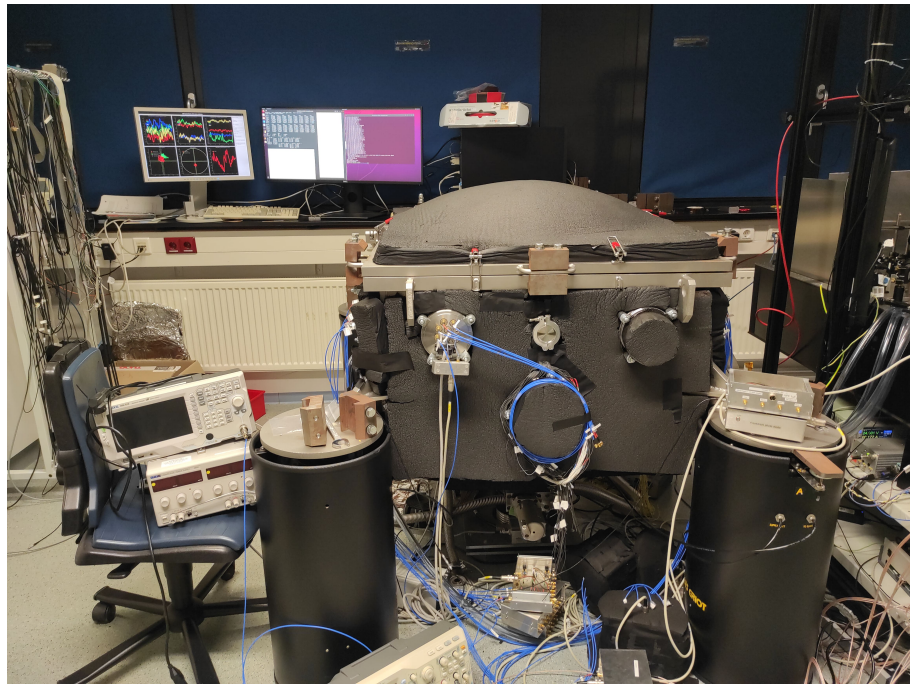


Figure 3.26: Picture of the vacuum chamber (VC). The PC, together with the real-time monitor, is visible on the top left.

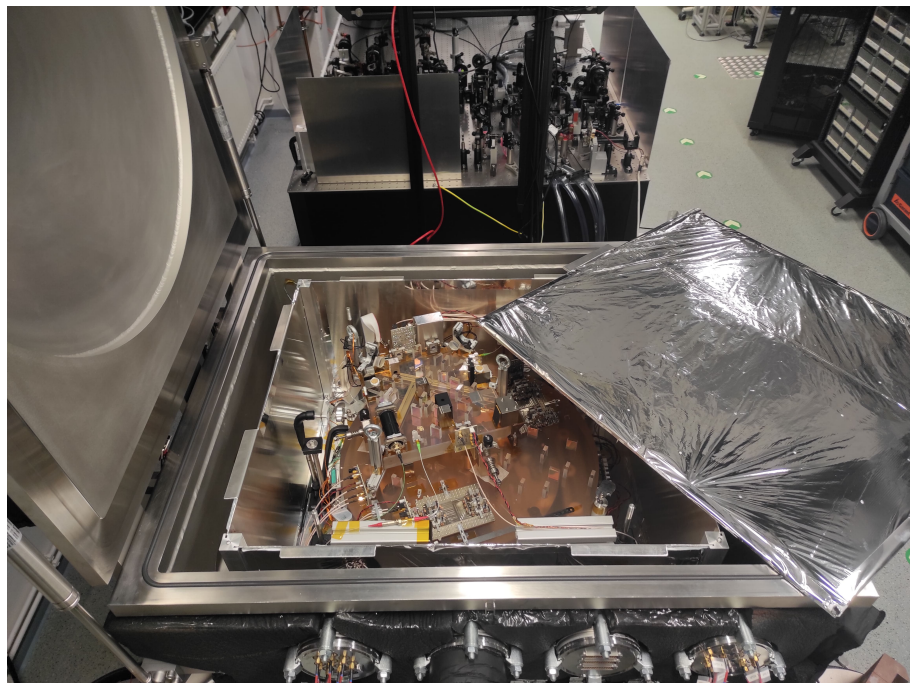


Figure 3.27: Picture of the vacuum chamber, with inside the TDOBS experiment, surrounded the thermal shield. The modulation bench is visible on the back of the VC.

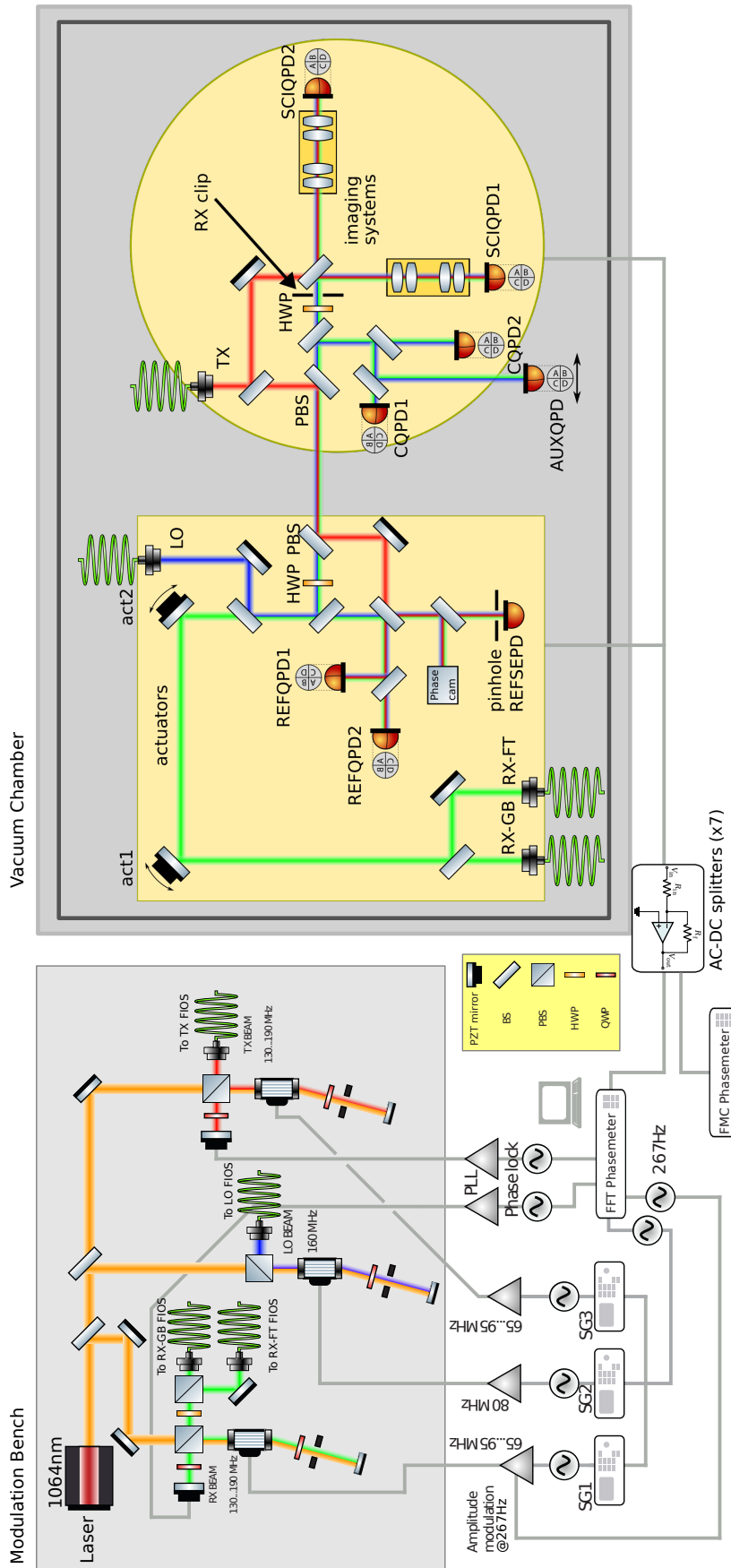


Figure 3.28: Overall scheme of TDOBS.

3.4 Conclusion

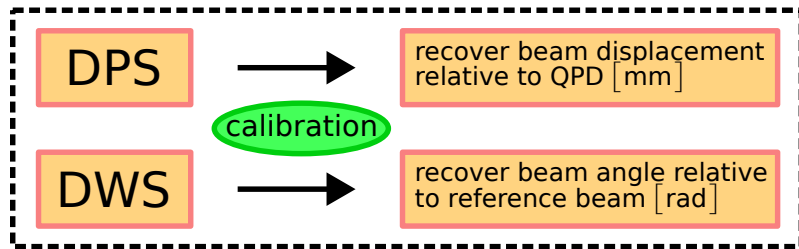
LISA plans to use DWS to mitigate the TTL. However, the current understanding of DWS performance has some gaps, particularly regarding its behavior under weak-light conditions and in the presence of beam tilts. TDOBS, an ultra-stable testbed representative of LISA’s optical bench, serves as an ideal platform for conducting these essential investigations.

TDOBS was upgraded from a simplified condition of using \sim kHz frequency beat notes to the use of beat notes in the LISA-heterodyne band (5-25 MHz). This work required the upgrade of the modulation bench (MB) and of the electronics of the PRs as well as the upgrade of the used phasemeter (PM). The trans-impedance amplifiers (TIAs) of all PRs were upgraded to amplify beat notes with frequencies up to 30 MHz. For the QPRs which are representative of LISA, low-noise TIAs were designed to reach equivalent input current noises as low as $2 \text{ pA}/\sqrt{\text{Hz}}$. A pre-development of the LISA PM was installed, capable of extracting the phase of beat notes with frequencies up to 40 MHz. A second-stage amplifier has been realized to match the amplitude of the beat note from the TIAs to the ADC range of the PM. Finally, to improve the thermal stability of the experiment, which is expected to affect the performance below \sim mHz frequencies, a thermal shield was installed around the baseplates of TDOBS.

Chapter 4

Calibration

The longitudinal pathlength sensing (LPS) can be self-calibrated since the relationship between pathlength and phase depends only on the wavelength of the laser beam, which is constant and known to sufficient accuracy. DWS and DPS signals also have a theoretical calibration, but these rely heavily on geometrical parameters of the experiment (see Section 2.3), which are always known to limited precision. The first step to operating TDOBS is to have an experimental calibration of DPS and DWS for all quadrant photodiodes (QPDs) and beam combinations in order to recover the position and the angle of the RX beams.



In this procedure, the absolute power impinging on a photodiode is never mentioned since both DPS and DWS signals are power-independent. This exact quantity is also rather difficult, if not impossible, to obtain, as that the used QPDs are smaller - or of comparable size - than the beams impinging on them, which makes it very difficult to measure beam power on individual segments.

This chapter describes the calibration procedure of the experiment. This starts with adding an external QPD, calibrating it, and then using this calibration to calibrate all the other signals. This chapter also focuses on the actuation principle of the two steering mirrors and their precision, as well as on side effects of the beam tilting, such as the decrease of heterodyne efficiency. The measurements reported in this thesis were realized using the LO beam and either the RX-GB or RX-FT beams. The calibrations shown in this Chapter, therefore, are based on the use of these three beams, while the TX beam is unused.

4.1 The Auxiliary QPD

The calibration of either DPS or DWS requires the experimenter to induce, respectively, a known beam shift or beam angle and to relate this to the obtained signal. On the other hand, the TDOBS baseplate can induce beam angles, but these are not

quantifiable, as the actuators don't provide an absolute angle. Hence, to calibrate the experiment, an additional calibrated device is needed, and this is the auxiliary QPD (AUXQPD). This is added to the experiment as depicted in Figure 4.1. It is mounted outside of the LISA-OB, and the mount is equipped with two translation stages allowing vertical and horizontal shifts with a precision of $\sim 10 \mu\text{m}$. The active area's radius is 4 mm, chosen to be large enough to measure the DPS signals of the large RX-FT beam. As no beam from the LISA-OB is propagating in this specific direction, a mirror between BS24 and CQP1 has to be added to reflect the RX and LO beam in the direction of the AUXQPD. In this configuration, the RX-GB, RX-FT and LO beams impinge on the AUXQPD.

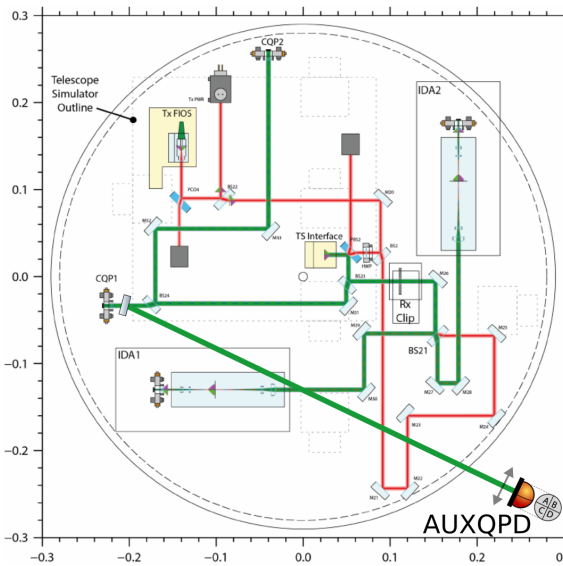


Figure 4.1: This Figure is a copy of Figure 3.6 (see that for details of the LISA-OB layout), but the AUXQPD has been added. The AUXQPD is located at the bottom right of the figure. It is not physically standing on the baseplate but is held by a dedicated mount placed on the main baseplate inside the VC. An additional mirror is placed in front of CQP1 to reflect the RX and LO beams to the AUXQPD. The LO beam, which has a fixed propagation axis, impinges on the center of the AUXQPD.

This shiftable QPD allows varying the position of the beam with respect to the QPD and hence to calibrate the DPS signal of the beam on the AUXQPD. This procedure has to be repeated for each beam and was performed for the RX-GB and RX-FT beams. It was not done for the LO beam, as it has a fixed propagation axis. The obtained calibration is the pillar on which all further calibrations of the experiment are based.

Unfortunately, the installation of the AUXQPD is incompatible with the thermal shield for spatial reasons, and hence, it had to be removed. Its DPS calibration is used to calibrate other QPD's DPS signals.

The DPS calibration curve is in theory, for a TEM_{00} beam, an error function (see equation (2.101)). One step toward relaxation of the used fit function is to use a polynomial with odd powers. An even further step is to simply use a polynomial. Only this last function was found to leave no large structure in the residuals and was hence preferred. Deviations from an error-function calibration can be caused, most likely, by gain- and offset- differences in the TIAs of the four QPD segments

4.1 The Auxiliary QPD

and a non-Gaussian beam shape.

The polynomial's order was varied until it was describing the calibration data sufficiently well; this procedure converged to the 17th order. Since the aim of this is to recover the displacement from the measured DPS value, it is convenient to fit the displacement against the DPS value. The result of the calibration process of the AUXQPD is reported in Figure 4.2. In this plot, each data point consists of the average of 100 measurements, and the error bar is calculated as the standard deviation of the average. This procedure leads to excessively small error bars, and for this reason, I plotted the residuals as non normalized. The same procedure was followed for all plots in this chapter.

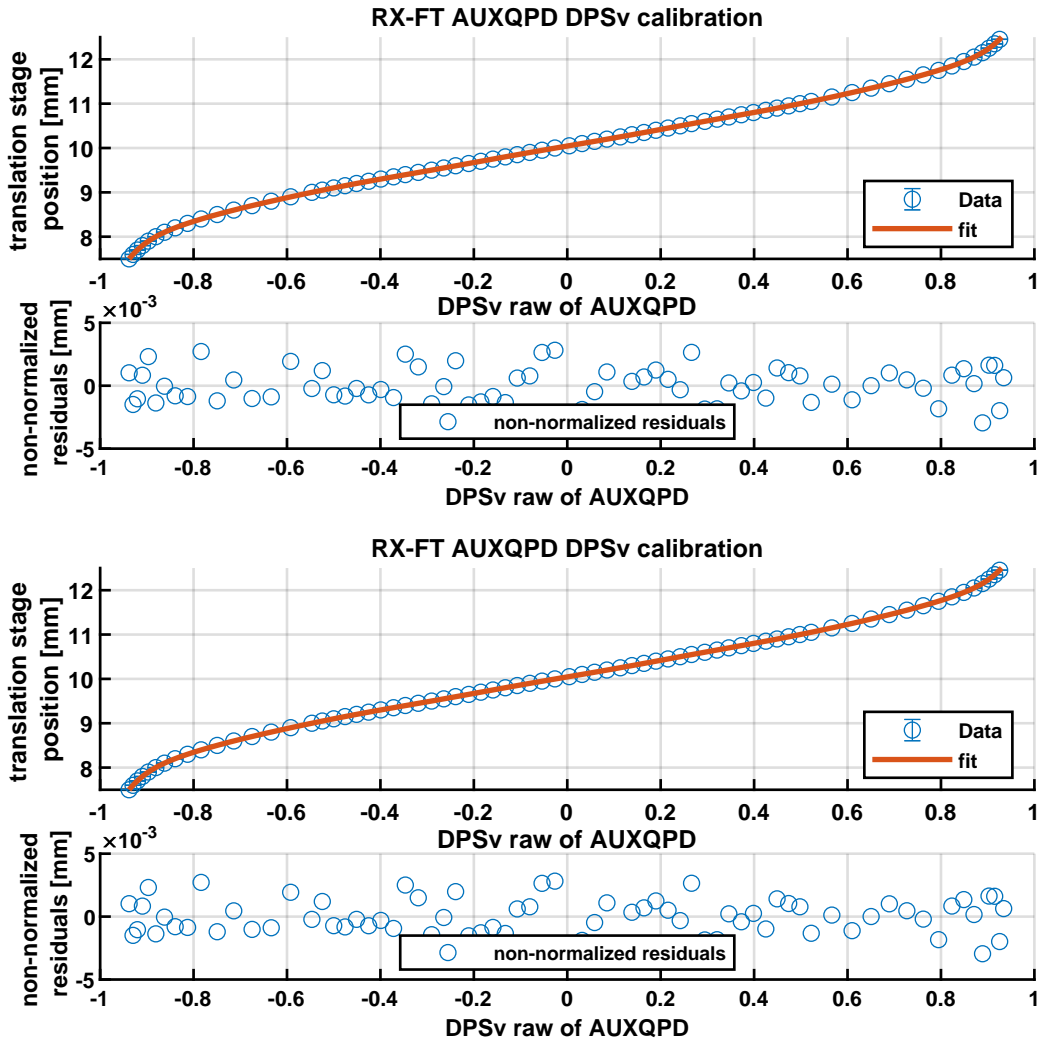


Figure 4.2: Vertical calibration of the DPS signal of the RX-GB (above) beam and RX-FT beam (below) on the AUXQPD. The horizontal calibrations and fit parameters are reported in Appendix C, Figure C.1.

It can be inferred from the distribution of the residuals that the RX-GB and RX-FT beams' position can be measured with a precision of a few μm .

4.2 Rotation of the RX beam

The RX beam can be rotated to simulate the tilts by using the two actuators on the TS (see Section 3.2.2). These are piezo step actuators which move by steps of roughly 5 μrad both vertically and horizontally. The steps are not constant in size and non-reproducible. A histogram of the step size is shown in Figure 4.3. This makes them good for performing small tilts of the RX beam.

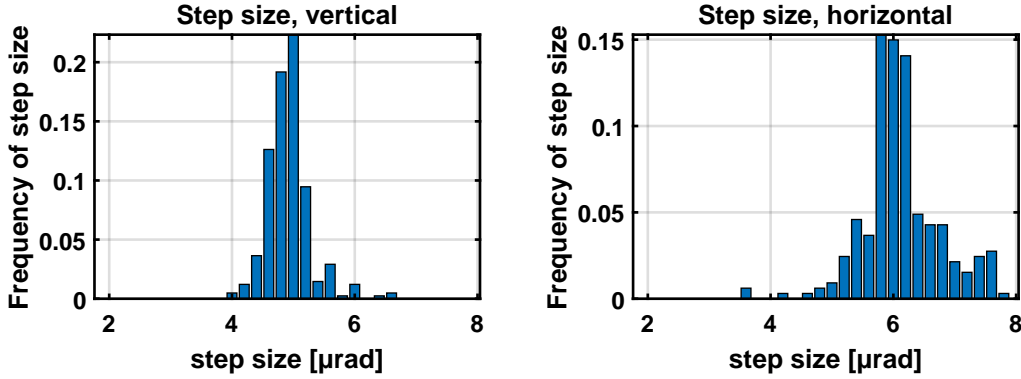


Figure 4.3: Histogram of the tilt angles of actuator 1, measured by rotating the actuator vertically (left) and horizontally (right) and measuring the induced RX beam displacement on the AUXQPD. The actuation angle peaks around 5 μrad for the vertical axis and around 6 μrad for the horizontal axis. The higher variation of the horizontal axis is evident in the following calibrations, as the distribution of the horizontal induced angles is visibly less regular than that of the vertical angles.

The beam rotation around the RX-clip is achieved by rotating both mirrors. Neglecting effects due to the tilt of the actuators themselves shifting the reflection points of the beams, it can be shown geometrically that, for both vertical and horizontal actuation, the beam reflected at the second mirror intersects the RX-clip with an offset δ_{RX} and angle α_{RX} given by

$$\delta_{RX} = d_{1-2} \tan(2\alpha_{M1}) + d_{2-RX} \tan(2(\alpha_{M1} + \alpha_{M2})) \quad (4.1)$$

$$\alpha_{RX} = 2(\alpha_{M1} + \alpha_{M2}), \quad (4.2)$$

where d_{1-2} is the distance between the two mirrors, d_{2-RX} is the distance between the second mirror and the target and $\alpha_{M1,2}$ are the tilt angles of the mirrors, as depicted in Figure 4.4. This relation can be inverted to obtain the angle $\alpha_{M1,2}$ to cross the RX-clip with an angle α_{RX} and an offset δ_{RX} .

$$\alpha_{M1} = \frac{1}{2} \arctan \left(\frac{\delta_{RX} - d_{2-RX} \tan(\alpha_{RX})}{d_{1-2}} \right) \quad (4.3)$$

$$\alpha_{M2} = \frac{1}{2} \arctan \left[\alpha_{RX} - \arctan \left(\frac{\delta_{RX} - d_{2-RX} \tan(\alpha_{RX})}{d_{1-2}} \right) \right] \quad (4.4)$$

In TDOBS, the offset δ_{RX} is typically kept at zero while the angle α_{RX} is intentionally varied, making the RX-clip the tilting pivot as happening in LISA with the RX and TX beam rotating around a fixed point. Since the angles are very small and the offset δ_{RX} is zero, equations (4.3) and (4.4) can be for simplicity linearized, and

the lengths replaced with the values from Table 4.1, resulting in equations (4.5) and (4.6). These are the equations implemented in the mirror rotation control functions.

$$\alpha_{M1} \approx \frac{-d_{2-RX}}{d_{1-2}} \frac{\alpha_{RX}}{2} \sim -\frac{25}{18} \alpha_{RX} \quad (4.5)$$

$$\alpha_{M2} \approx \left(1 + \frac{d_{2-RX}}{d_{1-2}} \frac{\alpha_{RX}}{2} \right) \sim \frac{34}{18} \alpha_{RX} \quad (4.6)$$

Practically, such a rotation where the actuators are tilted by a pre-calculated angle and once only commanded is impossible to achieve; This is due to the facts that a) the actuators perform a discrete step movement, which implies rounding the angles in equations (4.5, 4.6) and b) the executed angle is not precise. For this reason, the algorithm controlling the actuators first rotates them both by the pre-calculated angle, and then a correction phase follows where actuator 2 is rotated until the RX beam's DPS signal on REFQPD1 is zero in the used rotation axis. To minimize this correction phase, the α_{RX} tilt angles can be chosen such that $\alpha_{M1,2}$ are multiples of 5 μ rad. The procedure is the same for both vertical and horizontal tilts. The actuators can tilt up to $\pm 2^\circ$, giving a maximum beam tilt around the RX-clip of roughly 1° using equations (4.3,4.4). This is way beyond what is needed to probe LISA's worst case scenario tilt, as this angle is larger than the constellation's breathing mode (see Figure 1.4). The mirror actuation in TDOBS is taken care of by the FFT PM control software (see Subsection 3.3.4)

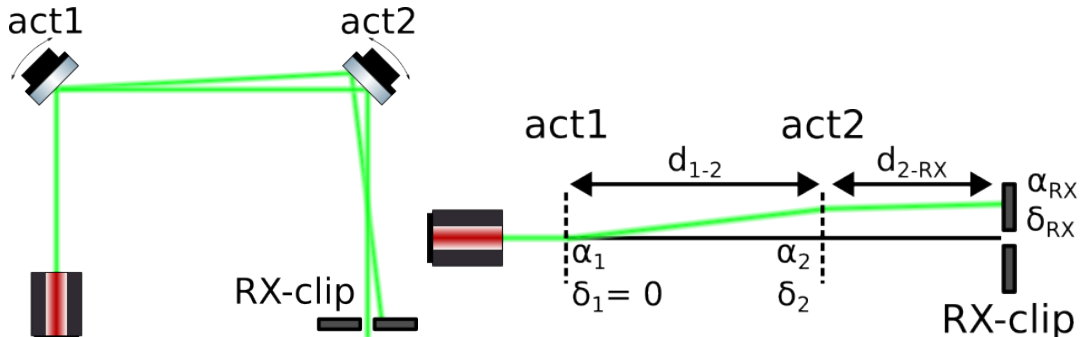


Figure 4.4: Left: realistic representation of how the actuators rotate the RX beam. Right: simplified 1D representation of how the beam tilts after reflection on the actuated mirrors. Figures inspired by [67].

To give an idea of the sizes in TDOBS, a list of the most relevant spatial separations between components is reported in Table 4.1:

Optic element 1	Optical element 2	Distance [mm]
RXGB FIOS	Actuator 1	245 \pm 20
Actuator 1	Actuator 2	180 \pm 10
Actuator 2	RX-clip & REFQPDs	500 \pm 50
RX-clip & REFQPDs	CQPD1	370 \pm 50
RX-clip & REFQPDs	CQPD2	788 \pm 50
RX-clip & REFQPDs	AUXQPD	858 \pm 80

Table 4.1: Table with the geometrical distances between optical components in TDOBS.

4.3 Secondary DPS calibration of the other QPDs

Further calibrations of the DPS signals of other QPDs can be achieved by tilting or shifting the RX beam using the actuators and measuring the applied tilt using the calibrated AUXQPD. This was done for CQPD2, REFQPD1 and REFQPD2. CQPD1 was not calibrated because it was not really needed. I will refer to these calibrations as *secondary* calibrations, as they rely on a previous direct calibration and propagate systematic errors of the first calibration. These calibrations are useful to quantify the departure from the IFM's nominal position, which has the RX beam centered on all QPDs. For these calibrations, lateral shift of the RX beam on the QPDs is achieved using just one of the actuators for angles up to 1 mrad, where the tilt is indistinguishable from a shift. This calibration principle is depicted in Figure 4.5. The number of total reflections has to be counted as this can cause minus signs in the lateral displacement. The so calibrated beam signals are REFQPD1, REFQPD2, CQPD2 for the RX-GB beam and CQPD2 for the RX-FT beam. The REFQPDs, with their small diameter, are utterly insensitive to the DPS signal of the RX-FT beam. The obtained calibrations are reported in Appendix C.

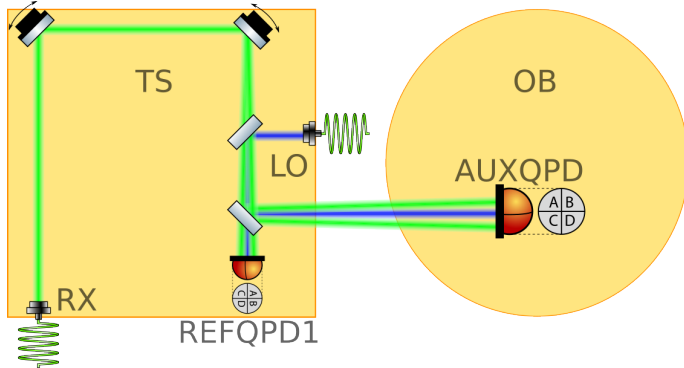


Figure 4.5: Example of the rotation of actuator 2 for the calibration of the DPS signal of REFQPD1. In the experiment, actuator 1 was used, but actuator 2 was rotated in the Figure for simplicity. On the LISA-OB only the AUXQPD is shown for simplicity.

4.4 DWS calibration of the REFQPDs

An exact DWS calibration requires full knowledge of which tilt the measurement beam is undergoing, as it depends, for instance, on the tilt pivot [41]. In LISA and TDOBS, the beams are always rotating around a well-defined point, and with this rule the DWS signals of the REFQPDs and SCIQPDs can be calibrated.

The measurement procedure is to contemporarily measure DWS and the RX beam's angle using an *optical lever* [48]. The RX beam is tilted around the RX-clip using the actuators. The induced angle can be measured using e.g. the AUXQPD or any other QPD of which the DPS signal was calibrated. As the RX beam is rotated, the measured DPS signal gives the lateral beam displacement Δx at the QPD. Given the geometrical distance between the RX-clip and AUXQPD is $d_{\text{RX-AUXQPD}}$, the physical angle between the RX beam and the LO beam can be recovered using

$$\alpha_{\text{RX}} = \arctan \left(\frac{\Delta x}{d_{\text{RX-AUXQPD}}} \right) \approx \frac{\Delta x}{d_{\text{RX-AUXQPD}}}. \quad (4.7)$$

This measurement principle is shown in Figure 4.6. The DWS value measured at REFQPD1 and REFQPD2 can be calibrated against the measured angle α_{RX} . This operation is done for both vertical and horizontal tilts. Every beam combination on a QPD needs to be calibrated. Another information which can be extracted by this measurement is the decrease of the heterodyne efficiency as a function of the RX beam angle α_{RX} . Note that the uncertainty of $d_{RX-AUXQPD}$ is the limiting factor on the precision of the calibration.

Such measurement can be carried out simultaneously on both REFQPDs or SCIQPDs, as they are optical copies. The used PM for the measurement is the FMC PM. The obtained calibration curve is fit with equation (2.139) using just the κ_1 and κ_3 coefficients; hence, the candidate fit function is $f(x) = p_1(x - x_0) + p_3(x - x_0)^3$. The curve's shape does, in principle, not depend on the used heterodyne frequency, but the phase offset x_0 can depend on the phase TF of each channel's detection chain (TIA plus AC-DC splitters); this value can vary for different heterodyne frequencies, especially in the 20 MHz region.

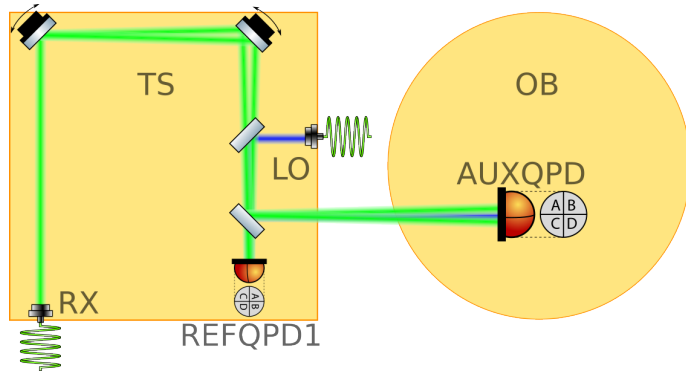


Figure 4.6: Rotation of the RX beam around the RX-clip using the two actuators. On the LISA-OB only the AUXQPD is shown for simplicity.

RX-GB & LO DWS

The calibration shown here was realized as explained using the RX-GB. The resulting calibration for REFQPD1 is shown in Figure 4.7 for both vertical and horizontal tilt, while the calibration for REFQPD2, which is almost identical, is shown in Appendix 2.3.3 in Figure D.1. The resulting fit parameters and obtained DWS gain κ_1 for REFQPD1 and REFQPD2 are reported in Table 4.2. Note that the resulting polynomial coefficients for the same axis differ by less than 1.7 times their standard error, stating a good quality of the optical copy properties of the REFQPDs. Surprisingly, also the values for the DWS *bias* x_0 for the same axis are very close. This is not to be expected, if the cause was the phase transfer function of the TIA, as the designs of the two TIAs are different. From Table 4.2 and Figure 4.7, it stands out that, in the horizontal DWS calibration, the angular spacing between the measurement points is less regular than that in the vertical DWS calibration. Furthermore, the horizontal DWS calibration has larger error bars. The cause of the worst spacing is given in Figure 4.3. The likely cause of the higher error bar is not understood.

In Figure 2.14, the DWS curve for such beams was modelled. A comparison between the numerical prediction and the measured curves is shown in Figure 4.8.

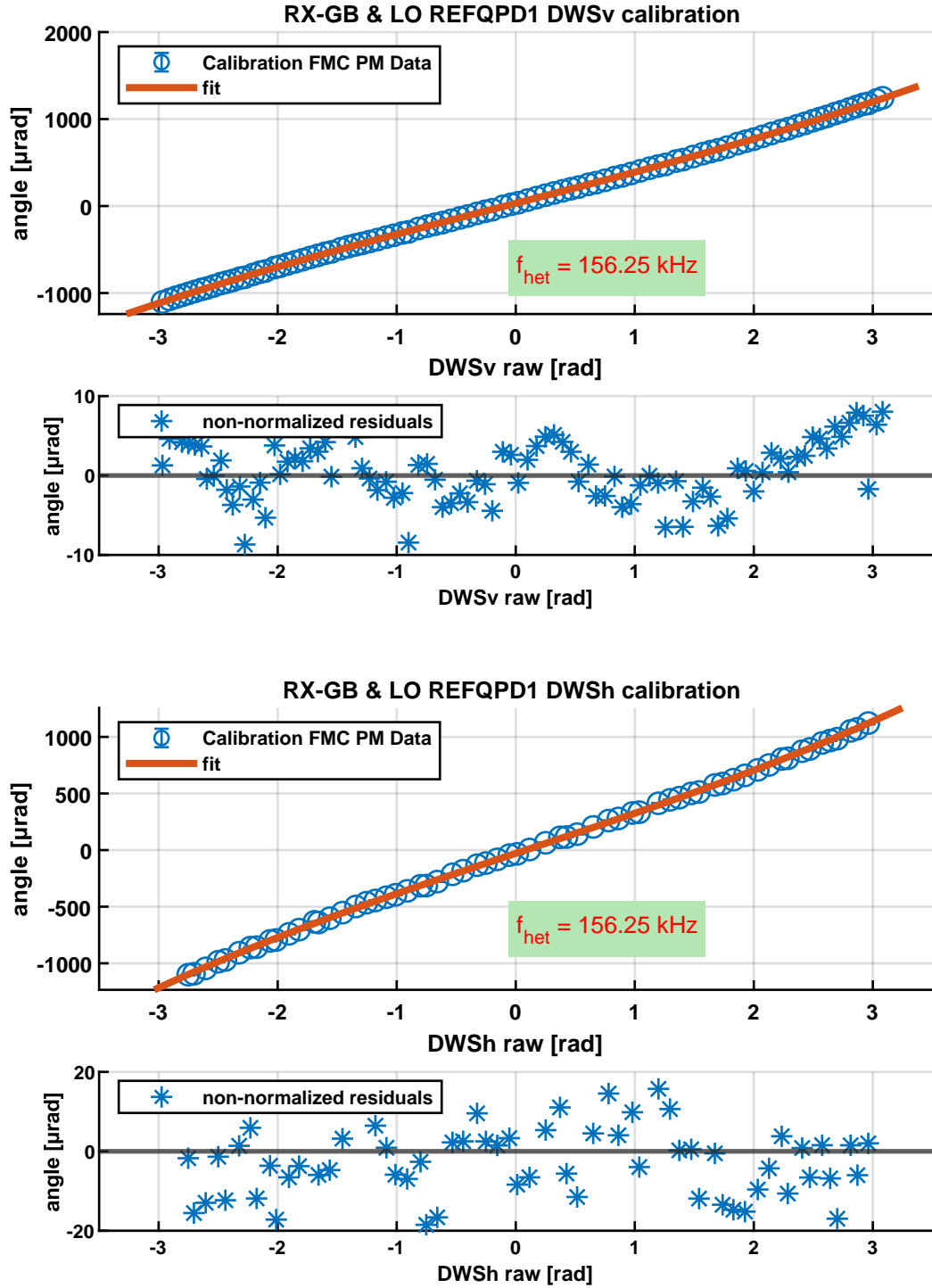


Figure 4.7: Resulting calibration of the RX-GB and LO beams DWS signal on REFQPD1. This calibration was realized using phase measurements from the FMC PM at a heterodyne frequency of 156.25 kHz. The measurement's fits are reported in Table 4.2. Despite the residuals showing some residual structure (visible especially in the DWS vertical calibration), there is no reason to increase the polynomial order. Such effects are likely due to wavefront imperfections.

Calibration	p_1 [$\mu\text{rad}/\text{rad}$]	p_3 [$\mu\text{rad}/\text{rad}$]	x_0 [rad]
REFQPD1 DWS _v	353.52 ± 0.61	3.65 ± 0.14	-0.089 ± 0.001
REFQPD1 DWS _h	350.47 ± 1.86	4.63 ± 0.44	0.083 ± 0.003
REFQPD2 DWS _v	354.92 ± 0.62	3.66 ± 0.15	-0.088 ± 0.001
REFQPD2 DWS _h	351.98 ± 1.84	4.63 ± 0.44	0.080 ± 0.003

Table 4.2: Table with the calibration parameters of the RX-GB and LO beams DWS signal on REFQPD1 and REFQPD2 (Figure 4.7). The function used for the fit is $y(x) = p_1(x - x_0) + p_3(x - x_0)^3$. At a tilt angle of zero, the DWS gain is $\kappa_1 = 2825 \pm 10 \text{ rad/rad}$.

The measured DWS κ_1 is $\sim 13.4\%$ lower than the predicted one. The DWS bias x_0 is the only parameter which is expected to depend on the heterodyne frequency, as its value depends on the phase TF of the whole detection chain of each segment (see Figure 3.18).

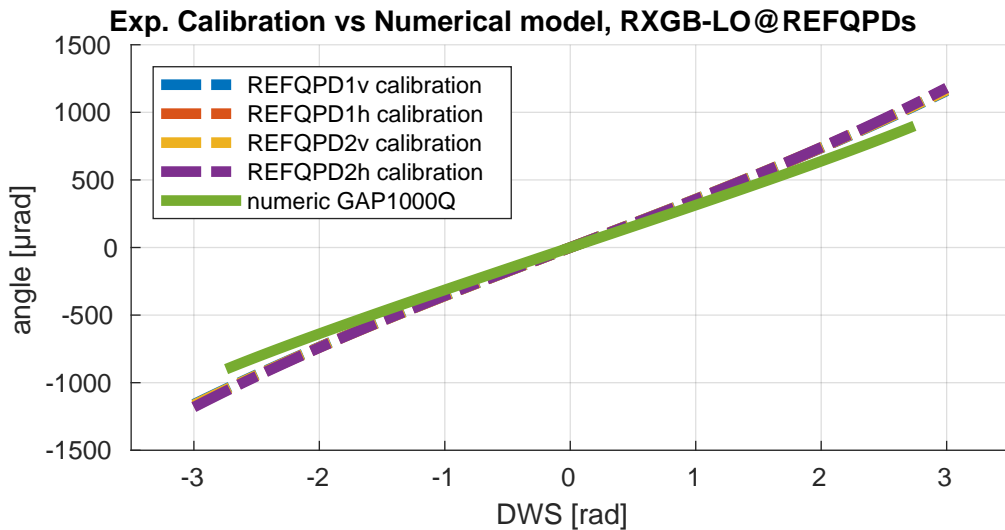


Figure 4.8: Comparison between the DWS-shifted RX-GB & LO DWS calibration of the REFQPDs and the DWS numeric model. The measurements are in excellent agreement with each other. Beam parameters are: $w_{\text{eff}} = 0.685\text{mm}$, $R_{\text{rel}} = -9519 \text{ mm}$ and $\rho = 0.1387$.

RX-FT & LO DWS

This calibration has required a different procedure than initially thought, as the 1 mm diameter REFQPDs are completely insensitive to the DPS signal of the 1cm large RX-FT beam once the beam is centered, meaning that the resulting DPS was constantly zero. In this condition, re-centering the RX-FT beam on the REFQPDs is impossible and rotating the RX-FT beam around the REFQPDs is unfeasible.

The implemented solution was to exploit the fact that the orientation of the wavefront of a plane wave does not depend on its rotation pivot¹. The RX-FT beam was hence rotated by actuating only actuator 2, giving raise to a rotation of the RX-FT with pivot at actuator 2 as in Figure 4.5. This method has the side effect of causing beam walk on the QPDs. As the RX-FT beam is much larger than

¹This intuitive statement is also mathematically proven by [41]

the REFQPDs, this method works as long as the measured beam portion on the REFQPDs is far from the edge of the RX-FT beam. This is relatively difficult to avoid as the centering itself of the RX-FT beam onto the REFQPDs has to be done by manually controlling the actuators and checking the beam's position with nothing more than a beam card. The attempts to center the RX-FT beam by manually tilting the actuators and noting down when the beam power was dropping failed due to the variability of step-sizes. The physical angle between the beams was, as previously, characterized by measuring the lateral displacement of the RX-FT beam on the AUXQPD, but with a different pivot.

$$\alpha_{RX} = \arctan \left(\frac{\Delta x}{d_{act2-AUXQPD}} \right) \approx \frac{\Delta x}{d_{act2-AUXQPD}} \quad (4.8)$$

The obtained calibration curve is fit with a generic polynomial for necessity. From this, the coefficient κ_1 can be derived. In this case, κ_3 is expected to be negligible (see Figure 2.15).

Parameter	Vertical			Horizontal		
p_0	-612.3	\pm	0.1	-408.1	\pm	0.1
p_1	376.0	\pm	0.9	281.7	\pm	0.1
p_2	-18	\pm	6	6.14	\pm	0.09
p_3	-183	\pm	36	0.58	\pm	0.03
p_4	605	\pm	91	-		
p_5	-947	\pm	116	-		
p_6	805	\pm	83	-		
p_7	-370	\pm	33	-		
p_8	86.4	\pm	7.2	-		
p_9	-8.03	\pm	0.63	-		

Table 4.3: Table with the calibration parameters of the RX-FT and LO beams DWS signal on REFQPD1 (Figure 4.9). Polynomials of order 9 and 4 were found to describe accurately enough the vertical and horizontal calibration curves, respectively.

The vertical calibration in Figure 4.9 manifests a weird change in slope around $DWS_v = 1.4$ rad, while the horizontal calibration looks only slightly non-linear. This is due to the difficulty in controlling the beam's position. Figure 4.10 compares the measured DWS calibration curve with the modelled one, which was numerically derived from the same equations (2.133, 2.134) by using as $w_{eff} = w_{LO}$ and $R_{rel} = R_{LO}$ ² and is plotted in Figure 2.15. The numerically calculated curve is in excellent agreement with the measured horizontal curves in the whole measurement range and with the measured vertical curves for DWS values in the range $DWS_v \in [-2, 1]$ rad, while it departs between $DWS_v \in [1, 3]$ rad. I interpret this effect in the vertical calibration to be caused by bad centering of the beam on the QPD, as especially the vertical position is the most difficult to judge because of parallax. From here on, the calibration function will be assumed to be the fit of the numerically calculated one in Figure 2.15, of which the fit parameters and DWS gain at null angle κ_1 are shown in Table 4.10.

²This can be derived from equation (2.25) by replacing $w_m, R_m \rightarrow \infty$

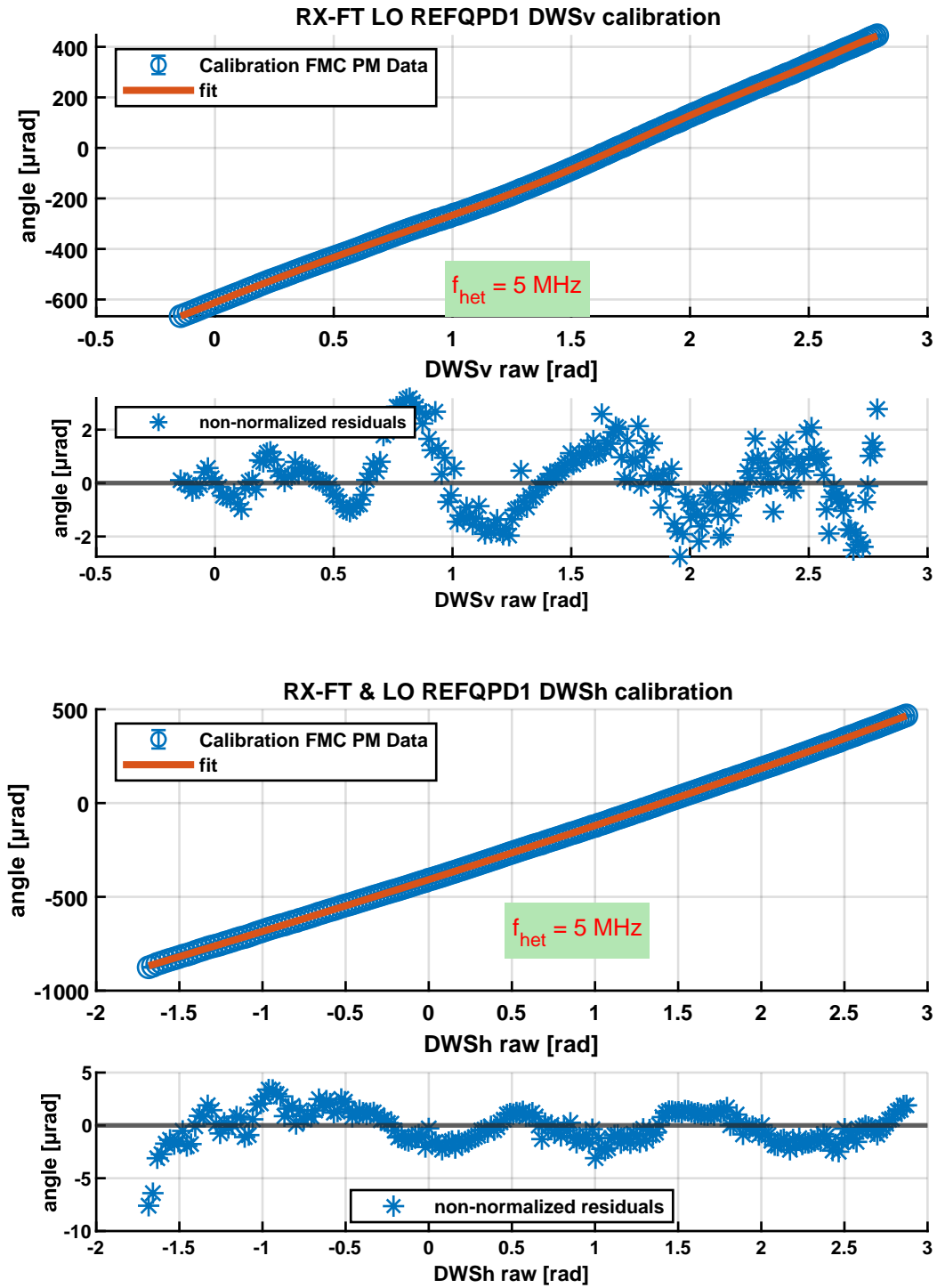


Figure 4.9: Resulting calibration of the RX-FT and LO beams DWS signal on REFQPD1. This calibration was realized using phase measurements from the FMC PM at a heterodyne frequency of 5 MHz. The measurement's fit is reported in Table 4.3.

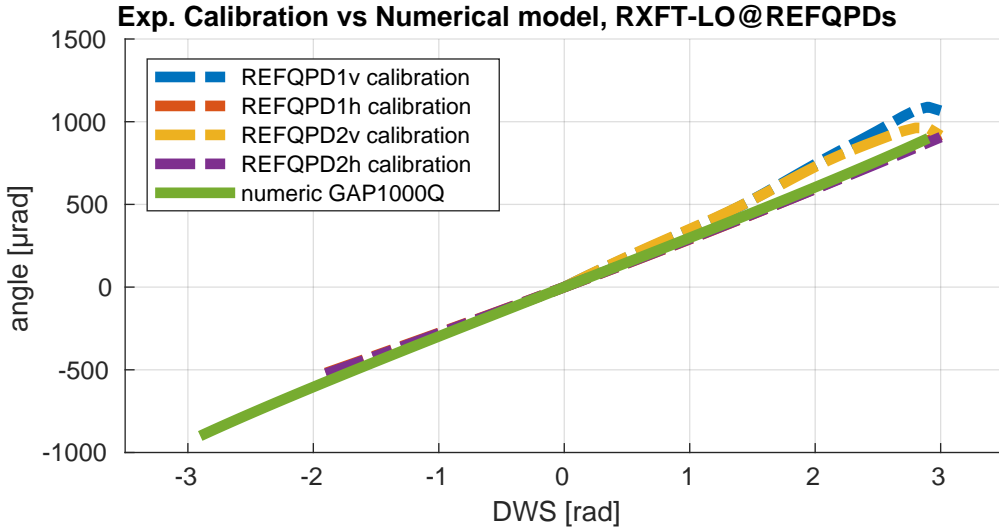


Figure 4.10: Comparison between the DWS-shifted RX-FT & LO DWS calibration of the REFQPDs and the DWS numeric model for the GAP1000Q QPD. Beam parameters are: $w_{\text{eff}} = 0.874\text{mm}^{-1}$, $R_{\text{rel}} = 6545$ mm and $\rho = 0.3446$.

Parameter	Value	±	Error
p_1	2.95	±	0.18
p_3	1.826	±	0.026
x_0	0	±	0.0004

Table 4.4: Fit of the numerically calculated calibration curve for the RX-FT and LO beams on a GAP1000Q shown in Figure 2.15 and reported in Figure 4.10. The fit function is $y(x) = p_1(x - x_0) + p_3(x - x_0)^3$. At a tilt angle of zero, the DWS gain is $\kappa_1 = 3390 \pm 2$ rad/rad.

4.4.1 Angle between the REFQPDs

As the REFQPD1 and REFQPD2 were glued by hand on the PEEK support, their orientation is limited by the skill of the operator to a $\sim 5^\circ$ precision. This means that the vertical and horizontal axes of the two QPDs are slightly tilted with respect to each other, and this limits the comparison of their DWS measurements. This can be corrected by comparing the DWS signals measured by REFQPD1 with the rotated DWS signals measured by REFQPD2. This can be done by stacking together in a vector the vertical and horizontal DWS measurements by REFQPD2 and applying a rotation matrix.

$$\begin{pmatrix} \text{DWS}'_{2,v} \\ \text{DWS}'_{2,h} \end{pmatrix} = \begin{pmatrix} \cos(\alpha) & -\sin(\alpha) \\ \sin(\alpha) & \cos(\alpha) \end{pmatrix} \begin{pmatrix} \text{DWS}_{2,v} \\ \text{DWS}_{2,h} \end{pmatrix} \quad (4.9)$$

The value of the angle can be obtained from a DWS calibration measurement calculating the quantity $\Upsilon^2(\alpha)$

$$\Upsilon^2(\alpha) = \sum_i \vec{V}_i \cdot \vec{V}_i \quad \vec{V}_i = \left[\begin{pmatrix} \text{DWS}_{1,v} \\ \text{DWS}_{1,h} \end{pmatrix}_i - R(\alpha) \begin{pmatrix} \text{DWS}_{2,v} \\ \text{DWS}_{2,h} \end{pmatrix}_i \right] \quad (4.10)$$

where the index i indicates each individual measurement point, and varying the angle α until a minimum is found. This procedure is reported in Figure 4.11, and

shows to reach a minimum very close to zero. The angle estimated by this procedure is $\alpha_{\text{REFQPD 1-2}} = -2.542^\circ \pm 0.05^\circ$. A comparison between the data of REFQPD1 and REFQPD2 before and after rotation is shown in Figure 4.11, right, and the overlap between REFQPD1 and rotated REFQPD2 is very good.

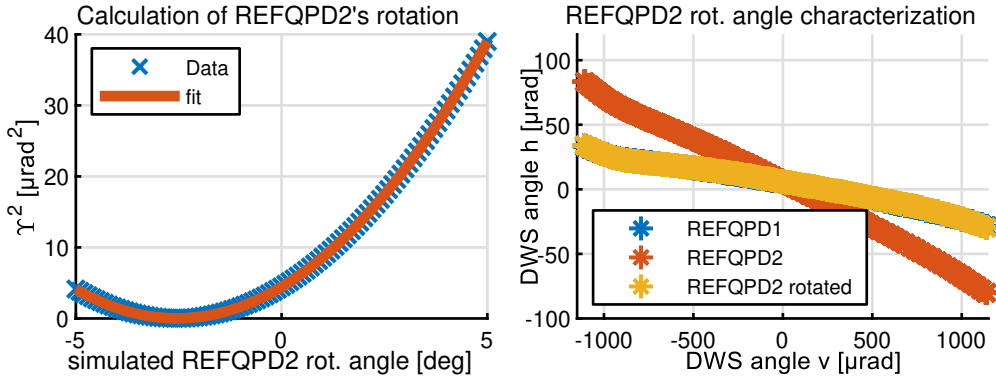


Figure 4.11: Left: minimization of $\chi^2(\alpha_{\text{REFQPD 1-2}})$. Right: Comparison between the DWS measurements by REFQPD1, REFQPD2 unrotated and the REFQPD2 rotated.

Parameter	Value	\pm	Error
p_0	0.035	\pm	0.013
x_0	-2.54	\pm	0.06
p_2	0.68	\pm	0.13

Table 4.5: Fitting parameters for the fit in Figure 4.11, left. The fitting function is $\chi^2(x) = p_0 + p_2(x - x_0)^2$.

This procedure has to be repeated every time the REFQPDs are unmounted, as the mounting operation is not reproducible. Variations are of the order of 2° .

4.4.2 Heterodyne efficiency as a function of the tilt angle, REFQPDs

This result is less relevant than the DWS calibration itself but is important to describe the beat note amplitude that the PM receives in case of beam tilt. Besides, one can get this characterization almosts 'for free', as this information can be extracted from the same data of the DWS calibration. As shown in Sub-subsection 2.3.3, another effect of the beam tilt is a reduction of the heterodyne efficiency $\sqrt{\eta_{\text{het}}}$ of the measured beat note. I estimated this effect by means of numerical integration in the case of the RX-GB & LO and RX-FT & LO beam interference on the REFQPDs. The result is as in the case of the DWS calibration, not precise but in good accordance with the derived model (see Figure 4.12). The fact that the curves don't peak at zero μrad but at a slightly positive angle is caused likely by a small lateral shift of one of the two beams (or a combination of the two).

The measured ξ is

- RX-GB & LO: $\xi_{\text{RX-GB \& LO, REFQPD}} = (6.32 \times 10^{-4} \pm 2 \times 10^{-6}) \mu\text{rad}^{-1}$, implying a beat note amplitude decreases by a factor of 10 for an angle of 2.38 mrad.
- RX-FT & LO: $\xi_{\text{RX-FT \& LO, REFQPD}} = (7.42 \times 10^{-4} \pm 5 \times 10^{-6}) \mu\text{rad}^{-1}$, implying a beat note amplitude decreases by a factor of 10 for an angle of 2.04 mrad.

The heterodyne efficiency of the individual QPD segments is expected to peak at different tilt angles, as shown in paragraph 2.3.3. This has not been characterized, as the expected value ($\pm 0.25 \mu\text{rad}$ from Table 2.1) is much smaller than the angular sensitivity reported in Table 4.6.

The angles at which the heterodyne efficiencies decrease by a factor of 10 are huge angles if compared to the maximum tilt which would happen during LISA's operation, which is of the order of 10 nrad [34]. It is important to keep this in mind as in Section 5.2 it will be shown that the phase noise of the PM depends on the input signal's amplitude. The decrease of the beat note's amplitude due to a tilt is one of the possible reasons of higher DWS noise in the case of beam tilts.

parameter	REFQPD1	REFQPD2	Simulated
a []	0.9954 ± 0.0011	0.9957 ± 0.0011	1
s [μrad]	1113 ± 4	1122 ± 4	978
x_0 [μrad]	36.95 ± 1.9	37.2 ± 1.9	0

Table 4.6: Fit parameters from Figure 4.12, top. The function used for the fit is $f(x) = a \exp\left(-\frac{1}{2} \left(\frac{x-x_0}{s}\right)^2\right)$. ξ can be derived as $\xi = \frac{1}{\sqrt{2}s}$.

parameter	REFQPD1	REFQPD2	
a []	1.005 ± 0.002	1.004 ± 0.002	1
s [μrad]	986.6 ± 6.4	972.5 ± 6.3	953.3
x_0 [μrad]	-527.0 ± 6.585	-519.5 ± 6.5	0

Table 4.7: Fit parameters from Figure 4.12, bottom. The function used for the fit is $f(x) = a \exp\left(-\frac{1}{2} \left(\frac{x-x_0}{s}\right)^2\right)$. ξ can be derived as $\xi = \frac{1}{\sqrt{2}s}$.

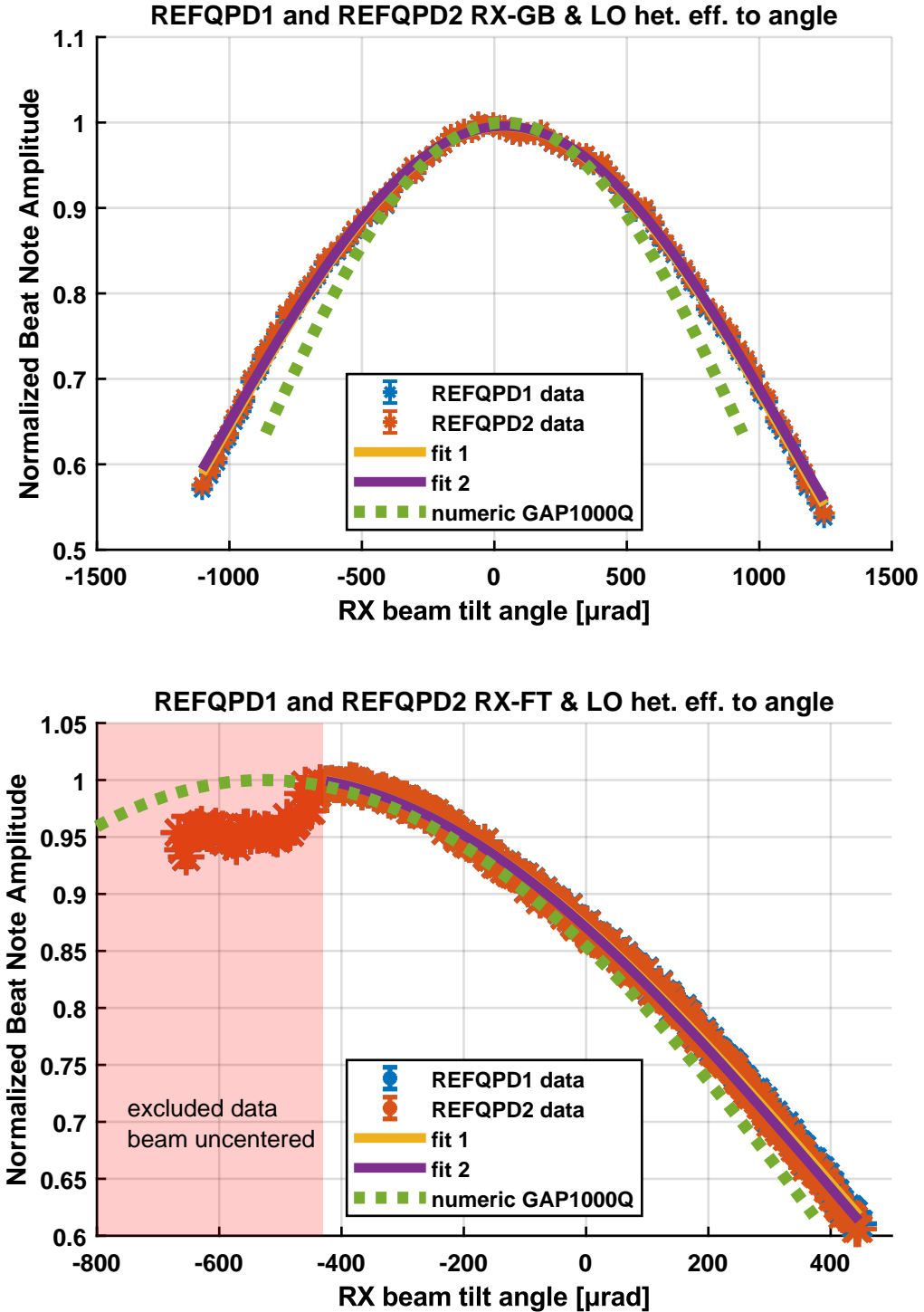


Figure 4.12: Measurement of the beat note's amplitude on the REFQPDs as a function of the RX beam's tilt angle for the RX-GB & LO (top) and RX-FT & LO (bottom) beams. The amplitude is calculated by averaging the amplitudes of the four segments and then normalized to the highest value. The decrease in the heterodyne efficiency can be fitted with a Gaussian curve. The obtained fit curve and parameters are reported in Tables 4.6 and 4.7, respectively.

4.5 DWS calibration of the SCIQPDs

The procedure in this section follows the one for the REFQPDs in Section 4.4. When the RX-GB beam rotates around the center of REFQPDs, it rotates, due to the imaging systems (ISs), also around the center of the SCIQPDs. Consequently, if it was possible to rotate the RX-FT beam around the center of the REFQPDs, this would be true also for the RX-FT beam. Due to the issue that the REFQPDs are insensitive to the DPS signal of the RX-FT beam, the RX-FT & LO beams' DWS signal was not calibrated.

Imaging System Characterization

Before entering into the details of the calibration, I report on the alignment and positioning precision of the ISs and SCIQPDs. The ISs works correctly only if both ISs and SCIQPDs are longitudinally placed at the proper distance from the RX-clip. If the positioning is wrong by a longitudinal mismatch Δz , as the RX beam is rotated, it would walk on the SCIQPDs. The beam-walk amplitude Δx is proportional both to the longitudinal mismatch and the tilt angle, or $\Delta x \propto \Delta z \cdot \varphi$. The imaging quality can be tested with the same data of the calibration by looking at the beam's position on the SCIQPDs as a function of the RX beam's tilt angle. The result is reported in Figure 4.13. The beam position on the SCIQPDs was fit with a first-order polynomial $f(x) = p_0 + p_1 x$, where p_0 is the initial beam offset and p_1 is the beam-walk coefficient. The measured coefficients are reported in Table 4.8 and 4.9, with the relevant p_1 coefficients marked in bold. The measured p_1 coefficients for the SCIQPDs for rotations around both axes are found to be comparable with those of REFQPD1, the sensor QPD used in-loop to rotate the RX beam around its center. This means that the measured beam walk is comparable to that on the in-loop QPD. Hence, I conclude that the imaging is working as good as possibly measurable.

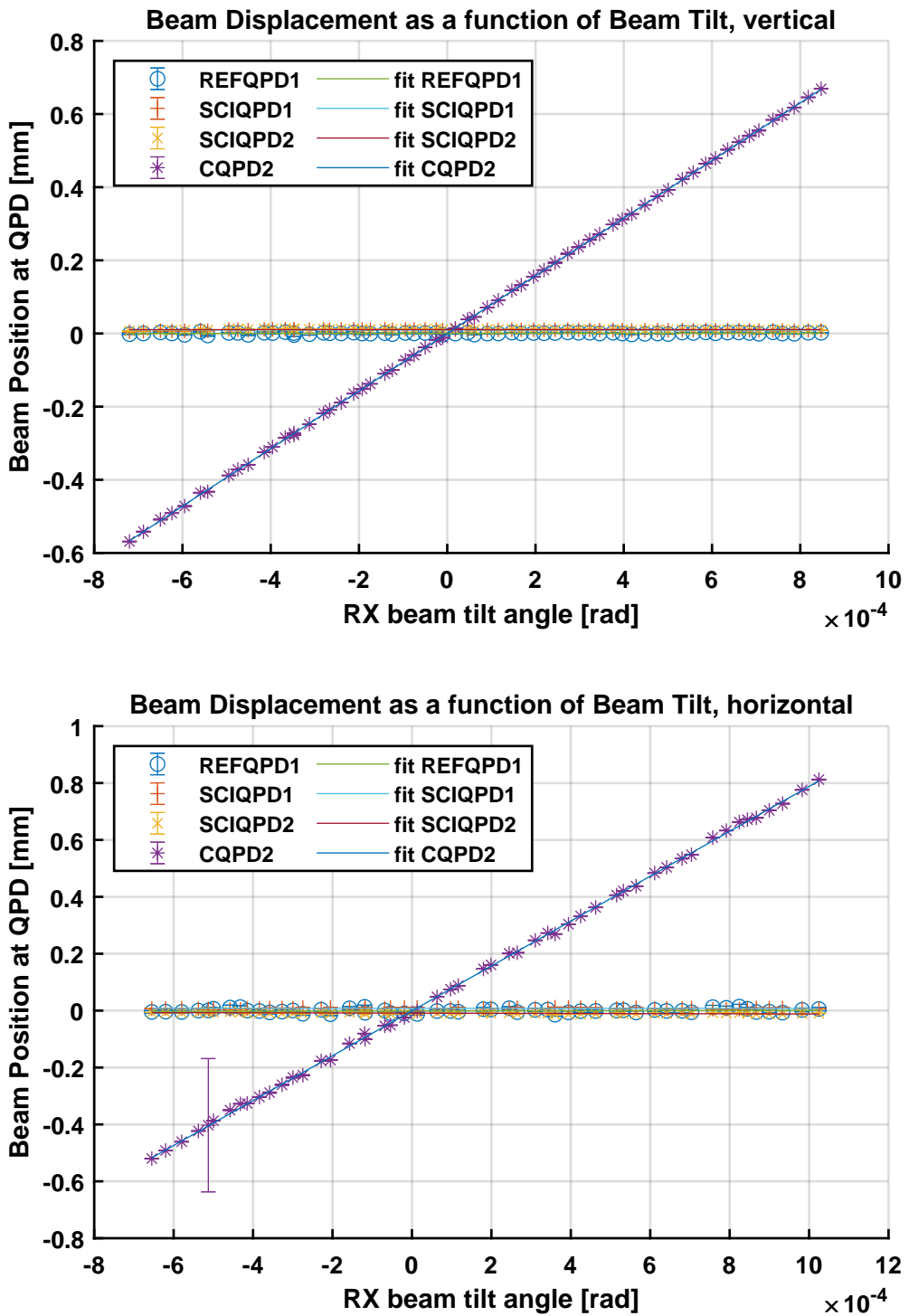


Figure 4.13: DPS measured lateral displacement on the QPDs as a function of the RX beam's tilt angle and first-order polynomial fit. The fit coefficients are reported in Tables 4.8 and 4.9.

QPD	p_0 [mm]			p_1 [mm/rad]		
REFQPD1	4.9×10^{-4}	±	1.2×10^{-4}	0.66	±	0.24
SCIQPD1	9.473×10^{-4}	±	3×10^{-6}	-0.341	±	0.006
SCIQPD2	1.0392×10^{-2}	±	3×10^{-6}	0.184	±	0.007
CQPD2	3.5×10^{-4}	±	7×10^{-5}	788	±	0.16

Table 4.8: Vertical fit parameters from Figure 4.13, top. The function used for the fit is $f(x) = p_0 + p_1 \cdot x$.

QPD	p_0 [mm]			p_1 [mm/rad]		
REFQPD1	-1.3×10^{-3}	±	7×10^{-4}	1.7	±	1.6
SCIQPD1	8.134×10^{-3}	±	5×10^{-6}	-0.073	±	0.008
SCIQPD2	-8.840×10^{-3}	±	5×10^{-6}	-2.87	±	0.01
CQPD2	-8×10^{-4}	±	1×10^{-4}	790.0	±	0.2

Table 4.9: Horizontal fit parameters from Figure 4.13, bottom. The function used for the fit is $f(x) = p_0 + p_1 \cdot x$.

RX-GB & LO DWS

The results of the DWS calibration of the SCIQPD1 are reported in Figures 4.14 and 4.15. The angles on the y -axis are magnified by the ISs, with magnification $m = 2.5$. Note that because of the specific interferometrical topology, the horizontal axis of SCIQPD1 QPDs is reversed.

Calibration	p_1 [$\mu\text{rad}/\text{rad}$]	p_3 [$\mu\text{rad}/\text{rad}^3$]	x_0 [rad]
REFQPD1 DWS _v	478.6 ± 3.3	13.0 ± 0.85	0.145 ± 0.003
REFQPD1 DWS _h	-501.2 ± 11.2	-10.2 ± 2.50	$+0.296 \pm 0.012$
REFQPD2 DWS _v	480.5 ± 3.3	12.5 ± 0.83	0.158 ± 0.003
REFQPD2 DWS _h	505.0 ± 11.2	9.76 ± 2.51	-0.271 ± 0.012

Table 4.10: Table with the calibration parameters of the RX-GB and LO beams DWS signals SCIQPD1 and SCIQPD2. The fitting function is $y(x) = p_1(x - x_0) + p_3(x - x_0)^3$. At a tilt angle of zero, the DWS gain is $\kappa_1 = 2030 \pm 25$ rad/rad. Taking into account the ISs, which have a magnification of $m = 2.5$, the total DWS gain is $\kappa_{1, \text{mag}} = 5075 \pm 63$ rad/rad.

A comparison between the numerical prediction and the measured curves is shown in Figure 4.16. The measured DWS κ_1 is $\sim 10\%$ higher than the predicted one. The overall DWS gain at null angle $\kappa_{1, \text{mag}}$ of the IS plus GAP1000Q for the SCIQPDs is almost twice as that of the REFQPDs. A quick consideration in Appendix E.3, which assumes QPD sizes are much larger than the beam sizes, shows that ISs effectively give no increase in the gain factor increase when measuring DWS, as the angular magnification given by the IS is factored out by the beam compression. The sensitivity, defined in equation (2.71), may increase. In the case of the REFQPDs and SCIQPDs, as the RX-GB and LO beams impinging on the REFQPDs are much larger than the QPD's size, the overall DWS gain at zero angle is 80% higher than that of the REFQPDs.

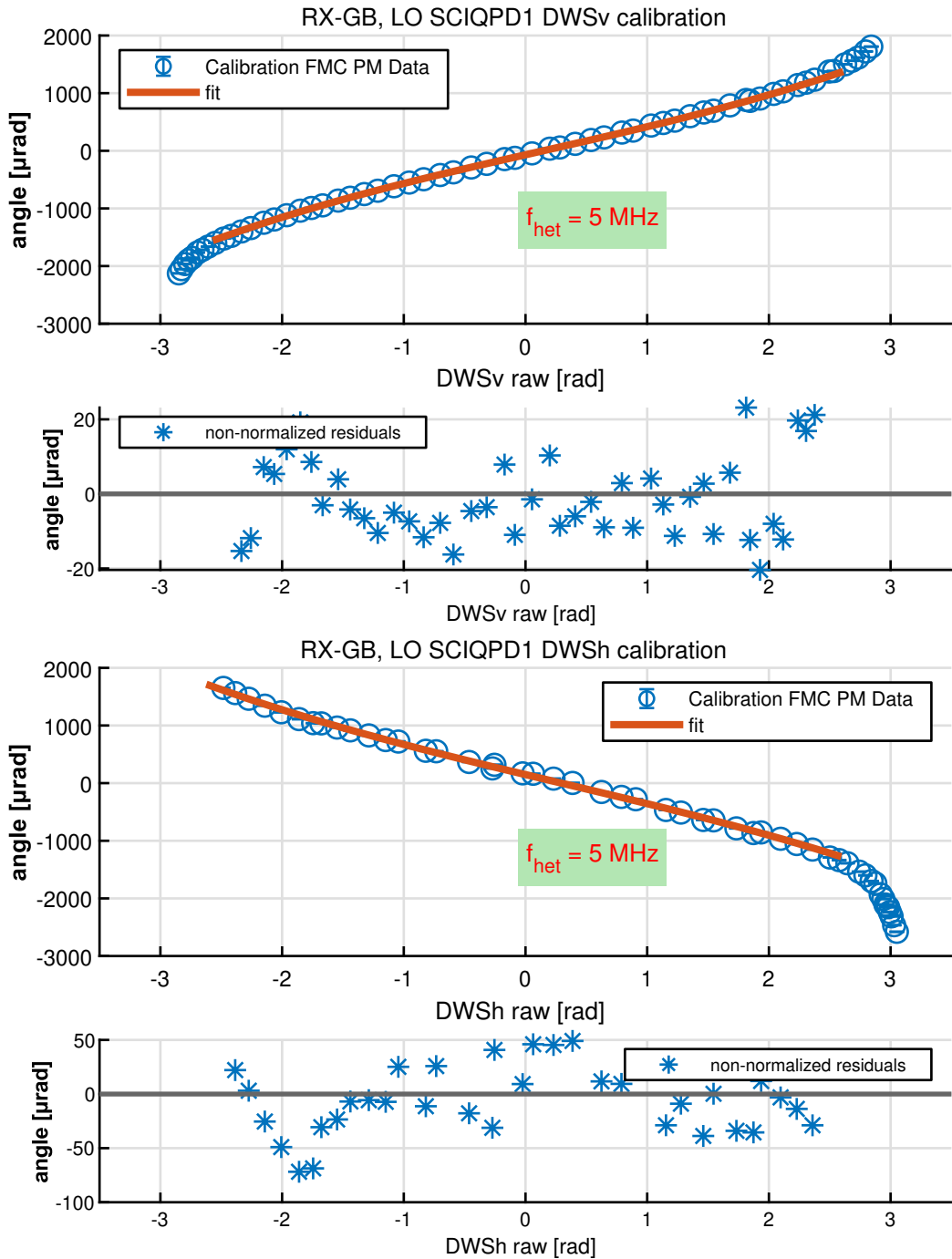


Figure 4.14: Resulting calibration of the RX-GB and LO beams DWS signal on SCIQPD1. This calibration was realized using phase measurements from the FMC PM at a heterodyne frequency of 5 MHz.

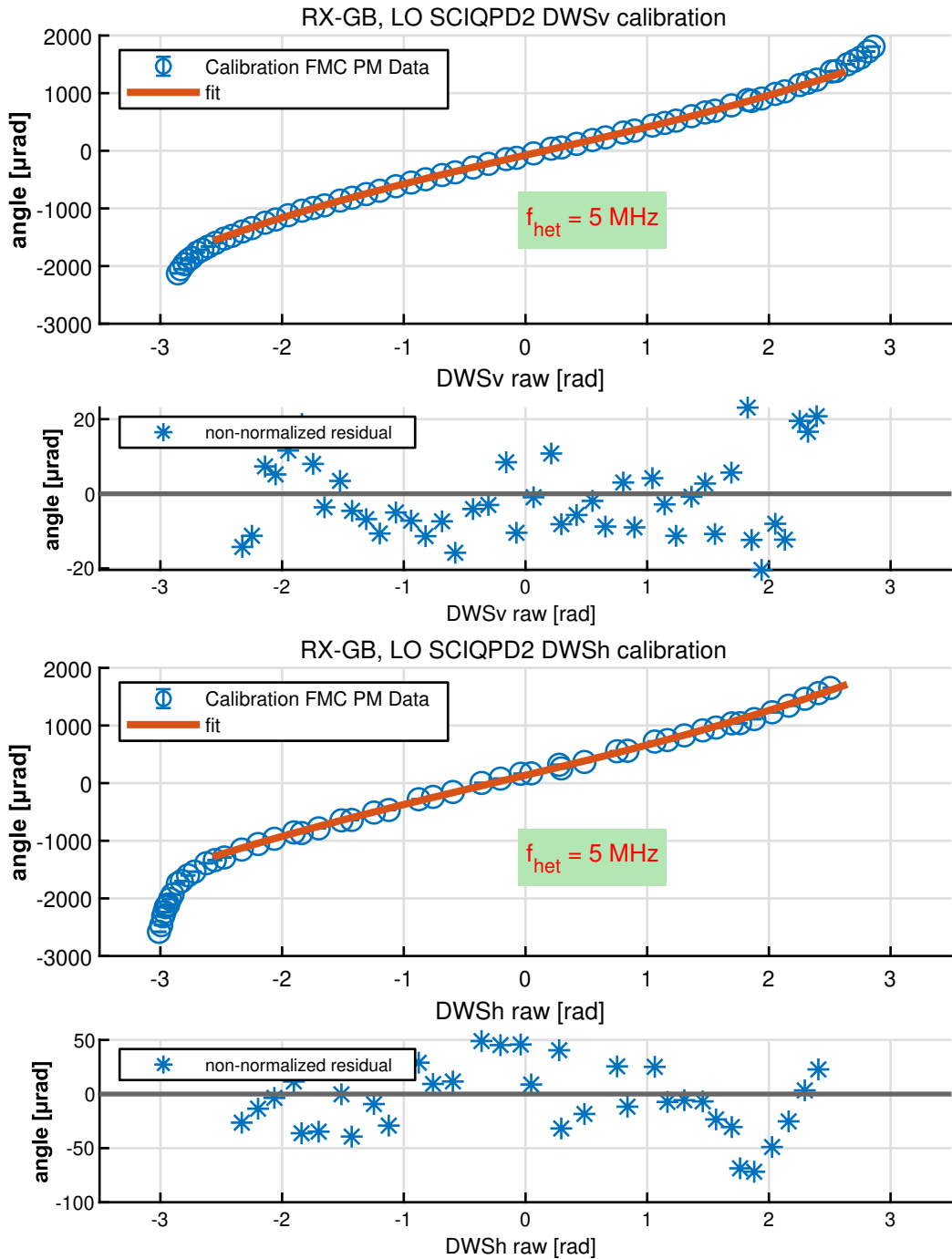


Figure 4.15: Resulting calibration of the RX-GB and LO beams DWS signal on SCIQPD2. This calibration was realized using phase measurements from the FMC PM at a heterodyne frequency of 5 MHz.

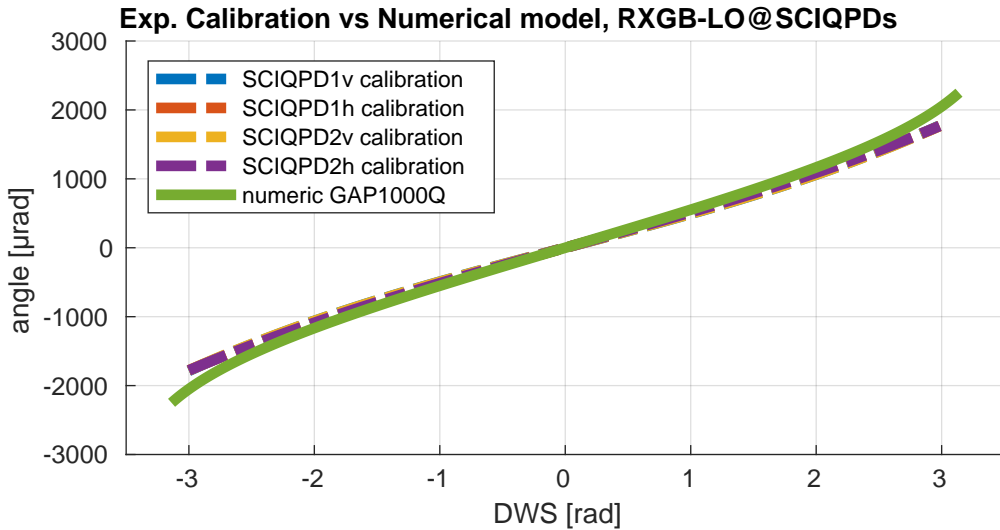


Figure 4.16: Comparison between the DWS-shifted RX-GB & LO DWS calibration of the SCIQPDs and the DWS numeric model. The measurements are in very good agreement with each other. Beam parameters are: $w_{\text{eff}} = 0.267\text{mm}^{-1}$, $R_{\text{rel}} = 1496\text{ mm}$ and $\rho = 0.141$.

4.5.1 Angle between the SCIQPDs

The angle between the SCIQPDs was characterized using the same method as for the REFQPDs (see Subsection 4.4.1). The resulting angle is $\alpha_{\text{SCIQPD 1-2}} = -6.157^\circ \pm 0.014^\circ$.

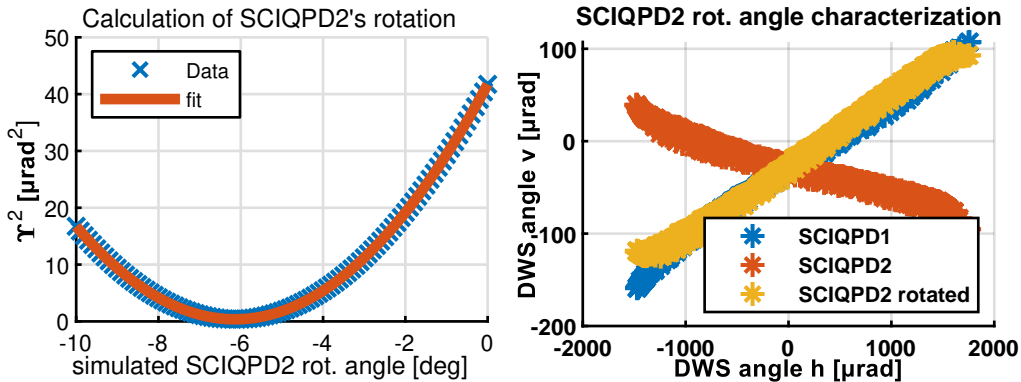


Figure 4.17: Left: characterization of the relative rotation angle between the QPDs by varying ξ^2 as a function of the rotation angle. Right: Comparison between the data measured by SCIQPD1, SCIQPD2 and the rotated SCIQPD2 data.

Parameter	Value	±	Error
p_0	0.441	±	0.002
x_0	-6.16	±	0.01
p_2	1.1	±	0.1

Table 4.11

4.5.2 Heterodyne efficiency as a function of the tilt angle, SCIQPDs

Heterodyne efficiency decrease was characterized using the same method as for the REFQPDs (see Subsection 4.4.2). The measured $\xi_{\text{RX-GB \& LO, SCIQPD}}$ is $\xi^2 = (5.20 \times 10^{-4} \pm 2.6 \times 10^{-5}) \mu\text{rad}^{-1}$, implying a beat note amplitude decreases by a factor of 10 for an angle of 2.9 mrad, again way more than what is expected to happen in LISA.

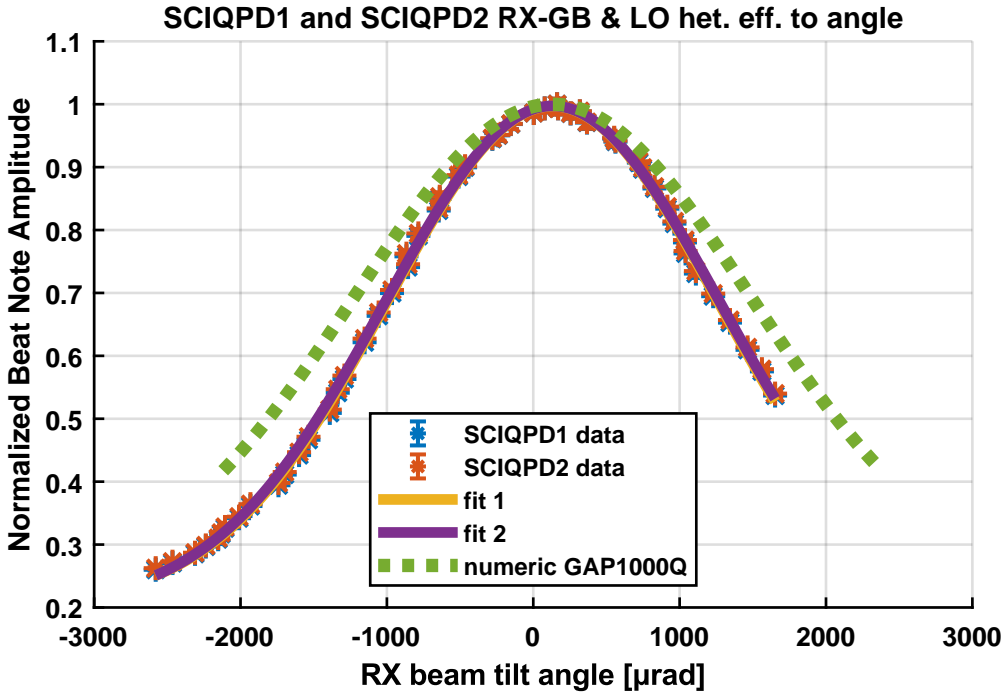


Figure 4.18: Measurement of the beat note’s amplitude on the SCIQPDs as a function of the RX beam’s tilt angle for the RX-GB & LO beams. The amplitude is calculated by averaging the amplitudes of the four segments and then normalized to the highest value. The decrease in the heterodyne efficiency can be fitted with a Gaussian curve. Fit parameters are in Table 4.12.

Parameter	SCIQPD1		SCIQPD2		Simulated
a []	1.38	\pm 0.12	1.4	\pm 0.13	1
s [μrad]	1356	\pm 69	1379	\pm 73	1542
x_0 [μrad]	38.3	\pm 1.6	38.5	\pm 1.6	132
z []	-0.39	\pm 0.12	-0.41	\pm 0.13	0

Table 4.12: Fit parameters from Figure 4.18. The function used for the fit is $f(x) = a \exp\left(-\frac{1}{2} \left(\frac{x-x_0}{s}\right)^2\right) + z$. The parameter ξ can be derived as $\xi = \frac{1}{\sqrt{2}s}$. This function provides an excellent fit, despite requiring an offset parameter. Further unexpected is that the estimated value of z is negative.

4.6 Conclusion

The DPS signals of the RX-GB and RX-FT beams were calibrated on all QPDs with the exception of CQP1, allowing to recover the displacement of the RX beams from the center of the QPD. This has allowed to calibrate the DWS signal of the RX and LO beams on the REFQPDs and SCIQPDs, by measuring the RX beams' angle using an optical lever. The resulting DWS calibrations have been compared to the analytical DWS model derived in Section 2.3.3, and were found to be roughly 10% off the predictions. As these predictions depend on many geometric parameters of the experiment which are known to similar precision, this result is satisfactory.

Chapter 5

LISA Requirements, Noise Hunting and Characterization

As already mentioned, the TDOBS experiment was operated during this thesis to test precision DWS sensitivity in LISA-like conditions, including beam tilts and misalignments. This chapter reports the noise goal, the efforts made in order to reduce the experimental noise as well as a characterization of the noise floor of the experiment.

5.1 Noise Requirements

5.1.1 Noise Requirements for LISA

The limiting noise sources in LISA are those shown in Figure 1.11. This Figure assumes that all avoidable technical noise sources have been reduced as far as possible. TTL is not listed in Figure 1.11, as it can be subtracted if measured accurately enough [58]. In order for the constellation to keep alignment and for the TTL subtraction in post-processing to work, the sensitivity of the angular measurements provided by DWS must fulfill specific requirements which have been estimated by the LISA team and collected by ESA; these are indicative allocated noise amounts that the mission can allow in order to reach its target sensitivity which keep changing as the mission's design proceeds. As of 2025, the last update on these requirements can be found in [29]. This thesis is interested in the requirements of the interferometric detection system (IDS) in terms of LPS and DWS, as well as in the requirements for the noise added by the PM during the phase measurement. IDS requirements are specific for each IFM and are relaxed at lower frequencies since the overall instrumental noise is limited by the TM's acceleration noise¹. This relaxation is expressed in terms of *noise shape functions*, one for LPS, $u_{\text{IDS}}(f)$, and one for DWS, $u_{\text{DWS}}(f)$.

$$u_{\text{IDS}}(f) = \sqrt{1 + \left(\frac{2 \text{ mHz}}{f}\right)^4} \quad u_{\text{DWS}}(f) = \sqrt{1 + \left(\frac{0.7 \text{ mHz}}{f}\right)^4} \quad (5.1)$$

The requirements on the LPS and DWS sensitivity are listed in Table 5.1 and are expressed at OB-level, i.e. they refer to the properties of the beams after the exit pupil of the telescope and before the entrance pupil of the ISs. In this frame,

¹see Figure 1.11.

5.1 Noise Requirements

the phase difference between beam pairs in an IFM shall be measured according to the LPS requirements in Table 5.1 and the tilt between the wavefront of two beams shall be measured according to the DWS requirements in Table 5.1.

DWS TMI	$5 \cdot u_{DWS} \text{ nrad}/\sqrt{\text{Hz}}$
DWS ISI	$30 \cdot u_{DWS} \text{ nrad}/\sqrt{\text{Hz}}$
LPS RFI	$2 \cdot u_{IDS} \text{ pm}/\sqrt{\text{Hz}}$
LPS TMI	$2.6 \cdot u_{IDS} \text{ pm}/\sqrt{\text{Hz}}$
LPS ISI	$9 \cdot u_{IDS} \text{ pm}/\sqrt{\text{Hz}}$

Table 5.1: OB-level LISA requirements $req_{DWS/LPS, \text{IFM}, \text{OB}}$ with $\text{IFM} \in (\text{ISI}, \text{TMI}, \text{RFI})$. Source: [29].

This requirement should be met in a specific angular tilt range of the RX or TX beam. For the ISI, the requirement should be achieved up to $405 \mu\text{rad}$ of RX beam off-pointing at OB-level [29]. For the TMI, the requirement on the TX beam's tilt range is still to be defined [29].

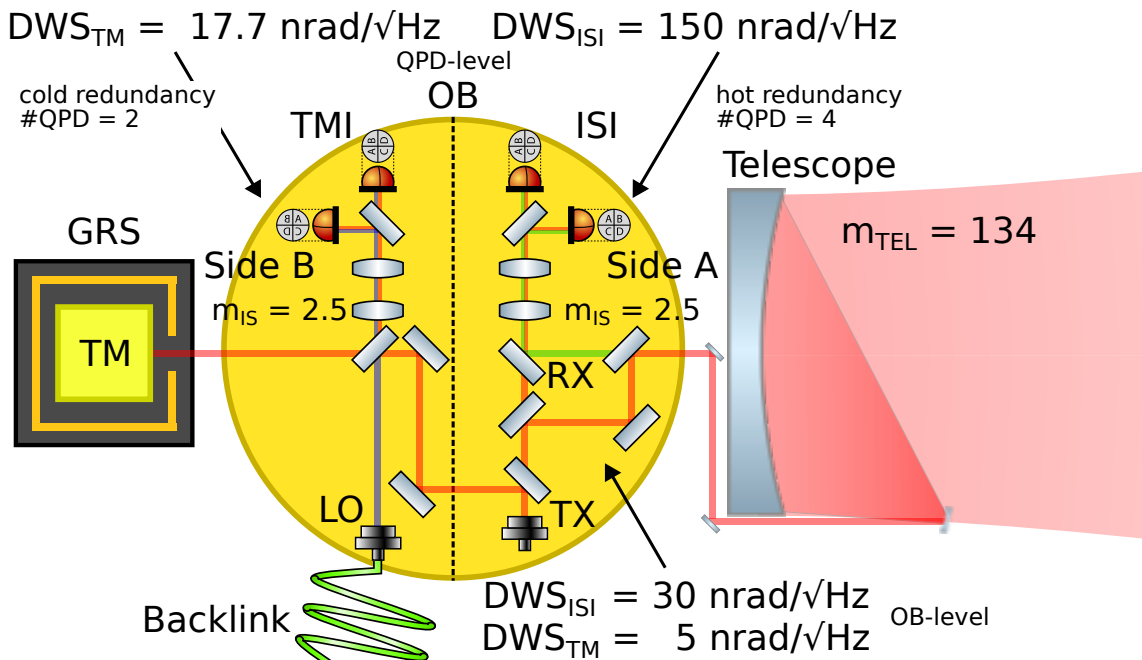


Figure 5.1: Simplified scheme of the OB in LISA with specification of where the requirements apply. Only two QPRs per IFM are shown instead of the nominal four.

Note that:

- At OB-level the RX beam has already propagated through the telescope, which has a magnification factor of $m_{tel} = 134$. Therefore the $30 \text{ nrad}/\sqrt{\text{Hz}}$ requirement at OB-level is a requirement of $0.22 \text{ nrad}/\sqrt{\text{Hz}}$ for rotations around the telescope in free space.
- If the TM tilts by an angle α , the TX beam reflecting on the TM tilts by twice that angle. Hence, the $5 \text{ nrad}/\sqrt{\text{Hz}}$ requirement at OB-level is a requirement of $2.5 \text{ nrad}/\sqrt{\text{Hz}}$ for TM rotations.

The values listed in Table 5.1 are more stringent than the requirements at QPD-level. As the beams propagates to each IFM they are split twice to implement redundant balanced detection [33]. The ISI is 'hot-redundant', i.e. using simultaneously $n_{\text{QPD, ISI}} = 4$ QPDs to maximize the signal-to-noise ratio (SNR), while the TMI and the RFI are 'cold-redundant', i.e. using simultaneously $n_{\text{QPD, TMI/RFI}} = 2$ QPDs and having the other two as for backup. As the power impinging on each QPD is one quarter of that of the initial beam and the main noise sources being shot noise and electronic noise at the TIA (see Table 5.2) [29, 30], splitting the beam lowers the C/N_0 of each segment's output by a factor of 2². The same C/N_0 as if there was no beam splitting can, in principle, be recovered by combining the four QPDs' measurements. This lowers the QPD-level requirement with respect to the OB-level requirement on DWS and LPS by a factor of $\sqrt{n_{\text{QPD, IFM}}}$ with $\text{IFM} \in (\text{ISI}, \text{TMI}, \text{RFI})$.

Noise source	ISI	TMI	RFI	units
Shot noise	1.22×10^{-4}	1.72×10^{-6}	9.82×10^{-7}	$\text{rad}/\sqrt{\text{Hz}}$
Electronic noise	6.02×10^{-5}	1.96×10^{-6}	1.93×10^{-6}	$\text{rad}/\sqrt{\text{Hz}}$
RIN	4.52×10^{-5}	3.90×10^{-7}	6.92×10^{-7}	$\text{rad}/\sqrt{\text{Hz}}$
Total per segment	1.43×10^{-4}	2.64×10^{-6}	2.27×10^{-6}	$\text{rad}/\sqrt{\text{Hz}}$
Total per QPD	8.15×10^{-5}	1.36×10^{-6}	1.28×10^{-6}	$\text{rad}/\sqrt{\text{Hz}}$
Total per IFM	3.46×10^{-5}	9.24×10^{-7}	7.71×10^{-7}	$\text{rad}/\sqrt{\text{Hz}}$

Table 5.2: Phase noise contributions in the IFMs in LISA per QPD segment and noise totals per segment, QPD and IFM. The estimation per QPD adds shot noise and electronic noise incoherently and RIN coherently, as it would happen for LPS; for DWS the RIN contribution would be strongly suppressed (see 2.1.5). The 'per IFM' estimation combines 4 QPDs for the ISI (hot redundant) and 4 QPDs for TMI and RFI (cold redundant) and suppresses RIN by a factor of 0.15 [33]. Values from [31].

The angles of the measurement beam at the QPDs for ISI and TMI are further magnified by the ISs. These have a magnification of $m_{\text{IS}} = 2.5$ [35], effectively increasing the sensitivity of the setup. The DWS and LPS requirements at QPD-level are hence

$$\text{req}_{\text{LPS, TMI, QPD}} = \sqrt{2} \cdot \text{req}_{\text{LPS, TMI, OB}} \quad (5.2)$$

$$\text{req}_{\text{LPS, ISI, QPD}} = \sqrt{4} \cdot \text{req}_{\text{LPS, ISI, OB}} \quad (5.3)$$

$$\text{req}_{\text{DWS, TMI, QPD}} = \sqrt{2} \cdot 2.5 \cdot \text{req}_{\text{DWS, TMI, OB}} \quad (5.4)$$

$$\text{req}_{\text{DWS, ISI, QPD}} = \sqrt{4} \cdot 2.5 \cdot \text{req}_{\text{DWS, ISI, OB}}. \quad (5.5)$$

The phase noise requirements at QPD-level associated with the DWS and LPS requirements can be derived from the knowledge of the wavelength λ and of the beam parameters at the QPD in each IFM of LISA.

The LPS case is straightforward. The LPS gain is $k = \frac{\lambda}{2\pi}$ and the phase requirements derived from LPS are

$$\text{req}_{\varphi-\text{LPS, IFM, QPD}} = \frac{1}{k} \text{req}_{\text{LPS, IFM, QPD}}. \quad (5.6)$$

²This statement is an approximation which neglects RIN as in the ISI and TMI RIN is smaller than the dominant noise source by at least a factor 5.

DWS TMI	$17.7 \cdot u_{\text{DWS}} \text{ nrad}/\sqrt{\text{Hz}}$
DWS ISI	$150 \cdot u_{\text{DWS}} \text{ nrad}/\sqrt{\text{Hz}}$
LPS RFI	$2.8 \cdot u_{\text{IDS}} \text{ pm}/\sqrt{\text{Hz}}$
LPS TMI	$3.7 \cdot u_{\text{IDS}} \text{ pm}/\sqrt{\text{Hz}}$
LPS ISI	$18 \cdot u_{\text{IDS}} \text{ pm}/\sqrt{\text{Hz}}$

Table 5.3: QPD-level LISA requirements $\text{req}_{\text{DWS/LPS, IFM, QPR}}$ with $\text{IFM} \in (\text{ISI}, \text{TMI}, \text{RFI})$.

Where $\text{IFM} \in (\text{ISI}, \text{TMI}, \text{RFI})$. The DWS case is more complex, as the DWS gains κ_1 , IFM depends on the beam parameters, which are not finalized yet. This is because they depend on the design of the ISs, which, as mentioned, is not yet fixed. The current status is:

- The Gaussian beam's (hence the TX and LO) parameters lie in the range $0.34 \text{ mm} < w_0 < 0.46 \text{ mm}$ and $|z_0| < 160 \text{ mm}$, with $z_0 = 0 \text{ mm}$ indicating the position of the QPD. The two beams can be considered independent. This information was provided by Ewan Fitzsimons.
- The RX beam consists of a 30 cm diameter clipped flat-top beam compressed first by the telescope ($m_{\text{tel}} = 134$) and then by the ISs with $m_{\text{IS}} = 2.5$. Both telescope and the ISs can be considered ISs of the type in equation (E.9), which compresses the beam diameter by a factor of m_{IS} and the wavefront curvature by a factor of $1/m_{\text{IS}}^2$. At the surface of the QPDs the RX beam is hence a flat wavefront with a uniform intensity profile with a diameter of $\sim 0.89 \text{ mm}$. For the purpose of the following calculations, the RX beam is parametrized as $w_{\text{RX}}, R_{\text{RX}} = \infty$.
- The QPD's diameter is 1.5 mm [54].

From this information, a range of κ_1 values can be estimated for both the TMI and the ISI. I carried out this analysis assuming no relation between the two beams' parameters. Equation (2.137) helps to break down this range into the best- and the worst-case scenarios. κ_1 depends mainly on the effective beam spot size at the QPD w_{eff} , while ρ ³ gives a fine adjustment. The maximum value of $F(\rho)$ is $F(\rho) = 1$ and occurs if the radii of curvature are the same, while the minimum of $F(\rho)$ occurs when the radii of curvature of the beams are equal, smallest and have opposite sign. From equation (2.137) one can see that

- the best-case scenario is when, at the QPD, the beam spot sizes are the largest and the two radii of curvature are equal in magnitude and with the same signs.
- the worst-case scenario is when, at the QPD, the beam spot sizes are minimum and the two radii of curvature are equal, smallest and with opposite sign.

The values of κ_1 for the best-case and worst-case scenarios were calculated using the method reported in Sub-subsection 2.3.3. As in LISA the beam size is smaller

³The parameter ρ is introduced in Section 2.3.3 and represents the effective-waist-normalized wavefront mismatch, or relative wavefront-mismatch.

than the QPD's size, the approximation to an infinite QPD roughly holds, giving the values $\kappa_{1,\infty}$, $\kappa_{3,\infty}$. The values for a finite size QPD are also calculated using the numerical results in Figures 2.11 and 2.12, and are indicated with $\kappa_{1,\circ}$, $\kappa_{3,\circ}$. The values calculated with a full numerical integration are indicated as $\kappa_{1,\#}$, $\kappa_{3,\#}$. The resulting $\kappa_{1,3}$ coefficients are listed in Table 5.4.

Parameter	Unit	TMI		ISI	
		best	worst	best	worst
w_{eff}	mm	0.336	0.240	0.475	0.34
$ R_{\text{rel}} $	mm	444	∞	888	∞
$ \rho $	-	0	0.38	0	0.38
$ 1 - F(\rho) $	-	0	0.024	0	0.024
$\kappa_{1,\infty}$	rad/rad	2237	1601	3139	2265
$\kappa_{3,\infty}$	rad/rad ³	-2.00×10^8	-7.35×10^7	-5.27×10^8	-2.08×10^8
$\kappa_{1,\circ}$	rad/rad	2129	1577	2789	2152
$\kappa_{3,\circ}$	rad/rad ³	-1.85×10^8	-7.27×10^7	-3.78×10^7	-1.9×10^8
$\kappa_{1,\#}$	rad/rad	2268	1595	2842	2228
$\kappa_{3,\#}$	rad/rad ³	-1.56×10^8	-5.49×10^7	-2.09×10^8	-1.56×10^8

Table 5.4: κ_1 and κ_3 coefficients calculated in the best and worst scenario for a) an infinite QPD using equations (2.140, 2.141) and (denoted by ∞), b) for a finite QPD with the semianalytical model in Figures 2.11 and 2.12 (denoted by \circ) and c) for a finite QPD using numerical integration (denoted by $\#$). The table also reports the values of the beam parameters. The respective numerical simulations are shown in Figure 5.2.

Despite it not being the worst-case scenario for the DWS gain, the maximum possible value of $|\rho|$ for both the ISI and the TMI for the given beam parameters is $|\rho| = 0.469$. This is a considerably high value, which has a non negligible impact regarding in the light of the considerations in Figure 2.21. A high value of $|\rho|$ cause a significant shift of the tilt angle at which a QPD segment has its maximum heterodyne efficiency.

The conversion from the LISA DWS requirement to the phase requirement for the DWS signals can be conservatively carried out using the worst-case scenario coefficient $\kappa_{1, \text{IFM, worst}}$ with $\text{IFM} \in (\text{ISI}, \text{TMI})$.

$$\text{req}_{\varphi\text{-DWS, IFM, QPD}} = \kappa_{1, \text{IFM, worst}} \text{req}_{\text{DWS, IFM, QPD}} \quad (5.7)$$

The resulting phase requirements are listed in Table 5.5.

phase DWS TMI	$2.96 \times 10^{-5} \cdot u_{\text{DWS}} \text{ rad}/\sqrt{\text{Hz}}$
phase DWS ISI	$3.42 \times 10^{-4} \cdot u_{\text{DWS}} \text{ rad}/\sqrt{\text{Hz}}$
phase LPS RFI	$1.67 \times 10^{-5} u_{\text{IDS}} \text{ rad}/\sqrt{\text{Hz}}$
phase LPS TMI	$2.17 \times 10^{-5} u_{\text{IDS}} \text{ rad}/\sqrt{\text{Hz}}$
phase LPS ISI	$1.06 \times 10^{-4} u_{\text{IDS}} \text{ rad}/\sqrt{\text{Hz}}$

Table 5.5: QPD-level phase requirements for LISA.

Both LPS and DWS are derived from the combination of the phase measurements from the four segments of a QPD. Assuming that all segments are affected by the

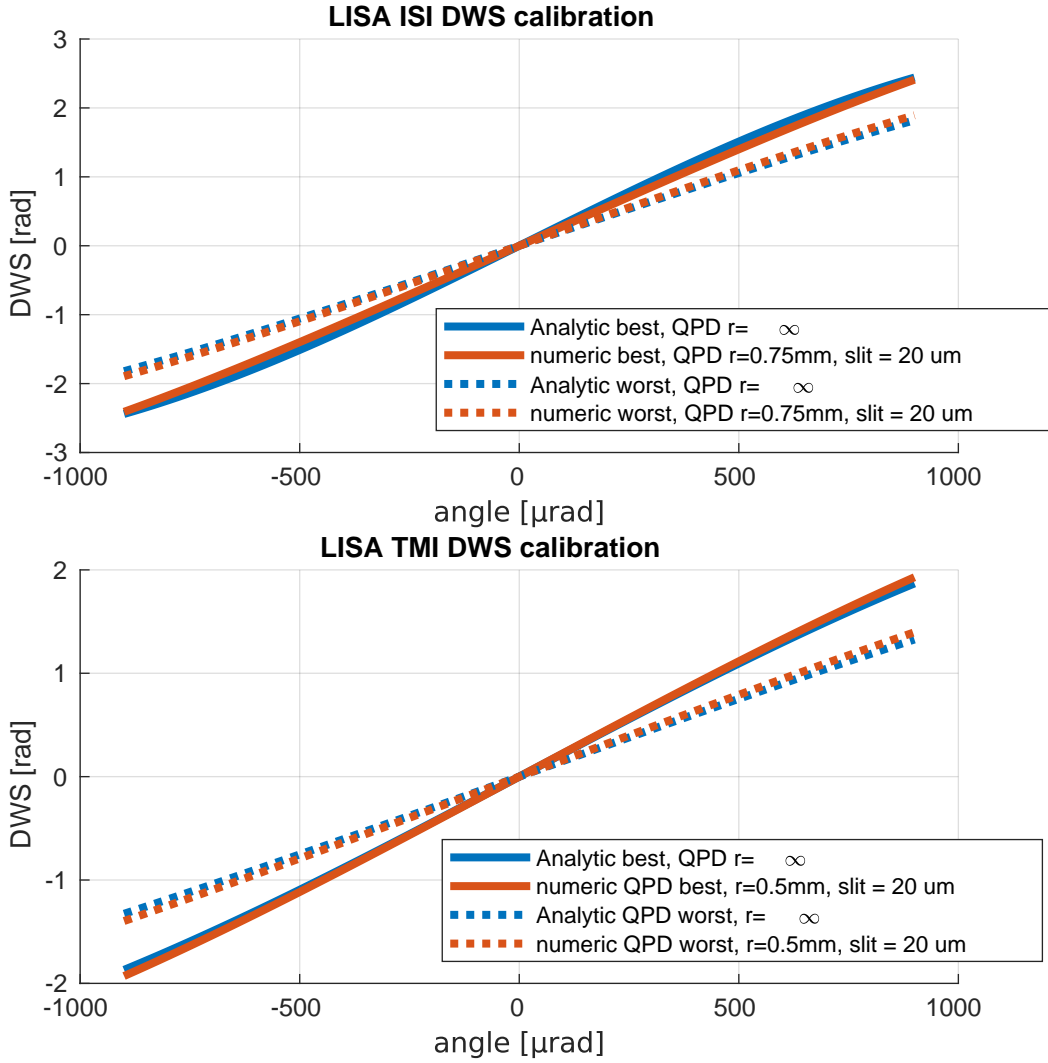


Figure 5.2: Best- and worst-case scenario DWS curves in the ISI (top) and TMI (bottom).

same phase noise level $\tilde{\varphi}_{\text{seg}}$ and that these phase noises are uncorrelated as they are dominated by shot and electronic noise (see Table 5.2). Hence

$$\tilde{\varphi}_{\text{QPD,LPS}} = \frac{1}{4} 2 \cdot \tilde{\varphi}_{\text{seg}} = \frac{1}{2} \tilde{\varphi}_{\text{seg}} \quad (5.8)$$

$$\tilde{\varphi}_{\text{QPD,DWS}} = \frac{1}{2} 2 \cdot \tilde{\varphi}_{\text{seg}} = \tilde{\varphi}_{\text{seg}}. \quad (5.9)$$

$$(5.10)$$

Table 5.6 lists the phase requirements at QPD segment level. Note that the DWS requirement for the TMI is the most stringent.

From here onwards, the most stringent requirement will be shown on plots if reached, while more than one requirement will be shown if the most stringent one is not met.

5.1.2 Noise Requirement on the Phasemeter

In LISA, the PM extracts the phase signal from the beat note measured in each QPD segment. The beat note itself has an associated C/N_0 , typically expressed in dB/Hz

5.1 Noise Requirements

phase DWS TMI	$4.17 \times 10^{-5} u_{\text{DWS}} \text{ rad}/\sqrt{\text{Hz}}$
phase DWS ISI	$3.42 \times 10^{-4} u_{\text{DWS}} \text{ rad}/\sqrt{\text{Hz}}$
phase LPS RFI	$3.34 \times 10^{-5} u_{\text{IDS}} \text{ rad}/\sqrt{\text{Hz}}$
phase LPS TMI	$4.34 \times 10^{-5} u_{\text{IDS}} \text{ rad}/\sqrt{\text{Hz}}$
phase LPS ISI	$2.12 \times 10^{-4} u_{\text{IDS}} \text{ rad}/\sqrt{\text{Hz}}$

Table 5.6: QPD segment level phase requirements for LISA.

or $\text{rad}/\sqrt{\text{Hz}}$. This is mainly due to mostly shot noise and electronic noise, which are the limiting noise to the sensitivity of LISA. While extracting the phase of the beat note, the PM is required to add no further noise beyond a specific threshold. This threshold is made to depend on the C/N_0 of the input beat note, as the PM's performance depends on it, and is defined in terms of additive phase noise to the LPS signal in case of the RFI and phase noise to DWS and LPS for RFI and ISI. As expressed, the requirement is not dependent on the amplitude of the signal to the PM. The requirements are reported in Table 5.7.

RFI	$8.9 \times 10^{-6} u_{\text{IDS}} \text{ rad}/\sqrt{\text{Hz}}$	$4.46 \mu\text{rad}/\sqrt{\text{Hz}}$	107 dBHz
TMI	$8.9 \times 10^{-6} u_{\text{IDS/DWS}} \text{ rad}/\sqrt{\text{Hz}}$	$5.62 \mu\text{rad}/\sqrt{\text{Hz}}$	105 dBHz
ISI	$2.36 \times 10^{-5} u_{\text{IDS/DWS}} \text{ rad}/\sqrt{\text{Hz}}$	$178 \mu\text{rad}/\sqrt{\text{Hz}}$	75 dBHz

Table 5.7: Phase readout requirements for the PM in LISA. Source: [23]

5.1.3 Noise Requirements for TDOBS

TDOBS aims to demonstrate that the performance planned for LISA in terms of DWS (and to a lesser extent LPS) can be reached, while simultaneously testing instrumental pre-developments of the PM. To meet LISA's requirements, TDOBS has to either reach the LPS phase performance in Table 5.3 or meet the equivalent phase requirements in Table 5.5. The angular DWS requirements have to be adjusted for the different beam and QPD sizes of TDOBS using the DWS calibration parameters measured in Chapter 4 and equation (5.11). This gives the LISA equivalent DWS requirement for TDOBS. The resulting values are reported in Table 5.8.

$$\text{req}_{\text{DWS, QPD, TDOBS, IFM}} = \frac{\kappa_{1, \text{TDOBS}}}{\kappa_{1, \text{, IFM, , worst, LISA}}} \text{req}_{\text{DWS, IFM, QPD}} \quad (5.11)$$

with $\text{IFM} \in (\text{ISI, TMI})$.

DWS TMI	$14.7 \cdot u_{\text{DWS}} \text{ nrad}/\sqrt{\text{Hz}}$
DWS ISI	$101 \cdot u_{\text{DWS}} \text{ nrad}/\sqrt{\text{Hz}}$
LPS RFI	$2.8 \cdot u_{\text{IDS}} \text{ pm}/\sqrt{\text{Hz}}$
LPS TMI	$3.7 \cdot u_{\text{IDS}} \text{ pm}/\sqrt{\text{Hz}}$
LPS ISI	$18 \cdot u_{\text{IDS}} \text{ pm}/\sqrt{\text{Hz}}$

Table 5.8: QPD-level TDOBS requirements $\text{req}_{i, \text{QPD, TDOBS}}$, $i \in (\text{DWS, LPS})$.

The performance at OB-level which would descend from this cannot be directly verified as a set of 4 QPRs in optical copies is not available. TDOBS can instead verify the performance at QPD-level, always under the assumption that the phase noise is uncorrelated among quadrants and QPDs.



Figure 5.3: Scheme of the comparison principle between LISA's DWS measurements and TDOBS's DWS measurements.

5.2 TDOBS: DWS and LPS noise budget

This section lists the noise sources which are known to be present in TDOBS. A detailed description is given of the characterized noise sources, and in the end follows a noise budget of the experiment.

The noises can be categorized in two groups: the C/N_0 -dependent and independent noises. The first category changes the noise density if, for instance, the power of a laser beam is reduced, while the latter does not. A scheme of the measurement chain in TDOBS, including a list of noises at their input stage, is shown in Figure 5.4. These noises have different causes (and units) depending on the particular stage of the measurement chain at which they enter the signal. The induced phase noise is calculated using equation (2.71), which compares the noise's ASD to the RMS amplitude of the signal at the PM's input. Alternatively, the noise can be converted to equivalent noise at some reference stage of the chain, e.g. the laser beam stage. The conversion factors between stages of the measurement chain are listed in the equations (5.14, 5.15). The involved parameters are the laser's wavelength λ via $k = \frac{2\pi}{\lambda}$, the used beam's powers $P_{1,2}$, the heterodyne efficiency $\sqrt{\eta_{het}}$, the PD's responsivity $A = 0.6 \text{ A/W}$ and the TIA's gain R_F .

$$\frac{d\varphi}{ds} = \frac{1}{k} [\text{m}] \quad (5.12)$$

$$\frac{dP}{d\varphi} = 2\sqrt{\eta_{het}} P_1 P_2 [\text{W}] \quad (5.13)$$

$$\frac{di}{dP} = A [\text{A/W}] \quad (5.14)$$

$$\frac{dV}{di} = R_F [\Omega] \quad (5.15)$$

After the conversion of each noise contribution into power noise contribution, the phase noise can be computed using the inverse C/N in equation (2.71). The obtained noises amounts refer to the noise on a single segment of a QPD and don't yet take into account any noise mitigation due to common mode subtraction.

This procedure leads to calculating the noise contribution to one specific signal, as e.g. the beat note output of QPD segment. Partial cancellation of some noise contributions might occur when combining the individual beat notes' phases in post-processing, as in DWS. This aspect is also discussed within the current section.

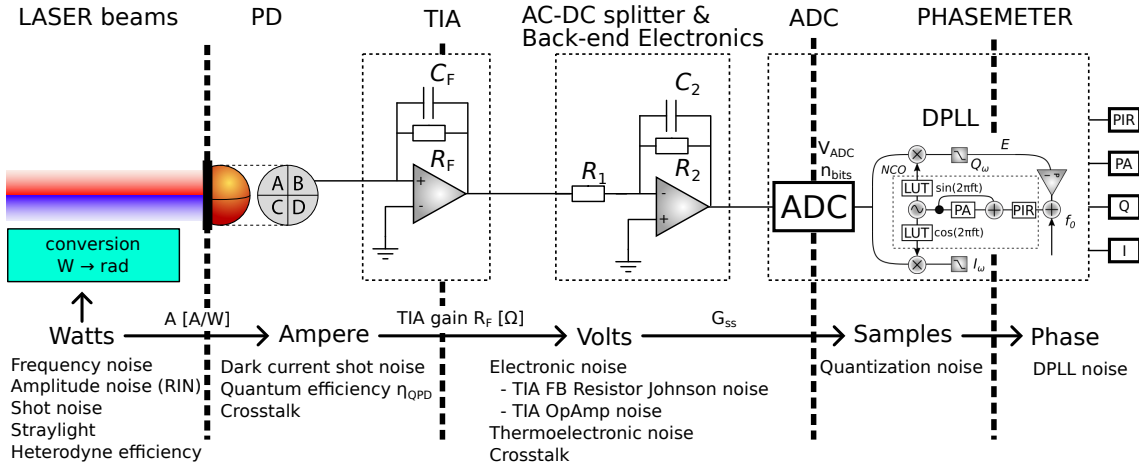


Figure 5.4: Scheme of TDOBS's one-channel measurement chain, with the stage to stage conversion coefficients and the noise contributions entering each step.

5.2.1 Carrier-to-Noise density ratio-dependent phase noises

The C/N_0 -dependent phase noises are, in general, noises of fixed ASD entering a system. When compared to the local signal strength by equation (2.71), their phase noise contribution decreases if the signal's RMS amplitude is increased. These are shot noise (2.82), electronic noise from the TIA (3.5), current shot noise due to the dark current of the PD and quantization noise from the ADC. The last two were not mentioned so far, and their value can be found using equations (5.16, 5.17).

$$\tilde{i}_{\text{dark}} = \sqrt{2q i_{\text{dark}}} \quad \text{A}/\sqrt{\text{Hz}} \quad (5.16)$$

$$\tilde{V}_{\text{ADC}} = \frac{V_{\text{ADC}} 2^{-n_b}}{\sqrt{6 f_s}} \quad \text{V}/\sqrt{\text{Hz}} \quad (5.17)$$

These depend on the dark current of the PD i_{dark} , on the sampling frequency f_s , on the range V_{ADC} , and on the number of bits n_b of the ADC. Typical values for the dark current of a PD are of the order of nA (see Table 3.3). The values for the ADC in the FMC PM are $n_b = 11.7^4$, $V_{\text{ADC}} = 2\text{V}$ and $f_s = 80\text{MHz}$. The phase noise contribution of these two noises, together with those of the previously mentioned

⁴The effective number of bits is used, accounting for additional noise and distortion from the ADC itself.

noise sources in the Subsections 2.1.5 and 3.3.2 are

$$\tilde{\varphi}_{\text{shot}} = \sqrt{\frac{(\bar{P}_1 + \bar{P}_2)h\nu_l}{\eta_{\text{QPD}}\eta_{\text{het}}\bar{P}_1\bar{P}_2}} \quad \text{rad}/\sqrt{\text{Hz}} \quad (2.82)$$

$$\tilde{\varphi}_{i_{\text{dark}}} = \frac{1}{A\sqrt{\eta_{\text{het}}\bar{P}_1\bar{P}_2}}\sqrt{q i_{\text{dark}}} \quad \text{rad}/\sqrt{\text{Hz}} \quad (5.18)$$

$$\tilde{\varphi}_{\text{en}}(f) = \frac{1}{A\sqrt{2\eta_{\text{het}}\bar{P}_1\bar{P}_2}}\sqrt{\frac{4k_B T}{R_F} + \tilde{i}_{\text{ACE}}^2 + (2\pi f(C_{\text{PD}} + C_{\text{ACE}})\tilde{e}_{\text{ACE}})^2} \quad \text{rad}/\sqrt{\text{Hz}} \quad (5.19)$$

$$\tilde{\varphi}_{\text{ADC}} = \frac{1}{G_{\text{ss}}R_FA\sqrt{2\eta_{\text{het}}\bar{P}_1\bar{P}_2}}\frac{V_{\text{ADC}}2^{-n_b}}{\sqrt{6f_s}} \quad \text{rad}/\sqrt{\text{Hz}}, \quad (5.20)$$

where $G_{\text{ss}} = [2.87, 28.7, 57.4]$ V/V is the AC gain of the AC-DC splitter, which acts as second stage amplifier. This value can be varied as mentioned in Subsection 3.3.3.

5.2.2 Carrier-to-Noise density ratio-independent phase noises

The C/N₀-independent phase noises are, in general, additive phase noises or multiplicative noises of the signal. Frequency noise and thermoelectronic phase noise in the electronics belong to this first group. Straylight⁵ and cross coupling between signals with the same amplitude, as in a QPR, belong to the second group.

Optical noises

Laser Frequency noise and 2f-RIN are power-independent as the first is direct phase noise and the latter is multiplicative. 1f-RIN depends only on the power ratio between the two beams and not on the absolute power, and therefore is placed in this category.

$$\tilde{\varphi}_{1f\text{-RIN}} = \frac{\bar{P}_1\tilde{r}_1(1f_{\text{het}}) + / \boxplus \bar{P}_2\tilde{r}_2(1f_{\text{het}})}{\sqrt{2\eta_{\text{het}}\bar{P}_1\bar{P}_2}} \quad \text{rad}/\sqrt{\text{Hz}} \quad (2.73)$$

$$\tilde{\varphi}_{2f\text{-RIN}} = \frac{\tilde{r}_1 + / \boxplus \tilde{r}_2}{2\sqrt{2}} \quad \text{rad}/\sqrt{\text{Hz}} \quad (2.74)$$

$$\tilde{\varphi}_{\text{freq}} = 2\pi \frac{\Delta s}{c} \tilde{\nu} \quad \text{rad}/\sqrt{\text{Hz}} \quad (2.77)$$

As previously, the simple sum is to be used for correlated RIN, while \boxplus indicates the squared sum and is to be used in for uncorrelated RIN.

The relative power fluctuations were characterized in TDOBS, and the result is shown in Figure 5.5. Partial cancellation of RIN in DWS measurements or in general when using a reference interferometer was already discussed in Subsection 2.1.5. This is also the case for DWS, where the phase measurements of four segments

⁵This is true in the case only two beams are used.

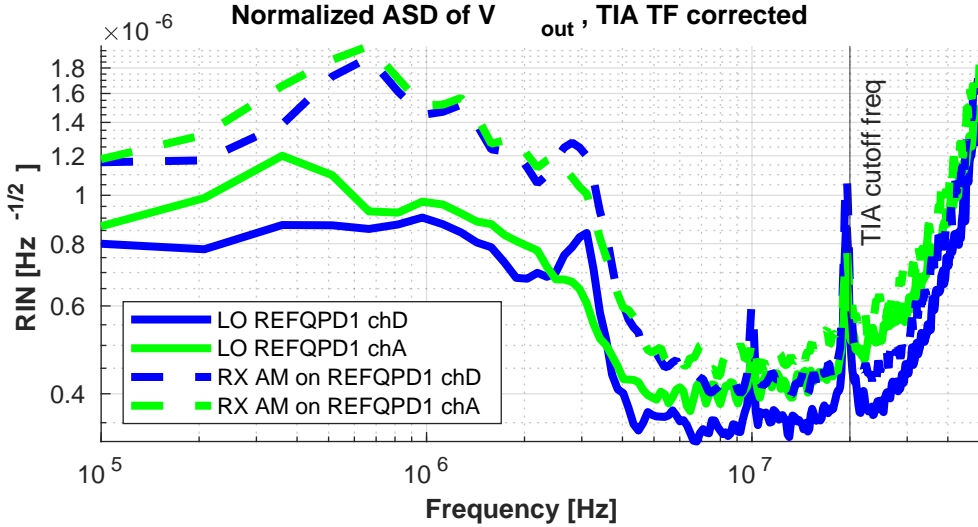


Figure 5.5: Measured RIN in TDOBS. Both RX and LO beams originate from the same laser source and are propagated through two different AOMs and fibers. This measurement was conducted using two segments of REFQPD1 and corrected by the shape of the TF of each channel (TIA + AC-DC splitter), performing the operation $RIN(f) = \tilde{V}_{out}(f)/\tilde{V}_{out} \cdot TF(f_{min})/TF(f)$. This results in a TIA-independent characterization of $\tilde{r}(f)$. The measured values concerning a $f_{het} = 5$ MHz beat note are $\tilde{r}(5\text{ MHz}) = 5 \times 10^{-7}/\sqrt{\text{Hz}}$ and $\tilde{r}(10\text{ MHz}) = 6 \times 10^{-7}/\sqrt{\text{Hz}}$. The increasing noise after the cutoff frequency is interpreted as non-RIN white noise, like electronic or quantization, dominating over the low-pass filtered signal and being 'amplified' by the TF-shape correction.

are combined. Neglecting phase delays due to the electronics, one can calculate the phase delay in equations (2.75, 2.76) as a function of the beam tilt angle. From the definition of DWS,

$$DWS_v := \varphi_{\text{top}} - \varphi_{\text{bottom}}. \quad (2.106)$$

This means that, for instance, that one could set

$$\varphi_{\text{top}} = \frac{\varphi_A + \varphi_B}{2} = \varphi \quad \varphi_{\text{bottom}} = \frac{\varphi_C + \varphi_D}{2} = \varphi_R. \quad (5.21)$$

From this one can then state that the phase-difference dependence in equation (5.23) is

$$\left| \sin \left(\frac{\varphi - \varphi_R}{2} \right) \right| = \left| \sin \left(\frac{\varphi_A + \varphi_B - \varphi_C - \varphi_D}{4} \right) \right| = \left| \sin \left(\frac{1}{2} DWS_v \right) \right|. \quad (5.22)$$

Similarly, for $2f$ -RIN in equation (5.24) $|\sin(\varphi - \varphi_R)| = |\sin(DWS_v)|$. To a second-order approximation in θ , if the beam is tilted by an amount θ , $DWS_v = \kappa_1 \theta$. Furthermore, in the presence of a tilt the heterodyne efficiency $\sqrt{\eta_{\text{het}}}$ decreases as a function of the tilt angle as $\sqrt{\eta_{\text{het}}}(\theta) = \sqrt{\eta_{\text{het}, 0}} e^{-\xi^2 \theta^2}$, where $\sqrt{\eta_{\text{het}, 0}}$ is the heterodyne efficiency of the two parallel beams (see equation (2.146)). This is true for both the sum of the amplitudes of the four segments of a QPD (equation (2.152)) and for the individual QPD segments (equations (2.148, 2.149, 2.150, 2.151)) as long as the relative wavefront-mismatch ρ is sufficiently small (see Paragraph 2.3.3). For the rest of this thesis, this assumption will be used. Note that this is a simplified

model which is also taking into account vertical or horizontal tilts individually. This affects only $1f$ -RIN, as $2f$ -RIN is heterodyne-efficiency-independent. Finally, the phase noise of raw DWS is

$$\tilde{\varphi}_{1f\text{-RIN}} = \frac{\sqrt{2}(P_1\tilde{r}_1(1f_{\text{het}}) + / \boxplus P_2\tilde{r}_2(1f_{\text{het}}))}{\sqrt{\eta_{\text{het}, 0}\bar{P}_1\bar{P}_2}} e^{\xi^2\theta^2} \left| \sin\left(\frac{1}{2}\kappa_1\theta\right) \right| \quad (5.23)$$

$$\tilde{\varphi}_{2f\text{-RIN}} = \frac{\tilde{r}_1 + / \boxplus \tilde{r}_2}{\sqrt{2}} |\sin(\kappa_1\theta)|. \quad (5.24)$$

The coupling of laser frequency noise depends on the pathlength difference Δs between the two interfering beams from the position of the first split on the modulation bench (MB) to BS12 on the telescope simulator (TS) where they interfere. A higher limit of $\Delta s = 1$ m is assumed. The frequency stability itself was characterized in [44] to be $\leq 10^3 \text{Hz}/\sqrt{\text{Hz}}$. As frequency noise couples as an identical phase signal into each beat note measured on a QPD, it is expected to completely cancel in DWS [7].

Thermally induced electronic noise

One of the dominant noise sources at low frequencies is temperature coupling. This is due to the temperature dependence of the parameters of the passive and active electronic components in every circuit, e.g. $R_F \rightarrow R_F(T)$ and $C \rightarrow C_F(T)$. This varies the phase response of the circuit, adding a temperature-dependent phase signal into the beat note. Such temperature coupling is referred to as temperature/thermally induced electronic noise. I will call it for short *thermoelectronic phase noise*.

The mechanism can be modelled using a low-pass filter (LPF) as a toy model. Real electronics are more complex, but this is a suitable yet simplified picture of the matter, as most used electronics *de facto* are LPFs as the bandwidth of the generally used electronics are limited by the cutoff frequency of the amplifiers in the circuit. For example, in TDOBS the cutoff frequency is slightly above 25 MHz. The temperature-dependent phase transfer function (TF) of a LPF is

$$\varphi_{RC}(f, T) = -\arctan\left(2\pi R_F(T)C_F(T)f\right) = -\arctan\left(\frac{f}{f_c(T)}\right), \quad (5.25)$$

where $f_c(T) = (2\pi R_F(T)C_F(T))^{-1}$ is the temperature-dependent cutoff frequency. The variation of the temperature causes a variation of the $\varphi_{RC}(f, T)$, which cannot be distinguished from a beat note phase variation. By taking the partial derivative with respect to the temperature of the above equation one gets

$$\frac{\partial}{\partial T} \varphi_{RC}(f, T = T_0) = - \underbrace{\frac{ff_c(T_0)}{f^2 + f_c(T_0)^2}}_{\text{local TF phase slope}} \underbrace{\left(\frac{1}{R(T_0)} \frac{dR}{dT}(T_0) + \frac{1}{C(T_0)} \frac{dC}{dT}(T_0) \right)}_{\text{relative R and C variation}}. \quad (5.26)$$

The local TF's slope has a maximum value of 0.5 at $f = f_c$, meaning that such noise is higher in proximity to the cutoff frequency. As a reference value, the relative resistance and capacitance variations are ± 100 ppm/K for thick film resistors and ± 30 ppm/K for the capacitors [75] respectively. Mini-metal electrode leadless face (MELF) resistors can improve this up to ± 50 ppm/K [76]. A conservative estimation of the coupling magnitude is $|\frac{\partial \varphi_{RC}}{\partial T}| \sim 10^{-4}$ rad/K. The phase noise is then

$$\tilde{\varphi}_T = \left| \frac{\partial \varphi_{RC}}{\partial T} \right| \tilde{T}. \quad (5.27)$$

To achieve $\sim\text{μrad}$ phase stability within this toy model, the temperature stability of the LPF needs to be $10^{-2}\text{K}/\sqrt{\text{Hz}}$. For TDOBS, this stability is required for all electronics along the measurement chain (see Figure 5.4), from TIA to the AC-DC splitters and the BEE in the PM. Simulation program with integrated circuit emphasis (SPICE) programs allow the simulation of the temperature coupling of thermoelectronic noise $|\frac{\partial\varphi_{\text{RC}}}{\partial T}|$. For instance, for TIA #2 this is shown in Figure 5.6.

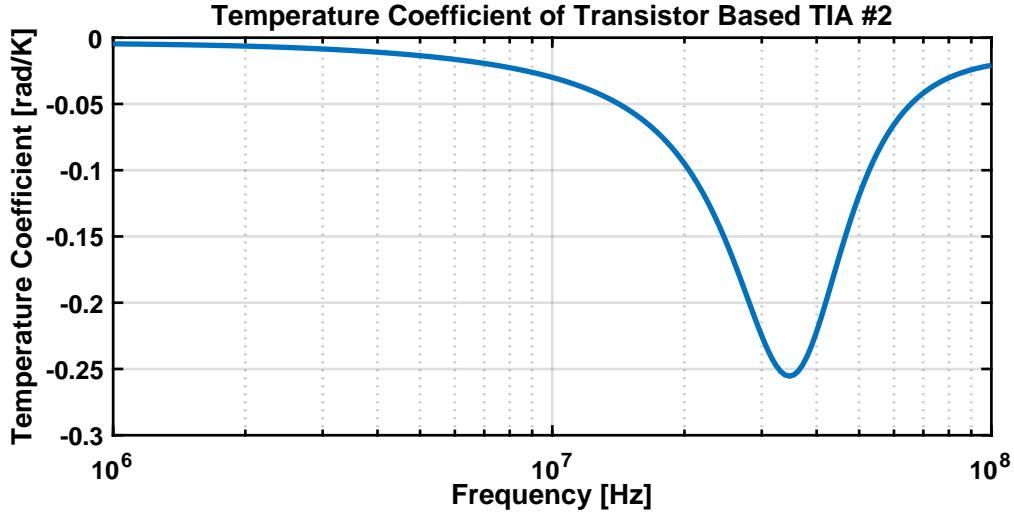


Figure 5.6: SPICE simulation of the temperature coupling coefficient of the transistor-based TIA #2. As expected the coupling is highest around the cutoff frequency.

A similar conclusion is drawn by [39, subsection 3.2.1] in the case of a TIA. In an experimental investigation with a similar PM model as in TDOBS, [9] estimates that the FMC PM temperature stability needed to reach the LISA requirement is

$$\tilde{T}_{\text{PM}} = 5.5 \times 10^{-2} u_{\text{IDS}}(f) \text{K}/\sqrt{\text{Hz}}, \quad (5.28)$$

which especially at $\sim\text{mHz}$ frequencies in a laboratory is not easy to achieve. Unlike frequency noise, the thermoelectronic phase noises affecting two beat notes are never fully correlated, as the local temperature fluctuations and electronic component's coefficients differ.

Due to the high thermal inertia of the VC and the presence of the thermal shield, temperature fluctuations are not a problem for the FEE. The temperature stability inside the VC is shown in Figure 5.7. This reaches a stability better than $10^{-4}\text{K}/\sqrt{\text{Hz}}$ above 10 mHz, and no phase noise contribution is expected from the electronics inside the VC as the TIAs of the PRs. Thermoelectronic phase noise from the TIA is not expected to be critical, as $|\frac{\partial\varphi_{\text{RC}}}{\partial T}|(f = 25 \text{ MHz}) = 0.15 \text{ rad/K}$ and temperature stability \tilde{T} of the TS is $\sim 10^{-4} \text{ K}/\sqrt{\text{Hz}}$ at 1 mHz. This gives $\sim 10^{-5} \text{ rad}/\sqrt{\text{Hz}}$ of thermoelectronic phase noise. Thermoelectronic phase noise is expected to couple much more on the AC-DC splitters and on the PM, as they are located outside the VC.

Straylight and Ghost Beams

During noise hunting in TDOBS several straylight sources and ghost beams were found. The causes of these lie directly in the design of TDOBS. The magnitude of

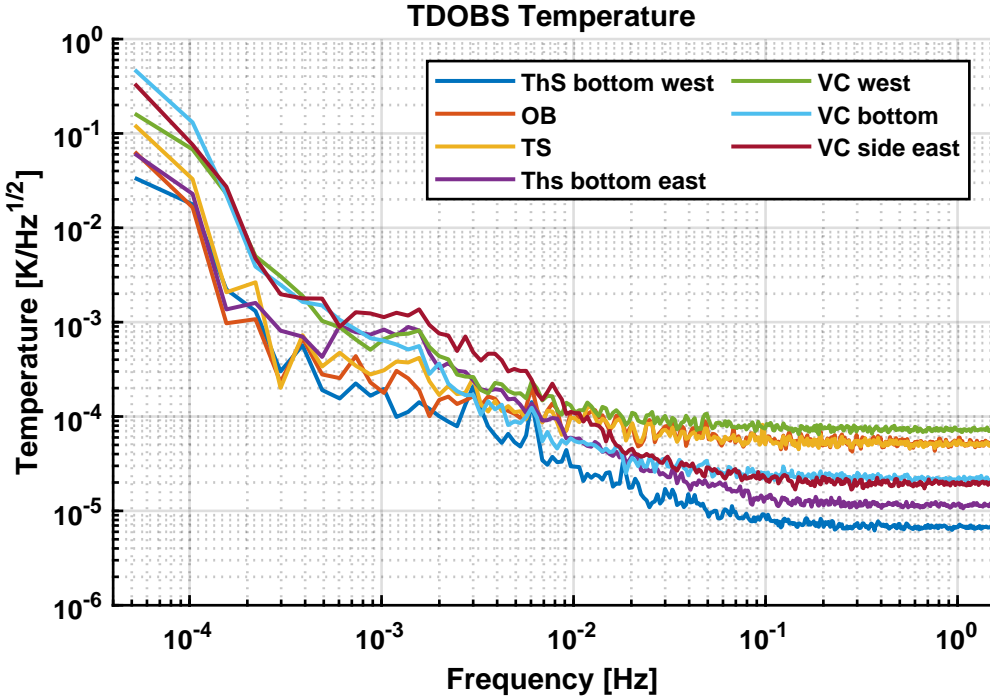


Figure 5.7: Logarithmic amplitude spectral density (LASD) of the temperature inside the VC. The residual thermal expansion of the Zerodur® gives a pathlength noise of a few pm.

the phase noise induced from them is roughly 2 orders of magnitude smaller than the pathlength variations measured in [72, 16] and was to my understanding no problem. This section is a brief list of some found straylight sources and ghost beam paths which, if present, would cause dominant features in TDOBS's measurements.

Straylight and ghost beams couple into the interferometric measurements as a small vector noise (SVN). A stray reflection or ghost beam of either of the two interfering beams propagating through a non-nominal path and impinging on the PD generates a parasitic beat note with different phase dynamics, adding a small stray-phasor to the beat note's phasor. A deeper discussion is in Appendix A. Figure 5.8 shows an example of measured SVN. This is clearly distinguishable from white noise in both the time and frequency domains. For instance, it shows up in the ASDs as a shoulder around 200 mHz in Figure 5.8.

This subsubsection lists the ghost beams found in TDOBS which, if not rejected by beam dumps or apertures, are visible in the measured signal.

REFQPDs, RX-GB ghost beam from the Flat-Top beam generator A relatively large SVN was observed while measuring the interference between RX-GB and LO beam at the REFQPDs and also showed up in a few DWS measurements taken with the AUXQPD. The cause was quickly identified and is shown in Figure 3.7, left. It is due to a stray reflection caused by BS12, the RX power monitor (RX PWR on Figure 3.7) and the Flat-Top beam generator: as the RX-GB beam is injected from the FIOS, it propagates to BS12, where half of the beam's power is directed to the experiment, while the other half is impinging on a couple of SEPDs

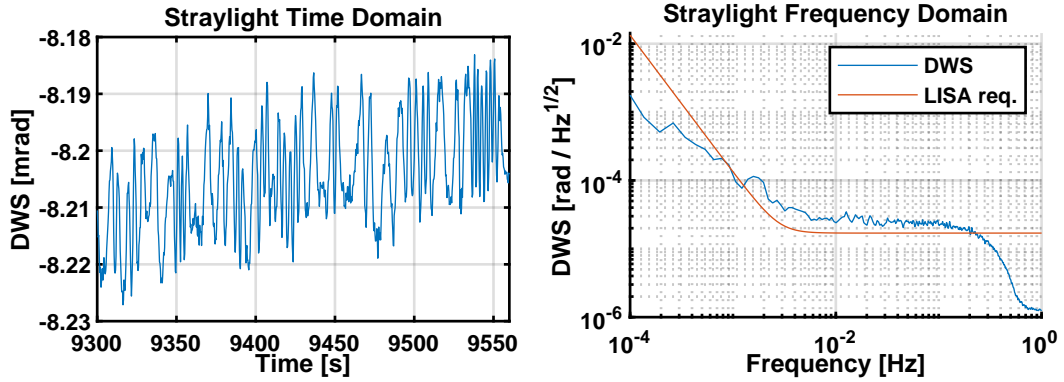


Figure 5.8: Manifestation of small vector noise due to straylight or ghost beams in the time domain (left) and frequency domain (right), featuring in this case a cutoff frequency around 100 mHz.

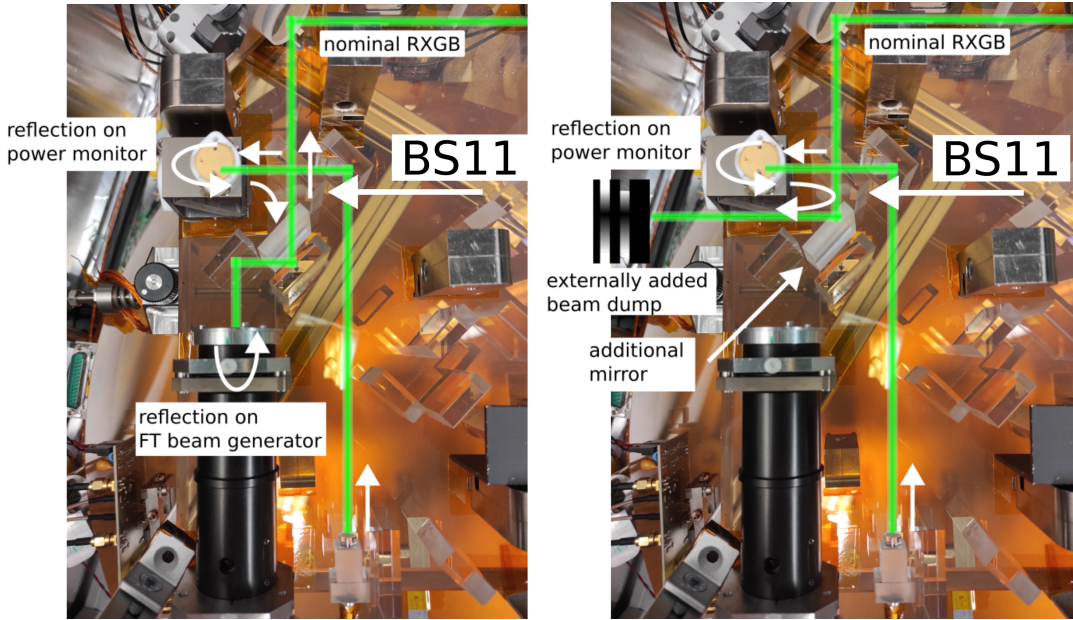


Figure 5.9: Picture of the TS, with detail on the RX-FT beam generator and RX-GB FIOS. The green beam shown is the RX-GB beam. Left: what would happen on the TS neglecting the additional mirror. Right: the additional mirror was added to deflect the stray reflection from the RX power monitor to a beam dump.

for power monitoring, named RX PWR⁶. These RX PWR cause a strong back reflection, propagating to BS12, where it is split again. Part of the back reflection propagates to the Flat-Top beam generator, and gets once more reflected backwards. This back reflection now propagates as a stray RX-FT beam and impinges on all detectors. Provided that the RX PWR cannot be removed and that there is no space to install a beam-dump on the TS, this issue was solved by adding a mirror between BS12 and PC38 to reflect the ghost beam out of the TS, and by then dumping it as depicted in Figure 5.9 right using an externally mounted beam dump.

REFQPDs, ghost beam on the TX beam's path This very weak straylight source was found and dumped, but the cause is not understood. SVN due to stray-

⁶These SEPDs are currently not in use, and hence were not mentioned.

light was observed on the REFQPDs and on the REFSEPD. After many trial and error attempts, it was found that this vector noise vanishes if a beam dump is placed in-between the periscope optics between TS and LISA-OB. This situation is inconvenient as no QPD on the LISA-OB could be used anymore. Further attempts have proved that the same result occurs if the path that the TX would take on the TS is dumped⁷. This situation is shown in Figure 5.10: on the left the 'TX-like' ghost beam is drawn in red. This propagates on the TS between PBS1 and the HWP, and ends up interfering with the RX and LO beams at the REFQPDs. On the right the TX beam path is dumped. The origin of this TX-like ghost beam has not yet been found.

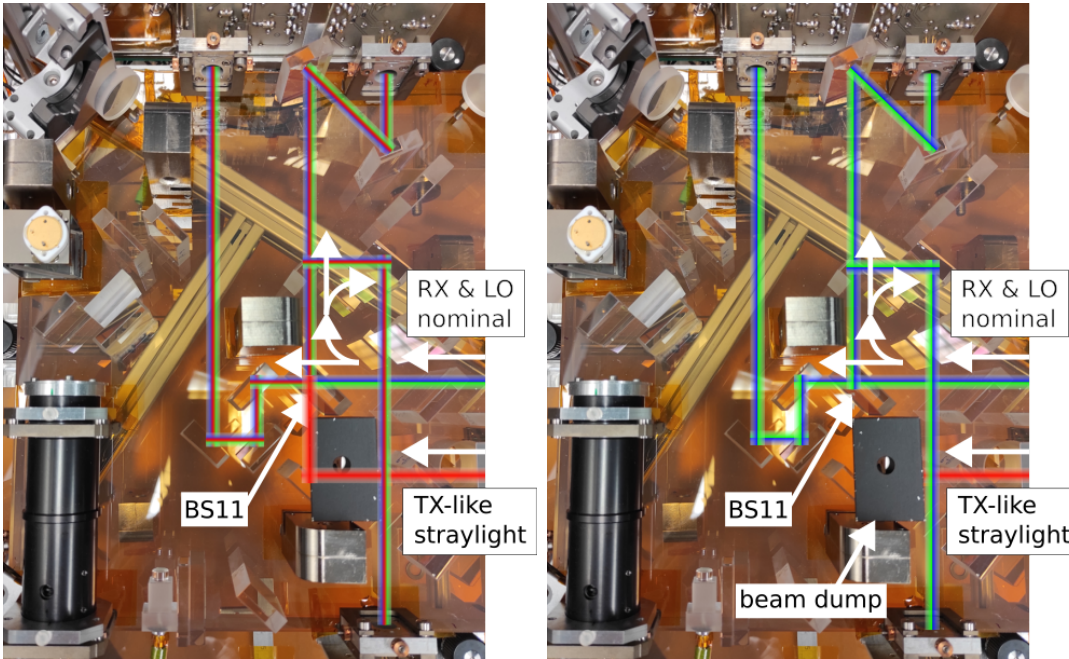


Figure 5.10: Picture of the TS, with the understood path of the straylight drawn in red (left). If not dumped, this couples to the beat note on the REFQPDs and REFSEPD. A beamdump on the TX beam path solves this issue (right).

REFQPDs, Straylight from Photodiode back reflection Ghost beams due to back reflections from the REFQPDs and the REFSEPD were found on the TS. As the photodiodes are not mounted at an angle, these back reflections propagate backwards only with a small angle deflection from the incoming beam and are initially confined to the TS. These three back reflections are initially bright enough to be found with a viewer beam card if the lights in the lab are switched off. I followed them to map all surfaces where they impinge, after numerous further splits. These beams, anyhow end up either outside of the TS, being dumped on the thermal shield, or absorbed by some mount on the TS. Part of the light is also directed toward the periscope optics but does not propagate further on the LISA-OB.

SCIQPDs, LO straylight from LO beam power monitor After reflection on the polarization cleaner, part of the power of the LO beam is deflected by BS13

⁷The TX beam is currently not being used.

toward a power monitor⁸. As in the case of the RX-FT straylight, the power monitor causes a back reflection that propagates backwards and through the BS13. This ghost beam is reflected backwards by the RX-FT beam dump and then reflected again by BS13 as a stray LO beam. This straylight mechanism is depicted in Figure 5.11, which shows on the left the nominal path of the LO beam, and on the right the path of the LO beam with the ghost beam. This effect was not seen on the REFQPDs, and neither noticed previously on the AUXQPD, but it was evident on the SCIQPDs. The reason for this is not understood. Placing a beam dump in front of the LO power monitor gets rid of the shoulder on the SCIQPDs' ASD.

The measurements on the SCIQPDs appear to be limited by two vector noise sources due to straylight, which appear to be common mode. So far, only one was identified. More is discussed in Subsection 5.4.2.

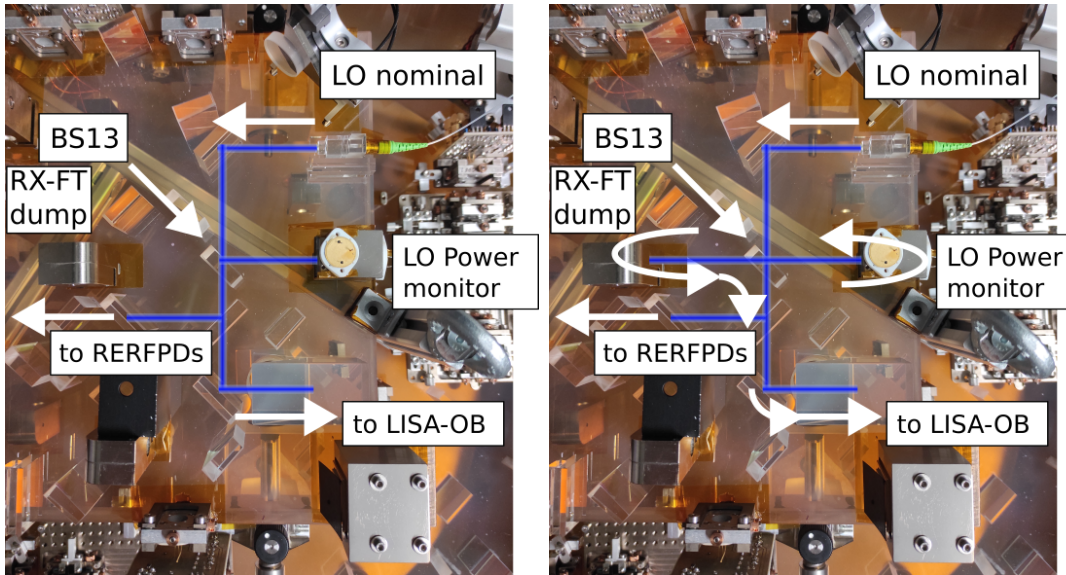


Figure 5.11: Picture of the TS, with detail of the nominal path of the LO beam (left) and of the spurious reflection on the LO power monitor and RX-FT beam dump (right).

Electronic Crosstalk

Electronic crosstalk can be modelled as a small vector noise (SVN) similar to straylight, with the main difference of depending on the carrier's frequency. The expression for the phase error can be derived by adapting equation (A.7). As in the circuits in TDOBS (PM, AC-DC splitters and TIA) the signals have similar amplitudes, the parasitic amplitude is the signal's amplitude times a frequency dependent cross-coupling coefficient $A_p = c(f)A_s$.

$$\Delta\varphi_{\text{err, cross}} = \frac{A_p}{A_s}(\varphi_p - \varphi_s) = c(f)(\varphi_p - \varphi_s) \quad (5.29)$$

5.2.3 Noise Budget

This Subsection derives an indicative noise budget of the experiment, taking into account the noise sources listed so far in this Section which contribute to phase

⁸also not currently in use.

noise in a frequency-independent way. In this noise budget, indicative values of the parameters are used to calculate the noise floor. A better calculation requires the full knowledge of the experimental parameters. Thermoelectronic phase noise and straylight are excluded from this noise budget. Frequency noise is included as a rough estimation. This budget does not yet take into account the phase noise introduced during the beat note's tracking by the DPLL.

As the phase noise depends on the amplitude of the beat note $A = \sqrt{\eta_{\text{het}} \bar{P}_1 \bar{P}_2}$, I opted to plot this as a function of the RX beam power. The used parameters in this budget are $P_{\text{LO}} = 28 \mu\text{W}$ per QPD segment, $G_{\text{ss}} = 2.87 \text{ V/V}$, $\eta_{\text{het}} = 0.86$ as for the RX-GB & LO beams. The resulting noise budget is shown in Figure 5.12.

If all noise sources are uncorrelated, the left y-axis in Figure 5.12 also corresponds to the raw DWS noise. The dashed curves in Figure 5.12 represent noise sources which either vanish or mostly cancel in differential measurements, as DWS. This holds for frequency noise [7] and RIN. According to equations (5.23, 5.24) RIN cancels if the laser beams are parallel. If the alignment precision is a conservative 1 mrad then it is suppressed by a factor of $\sim 10^3$.

The takeaway message from Figure 5.12 is that the two main noise sources for TDOBS are shot noise and electronic noise from the TIA, hence motivating the use of a low noise TIA. Dark current from the QPD and ADC quantization noise are more than one order of magnitude below this and are never an issue, even at low powers. Laser frequency noise and both $1f$ - and $2f$ -RIN give dominant phase noise contributions at segment-level, but they are strongly suppressed in segment-combination signals as DWS.

5.3 Phasemeter's noise floor

The phase noise due to the FMC PM is a more complex topic and deserves a separate Section. One of the main goals of TDOBS is to test the performance of the FMC phasemeter (PM) as pre-development of the LISA PM while feeding it with optical signals, whereas most tests, as in [9] rely on SG inputs.

The PM is itself one of the main noise sources in the setup. The added phase noise density depends on the input signal's amplitude, frequency, and on the temperature stability of the experiment due to thermoelectronic phase noise. The amplitude dependency in LISA is suppressed by the presence of a variable gain controller, but as TDOBS lacks this feature, this is a relevant parameter space to test. I therefore tested the PM's capability of extracting the phase from an electrical signal. This was performed in several amplitude and frequency conditions under a so-called *split test*. In this procedure, one or multiple copies of the same signal are fed into the PM and the readout phases are compared. This test has the advantage of being independent of the source's phase stability but is insensitive to crosstalk. More details on this procedure can be found in [9, section 4.1.2]. The input signal was generated by means of a signal generator (SG) and split using an in-house populated 8-way splitter designed by Oliver Gerberding. A copy of the signal was fed to each input of the FMC PM, and the output phases were read as if they were coming from eight segments of two QPDs.

The P and I gain parameters of the FMC PM's digital phase-locked loop (DPLL) loop were set to respectively $P=15$ and $I=5$, as these values proved to give the best performance (see Subsection 3.3.4). For lower gain values, the PM performance

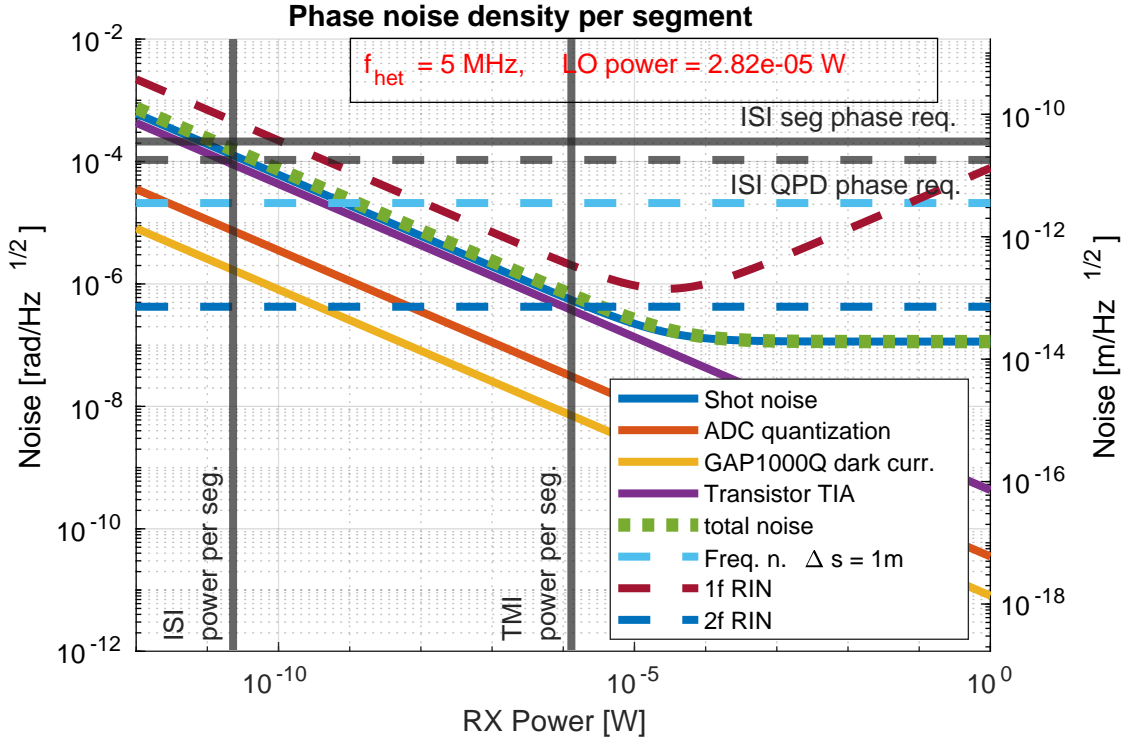


Figure 5.12: Noise budget of a single QPD's segment in TDOBS modelled above, expressed in either raw phase $\text{rad}/\sqrt{\text{Hz}}$ or $\text{m}/\sqrt{\text{Hz}}$ as a function of the RX beam power. Uncorrelated noises between segments are represented as solid lines, while correlated noises, which would be partially or even mostly cancelled in DWS measurements, are represented as dashed lines. Excluding correlated noises, at this specific LO beam power the total noise is dominated by laser shot noise and electronic noise from the TIA.

proved slightly worse, while for values of $P=16$ and $I=6$, the DPLL was not capable of locking to the beat note. Such values were consequently used during the optical test throughout the whole of this thesis. Active temperature stabilization was on, and ADC clock jitter was corrected using the pilot tone (PT).

The expected ASD of the noise from the FMC PM is frequency-dependent. This is due to quantization noise in the finite impulse response (FIR) filters in the FMC PM: as the measured quantity is frequency and quantization noise is white, the corresponding phase noise has a $1/f$ trend due to integration [9, subsection 2.7.2]. Furthermore, thermoelectronic phase noise is expected to be a limiting factor as the environmental thermal stability in the lab is roughly around $1 \text{ K}/\sqrt{\text{Hz}}$ at 1mHz. This is evident in the next Subsections as the frequency- and amplitude-dependency of the noise were tested in different temperature situations.

Noise as a function of the input amplitude

The FMC PM's noise floor was characterized at a constant heterodyne frequency of 5 MHz for various SG signal amplitudes. The measured ASDs are shown in Figure 5.13. A fit of the average LASD separated for simplicity in low-frequency band (1-10 mHz), mid-frequency band (10-100 mHz) and high-frequency band (0.1-1 Hz) is shown in Figure 5.14

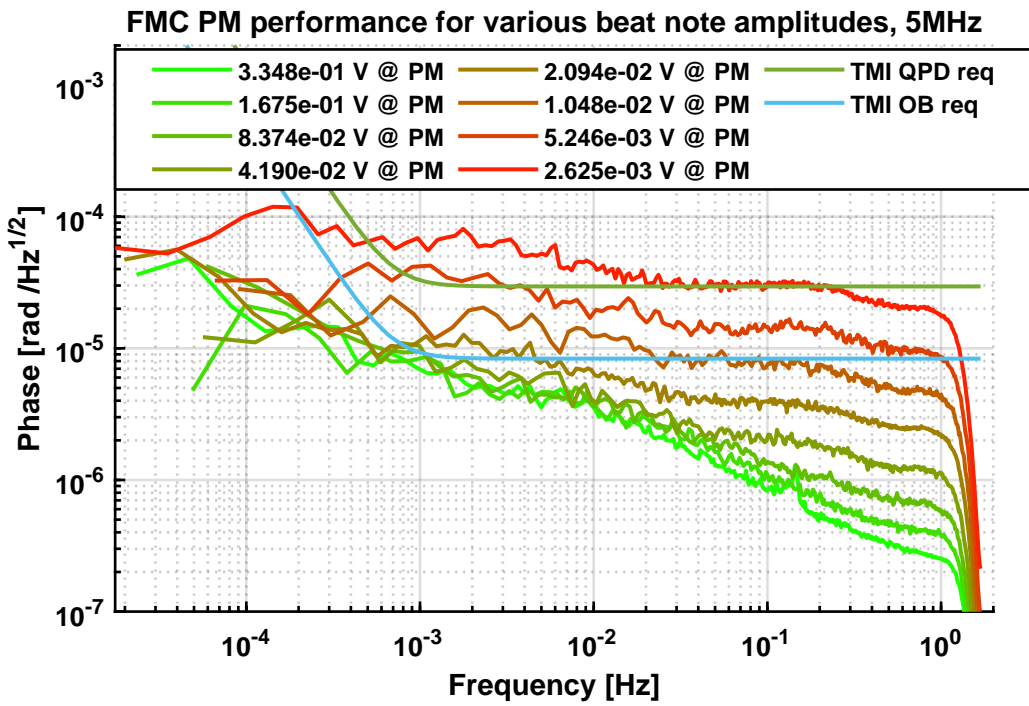


Figure 5.13: LASD of the measured phase noise for electrical signals of same frequency and various amplitudes to the FMC PM.

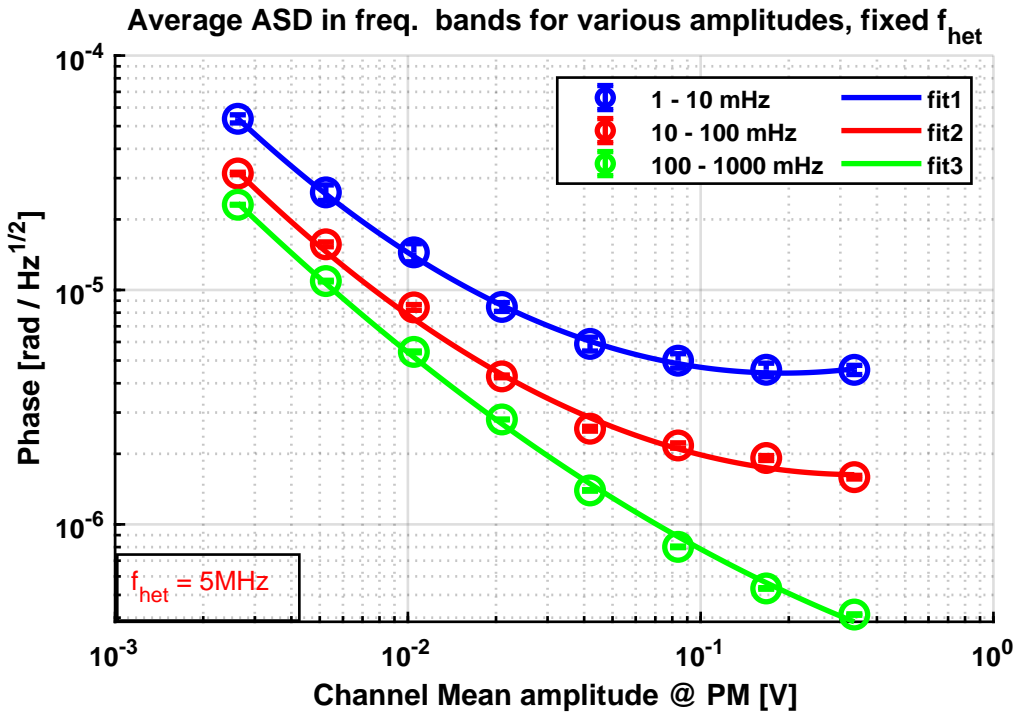


Figure 5.14: Fit of the LASDs from Figure 5.13 averaged in three separated bandwidths to resemble the low-frequency, mid-frequency and high-frequency noise of the FMC PM. Fit parameters are in Table 5.9.

Parameter	0.001-0.01 Hz		0.01-0.1 Hz		0.1-1 Hz	
p_0	-5.193	\pm	0.087	-5.729	\pm	0.032
p_1	0.45	\pm	0.13	0.260	\pm	0.045
p_2	0.313	\pm	0.041	0.286	\pm	0.014
						0.163 \pm 0.005

Table 5.9: Parameters from the fit in Figure 5.14. The fit function is a 2nd order polynomial $f(x) = p_0 + p_1x + p_2x^2$, where $x = \log_{10}(\text{Amplitude})$ and $y = \log_{10}(\text{Phase})$

Noise as a function of the input frequency

The FMC PM's noise floor was characterized at a constant signal amplitude of 0.8 V at the PM's input for various SG frequencies within the LISA heterodyne band. The measured ASDs are shown in Figure 5.15. A fit of the average LASD separated for simplicity in low-frequency band (1-10 mHz), mid-frequency band (10-100 mHz) and high-frequency band(0.1-1 Hz) is shown in Figure 5.14. Above 3 mHz the ASDs have the same shape and rise as the signal's frequency is increased.

This measurement was affected by high temperature fluctuations. This is due to the fact that the main air conditioning circuit in the laboratory broke in August 2024; this air conditioning circuit featured a continuous negative feedback loop able to keep a stable temperature. This was replaced with a secondary air conditioning circuit using a bang-bang control, turning on and off roughly every 30 minutes. This periodicity causes the peak visible in Figure 5.15 around 0.5 mHz. The peak around 2 mHz is caused by the active temperature control, which was used to mitigate the temperature drift. A broader estimation of the coupling of temperature noise is carried out at the end of this Subsection. It is immediately noticeable how the phase noise density for a 5 MHz beat note measured in Figure 5.15 in the red-shaded area is worse than that in Figure 5.13 by one order of magnitude just because of different air conditioning.

Parameter	0.001-0.01 Hz		0.01-0.1 Hz		0.1-1 Hz	
p_0	-64	\pm	40	-7	\pm	6
p_1	16	\pm	11	-0.5	\pm	1.9
p_2	-1.1	\pm	0.7	0.10	\pm	0.13
						0.16 \pm 0.05

Table 5.10: Parameters from the fit in Figure 5.16. The fit function is a 2nd order polynomial $f(x) = p_0 + p_1x + p_2x^2$, where $x = \log_{10}(\text{Amplitude})$ and $y = \log_{10}(\text{Phase})$

Conclusion

In both the amplitude and frequency dependency measurements, the noise in the high-frequency band is lower and increases roughly linearly with the investigated parameter. This is interpreted as the phase noise density is being limited by the PM's performance in this band. In the low-frequency end almost no change is visible at high signal amplitude and between 15 and 25 MHz frequency. This is interpreted as the temperature noise being dominating. The mid-frequency band has an in-between behaviour.

The temperature stabilities during the measurements in Figures 5.13 and 5.15 are shown in Figure 5.17. It is evident how, for frequencies lower than 3 mHz, in the amplitude performance measurement (Figure 5.13) the performance at the

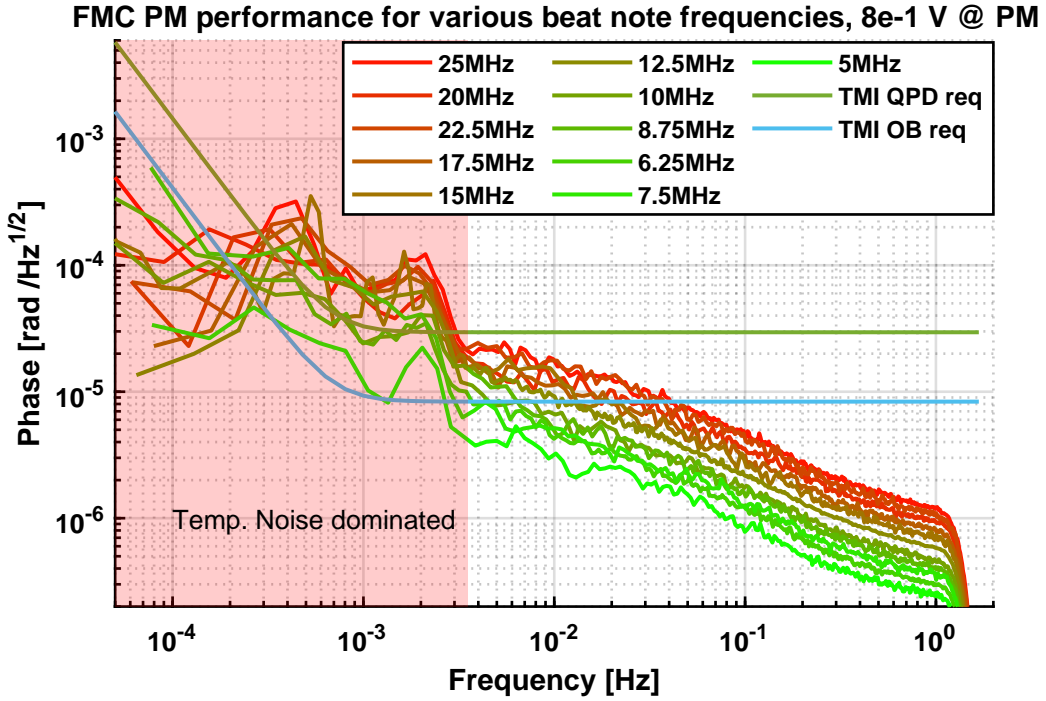


Figure 5.15: LASD of the measured phase noise for electrical signals of same amplitude and different frequencies to the FMC PM. The red shaded area shows the frequency band that is limited by temperature noise.

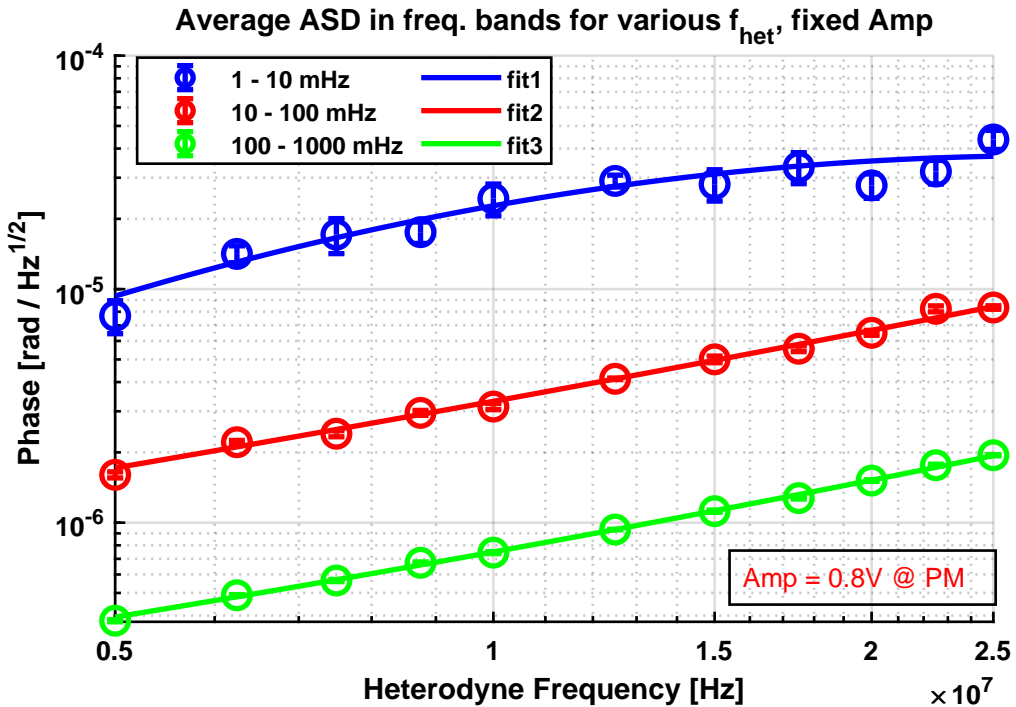


Figure 5.16: Fit of the LASDs from Figure 5.15 averaged in three separated bandwidths to resemble the low-frequency, mid-frequency and high-frequency noise of the FMC PM. Fit parameters are in Table 5.10.

lowest amplitude is better than the 5 MHz performance in Figure 5.15, despite this last using a higher-amplitude signal. The relevance of the thermoelectronic phase noise in the two measurements in Figures 5.13 and 5.15 can also be checked by calculating the temperature-to-phase logarithmic magnitude-squared coherence (shown in Figure 5.18). When the bang-bang air conditioning circuit is on, PM temperature and phase are correlated between 0.5 mHz and 3 mHz.

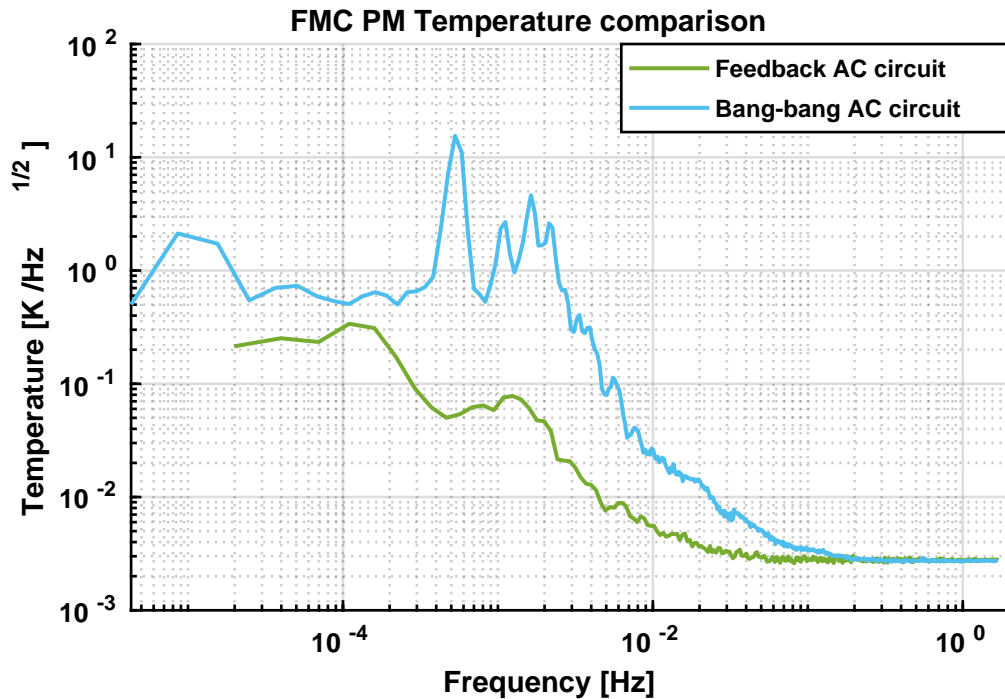


Figure 5.17: Temperature stability of the FMC PM during the two measurements in Figures 5.13 (Feedback AC circuit) and 5.15 (Bang-bang AC circuit).

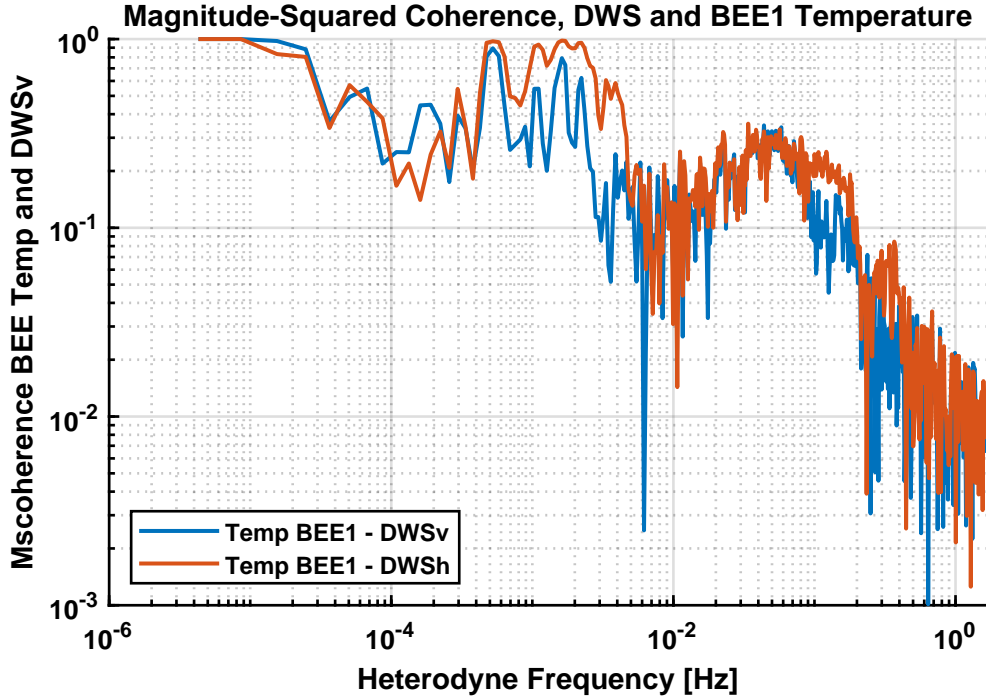


Figure 5.18: Logarithmic magnitude-squared coherence of the FMC PM's temperature and the readout phase during the two measurements in Figures 5.13 (Feedback AC circuit) and 5.15 (Bang-bang AC circuit). BEE1 refers to the temperature measured by the sensor placed next to the BEE of channels 1-4.

5.4 TDOBS: DWS and LPS noise floor

This Subsection shows the best DWS and LPS performance achieved in TDOBS obtained during measurements where the beat note was tuned to have the highest C/N_0 . This noise floor is the baseline for Chapter 6, where the DWS noise is characterized as the experimental conditions depart from optimal.

5.4.1 The Performance Measurement Setup

The RX and LO beams were used for this measurement. The use of the TX beam would have been equivalent. An RX beam is required as the DWS needs calibration. The beat note of the two beams is measured from two QPDs is measured using the eight channels of the FMC PM. The chosen pair of QPDs are selected to be optical copies, as the REFQPDs or the SCIQPDs. During the measurement, the actuators are kept still in the nominal position, resulting in an ideally null DWS measurement on both photodiodes. This helps maximize the heterodyne efficiency and guarantees a better suppression of RIN. The beam powers are set as high as possible (roughly 120 dBHz) to minimize the coupling of C/N_0 -dependent phase noises. The limit to the maximum beat note amplitude that the QPRs can receive is determined by the slew rate of the OpAmps in the measurement chain. Note that this implies the use of lower powers at higher heterodyne frequencies. A pilot tone (PT) at a frequency of 72 MHz is introduced to suppress ADC sampling jitter noise. Measurements were performed at atmospheric pressure, as this was understood not to be a limiting noise

contribution to the experiment's sensitivity.

The OPD stabilization (see Section 3.2.2) stabilizes the pathlength difference between RX and LO beam to a few nm/ $\sqrt{\text{Hz}}$. This exact value depends on the used heterodyne frequency and on the signal's amplitude and degrades significantly at high heterodyne frequencies as this control loop is implemented on the FFT PM, which was not built to operate at MHz frequencies. Measurements have shown that the resulting DWS performance is not limited by the OPD loop's performance.

The measurements shown in this Subsection were realized in September 2024, after the TIA on the REFQPDs was upgraded to the transistor-based TIA #2, and are therefore limited below ~ 3 mHz by the thermoelectronic phase noise. The SCIQPDs are still using TIA #1. This period was, unfortunately, the worst in terms of the thermal stability of the laboratory. The comparative thermoelectric phase noise measurements from the AC-DC splitters and PM were taken in October 2024, when due to more stable external weather conditions, the temperature stability in the lab was improved.

5.4.2 The Performance Measurement Results

The DWS signal measured on one QPD was far from stable. The cause was found to be thermal drift in the actuators. This is shown in Figure 5.19. The actuators have a thermal drift coefficient given by the manufacturer of $4 \text{ }\mu\text{rad K}^{-1}$ [57] which can explain the measured drift. Such drift causes a variation of the angle of incidence of the RX beam and, therefore, a very large DWS signal. As an example, the drift shown in Figure 5.19 is roughly a constant 0.07 nrad/s and a total angular drift of $1 \text{ }\mu\text{rad}$. As both actuators are randomly drifting, the pivot of the rotation of the RX beam is not the QPD's surface. Despite this fact, as the angular variations are extremely small, the DWS calibration is still valid using the parameters characterized in Chapter 4 as if the rotation happened around the QPD's center.

As visible in Figure 5.19, the DWS measurements from the two optical copy QPDs are extremely close. Combining the two allows to subtract the DWS signal and synthesize a virtual signal-less QPD. This results in a null DWS measurement limited by the sensing noise, which is what the performance measurement is targeting. The limiting noise sources were understood to be uncorrelated hence the resulting quantity is divided by $\sqrt{2}$.

$$\text{DWS/LPS}_{\text{REFQPD } 1-2} = \frac{1}{\sqrt{2}} \left(\text{DWS/LPS}_{\text{REFQPD1}} - \text{DWS/LPS}_{\text{REFQPD2}} \right) \quad (5.30)$$

I will from now on call the quantity in equation (5.30) *differential* DWS or LPS. The performance of the subtraction can be improved by estimating a proportionality constant between the two QPDs' DWS signals. This was done, and the resulting deviations from 1 of at most 0.05. This was found to give no significant improvement to the following results, as likely the direct subtraction reduces the signal to a level which is lower than the noise.

DWS performance of the RX-GB and LO beams on the REFQPDs

The REFQPDs have a radius of 0.5 mm, while the RX-GB and LO beams have radii of respectively 1.038 mm and 0.874 mm at the REFQPDs' position. This leads to

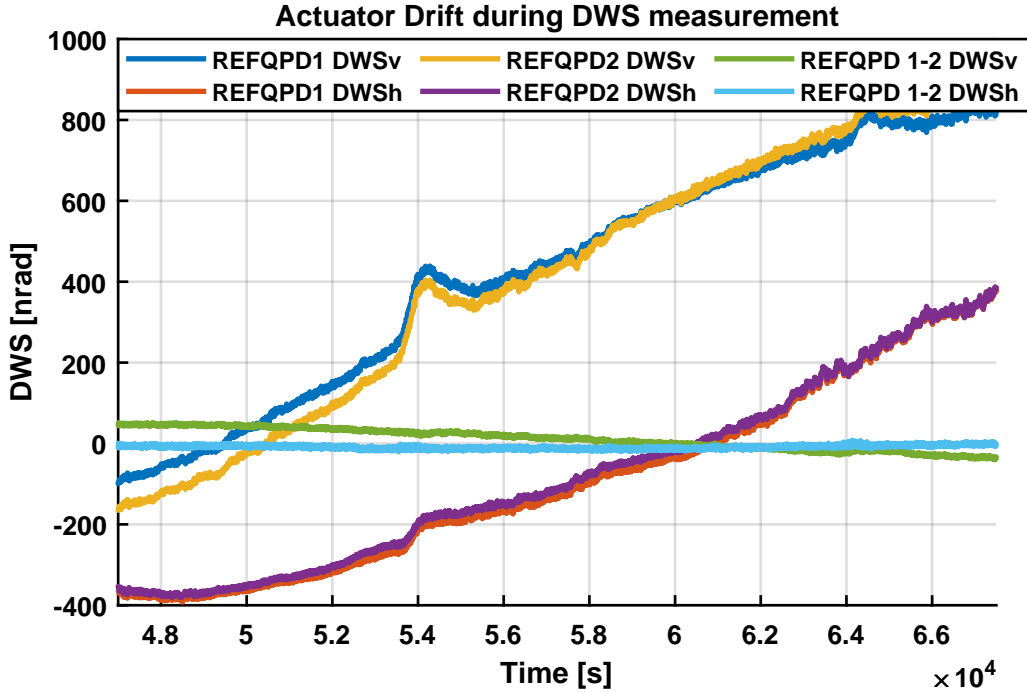


Figure 5.19: Time plot of the DWS drift using the data from the measurement in Figure 5.23, where the DWS signal of the RX-GB & LO beams is measured on the REFQPDs. The average drift velocity is of the order of $1 \mu\text{rad}$ during a period of 1.8×10^4 s. As the measured DWS from REFQPD1 and REFQPD2 is very close, taking the difference between the two measurements yields an almost null measurement. In this plot, the DWS offsets between REFQPD1 and REFQPD2 were subtracted for readability.

only a small fraction of the beam powers impinging on the four segments, less than 50% as characterized in Table 3.7. This potential issue is even more relevant for the RX-FT beam, which has roughly a 2 cm diameter. Prior to these measurements, additional phase noise due to scattering of the 'non-detected' power onto the QPD's package could not be ruled out.

The DWS performance was characterized at the heterodyne frequencies of $f_{\text{het}} = [1.25, 5, 25]$ MHz. The power values and second-stage amplification used during these three measurements are reported in Table 5.11.

Figures 5.20, 5.23 and 5.25 show the measured DWS performance at the heterodyne frequencies f_{het} of 1.25 MHz, 5 MHz and 25 MHz, respectively. The plots show the measured DWS performance together with the LPS signal. The left y-axis (DWS [rad]) and the right y-axis (LPS [pm]) are scaled in order to correspond to the same segment phase magnitude. Figure 5.27 compares the differential DWS performance measured at these three heterodyne frequencies. The performance tends to worsen as the heterodyne frequency is increased.

1.25 MHz The $f_{\text{het}} = 1.25$ MHz measurement is used to rule out the presence of noises of optical origin. As the phase noise increases at higher heterodyne frequencies due to mainly electronic and thermoelectronic phase noise, while straylight or residual TS thermal expansion would not depend on this, a low heterodyne frequency measurement states which performance could in principle be reached also at

Parameter	1.25 MHz	5 MHz	25 MHz
$P_{\text{RX-GB}}$	1.2 μW	0.46 μW	0.092 μW
P_{LO}	8.5 μW	2.4 μW	0.49 μW
G_{ss}	2.87 V/V	2.87 V/V	57.4 V/V

Table 5.11: Parameters of the experiment during the Rx-GB & LO on REFQPDs performance measurements.

higher heterodyne frequencies. The amplitude of the signal at the PM is 0.023 V, which is not optimal, but using one of the available second-stage gain circuits would have caused it to exceed the PM’s ADC range.

The vertical and horizontal DWS measurements from REFQPD1 in Figure 5.20 satisfy the LISA QPD-level DWS requirement only above 40 mHz. Below this frequency, the DWS noise is dominated by the RX-GB beam’s motion, and the measured noise differs between DWS_v and DWS_h . At ~ 0.5 Hz the LASD is limited by a different white-looking noise, and the DWS_v and DWS_h LASDs are similar. The beam motion is characterized by a roughly $1/f$ LASD and a small peak slightly after 100 mHz. By subtracting the beam motion measured by REFQPD2, which is not plotted as it is basically identical to that of REFQPD1, the RX-GB beam motion is removed and the differential DWS performance (labelled as REFQPD 1-2) is obtained. The REFQPD 1-2 DWS LASD matches that of REFQPD for frequencies higher than 0.7 Hz, while the noise is better by one order of magnitude at 1 mHz. The differential DWS_v and DWS_h measurements appear to be limited by the same noise floor on the whole frequency range and satisfy the LISA QPD-level DWS requirement in the whole band and the OB-level DWS requirement above 3 mHz. The LPS measurement from REFQPD1 matches the relative pathlength stabilization given by the REFSEPD in the non-thermoelectronic-noise-dominated band. The differential LPS measurement’s performance is very close to that of the differential DWS in the whole measurement band.

Figure 5.21 shows the magnitude-squared coherence of the differential DWS_v and DWS_h from the measurement in Figure 5.20. While both vertical and horizontal DWS from REFQPD1 had a peak around 100 mHz due to the RX-GB beam motion; no higher correlation occurs around 100 mHz, meaning the RX-GB beam motion is completely removed in the *differential* DWS.

Figure 5.22 shows the ASDs of the raw phase from the differential DWS and LPS from the measurement in Figure 5.20. The differential LPS signal is multiplied by 2 to compensate for the differences in the $\frac{1}{4}$ and $\frac{1}{2}$ factors in the definition of the LPS and DWS, respectively. The plot also reports a combined estimation of electronic noise from the TIA plus the shot noise, as well as the result of a split test performed with an SG-generated electrical signal fed through first to an AC-DC splitter and then to the PM, where the signal’s amplitude at the PM is the same of the measured signal from the TIA. This measurement is meant to reflect the additional noises due to thermoelectronic phase noise that the optical beat note picks up outside the VC, where the temperature stability is worse. This measurement is a factor of 3 away from the measured phase noise in the whole band. Given that these DWS and AC-DC & PM measurements were taken in different moments, I consider this difference understandable. On the high frequency end, the TIA plus shot noise is a factor of 2 away from the measured phase noise, which is also understandable given the

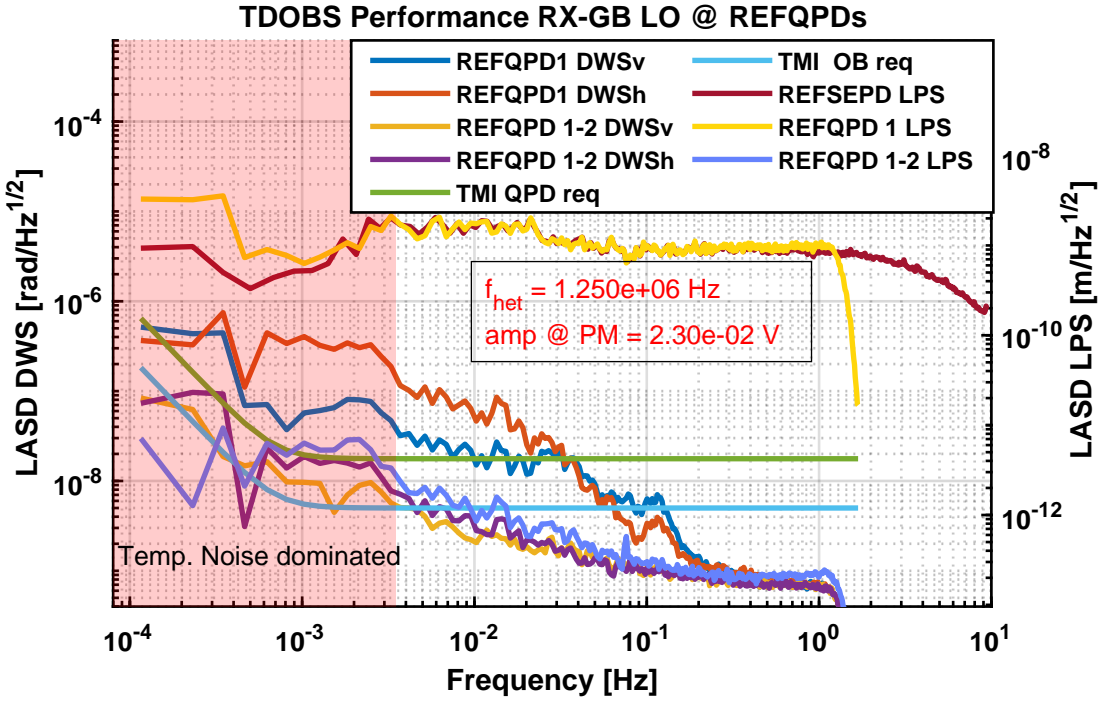


Figure 5.20: Calibrated DWS and LPS performance using the RX-GB & LO beams, the REFQPDs, 1.25 MHz heterodyne frequency and TIA #2. The requirement to be met is the TMI QPD requirement, while the TMI OB requirement is also reported as the QPD requirement is fullfilled in most of the band.

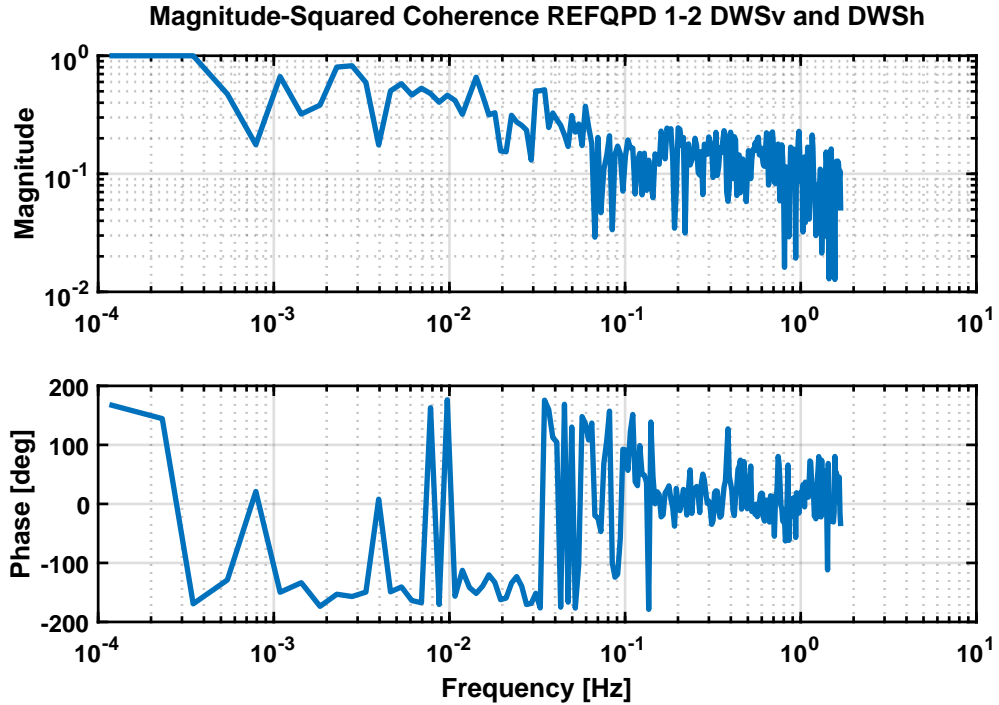


Figure 5.21: Logarithmic Magnitude-Squared Coherence of REFQPD 1-2 DWS_v and REFQPD 1-2 DWS_h from Figure 5.20

uncertainty on the power values. No SVNs is visible on the LASD or on the time series, stating that straylight is negligible. The noise in this measurement is, hence, well understood.

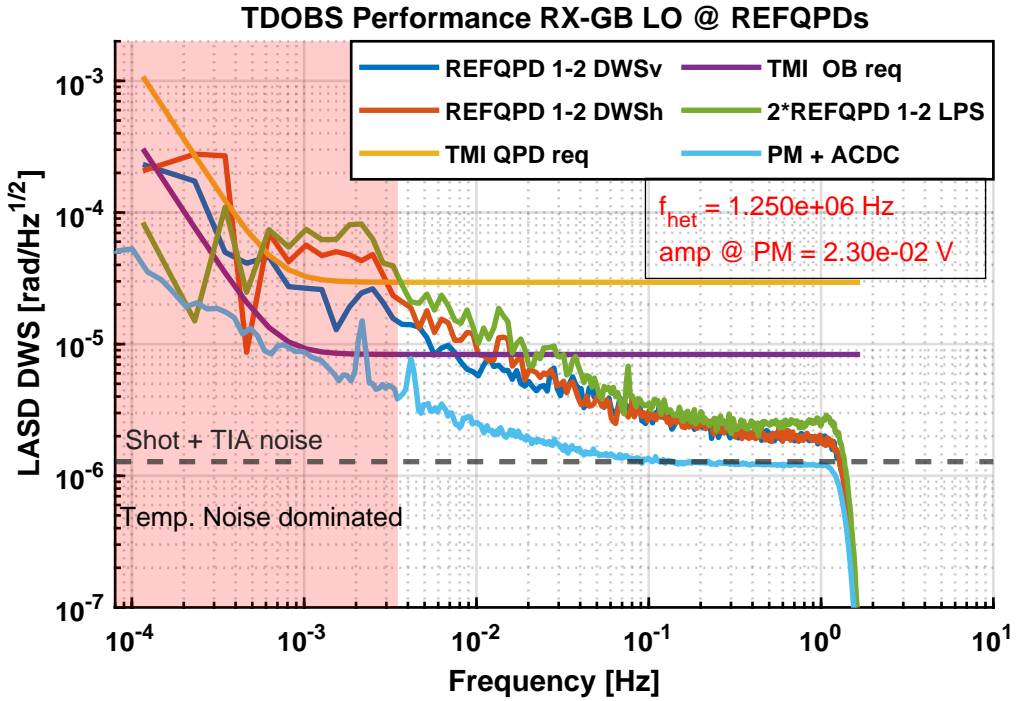


Figure 5.22: Raw DWS and LPS performance using the RX-GB & LO beams, the REFQPDs, 1.25 MHz heterodyne frequency and TIA #2, compared to a model of the combined electronic and shot noise and a measurement of the thermoelectronic phase noise.

5 MHz The $f_{\text{het}} = 5$ MHz measurement in Figure 5.23 performs extremely similarly to the $f_{\text{het}} = 1.25$ MHz measurement, but the REFQPD 1-2 noise is slightly higher. All of what is mentioned for the $f_{\text{het}} = 1.25$ MHz measurement also applies here, as the single QPD's DWS sensitivity is limited by RX-GB beam motion while the differential DWS measurement has considerably lower noise. Also in this measurement the differential DWS and differential LPS reach the same noise floor. The differential DWS measurements satisfy the LISA QPD-level requirement in the whole band except for a small range around the corner frequency of 0.7 mHz and satisfy the LISA OB-level requirement for frequencies higher than 10 mHz.

Figure 5.24 is the same as Figure 5.22 but measured at $f_{\text{het}} = 5$ MHz. In this measurement, the phase noise from the AC-DC splitters and the PM comes very close to the measured phase performance at low frequencies, being within a factor of 2 despite having been measured in a moment of better temperature stability. The modelled TIA and shot noise matches the measured noise on the high-frequency end. The noise in this measurement is, hence, well understood.

25 MHz The $f_{\text{het}} = 25$ MHz measurement in Figure 5.25 is dominated, for all three REFQPD1, REFQPD2 and REFQPD 1-2, by an uncorrelated noise source, as

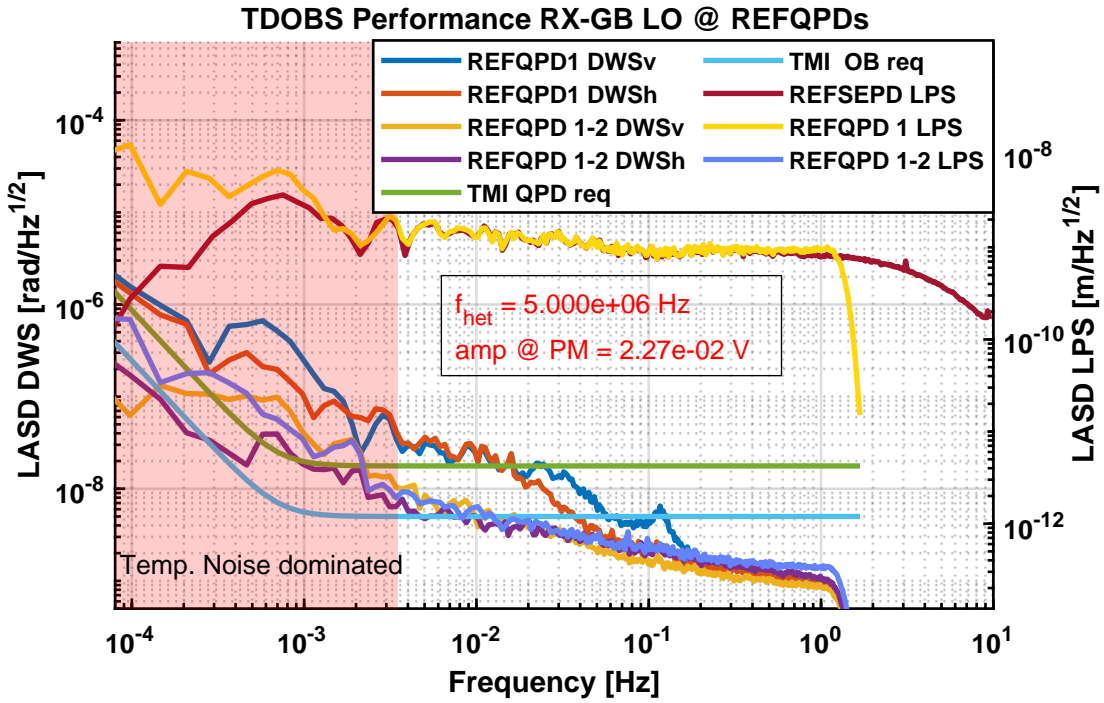


Figure 5.23: Calibrated DWS and LPS performance using the RX-GB & LO beams, the REFQPDs, 5 MHz heterodyne frequency and TIA #2.

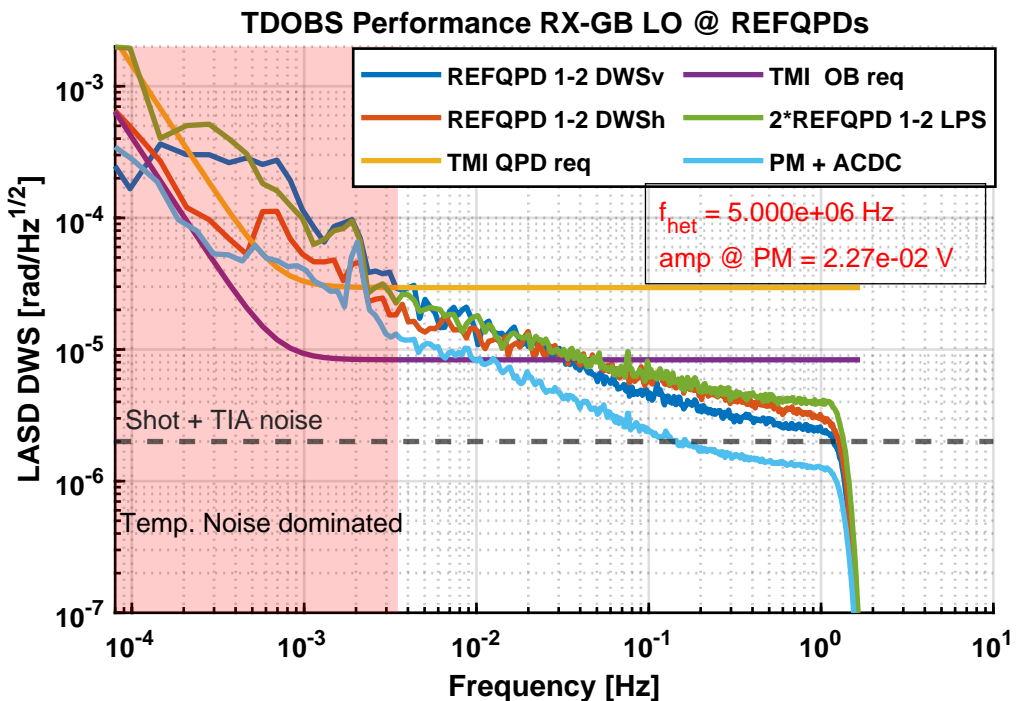


Figure 5.24: Raw DWS and LPS performance using the RX-GB & LO beams, the REFQPDs, 5 MHz heterodyne frequency and TIA #2, compared to a model of the combined electronic and shot noise and a measurement of the thermoelectronic phase noise.

REFQPD 1-2 is no better than REFQPD1. The DWS measurement never satisfies the LISA OB-level requirement and satisfies the LISA QPD-level requirement only for frequencies higher than 100 mHz.

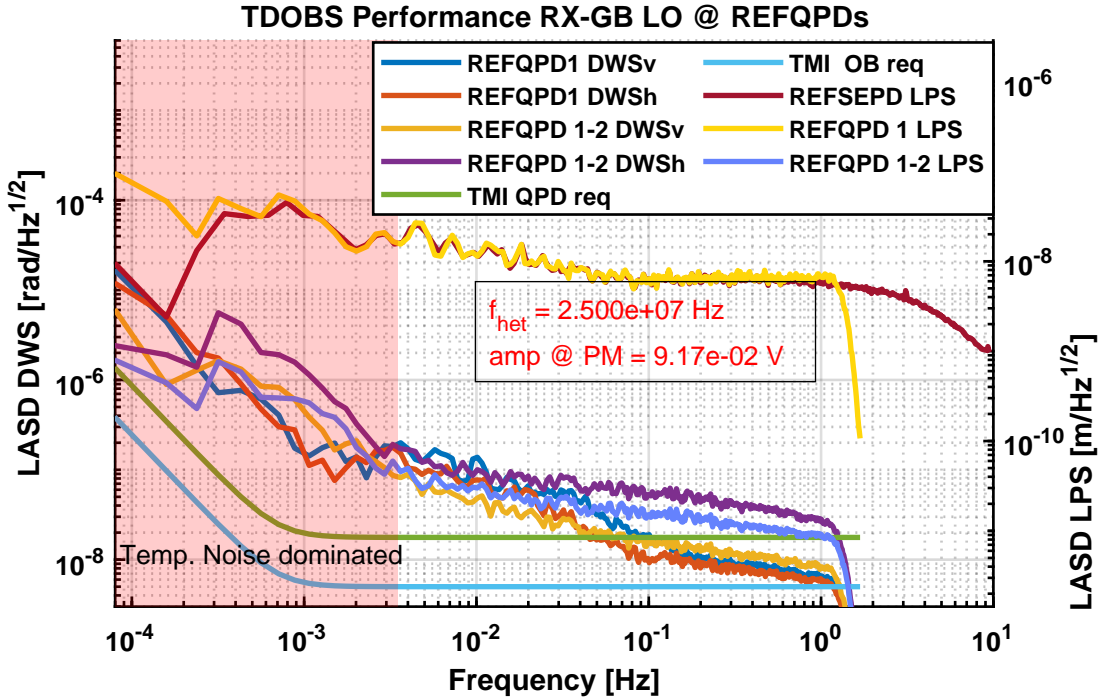


Figure 5.25: Calibrated DWS and LPS performance using the RX-GB & LO beams, the REFQPDs, 25 MHz heterodyne frequency and TIA #2.

Figure 5.26 is the same as Figure 5.22 but measured at $f_{\text{het}} = 25$ MHz. In this measurement, the phase noise from the AC-DC splitters and the PM is roughly a factor of 10 away from the measured DWS phase noise and therefore is unable to explain the measured phase noise. The modelled TIA and shot noise are not a limitation of this measurement. The noise in this measurement is, hence, not understood.

DWS performance comparison Figure 5.27 plots together the differential DWS performance of the three measurements above (Figures 5.20, 5.23, 5.25). Excluding the DWSH measurement at $f_{\text{het}} = 25$ MHz, all ASDs have approximately the same shape but are scaled by a different factor. This matches the statement that the limiting noise contribution is thermoelectronic noise, which has a coupling coefficient which increases with the heterodyne frequency.

Conclusion The DWS measurements using the REFQPDs perform very well at low heterodyne frequencies, reaching the LISA QPD-level requirement. The performance at $f_{\text{het}} = 25$ MHz is much worse. The noise sources are understood as being dominated by thermoelectronic noise in almost the whole detection band and by TIA and shot noise between ~ 0.5 Hz and 1 Hz. Better thermally isolating the AC-DC splitters and the PM leaves space to improve the DWS performance of TDOBS.

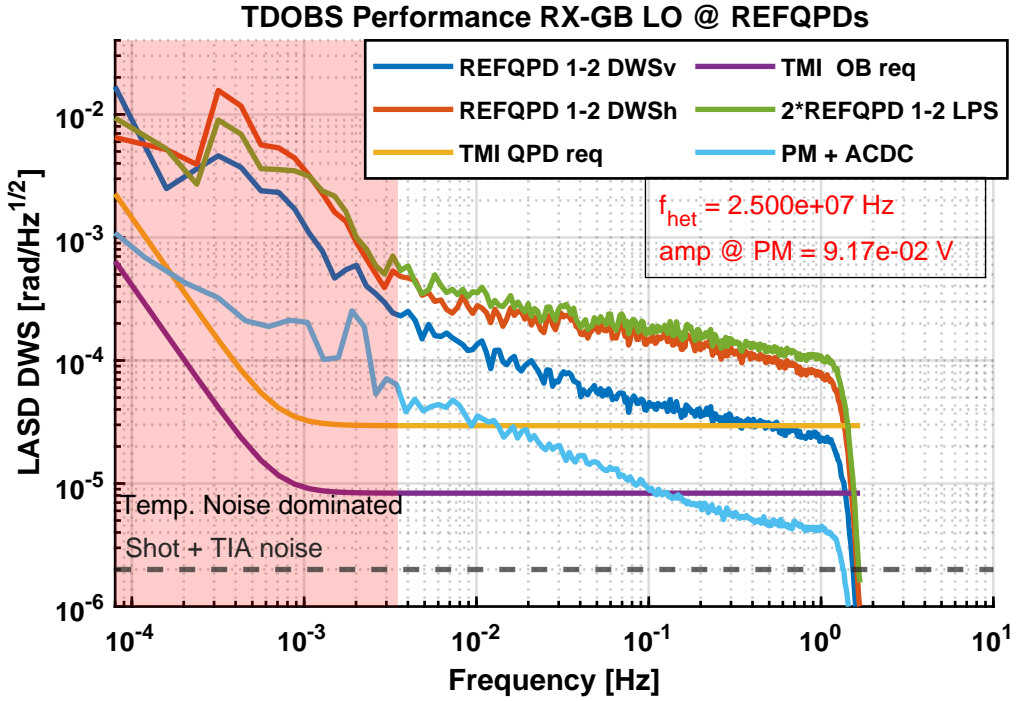


Figure 5.26: Raw DWS and LPS performance using the RX-GB & LO beams, the REFQPDs, 25 MHz heterodyne frequency and TIA #2, compared to a model of the combined electronic and shot noise and a measurement of the thermoelectronic phase noise.

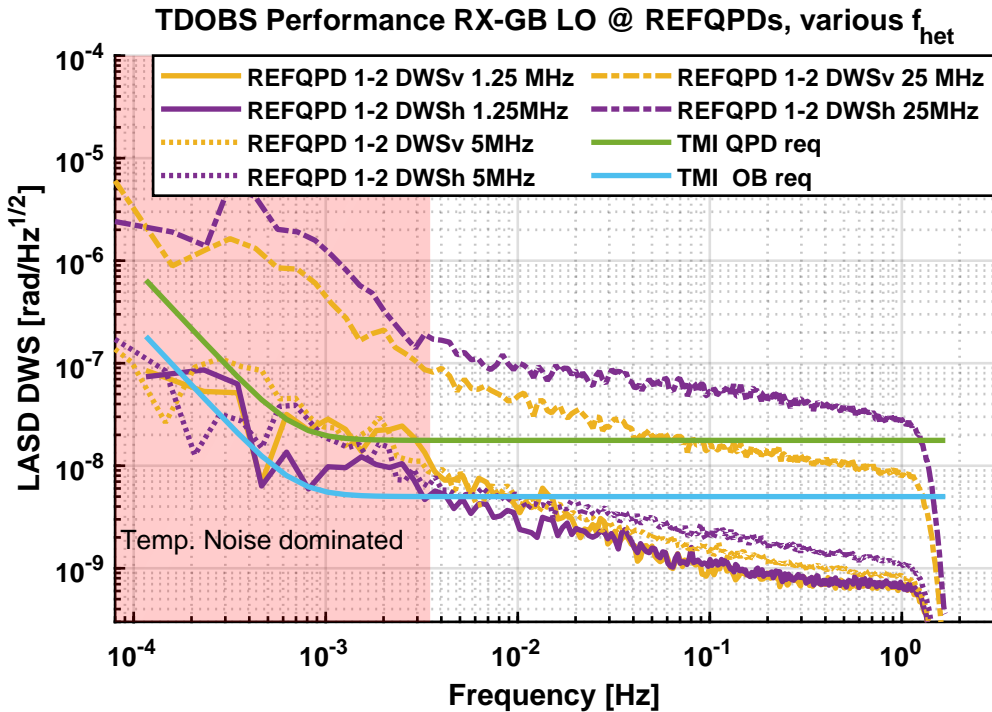


Figure 5.27: Comparison of the DWS performances using the RX-GB & LO beams, the REFQPDs and TIA #2 obtained at the heterodyne frequencies of 1.25 MHz (Figure 5.20), 5 MHz (Figure 5.23) and 25 MHz (Figure 5.25).

DWS performance with the RX-FT and LO beam on the REFQPDs

This measurement was performed using the flat top beam, RX-FT beam, with beam powers of $P_{\text{RX-FT}} = 0.21 \mu\text{W}$ and $P_{\text{LO}} = 5.3 \mu\text{W}$ per QPD segment, a second-stage gain of $G_{\text{ss}} = 2.87 \text{ V/V}$ and at a heterodyne frequency of $f_{\text{het}} = 5 \text{ MHz}$.

As the DWS gain is 20% larger than for the RX-GB & LO beams case, this measurement is expected to give a mildly better DWS angular readout noise if all other conditions are unchanged. This is approximately the case, as the power levels and beat note amplitudes are similar.

Figure 5.28 shows the measured DWS angular noise. As for the previous measurements using the RX-GB & LO beams, the DWS measurement from REFQPD1 is limited by the RX-GB beam's motion, with the characteristic $1/f$ trend and the peak shortly after 100mHz on the LASD. In the differential DWS the suppression of the RX-GB beam motion is not perfect, as a small peak at 100 mHz remains even after the subtraction. The differential DWS_v and DWS_h and LPS reach a common noise floor. This noise floor is slightly higher than that of the RX-GB & LO beams, but the difference is not significant.

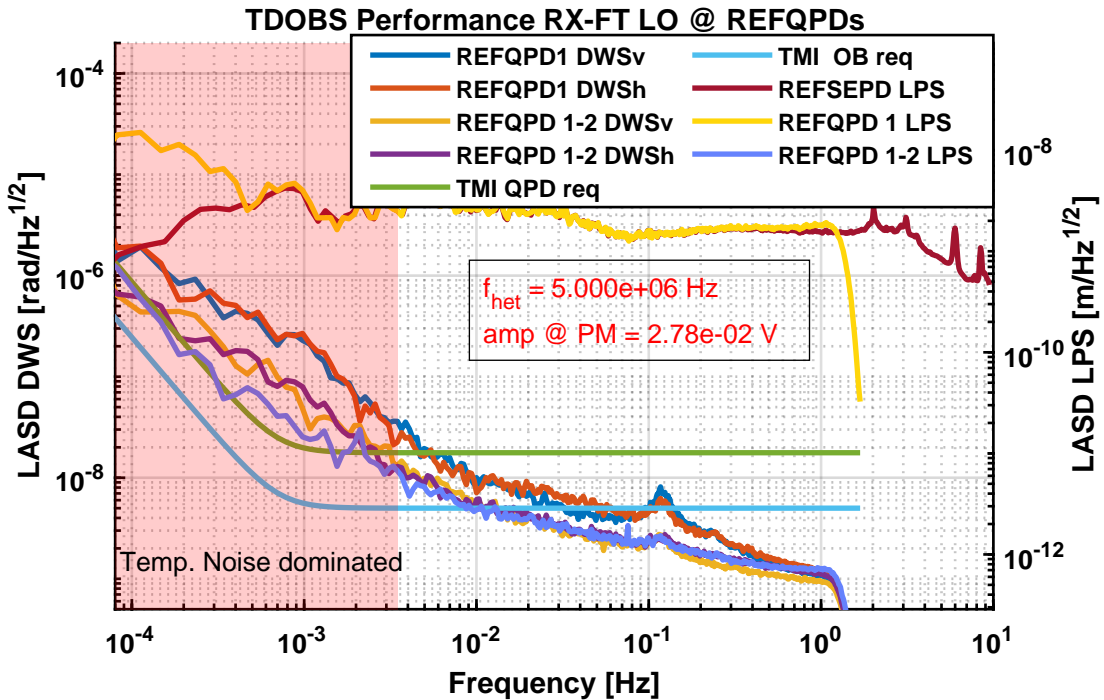


Figure 5.28: TDOBS performance with RX-FT & LO beams on the REFQPDs, 5 MHz heterodyne frequency and TIA #2

Figure 5.29 is the same as Figure 5.24 but measured using the RX-FT & LO beams. In this measurement, the phase noise from the AC-DC splitters and the PM is roughly a factor of 2 lower than the measured DWS phase noise, and therefore would be able to explain the measured phase noise. The modelled TIA and shot noise contributes to the measured DWS and LPS noise on the high-frequency end of the measured LASD. Hence, the noise in this measurement is understood.

The raw DWS performances from Figures 5.23 and 5.28 are shown together in Figure 5.30. These are found to be roughly equivalent, meaning that the DWS

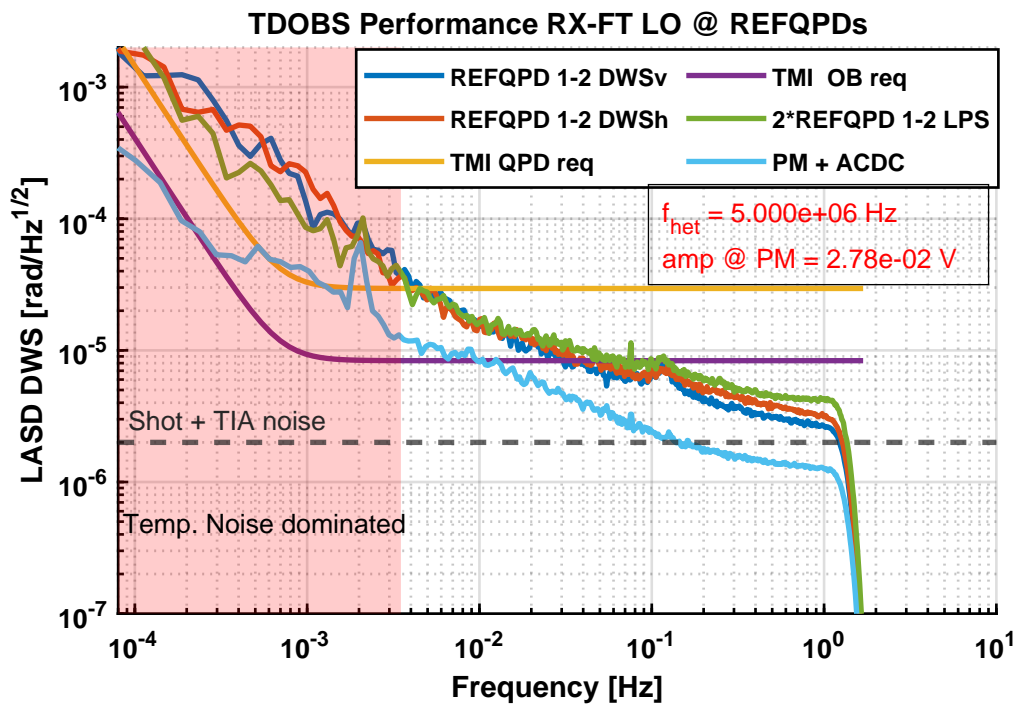


Figure 5.29: TDOBS performance with RX-FT & LO beams on the REFQPDs, 5 MHz heterodyne frequency and TIA #2

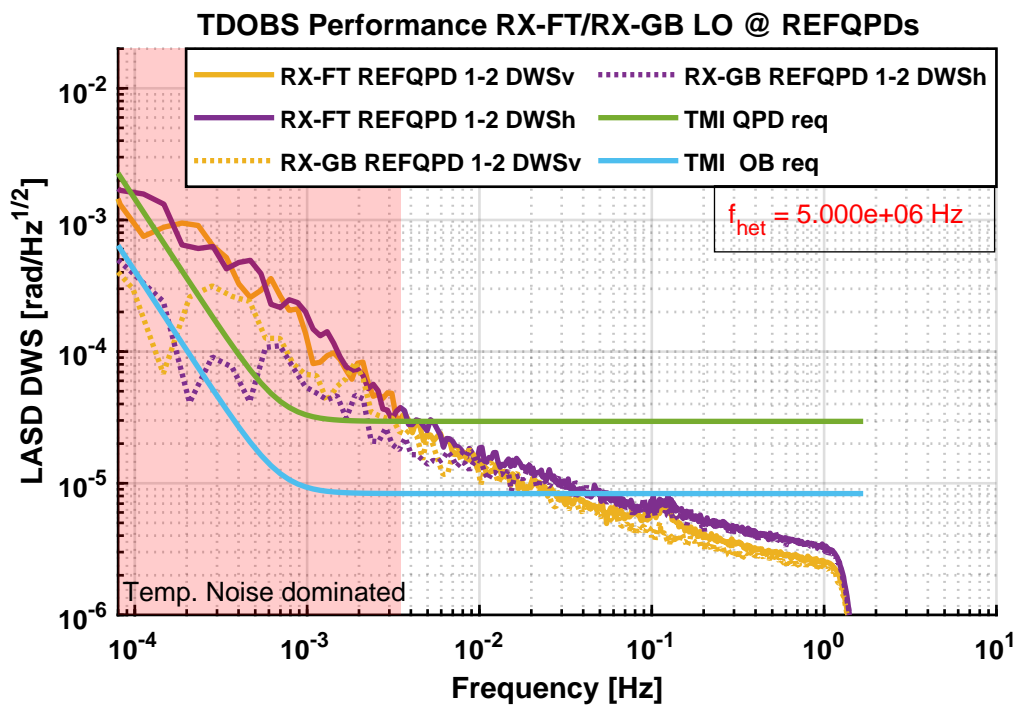


Figure 5.30: Raw performance comparison of the measured DWS with RX-GB & LO and RX-FT & LO on the REFQPDs

performance is not limited by the specifically used beams but rather by other noise sources along the measurement chain. This matches the understanding from Figures 5.22, 5.24, 5.26 and 5.28, where the main suspect is the thermoelectronic noise from the AC-DC splitters and the PM.

Conclusion For the DWS measurements using the RX-FT & LO beams the same holds as for the measurements using the RX-GB & LO beams. The noise contributions are understood and are the same. The use of a Flat-Top beam gives no sensitivity disadvantage with respect to a Gaussian beam, as the reached raw phase performance is equivalent.

DWS performance with the RX-GB and LO beam on the SCIQPDs

The SCIQPDs detect almost the totality of the beams impinging on them (see Table 3.7) due to the beam compression given by the imaging systems (ISs) placed in front of them. For this reason, they are not expected to be affected by straylight due to beam clipping.

The overall DWS gain at null angle, inclusive of IS and κ_1 coefficient at the QPD, is 80% larger than for the REFQPDs; leading to an expected lower noise floor. Note that the SCIQPDs still use the OpAmp-based TIA #1, giving a higher TIA noise. The second-stage amplification was set to $G_{ss} = 28.7$ V/V, while the beam powers were again of the order of 1 μ W per beam per segment.

As mentioned in Subsection 5.2.2, one straylight source was not found for this peculiar configuration during the noise hunting. The excess noise due to straylight can be seen in Figure 5.31, where the time series of the measured DWS and differential DWS during a 100 s time interval of this DWS performance measurement is shown. A small vector noise (SVN) affecting all measured DWS signals measured by REFQPD1 and REFQPD2 is visible. For unknown reasons, the vertical DWS from REFQPD1 is much less affected. The amplitude of the phase error around the measured signal is 100 μ rad, meaning that the intensity of the stray beam is roughly 100 pW. This SVN only partially cancels out in the vertical differential DWS measurement and does not appear to be reduced in the horizontal differential DWS measurement.

Figure 5.32 shows the IS-calibrated DWS performance using the RX-GB & LO beams on the SCIQPDs. Apparent similarities are visible with the single QPD DWS measurements in Figures 5.20 and 5.23 using the REFQPDs, as the ASDs are dominated by the RX-GB beam's motion, with the characteristic peak at ~ 100 mHz. The height of the peak in the calibrated ASDs in Figure 5.32 roughly matches that measured in Figures 5.20 and 5.23, as expected. The DWS_v measurement from REFQPD1, which is less affected by the SVN, reaches the detector's sensitivity in the last tip of the LASD between 0.7 Hz and 1 Hz.

The differential DWS_v measurement shows a good cancellation of the RX-GB beam's motion, while in the differential DWSh a peak of comparable height is still visible. The amplitude of the SVN is reduced for the differential DWS_v measurement, but it is not for the differential DWSh. Figure 5.32 also shows the calculated shot plus electronic noise for the used beam powers, which appears to have been overestimated if compared to the REFQPD1 DWS_v curve in Figure 5.32.

Figure 5.33 compares the measured differential DWS performance at $f_{het} =$

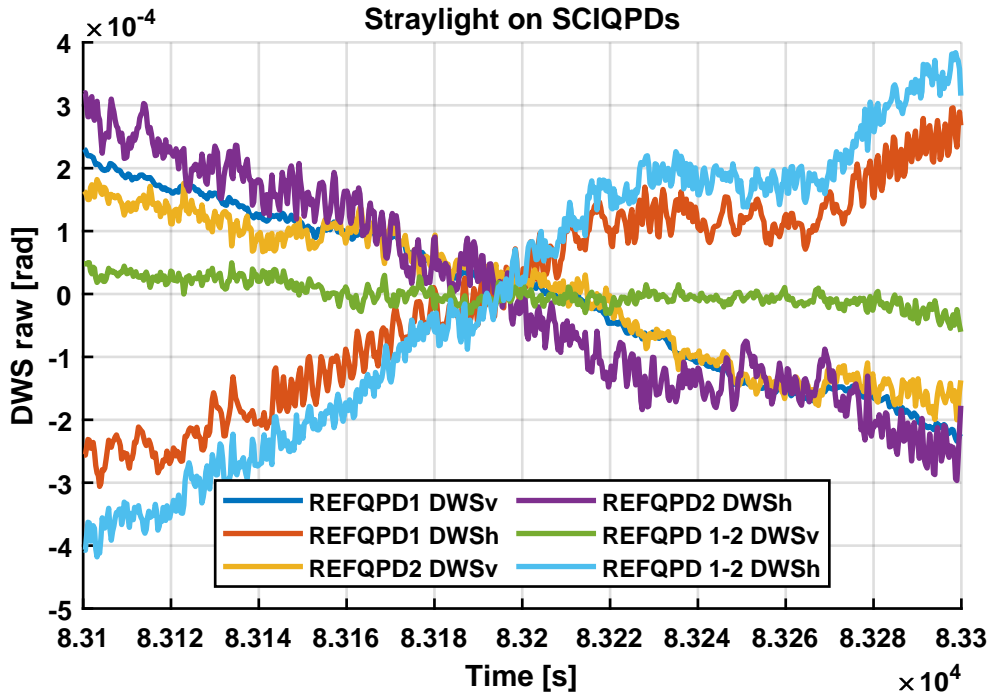


Figure 5.31: Time series of the RX-GB & LO beams on the SCIQPDs DWS performance measurement. From this plot, is clearly visible how all traces are affected by SVN. The REFQPD1 DWS_v trace is much less affected. The suspect for this is an efficient cancellation of the SVN in the DWS calculation.

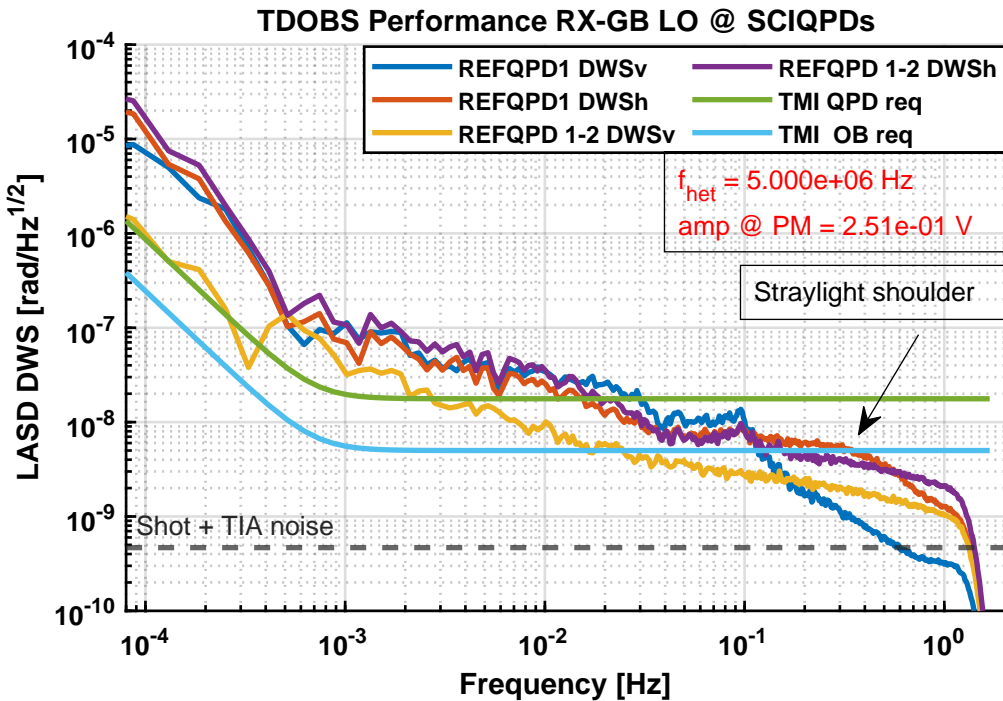


Figure 5.32: TDOBS performance with RX-GB & LO beams on the SCIQPDs, 5 MHz heterodyne frequency and TIA #1. This plot takes into account the magnification $m_{iS} = 2.5$ given by the IS.

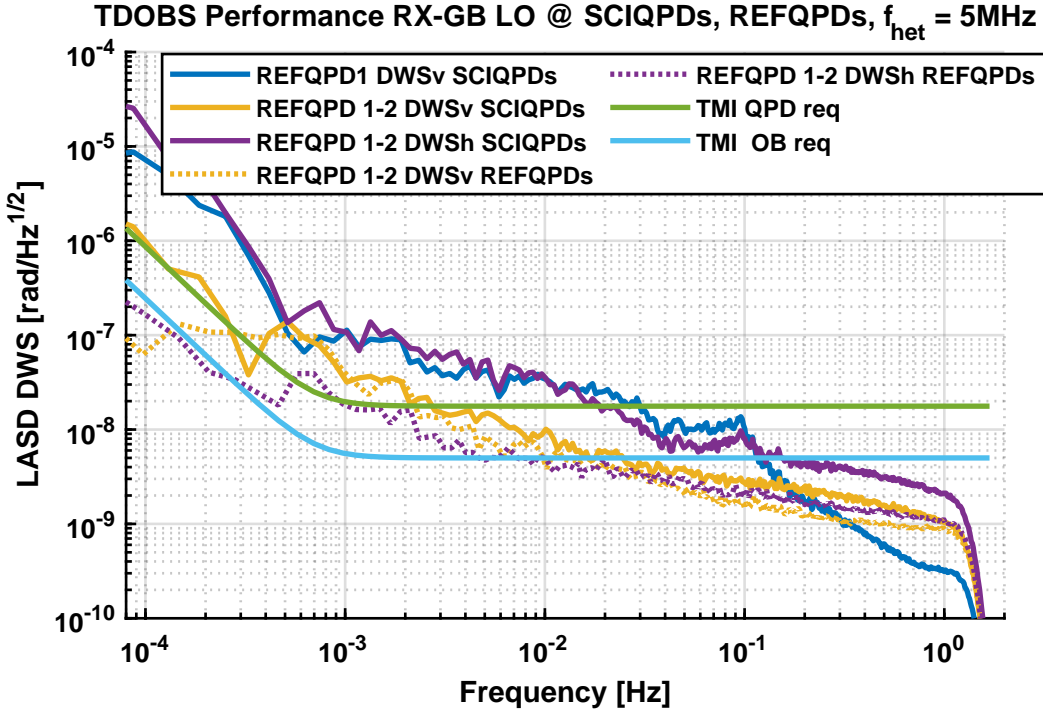


Figure 5.33: TDOBS performance with RX-GB & LO beams on the SCIQPDs, 5 MHz heterodyne frequency and TIA #1. This plot takes into account the magnification $m_{iS} = 2.5$ given by the IS.

5 MHz using the RX-GB & LO beams obtained using the REFQPDs and the SCIQPDs. As predicted, the sensitivity of the SCIQPDs can, in principle, be much higher due to the higher overall DWS gain. Unfortunately, due to the straylight this is reached only at the high-frequency end of the LASD of REFQPD1 DWS_v measured by the SCIQPDs, where the angular sensitivity reached by REFQPD1 alone is better by a factor of 3 than that of the differential DWS from the REFQPDs. In the rest of the band, the differential DWS from the SCIQPDs is dominated by the SVN, which is likely combined with thermoelectronic phase noise at low frequencies. The reached performance is slightly worse than that of the REFQPDs.

5.5 Conclusion

In the first part of this chapter the noise requirements given by ESA for LISA were broken down to OB-level and QPD-level requirements. Such distinction is essential, as the interferometers in LISA use a different number of QPDs than TDOBS. By comparing the DWS gains, equivalent angular DWS requirements were derived for TDOBS.

In the second part of this chapter, a phase noise budget of TDOBS, which can easily be transformed in either a DWS or LPS noise budget. Individual contributions for TDOBS were characterized using the experimental description from Section 3.3 and measured. This part also reports on the finding and mitigation of straylight, mostly in the TS. The dominant noise sources are found to be shot noise and electronic noise from the TIA.

The last part of this chapter reports on the performance measurements that were performed in various interferometric configurations and at various heterodyne frequencies, using either the RX-GB beam or the RX-FT beam, together with the LO beam impinging either on the REFQPDs or the SCIQPDs. These have have confirmed the noise budget at low heterodyne frequencies, where on the high-frequency end the dominating noise sources are shot noise and electronic noise, while lower frequencies are limited by thermoelectronic phase noise. The noise at high heterodyne frequencies (25 MHz) is higher than the noise budget predicts, and is not fully understood. No phase noise due to straylight was found to affect the REFQPDs, while the performance at the SCIQPDs was found to be limited by straylight.

Possible improvements to TDOBS's sensitivity could come by modifying the AC-DC splitters' circuit or by improving their temperature stability as well as that of the PM. This could potentially also solve the excess of DWS noise measured at high heterodyne frequencies. The potentially much more sensible SCIQPDs are limited by an unsolved small vector noise (SVN) due to straylight, which is to be solved in the future. In the current situation, the REFQPDs are therefore the candidate QPDs to be used for performing LISA related investigations.

Chapter 6

LISA-like Noise Investigations

TDOBS is a simplified version of the OB in LISA and can simulate the interference which will happen in LISA, with variable heterodyne frequency, MHz compatible photoreceivers and synthetic tilts. This chapter reports the result of some investigations of high relevance for the LISA mission, which address some gaps of the current knowledge on the DWS performance. These are tests of the DWS performance in weak-light conditions, as in the ISI, and of the DWS performance in presence of beam tilts.

6.1 DWS performance with low RX beam power

The inter-satellite interferometer (ISI) is operated with very weak light. The planned beam powers are 1 mW for the TX beam and 455 pW for the RX beam [30]. Taking into account only the power in the carrier ($\eta_{\text{car}} = 0.81$, Table 6.1) and after the beam splitting, this nominally corresponds to 50.6 pW per segment for the TX beam and 23 pW per segment for the RX beam. The DWS performance in TDOBS was tested in such weak-light conditions to prove the operability of LISA's phase readout.

As mentioned in section 5.2 and shown in Figure 5.12, the coupling of most noise sources, except thermoelectronic phase noise and cross-talk, depends on the C/N_0 in equation (2.71). The expectation for such a measurement is that given the very small signal amplitude, the C/N_0 -dependent noises are dominant. As the carrier's RMS amplitude is $\sqrt{2\eta_{\text{het}} P_{\text{LO}} P_{\text{RX}}}$ and hence proportional to $\sqrt{P_{\text{RX}}}$, the total phase noise $\tilde{\varphi}_{\text{tot}}$ and its contributions can be modelled to be proportional to the inverse square root of P_{RX} .

$$\tilde{\varphi}_{\text{tot}} = \frac{k_{\text{tot}}}{\sqrt{P_{\text{RX}}}} \quad \tilde{\varphi}_{\text{shot}} = \frac{k_{\text{shot}}}{\sqrt{P_{\text{RX}}}} \quad \tilde{\varphi}_{\text{en}} = \frac{k_{\text{en}}}{\sqrt{P_{\text{RX}}}} \quad (6.1)$$

where k_{tot} [rad Hz $^{-\frac{1}{2}}$ W $^{\frac{1}{2}}$] is an estimation of the total noise in signal, e.g DWS, and same for k_{shot} and k_{en} . This holds for shot noise (2.82), electronic noise (5.19), and approximately for PM noise if the signal's amplitude is very small. This last fact can be seen in Figure 5.14, where for very low signal powers the FMC PM noise approximately scales as the inverse of the amplitude of the input signal. These three noises are expected to be dominant from the budget in Figure 5.12.

The phase noise $\tilde{\varphi}_{\text{tot}}$ was measured as a function of P_{RX} to characterize the dependency of the total phase noise on the amplitude of the RX beam and understand the contributions to it. The first goal of this measurement is to verify the DWS

TDOBS		ISI LISA			
Parameter	Value	Parameter	Value	Value	
			worst	nominal	best
beams		beams		RX & TX	
$\sigma_{\text{RX-GB, REF}}$	0.371	σ_{RX}		1	
$\sigma_{\text{LO, REF}}$	0.488	σ_{TX}		1	
η_{car}	1	η_{car}		0.81	
η_{QPD}	0.7	η_{QPD}	0.8	0.93	0.93
$\sqrt{\eta_{\text{het}}}$	0.86 ± 0.01	$\sqrt{\eta_{\text{het}}}$	0.7	0.74	0.85
$\sqrt{\eta_{\text{QPD}}\eta_{\text{het}}}$	0.72	$\sqrt{\eta_{\text{QPD}}\eta_{\text{het}}}$	0.63	0.71	0.82
P_{LO}	28/44 μW	P_{TX}	37 μW	62 μW	110 μW
P_{RX}	variable	P_{RX}	23 pW	28 pW	65 pW
$\eta_{\text{car}} P_{\text{LO}}$	28/44 μW	$\eta_{\text{car}} P_{\text{TX}}$	30 μW	51 μW	89 μW
$\eta_{\text{car}} P_{\text{RX}}$	variable	$\eta_{\text{car}} P_{\text{RX}}$	19 pW	23 pW	53 pW
r_{REFQPDs}	0.5 mm	r_{QPD}		0.75 mm	

Table 6.1: Table with the parameters of the TDOBS interferometer and of the ISI in LISA. The parameters for LISA are taken from [30]. The power values P_{RX} , P_{LO} and P_{TX} refer to the beam power per QPD segment. The heterodyne efficiencies correspond to equation (2.27) calculated for the a Gaussian beam size of $0.34\text{mm} \leq w_0 \leq 0.46\text{ mm}$ mentioned in subsection 5.1.1. The σ parameters are taken from Table 3.7 and represent the fraction of beam power which impinges on the QPDs. $P_{\text{LO}} = 28\text{ }\mu\text{W}$ was used for the measurement with TIA #1, and $P_{\text{LO}} = 44\text{ }\mu\text{W}$ was used for the measurement with TIA #2.

performance itself in ISI-like conditions, and the second goal is to verify if the PM matches its requirements, which are listed in Subsection 5.1.2.

6.1.1 Setup Description

Two QPDs are used simultaneously to synthesize a null DWS measurement as described in Subsection 5.4.2. The REFQPDs were chosen over the SCIQPDs as they are affected by less noise (see Section 5.4). The chosen heterodyne frequency is 5 MHz, as the overall phase noise for heterodyne frequencies within the LISA heterodyne band is the lowest (see Section 5.4). As shown in Figure 5.30, the DWS performance obtained on the REFQPDs using the RX-GB & LO beams is very close to that of the RX-FT & LO beams; this test was hence performed with the much easier-to-handle RX-GB beam (see Sub-subsection 4.4). The used phasemeter is the FMC PM. The used LO beam power is slightly less than the worst-case TX power in the ISI. To comprehend the fidelity of TDOBS as a weak-light simulator for LISA, a list of the relevant beam parameters in both TDOBS and LISA is shown in Table 6.1. The three main differences are that

- In LISA, the beams are smaller than in the TS in TDOBS, while the QPD size is larger. This means that the whole power of the beams is detected by the QPDs, while for the REFQPDs the detected power is less than 50%. This has to be considered when calculating the phase noise due to shot noise.
- The heterodyne efficiency and the quantum efficiency of the QPDs are different. Shot noise, which is dominant at low powers, depends on the product

$\sqrt{\eta_{\text{QPD}}\eta_{\text{het}}}$. This quantity is calculated in Table 6.1; the GAP1000Q QPDs used in TDOBS happen to be representative of the nominal case of the ISI.

- In LISA the voltage signal from the TIA is amplified by a variable gain amplifier to match the input range of the PM. TDOBS uses a second-stage amplifier with only three gain options, $G_{\text{ss}} \in [2.87, 28.7, 57.4]$ V/V. This can limit the DWS performance at low beam amplitudes, as the PM adds phase noise if the input signal's amplitude is too small (see Subsection 5.3).

This measurement was first performed with the OpAmp based TIA #1 (section 6.1.3) and afterwards repeated following the upgrade to the transistor based TIA #2 (section 6.1.4). The results show an improvement in the phase noise due to a lower noise TIA.

6.1.2 Beam Power Control

The RX beam's power is controlled by regulating the amplitude of RF the signal fed to the RX AOM. The very small RX power impinging on the QPDs is estimated using the amplitude of the beat note A_b measured by the PM. As $A_b \propto \sqrt{P_{\text{RX-GB}}}$, after measuring a reference power $P_{\text{RX-GB}, 0}$ and a corresponding reference beat note amplitude $A_{b,0}$, the RX power can be recovered from the measured A_b as

$$P_{\text{RX-GB}} = P_{\text{RX-GB}, 0} \left(\frac{A_b}{A_{b,0}} \right)^2. \quad (6.2)$$

6.1.3 LMH6624 Opamp based TIA #1 Results

This measurement was performed in vacuum at a pressure of 1 mbar, while the temperature conditions in the lab were those described by the feedback AC circuit in Figure 5.17. A minimum second-stage amplification of $G_{\text{ss}} = 2.87$ V/V was used. The resulting LASDs are shown in Figure 6.1 alongside the DWS noise requirements for the ISI at OB- and QPD-level. It is very clear from this measurement how each LASD consists of C/N_0 -independent noise floor, on top of which C/N_0 -dependent noises become more relevant as the power is decreased. The 0.1-100mHz band is always dominated by the power-independent noise floor, while for frequencies higher than 100mHz the dominant noise is power-dependent. As stated in Section 5.4, this is understood to be thermoelectronic phase noise.

There is an exception in this measurement, as the shape of the LASD in the C/N_0 -independent band is different than that of the measured temperature LASD. The feature present in Figure 6.1 has been noticed only with this specific TIA model and only for a heterodyne frequency of 5 MHz. Evidence points to this as electronic cross-talk at the TIA, as straylight would be heterodyne-frequency-independent.

The phase noise density $\tilde{\varphi}_{\text{tot}, i}$ is estimated from the power-dependent band of the LASDs in Figure 6.1. The power-dependent phase noise is estimated by averaging the white part of each LASD. Note that the used frequency band varies as a function of the RX beam's power, from a minimum bandwidth of 0.1÷1 Hz to a maximum of 0.01÷1 Hz. Also, note that for the highest power measurement, the power-independent noise sources are still contributing. The RX power values $P_{\text{RX}, i}$ are calculated from equation (6.2). It is convenient to perform analysis calculating the

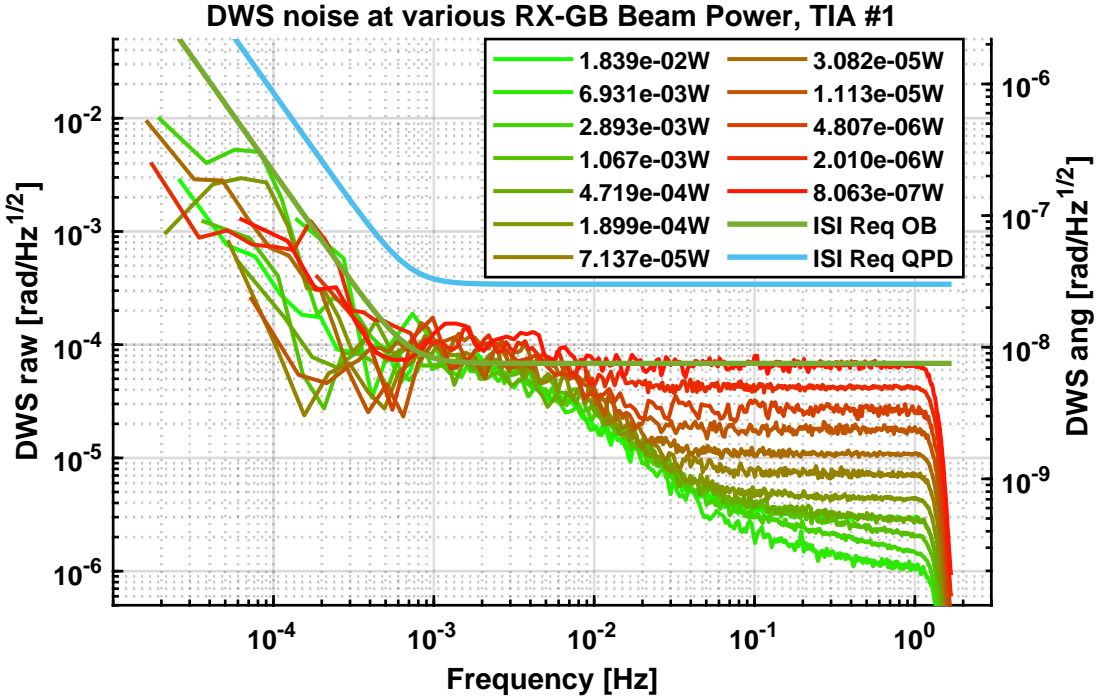


Figure 6.1: Measured differential DWS LASDs for various RX-GB beam powers at a 5 MHz heterodyne frequency. The LO beam power impinging on each segment of the QPD is 28 μ W. The RX beam power values per segment \bar{P}_{RX} are reported in the legend. The measured phase noises are better than the worst case ISI DWS requirement at QPD-level (ISI Req QPD), but as the RX-GB power is more than the RX beam in LISA the consequences of this are not straightforward.

\log_{10} of the measured quantities, as taking the logarithm of equation (6.1) yields the very simple expression

$$\log_{10}(\tilde{\varphi}_{\text{tot}}) = \log_{10}(k_{\text{tot}}) - \frac{1}{2} \log_{10}(P_{\text{RX}}), \quad (6.3)$$

which is a line with a fixed slope of $-1/2$. The data was linearly fit with the function $\log_{10}(\tilde{\varphi}_{\text{tot}}) = -\frac{1}{2} \log_{10}(P_{\text{RX}}) + p_0$ where $p_0 = \log_{10}(k_{\text{tot}})$ is the parameter needed for describing the overall noise of the setup. The data and the fit result are shown in Figure 6.2. The result shows that equation (6.1) is a good model to describe the dependence of the noise density on the power. The highest power points don't fully follow this trend as thermoelectronic phase noise still contributes.

Figure 5.12 also reports the DWS requirement for LISA at both OB- and QPD-level and the RX power values at which this requirement has to be reached. In this configuration TDOBS manages to reach the QPD performance requirement for LISA (see Table 5.5, the performance that TDOBS has to reach in order to demonstrate the operation of the ISI using four QPDs) but not that at OB-level (a more stringent requirement which would demonstrate the operation of LISA using just one QPD).

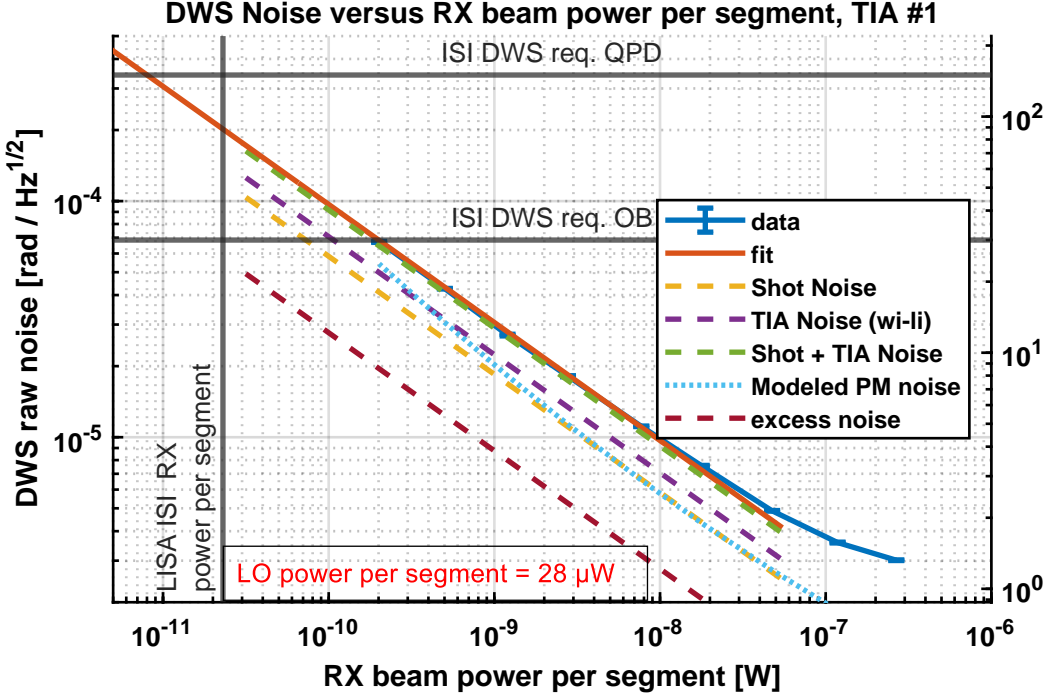


Figure 6.2: Measured DWS noise floor as a function of the RX-GB beam power plotted together with a linear fit and the understood power-dependent noise contributions. The PM noise contribution is modelled using the results in Subsection 5.3. The electronic noise from the TIA is modelled using the $\tilde{i}_{\text{en}, \#1, 5 \text{ MHz}}$ value measured in Figure 3.19. The fit function is $\log_{10}(\tilde{\varphi}_{\text{tot}}) = -\frac{1}{2} \log_{10}(P_{\text{RX}}) + p_0$. The four highest power points are excluded from the fit because other noise sources contribute. For convenience of comparison with the noise from the PM, the fit is executed using the uncalibrated DWS. The fitted value is $p_0 = -9.014 \pm 0.001$, which in terms of phase noise per power is $k_{\text{tot}} = 968.2 \pm 3.2 \text{ prad Hz}^{-\frac{1}{2}} \text{ W}^{\frac{1}{2}}$.

Noise Analysis

Let's assume that the measured noise was only due to shot noise and electronic noise; the electronic noise can then be characterized as

$$\begin{aligned}
 k_{\text{en}} &= \sqrt{k_{\text{tot}}^2 - k_{\text{shot}}^2} \\
 &= \sqrt{k_{\text{tot}}^2 - \frac{h\nu_l}{\eta_{\text{QPD}}\eta_{\text{het}}}} \\
 &= 782.3 \pm 5.3 \text{ prad Hz}^{-\frac{1}{2}} \text{ W}^{\frac{1}{2}}.
 \end{aligned} \tag{6.4}$$

This amount of phase noise corresponds to an equivalent input current noise density of the TIA of

$$\begin{aligned}
 \tilde{i}_{\text{en}} &= A \sqrt{2\eta_{\text{het}} P_{\text{RX}} P_{\text{LO}}} \tilde{\varphi}_{\text{en}} \\
 &= A \sqrt{2\eta_{\text{het}} P_{\text{LO}}} \sqrt{k_{\text{tot}}^2 - \frac{h\nu_l}{\eta_{\text{QPD}}\eta_{\text{het}}}} \\
 &= 3.021 \pm 0.067 \text{ pA}/\sqrt{\text{Hz}}.
 \end{aligned} \tag{6.5}$$

This is significantly more than $\tilde{i}_{\text{en}, \#1, 5 \text{ MHz}} = 2.73 \pm 0.04 \text{ pA}/\sqrt{\text{Hz}}$, which is the amount measured in Figure 3.19. This leads to the conclusion that some other power-dependent noise contribution is present. As in Figure 5.12 no other noise contribution is present that would come close the level of shot noise and TIA noise on a DWS measurement, this excess noise is interpreted as phase measurement noise by the FMC PM. This measurement was performed with low amplitude beat notes being fed to the PM, as the second-stage amplification was only $G_{\text{ss}} = 2.87 \text{ V/V}$. As shown in Figure 5.14 the FMC PM's noise on the low signal end is roughly proportional to the inverse of the amplitude, and the amplitude is proportional to $\sqrt{P_{\text{RX}}}$, making it a good approximation to also describe the phase readout noise of the FMC PM with equation (6.1) as

$$\tilde{\varphi}_{\text{PM}} = \frac{k_{\text{PM}}}{\sqrt{P_{\text{RX}}}}. \quad (6.6)$$

Hence, the PM's noise contribution as a function of the RX beam power is

$$\begin{aligned} k_{\text{PM}} &= \sqrt{k_{\text{tot}}^2 - k_{\text{shot}}^2 - k_{\text{en}}^2} \\ &= 277 \pm 59 \text{ prad Hz}^{-\frac{1}{2}} \text{ W}^{\frac{1}{2}}. \end{aligned} \quad (6.7)$$

The noise contributions characterized so far are listed in Table 6.2. Note that the estimated excess noise is significantly less than the modelled PM noise (visible in Figure 6.2). This likely means that shot noise and electronic noise have been overestimated. This is likely due to the use of wrong power values. Besides, note that this measurement is limited by electronic noise and shot noise. To the knowledge of the author, this is the first TIA-limited DWS measurement in LISA-like and weak-light conditions.

Noise source	Amount [prad Hz $^{-\frac{1}{2}}$ W $^{\frac{1}{2}}$]	
Electronic noise from TIA #1	707	\pm 22
Shot noise	600.5	\pm 7.0
FMC PM	277	\pm 59
Total	968.2	\pm 3.2

Table 6.2: Estimated noise contributions in the low RX power measurement using TIA #1, expressed in uncalibrated phase noise density per square root of power.

Phasemeter Requirement Verification

If there was no excess noise from the PM, the beat note's noise contributions would be those from shot noise and electronic noise. Added up, these give a power-dependent noise level of

$$\begin{aligned} (\text{C}/\text{N}_0)^{-1} \cdot (P_{\text{beat}})^{\frac{1}{2}} &= \sqrt{\frac{h\nu_l}{\eta_{\text{QPD}}\eta_{\text{het}}} + \left(\frac{\tilde{i}_{\text{TIA}}}{A\sqrt{2\eta_{\text{het}}P_{\text{LO}}}}\right)^2} \\ &= 928 \pm 17 \text{ prad Hz}^{-\frac{1}{2}} \text{ W}^{\frac{1}{2}}. \end{aligned} \quad (6.8)$$

The beat note fed to the PM would reach a C/N_0 of $C/N_{0, \text{req}} = 177 \mu\text{rad}/\sqrt{\text{Hz}}$ (see Subsection 5.1.2) for a RX beam power of

$$P_{\text{RX, req}} = \left(\frac{(C/N_{0, \text{req}})^{-1}}{(C/N_0)^{-1} \cdot (P_{\text{beat}})^{\frac{1}{2}}} \right)^2 = 27.5 \text{ pW.} \quad (6.9)$$

The phase noise contribution by the PM at this power $P_{\text{RX}} = P_{\text{RX, req}}$ is

$$\begin{aligned} \tilde{\varphi}_{\text{PM}} &= \frac{k_{\text{PM}}}{\sqrt{P_{\text{RX}}}} \\ &= 2.77 \times 10^{-10} \cdot (27.5 \times 10^{-12})^{-\frac{1}{2}} \\ &= 52.9 \pm 11 \mu\text{rad}/\sqrt{\text{Hz}}, \end{aligned} \quad (6.10)$$

which is more than the LISA PM in Table 5.7 allows. This means that by using TIA #1 and using too little second-stage amplification, albeit the LISA QPD-level requirement is reached, the PM requirement is not.

6.1.4 BFP740 Transistor and AD8038 Opamp based TIA #2

This measurement was performed at air pressure, while the temperature conditions in the lab were those described by the bang-bang AC circuit in Figure 5.17. second-stage amplification with a gain $G_{\text{ss}} = 57.4 \text{ V/V}$ is used from the fourth measurement onwards, as the amplitude of the beat note from the TIA was small enough to fit in the ADC range if amplified. In the first three measurements the second-stage amplification is still $G_{\text{ss}} = 2.87 \text{ V/V}$. A small reduction of the noise is visible when the second-stage amplification is added (see Figure 6.3). This is understood as a reduction in the phase readout noise by the FMC PM as the signal increased in amplitude. The resulting LASDs are shown in Figure 6.3 alongside the DWS noise requirements for the ISI at OB and QPD level and the power amounts at which such requirements have to be met.

As already mentioned in Section 5.4, the LASDs are totally thermoelectronic-noise-dominated for frequencies lower than 3 mHz. No other C/N_0 -independent noise source is present other than thermoelectronic phase noise, which determines the noise floor from 0.1 mHz all the way up to a few $\mu\text{rad}/\sqrt{\text{Hz}}$ at 1 Hz, together with the contribution of electronic and shot noise. In this configuration, TDOBS manages to reach the QPD performance requirement for LISA, but not that at OB-level.

The estimation of the phase noise contribution is done, as in the case of TIA #1, by averaging the white part of the LASDs in Figure 6.3. For this measurements, the DWS performance at the lowest beam powers is tested for frequencies as low as 3 mHz.

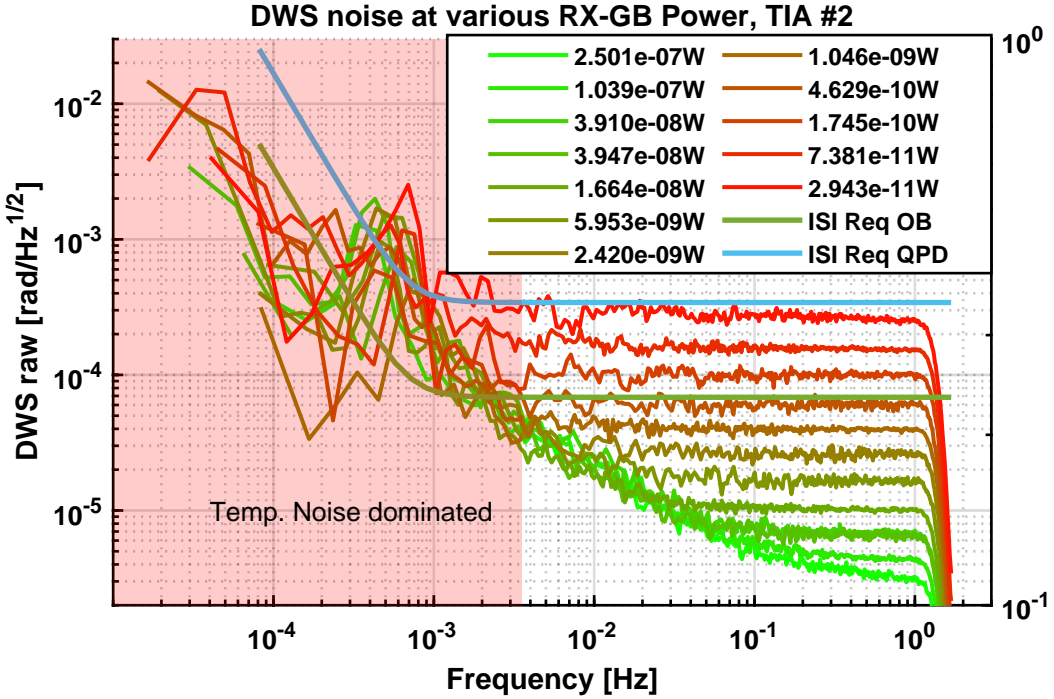


Figure 6.3: Measured differential DWS LASDs for various RX-GB beam powers at a 5 MHz heterodyne frequency. The LO beam power impinging on each segment of the REFQPDs is 44 μ W. The RX beam power values per segment \bar{P}_{RX} are reported in the legend. The measured noise curves are better than the worst-case ISI DWS requirement at QPD-level also for RX-GB powers lower than that of the RX beam in LISA (the power range is shown in Figure 6.4).

Noise Analysis

If the measured noise was only due to shot noise and electronic noise, the electronic noise would be

$$\begin{aligned}
 \tilde{\varphi}_{\text{en}} &= \sqrt{\varphi_{\text{tot}}^2 - \tilde{\varphi}_{\text{shot}}^2} \\
 &= \frac{1}{\sqrt{P_{\text{RX}}}} \sqrt{k_{\text{tot}}^2 - \frac{h\nu_l}{\eta_{\text{QPD}}\eta_{\text{het}}}} \\
 &= 290 \pm 15 \text{ prad Hz}^{-\frac{1}{2}} \text{ W}^{\frac{1}{2}}.
 \end{aligned} \tag{6.11}$$

This amount of phase noise corresponds to an equivalent input current noise density of

$$\begin{aligned}
 \tilde{i}_{\text{TIA}} &= A \sqrt{2\eta_{\text{het}} P_{\text{RX}} P_{\text{LO}}} \tilde{\varphi}_{\text{en}} \\
 &= A \sqrt{2\eta_{\text{het}} P_{\text{LO}}} \sqrt{k_{\text{tot}}^2 - \frac{h\nu_l}{\eta_{\text{QPD}}\eta_{\text{het}}}} \\
 &= 1.403 \pm 0.079 \text{ pA}/\sqrt{\text{Hz}}.
 \end{aligned} \tag{6.12}$$

This is less than the measured TIA #2 noise at 5 MHz from Figure 3.19, which is $\tilde{i}_{\text{en}, \#2, 5 \text{ MHz}} = 1.6208 \pm 0.0015 \text{ pA}/\sqrt{\text{Hz}}$.

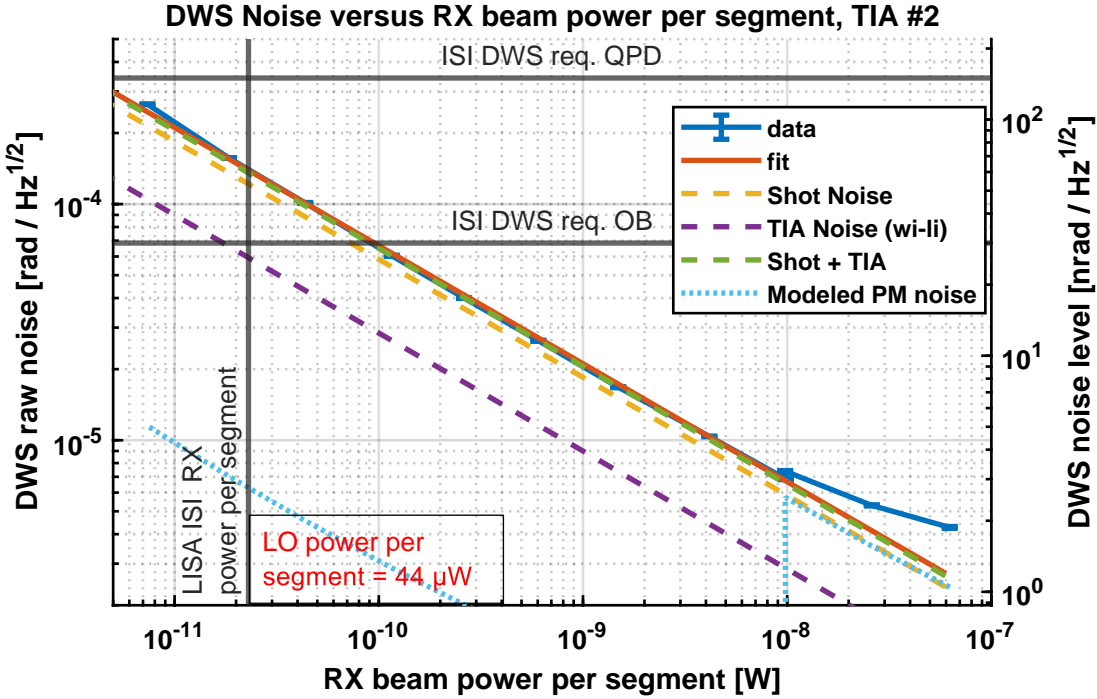


Figure 6.4: Measured DWS noise floor as a function of the RX-GB beam power plotted together with a linear fit for and the understood noise contributions. The PM noise contribution is modelled using the results in 5.3. Note that as the second-stage amplification is in use (measurement from 10^{-8} W and below), the phase noise contribution from the PM is strongly decreased. The electronic noise from the TIA is modelled using the measurement in Figure 3.19. The fit function is $\log_{10}(\tilde{\varphi}_{\text{tot}}) = -\frac{1}{2} \log_{10}(P_{\text{RX}}) + p_0$. The three highest power points are excluded from the fit, because other noise sources are visibly contributing, including a higher noise from the PM. The fitted value is $p_0 = -9.176 \pm 0.001$, which in terms of phase noise per power is $k_{\text{tot}} = 666.8 \pm 1.5 \text{ prad Hz}^{-\frac{1}{2}} \text{ W}^{\frac{1}{2}}$. TIA noise is estimated from the measurement in Figure 3.19.

Noise source	Amount $[\text{prad Hz}^{-\frac{1}{2}} \text{ W}^{\frac{1}{2}}]$	
Shot noise	600.5	\pm 7.0
Electronic noise from TIA #2	290.0	\pm 15
total	666.8	\pm 1.5

Table 6.3: Estimated noise contributions in the low RX power measurement using TIA #2.

To the knowledge of the author, this is the first shot noise limited DWS measurement in LISA-like and weak-light conditions.

Phasemeter Requirement Verification

As no excess noise is measured, the PM satisfies the requirement in Subsection 5.1.2. Note that the used second-stage amplification of 57.4 V/V, which was essential in reducing the excess phase noise from the PM, is still not representative of the gain of the variable gain amplifier which is implemented in the LISA PM's signal pre-conditioning electronics, as this will be of the order of 600 V/V [9].

6.1.5 Conclusion

In this section, the results of the first TIA-noise and shot-noise limited DWS measurements are reported, filling a significant gap in the current understanding of DWS performance.

The DWS performance was measured when interfering a strong beam, representative of the TX beam in the ISI, together with a very weak beam, representative of the RX beam in the ISI. The used setup has allowed to test weak-beam powers in the range of μW to tens of pW . When using such small signals, the dominant noise sources are shot noise from the laser and electronic noise from the TIA. The DWS and phase noise contributions were characterized as a function of the RX beam power while using two different low-noise TIA designs. The estimated phase noise contributions correspond to the estimations from Subsection 5.2.3, and hence fulfill the QPD-level ISI requirement. The OB-level ISI requirement cannot be fulfilled as the DWS performance is limited by shot noise.

Additional phase noise due to the PM's readout was also studied. This was at first enhanced by delivering a reduced signal amplitude to the PM. Such test is not representative of LISA, and the PM failed to fulfill its requirement. In the second test, as an amplified beat note was fed to the PM, no noise attributable to the PM was measured.

6.2 DWS performance in presence of a beam tilt

The DWS requirements for LISA have to be met for RX beam tilts of up to 405 μ rad at OB-level (see Subsection 5.1.1). As the imaging system (IS) in LISA have a magnification of $m_{IS} = 2.5$, this translates to a tilt range of 1 mrad at QPD-level. Currently, the DWS noise in presence of beam tilts is a gap in the current knowledge of DWS. This section reports the results of DWS noise measurements, where the angle of the RX beam is varied by means of the actuators.

6.2.1 Expectation

For simplicity, let the RX beam is assumed to tilt vertically. One can call this the *active* axis, while the horizontal is the *passive* axis, and DWS_v and DWS_h are the *active* and *passive* DWS, respectively. The presence of a tilt, no matter the direction, decreases the heterodyne efficiency between the interfering beams, as described in equation (2.146) in the case of a SEPD. As this decreases the amplitude of the signal, it consequently increases the phase noise level of all C/N_0 dependent noise sources. Furthermore, tilt also decreases the DWS gain. A numerical analysis however shows on the other hand that such decrease is negligible. In this section I will focus on shot noise, electronic noise and RIN.

As shot noise and electronic noise are expected to increase also in the same way on both axes due to the decrease of the heterodyne efficiency. DWS phase noise due to $1f$ -RIN also increases on each segment of the QPR due to the decrease of the heterodyne efficiency. However, it still cancels out on the passive axis as it is correlated among the QPD segments; on the active axis instead it depends on the tilt angle, as this reduces the correlation between the segments, as reported in equations (5.23, 5.24).

The behavior under tilt of the noise sources analized in this Section is summarized in equations (6.14, 6.15, 6.16, 6.17, 6.18, 6.19).

$$\sqrt{\eta_{het}} \rightarrow \sqrt{\eta_{het, 0}} e^{-\xi^2 \theta^2} \quad (6.13)$$

$$\tilde{\varphi}_{\text{shot, active \& passive}}(\theta) = \tilde{\varphi}_{\text{shot, 0}} e^{\xi^2 \theta^2} \quad (6.14)$$

$$\tilde{\varphi}_{\text{en, active \& passive}}(f, \theta) = \tilde{\varphi}_{\text{en, 0}}(f) e^{\xi^2 \theta^2} \quad (6.15)$$

$$\tilde{\varphi}_{1f\text{-RIN, active}} = \frac{\sqrt{2}(\bar{P}_1 \tilde{r}_1(1f_{het}) + / \boxplus \bar{P}_2 \tilde{r}_2(1f_{het}))}{\sqrt{\eta_{het} \bar{P}_1 \bar{P}_2}} e^{\xi^2 \theta^2} \left| \sin\left(\frac{1}{2} \kappa_1 \theta\right) \right| \quad (6.16)$$

$$\tilde{\varphi}_{1f\text{-RIN, passive}} = 0 \quad (6.17)$$

$$\tilde{\varphi}_{2f\text{-RIN, active}} = \frac{\tilde{r}_1(2f_{het}) + / \boxplus \tilde{r}_2(2f_{het})}{\sqrt{2}} |\sin(\kappa_1 \theta)| \quad (6.18)$$

$$\tilde{\varphi}_{2f\text{-RIN, active}} = 0 \quad (6.19)$$

The simple sum has to be used for correlated RIN, while the squared sum \boxplus has to be used in for uncorrelated RIN. As in TDOBS only one laser source is present, the simple sum has to be used. The value of ξ depends on the specific beam sizes and on the size of the QPD. This can be simulated for LISA using the numerical methods developed in Section 2.3.3. The plots of the normalized heterodyne efficiency as a

function of the beam tilt angles are shown in Figures 6.5 and 6.6. These Figures plot the heterodyne efficiency decrease as a function of the beam tilt angle for both the total QPD amplitude and for the one-segment amplitude. Since the assumption was made in Section 5.2.2 that ρ is negligible, it was set to zero in the calculation. In this configuration, both the QPD-amplitude and the one-segment amplitude have the same value of ξ . The resulting values of ξ are $\xi_{\text{ISI}} = 7.43 \times 10^{-4} \mu\text{rad}^{-1}$ and $\xi_{\text{TMI}} = 5.59 \times 10^{-4} \mu\text{rad}^{-1}$. As the values measured in Section 4.4.2 for the RX-GB & LO beams on the REFQPDs is $\xi_{\text{RX-GB \& LO, REFQPD}} = 6.32 \times 10^{-4} \mu\text{rad}^{-1}$, this is between the values for the ISI and the TMI in LISA. The interference of the RX-GB & LO beams on the REFQPDs can hence be used to test the noise as a function of the angle in the ISI and TMI.

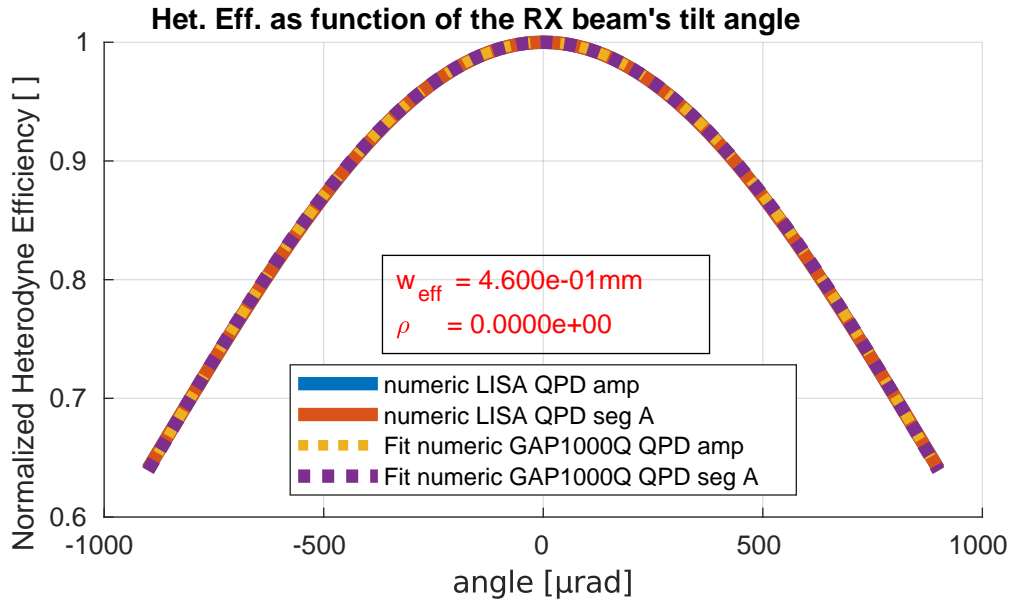


Figure 6.5: Numerically simulated decrease of heterodyne efficiency as a function of the RX beam tilt at QPD-level in the ISI, both for the total QPD amplitude and for the one-segment amplitude. The resulting value of ξ is $\xi_{\text{ISI}}^2 = 7.43 \times 10^{-4} \mu\text{rad}^{-1}$.

6.2.2 Setup Description

The QPDs are used simultaneously to synthesize a null DWS measurement as described in Subsection 5.4.2. Especially due to the beam tilt, it would be more convenient to perform such measurement using the SCIQPDs, as the REFQPDs detect less than 50% of the impinging laser beam and could be subject to straylight and the tilt could enhance this issue, which was so far not evident in any of the DWS measurements using the REFQPDs. Unfortunately, as the SCIQPDs are affected by a SVN caused by straylight which strongly limits their sensitivity (see Figures 5.31 and 5.32), this is not an option. Hence, I opted for using the REFQPDs, which feature the transistor-based TIA #2.

The chosen heterodyne frequency is 5 MHz, as the overall phase noise for heterodyne frequencies within the LISA heterodyne band is the lowest (see Section 5.4). The used beams are the RX-GB & LO beams.

As the target of this measurement is to characterize the increase of the interferometric noise due to tilts of the RX beam, the measurement is carried out in the

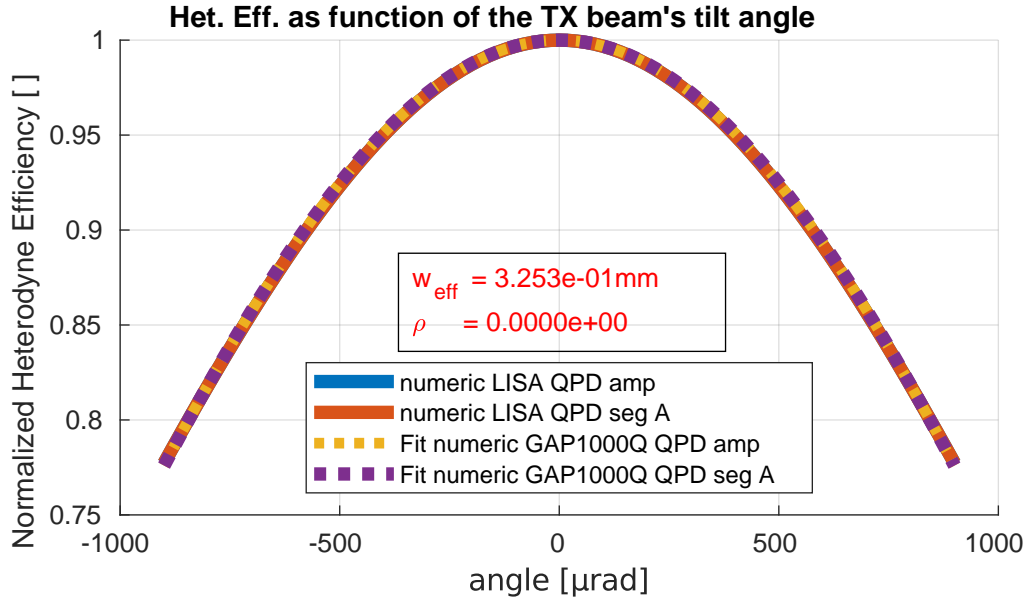


Figure 6.6: Numerically simulated decrease of heterodyne efficiency as a function of the RX beam tilt at QPD-level in the TMI, both for the total QPD amplitude and for the one-segment amplitude. The resulting value of ξ is $\xi_{\text{TMI}}^2 = 5.59 \times 10^{-4} \text{ } \mu\text{rad}^{-1}$.

0.1-1 Hz frequency band, as this band is limited by interferometric noise (i.e. a combination of shot noise and electronic noise). For lower frequencies the experimental sensitivity is limited by thermoelectronic phase noise, which is not angle-dependent and therefore not a target of this measurement. A similar approach in measuring the DWS noise in LISA Pathfinder was used by [6]. The power of the beams was reduced in order to enhance the portion of the spectrum which is dominated by interferometric noise. Mostly, the LO beam's power was reduced, as a good enough SNR is needed to actuate the RX-GB beam. This causes to have very small beat notes at the PM's input, but this was done on purpose to test the PM's performance, too.

The measurement is performed as a calibration measurement, where the RX beam is tilted in a range from approximately -1.5 mrad to 1.5 mrad in the same way as in a DWS calibration measurement. This peculiar range was chosen as within such range the DWS signal is limited in the $[-\pi, +\pi]$ range. Larger angles cause a fringe crossing and output DWS values of difficult interpretation. The sweep of the angle is linear, as the RX beam is first tilted to -1.5 mrad and then tilted by 20 μrad steps. This allows the possibility of a worsening of the alignment in time, hence the measurements at positive tilt angles could perform worse. For each rotation step, the RX-GB beam is kept still for 20 seconds and DWS noise is measured. This is enough to obtain an estimation of the noise in the desired frequency band. Furthermore, the use of a much broader tilt angle than what is expected to happen in LISA enhances the detectability of small effects.

The measurements were performed using two different power values for the LO beam, while the RX-GB beam was kept at constant power. The power was regulated using the method described in Subsection 6.1.2. The measurement with the lowest power was repeated twice with different second-stage gains to test the influence of the noise from the PM. These three measurements are called, for simplicity, high-power, low-power and low-power amplified. The measurement's parameters

are listed in Table 6.4.

Measurement	P_{RX-GB} [μ W]	P_{LO} [μ W]	G_{ss} [V/V]
High-power	2.4	2	2.87
Low-power	2.4	0.13	2.87
Low-power amplified	2.4	0.13	57.4

Table 6.4: Beam powers and second-stage amplification gains used during the DWS performance as a function of the angle measurement.

Note that the DWS gain varies during the measurement; numerically, such variation is negligible. As a reference, the divergence angles of the RX-GB and LO beams are $\Theta_{RX-GB} = 423 \mu\text{rad}$ and $\Theta_{LO} = 410 \mu\text{rad}$, respectively.

6.2.3 Results

High-power

Figure 6.7 shows the amplitude of the beat note as a function of the RX-GB beam tilt angle during this measurement. The data were fitted with a Gaussian curve, but the knowledge of the fit parameters gives no additional information beyond what is reported in Table 4.6 regarding the constant ξ . However, it is necessary to characterize the maximum amplitude of the beat note, which is $\sim 0.46 \text{ V}$. The curve is rather symmetric and centered at $\theta = 0 \mu\text{rad}$, indicating that the IFM was well aligned.

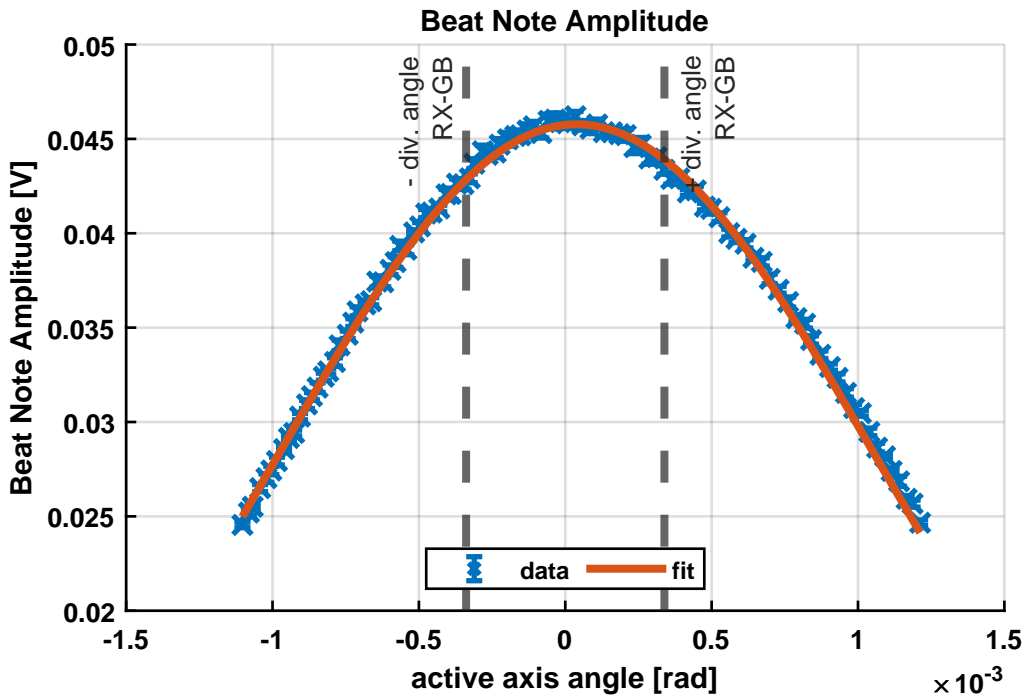


Figure 6.7: Plot of the beat note amplitude as a function of the RX-GB beam tilt angle. This measurement was fitted with a Gaussian curve, and the fit parameters are reported in Table 6.5.

Parameter	Value	±	Error
a [mV]	45.77	±	0.06
s [μ rad]	1037	±	4
x_0 [μ rad]	39	±	2

Table 6.5: Fit parameters from Figure 6.7. The function used for the fit is $f(x) = a \exp\left(-\frac{1}{2} \left(\frac{x-x_0}{s}\right)^2\right)$. ξ can be derived as $\xi = \frac{1}{\sqrt{2}s}$.

Figure 6.8 shows the measured angular DWS noise floor in the *active* axis alongside the main known noise contributors. These were calculated using equations (6.14, 6.15, 6.16, 6.18). An estimation of the angular noise due to the PM’s readout is also reported. This is based on the empirical model in Sub-subsection 5.3 using the 0.1-1 Hz band. The noise sources estimated as phase noise are converted into angular noise by means of the full non-linear DWS calibration for REFQPD1 in Table 4.2.

The measured angular DWS was also fit with a second-order polynomial, and the obtained coefficients are reported in Table 6.6. Figure 6.8 also reports the OB-level DWS requirement for the TMI, which is the most stringent one among the DWS requirements.

The measured DWS noise in the high-power active axis measurement complies with the LISA TMI requirement through the whole measured range. The measured DWS noise is found to have a minimum at roughly -400 μ rad, which is very distant from null tilt. Despite repeating the measurement, this feature did not vary. This excludes that this issue is related to the actuations by the steering mirrors.

The noise sources are a little overestimated, giving an total estimated noise which roughly a factor of 2 above the measured noise. This holds particularly for the electronic noise and 1f-RIN.

Figure 6.9 shows the measured angular DWS in the *passive* axis alongside the main known noise contributors. These were calculated using equations (6.14, 6.15). RIN is expected to not contribute to the angular noise in the passive axis and is hence not plotted (see equations 6.17, 6.19)). An estimation of the angular noise due to the PM’s readout is also reported. This is based on the empirical model in Sub-subsection 5.3. The noise sources estimated as phase noise are converted into angular noise by means of the full non-linear DWS calibration for REFQPD1 in Table 4.2.

The measured DWS noise in the high-power passive axis measurement complies with the LISA TMI OB-level requirement through the whole measured range. It is also surprisingly found to be higher than in the active axis, and to be higher for smaller tilts. This particular fact makes it such, that the estimated noise sources look correct, with exception for the electronic noise.

Low-power

The amplitude as a function of the beam tilt angle for this measurement is not shown, as it is just a rescaled version of Figure 6.5 with a maximum beat note amplitude at the PM input of 12 mV, and the minimum amplitudes are about 6.5 mV.

Figure 6.10 shows the measured angular DWS in the *active* axis alongside the

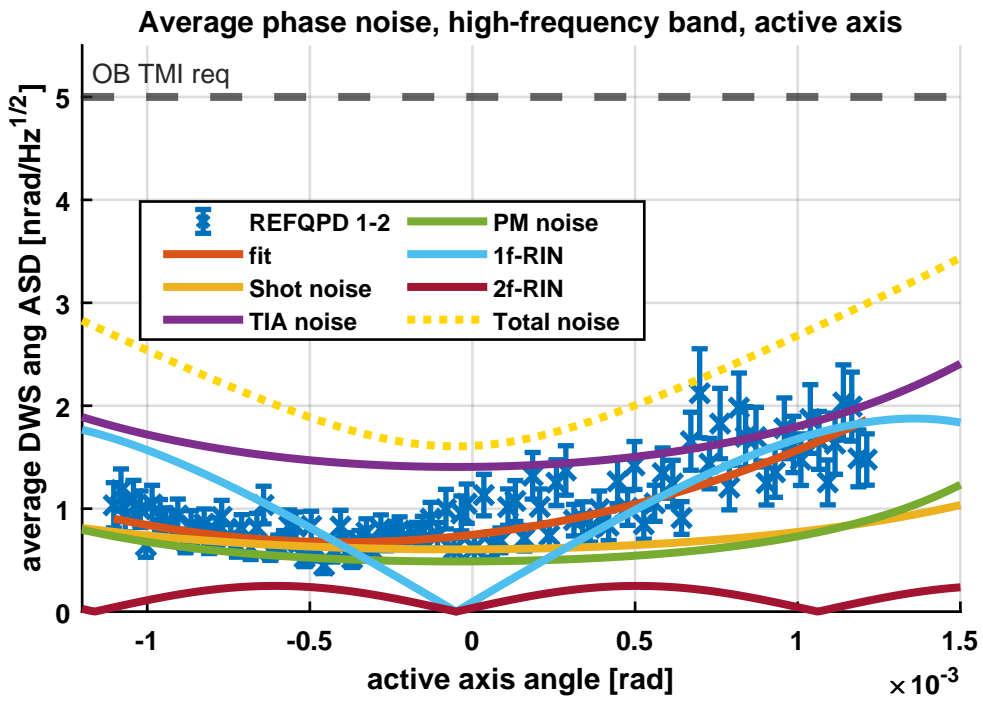


Figure 6.8: High-power angular DWS noise measured as a function of the RX-GB beam tilt in the *active* axis.

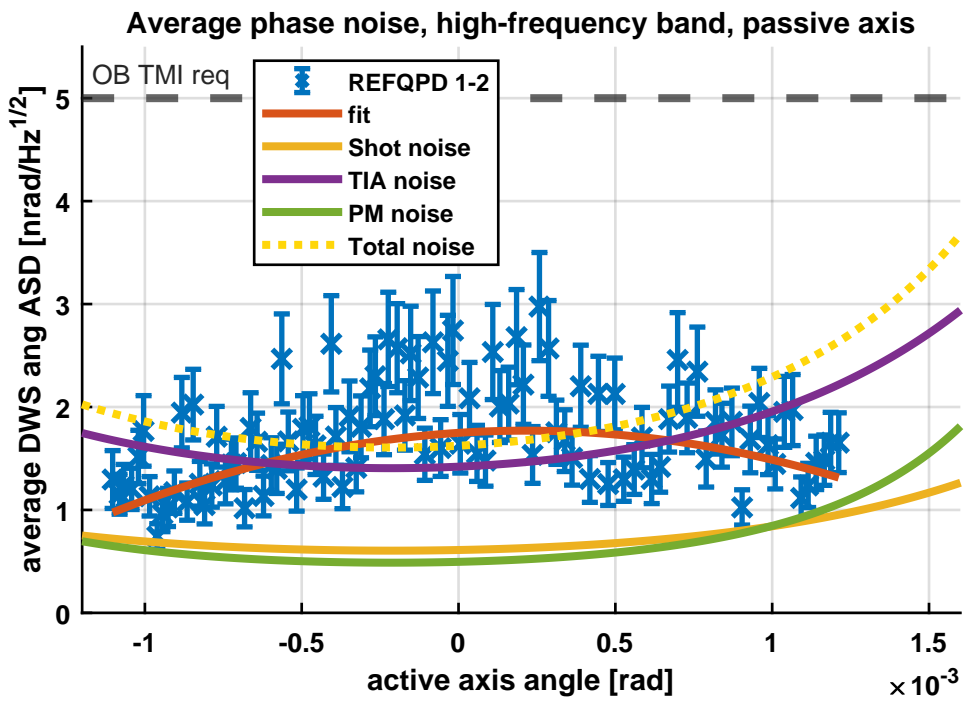


Figure 6.9: High-power angular DWS noise measured as a function of the RX-GB beam tilt in the *passive* axis.

Parameter	Active		Passive	
p_0 [nrad/ $\sqrt{\text{Hz}}$]	0.67	\pm 0.02	1.77	\pm 0.05
x_0 [mrad]	-0.396	\pm 0.04	0.21	\pm 0.05
p_2 [nrad/ $\sqrt{\text{Hz}}/\text{rad}^2$]	4.59×10^5	\pm 4.5×10^4	-4.6×10^5	\pm 6×10^4

Table 6.6: Fit parameters from the high-power DWS noise measurements in Figure 6.8 (active axis) and Figure 6.9 (passive axis). The function used for the fit is $f(x) = p_0 + p_2(x - x_0)^2$.

main known noise contributors, which are calculated in the same way as in Figure 6.8. The measured DWS noise in the high-power active axis measurement complies with the LISA TMI OB-level requirement through the whole measured range. The increase of the noise as a function of the angle is visibly stronger than in the low-power measurement, which can be clearly seen comparing the fit coefficients in Tables 6.7 and 6.6. This is expected to be driven mostly by the fact that the used beat note amplitude is very small. The minimum of the DWS noise is found to be close to $\theta = 0$ rad.

The estimated noise contributions in Figure 6.10 still appear to have been overestimated, especially around $\theta = 0$ μrad , while they look correct around $\theta = \pm 1$ mrad. The noise model used to derive the PM gives a slightly higher noise than measured. As the PM noise model has been tuned using a measurement principle identical to this one, but with SG generated signals, it is expected to rather underestimate the noise.

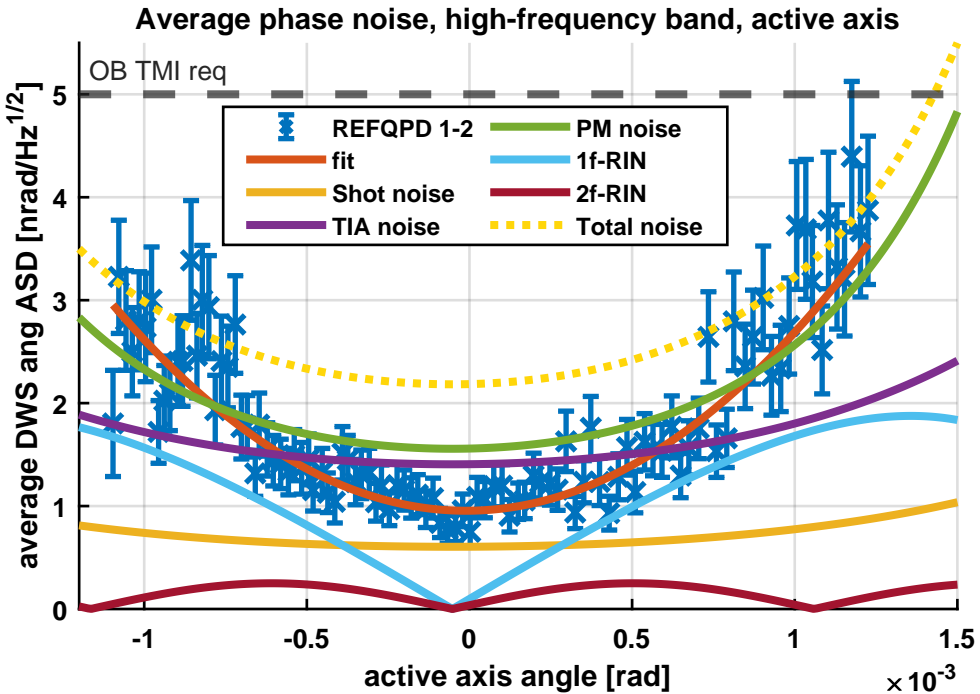


Figure 6.10: Low-power angular DWS noise measured as a function of the RX-GB beam tilt in the *active* axis.

Figure 6.11 shows the measured angular DWS in the *passive* axis alongside the main known noise contributors. The measured DWS noise in the high-power passive

axis measurement complies with the LISA TMI OB-level requirement through the whole measured range. The minimum of the DWS noise is found to be close to $\theta = 0$ rad. The noise increase as a function of the RX-GB beam tilt angle is smaller in the passive axis than in the active axis. This measurement is expected to be dominated by PM noise. Surprisingly the measured DWS noise does not follow the trend of the modelled PM noise but rather follows the same trend of the TIA noise. This measurement is probably the one where the modelled DWS noise and the measured DWS noise best match.

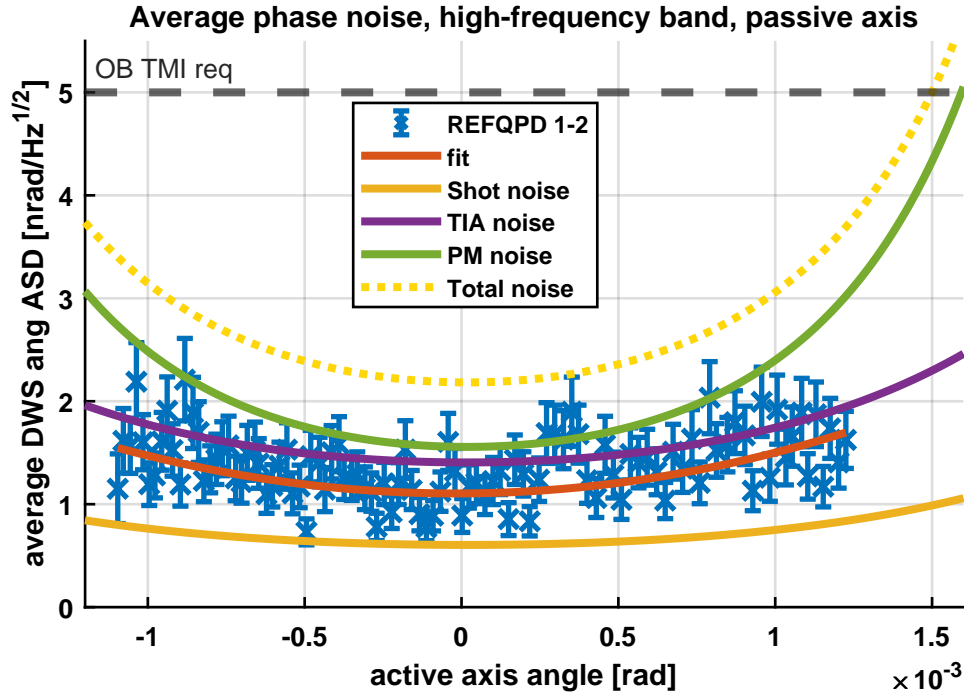


Figure 6.11: Low-power angular DWS noise measured as a function of the RX-GB beam tilt in the *passive* axis.

Parameter	Active		Passive	
p_0 [nrad/ $\sqrt{\text{Hz}}$]	0.95	\pm 0.03	1.10	\pm 0.03
x_0 [mrad]	-0.01	\pm 0.02	-0.01	\pm 0.05
p_2 [nrad/ $\sqrt{\text{Hz}}$ /rad 2]	1.70×10^6	\pm 9×10^4	3.8×10^5	\pm 6×10^4

Table 6.7: Fit parameters from the low-power DWS noise measurements in Figure 6.10 (active axis) and Figure 6.11 (passive axis). The function used for the fit is $f(x) = p_0 + p_2(x - x_0)^2$.

Low-power Amplified

The amplitude as a function of the beam tilt angle for this measurement is not shown, as it is just a rescaled version of Figure 6.5 with a maximum beat note amplitude at the PM input of 260 mV, and the minimum amplitudes are about 130 mV.

Figure 6.12 shows the measured angular DWS in the *active* axis alongside the main known noise contributors, which are calculated in the same way as in Figure 6.8. The measured DWS noise in the high-power active axis measurement complies with the LISA TMI OB-level requirement through the whole measured range. The increase of the noise as a function of the angle is milder than in the low-power measurement, but still stronger than that in the high-power measurement. This can be clearly seen comparing the fit coefficients in Tables 6.6, 6.7 and 6.8. This is expected as having increased the total gain by a factor of 20 has reduced the additional phase noise from the PM, whereas all other noise sources are the same as in the low-power measurement. The minimum of the DWS noise is found to be close to $\theta = 0$ rad.

The estimated noise contributions in Figure 6.12 still appear to have been overestimated, especially around $\theta = 0$, while they look correct around $\theta = \pm 1$ mrad. Neglecting TIA noise in Figure 6.12, which is clearly overestimated by at least a factor of 2, 1f-RIN is expected to be a main DWS noise contributor around $\theta = \pm 1$ mrad. No evidence of this appears in the measurement.

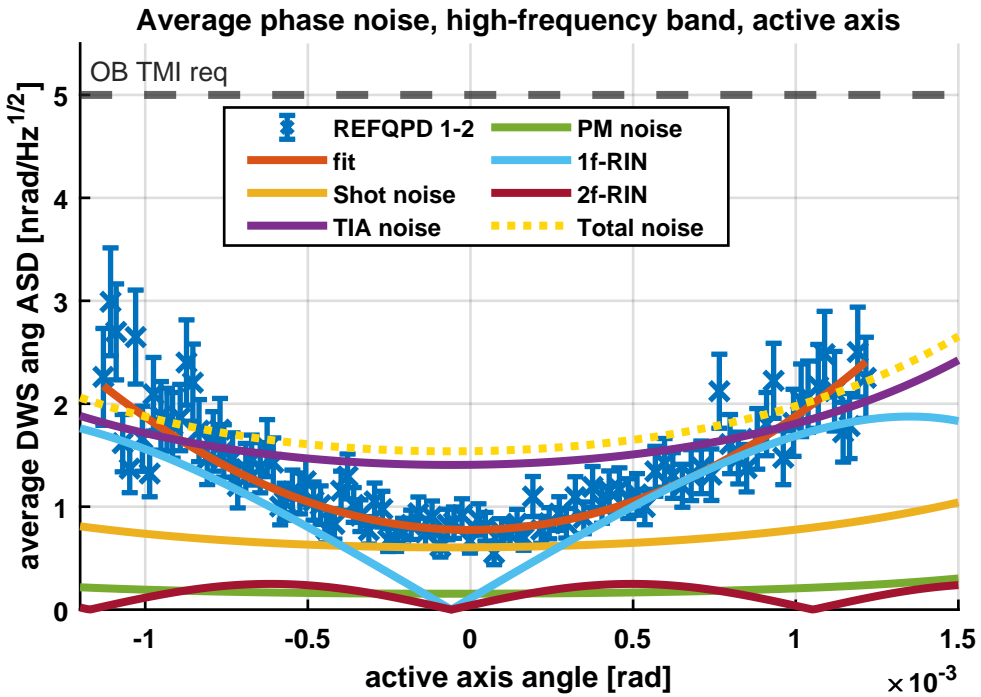


Figure 6.12: Low-power amplified angular DWS noise measured as a function of the RX-GB beam tilt in the *active* axis.

Figure 6.13 shows the measured angular DWS in the *passive* axis alongside the main known noise contributors. The measured DWS noise in the high-power passive axis measurement complies with the LISA TMI OB-level requirement through the whole measured range. The minimum of the DWS noise is found to be close to $\theta = 0$ rad. The noise increase as a function of the RX-GB beam tilt angle is smaller in the passive axis than in the active axis (see Table 6.8). This measurement is expected to be dominated by TIA and shot noise. The estimated total DWS noise appears to have been overestimated by a factor of 2 with respect to the measured DWS noise.

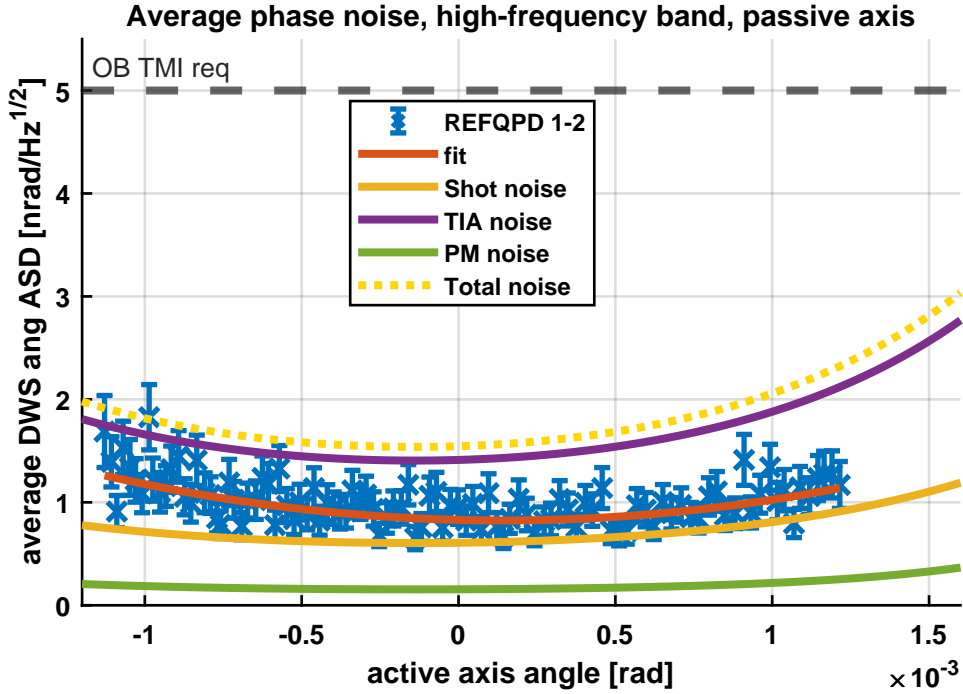


Figure 6.13: Low-power amplified angular DWS noise measured as a function of the RX-GB beam tilt in the *passive* axis.

Parameter	Active		Passive	
p_0 [nrad/ $\sqrt{\text{Hz}}$]	0.77	\pm 0.02	0.082	\pm 0.02
x_0 [mrad]	0	\pm 0.02	0.14	\pm 0.05
p_2 [nrad/ $\sqrt{\text{Hz}}$ /rad 2]	1.10×10^6	\pm 6×10^4	2.7×10^5	\pm 4×10^4

Table 6.8: Fit parameters from Figure 6.12 (active axis) and Figure 6.13 (passive axis). The function used for the fit is $f(x) = p_0 + p_2(x - x_0)^2$.

6.2.4 Conclusion

The DWS noise as a function of the angle was analyzed in a configuration which is representative of the TMI in LISA in terms of used QPRs and PM but not in terms of used beat note amplitude, as this was reduced on purpose. All three measurements show a moderate increase of the noise as a function of the angle, which in a tilt range of approximately ± 1.5 mrad never exceeds the TMI OB-level requirement.

The measured DWS noise contributions from shot noise, electronic noise, RIN and the PM were compared to the modelled DWS noise in both the tilted axis (the active axis) and the passive axis. The modelled DWS noises are usually found to have been overestimated. The most likely explanation for all noise sources other than PM noise is the high uncertainty in the beam powers used, which points to the known unreliability of laser powermeters. The empirical noise model for the FMC PM also has overestimated the DWS noise by roughly a factor of 2. The reason for this discrepancy remains unclear.

Chapter 7

The New DWS Architecture

This chapter briefly explains a new concept of tracking DWS signals from a PD. The principle is published in [43]. The operativity of such architecture has up to now been tested only with electrical input signals and optically only once [11]. The results from this are available in [9]. The operativity of this *new architecture* with signals of optical origin using TDOBS is reported in this Chapter.

7.1 The old and new QPD tracking architecture

The Old Architecture

As already explained in paragraph 1.3.2, a DPLL (see figure 1.9) is used to extract the amplitude, frequency and phase information from the voltage signal from one segment of a QPR. This process runs parallelly for each segment of the QPR, outputting per QPR an array of four frequencies (PIR), four amplitudes and four phases (PA). From these four measured phases the DWS signals - the physically interesting quantities for which QPDs are used - are calculated in post-processing. This architecture of calculating DWS signals was followed so far during this thesis. Mathematically this can be described by collecting the four segments' phase outputs in a vector and using a matrix \hat{M}

$$\begin{pmatrix} \varphi_{\text{LPS}} \\ \varphi_{\text{DWSh}} \\ \varphi_{\text{DWSv}} \\ \varphi_{\text{DWSc}} \end{pmatrix} = \begin{pmatrix} \frac{1}{4}(\varphi_A + \varphi_B + \varphi_C + \varphi_D) \\ \frac{1}{2}(\varphi_A - \varphi_B + \varphi_C - \varphi_D) \\ \frac{1}{2}(\varphi_A + \varphi_B - \varphi_C - \varphi_D) \\ \frac{1}{2}(\varphi_A - \varphi_B - \varphi_C + \varphi_D) \end{pmatrix} = \hat{M} \begin{pmatrix} \varphi_A \\ \varphi_B \\ \varphi_C \\ \varphi_D \end{pmatrix}, \quad (7.1)$$

where \hat{M} is the *mixing matrix* transforming the four segment's signals into the DWS signals.

$$\hat{M} = \begin{pmatrix} \frac{1}{4} & \frac{1}{4} & \frac{1}{4} & \frac{1}{4} \\ \frac{1}{2} & -\frac{1}{2} & \frac{1}{2} & -\frac{1}{2} \\ \frac{1}{2} & \frac{1}{2} & -\frac{1}{2} & -\frac{1}{2} \\ \frac{1}{2} & -\frac{1}{2} & -\frac{1}{2} & \frac{1}{2} \end{pmatrix} \quad (7.2)$$

To keep the same naming convention as in [43], the elements of the DWS signals vector $(\varphi_{\text{LPS}}, \varphi_{\text{DWSh}}, \varphi_{\text{DWSv}}, \varphi_{\text{DWSc}})^T$ are going to be renamed to $(x, \alpha, \beta, \varepsilon)^T$. This way of processing the readout from a QPR is the most straightforward and intuitive to implement and is the traditionally used way to track the phase on a QPR. A

scheme of this process is shown in Figure 7.1. I will refer to it as the *old architecture* of DWS tracking.

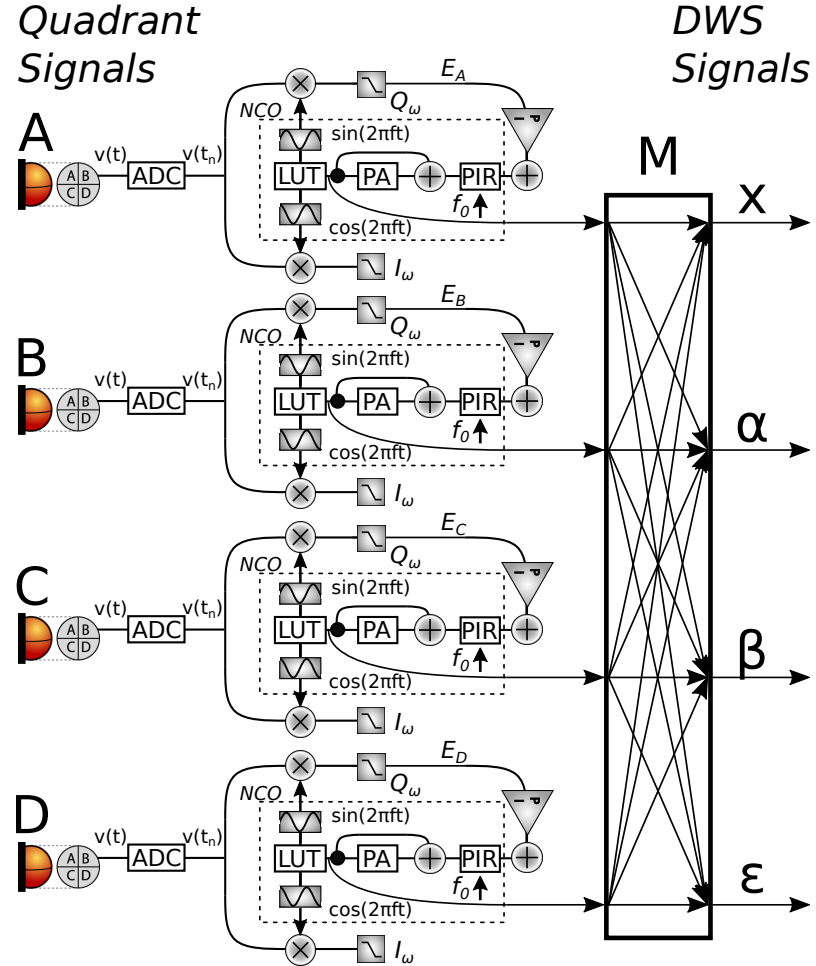


Figure 7.1: Scheme of the *old architecture* of DWS tracking. The four segments of a QPR are independently tracked and the physically meaningful DWS signals are computed in post processing.

The New Architecture

A new concept of DWS tracking scheme was proposed by G. Heinzel and published in [43] and is named, in contraposition to the previous scheme, *new architecture* of DWS tracking. This scheme proposes to have the DPLLs not anymore working on the individual QPR segments, but on combinations of these, and in specific on the DWS combinations. A scheme of this is depicted in Figure 7.2. The error signals are calculated from the output of each segment as in the case of the *old architecture*. They are mixed using the mixing matrix \hat{M} in equation (7.2) resulting in error signals $(E_x, E_\alpha, E_\beta, E_\varepsilon)^T$ of the length and DWS signals $(x, \alpha, \beta, \varepsilon)^T$. Four DPLLs use these errors signals and hence track directly the DWS signals. The outputs of the PI servos are directly the DWS quantities which the old architecture gives in further processing. To close the loop, the outputs of the four DPLLs are converted back into $(\varphi_A, \varphi_B, \varphi_C, \varphi_D)^T$ by the use of the unmixing matrix \hat{M}^{-1} , as these values are needed for the mixer in the error signal calculation. Note that only x is tracking

the quickly increasing phase term $\omega_{\text{het}} t$. The angular signals are not a beat note anymore, but a pure phase difference; therefore initial frequency and PA are not needed. The respective error signal has the dimension of a phase, while the error signal of the x loop has the dimension of a frequency.

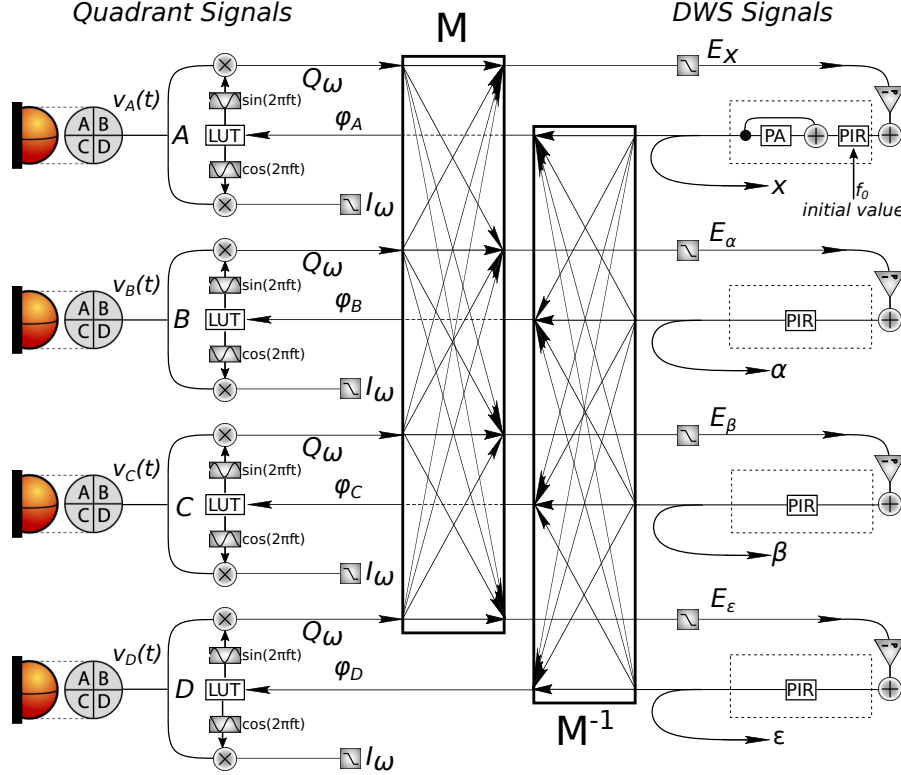


Figure 7.2: Scheme of the *new architecture* of DWS tracking. Combinations of the four QPR segments are being tracked, and the DPLLs output directly the physically meaningful DWS signals.

7.1.1 The Simulation

The equivalence of the two architectures' readout was confirmed by means of a simulation in **MATLAB SIMULINK**. In this simulation, the old architecture and the new architecture were implemented parallelly to demodulate the beat notes from four segments of a QPD. The same gain parameters were used for simplicity. A sinusoidal signal was injected in each segment, and no noise was added. Figure 7.3 shows the input signal together with the old architecture's output (Single-segment tracking) and the new architecture's output (Combined-signal tracking). This result has shown the successful tracking of the two segments of a QPD. Given the same input, same input parameters and in absence of noise, the two architectures produce the same output.

7.1.2 Signal-to-Noise Ratio Considerations

As described so far, and neglecting the missing PAs in the angular signals, the two architectures mathematically perfectly equivalent. They only difference between them is that the PI servos operate on the DWS error signals $(E_A, E_B, E_C, E_D)^T \rightarrow$

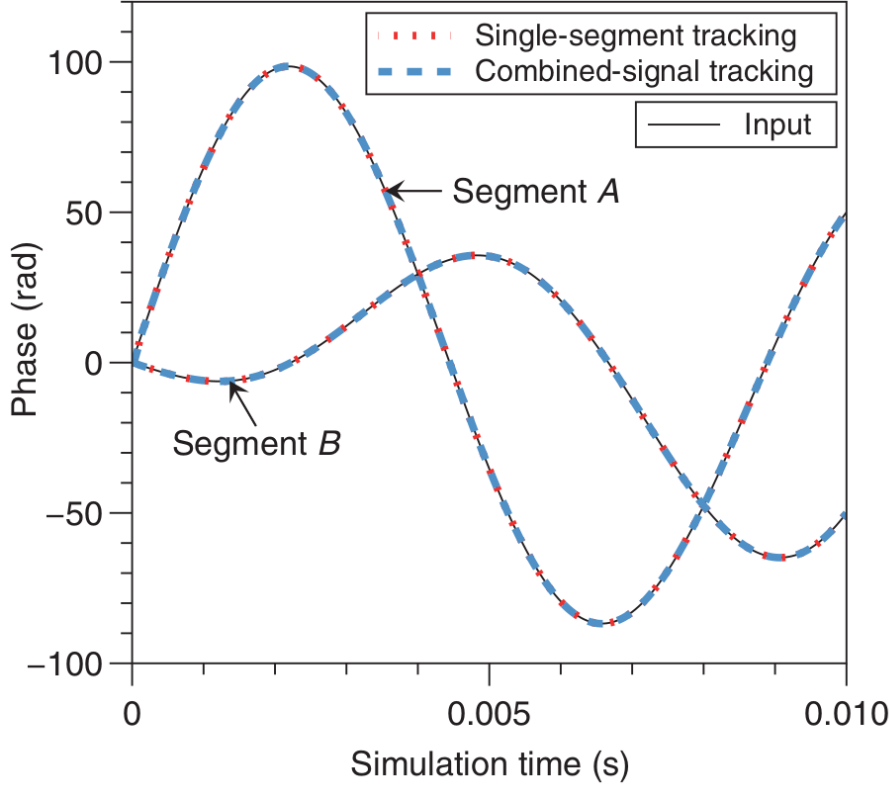


Figure 7.3: Result of the simulation, showing identical outputs of the two architectures when tracking two segments of a QPD. This result was published in [43]

$(E_x, E_\alpha, E_\beta, E_\varepsilon)^T$, and the unmixing of the outputs from the PI servos to recover the phases $(\varphi_A, \varphi_B, \varphi_C, \varphi_D)^T$. If the PI servos use exactly the same gain parameters, as they are linear operators, the two schemes are mathematically equivalent, and lead to identical outputs. This holds also for the SNR of the output DWS signals.

The advantages of the new architecture can be derived from the following considerations:

1. In the old architecture each signal has a very large dynamic range. This is due mostly due to the coupling of frequency noise, which gives a signal of the order of 10^5 rad/ $\sqrt{\text{Hz}}$ [9, Figure 1.6]. In the new architecture, this is the case only for the x signal. The angular signals $(\alpha, \beta, \varepsilon)^T$ have much smaller dynamics. By doing an analogue reasoning using the angle rate change in Figure 1.4, which is 0.02 deg/day, the equivalent DWS change rate is 1.2×10^{-5} rad/s. As there is going to be a active control of the spacecraft jitter and MOSA pointing, this estimation is strongly exaggerated.
2. As in the new architecture each DPLL is specialized on a specific signal to track, the PI gains can be tuned in each loop to better fit the dynamics of the specifically tracked signal. This is not possible in the old architecture, where each DPLL is tracking the full dynamics simultaneously. The x tracking loop can use the same P and I gains as the old architecture, while the angular signals tracking loops can use lower gains as the dynamics are smaller.
3. The obtained error signals $(E_x, E_\alpha, E_\beta, E_\varepsilon)^T$ have a higher SNR than the initial ones, as uncorrelated noise sources - as shot noise and electronic noise - add

quadratically.

4. The integer number of cycles in the PA is tracked only once as corresponds to physical reality.

To go more in detail on the last point, let P_1 and P_2 be the powers of two beams impinging on a QPD. The QPD is for simplicity assumed to have no slits, and the totality of the beams' power impinges on the four quadrants. Both beams are TEM₀₀ Gaussian beams centered on the QPD, hence each quadrant detects one fourth of the power of each beam. One beam (the reference beam) impinges perpendicularly onto the QPD, while the other beam (the measurement beam) can have small tilts of angle θ around the QPD's center. The heterodyne efficiency of the two beams on the four segments is assumed to be identical (even in presence of tilts, as in Subsubsection 2.3.3). Both beams are affected by RIN, which is assumed to be uncorrelated. The power P_i impinging on segment i with $i \in (A, B, C, D)$ can be derived by equation (2.70).

$$P_i = \frac{1}{4} \left(\underbrace{\bar{P}_1 + \bar{P}_2}_{\text{DC}} + \underbrace{\bar{P}_1 r_1 + \bar{P}_2 r_2}_{1f\text{-RIN}} + \underbrace{(r_1 + r_2) \sqrt{\eta_{\text{het}} \bar{P}_1 \bar{P}_2} \cos(\omega_{\text{het}} t + \varphi_i)}_{2f\text{-RIN}} + \underbrace{2 \sqrt{\eta_{\text{het}} \bar{P}_1 \bar{P}_2} \cos(\omega_{\text{het}} t + \varphi_i)}_{\text{signal}} \right) \quad (7.3)$$

At the QPD the beams' powers are converted into photocurrent. The QPD has responsivity A . Additional noise due to the QPD's dark current will be neglected. The electronic noise i_{en} from the TIA is described as equivalent input current noise and can be added to the segments' photocurrent. The current i_i heading to each TIA of the QPR is

$$i_i = \frac{1}{4} \left(\underbrace{\bar{i}_1 + \bar{i}_2}_{\text{DC}} + \underbrace{\bar{i}_1 r_1 + \bar{i}_2 r_2}_{1f\text{-RIN}} + \underbrace{(r_1 + r_2) \sqrt{\eta_{\text{het}} \bar{i}_1 \bar{i}_2} \cos(\omega_{\text{het}} t + \varphi_i)}_{2f\text{-RIN}} + \underbrace{2 \sqrt{\eta_{\text{het}} \bar{i}_1 \bar{i}_2} \cos(\omega_{\text{het}} t + \varphi_i)}_{\text{signal}} \right) + i_{\text{en}}. \quad (7.4)$$

Where $\bar{i}_i = A \bar{P}_i$ and A is the responsivity of the photodiode. Note that with the used simplifications all signals have the same amplitude, but different phase. The phase noise is calculated with equation (2.71). The RMS of the signals are all equal between each other.

$$\text{RMS}_i = \mathcal{RMS} \left\{ \frac{1}{2} \sqrt{\eta_{\text{het}} \bar{i}_1 \bar{i}_2} \cos(\omega_{\text{het}} t + \varphi_i) \right\} = \sqrt{\frac{1}{8} \eta_{\text{het}} \bar{i}_1 \bar{i}_2} \quad (7.5)$$

The ASDs of the noise is derived by several uncorrelated contributions.

$$\tilde{i}_{\text{shot, i}} = \sqrt{\frac{1}{2} q(\bar{i}_1 + \bar{i}_2)} \quad \tilde{i}_{\text{en, i}} = \tilde{i}_{\text{en}} \quad (7.6)$$

$$\tilde{i}_{1f\text{-RIN}} = \frac{1}{4} \sqrt{i_1^2 \tilde{r}_1^2 + i_2^2 \tilde{r}_2^2} \quad \tilde{i}_{2f\text{-RIN}} = \frac{1}{8} \sqrt{\eta_{\text{het}} \bar{i}_1 \bar{i}_2 (\tilde{r}_1^2 + \tilde{r}_2^2)} \quad (7.7)$$

The phase noise contributions of each noise are

$$\tilde{\varphi}_{\text{shot}, i} = 2\sqrt{\frac{q(\bar{i}_1 + \bar{i}_2)}{\eta_{\text{het}} \bar{i}_1 \bar{i}_2}} \quad (7.8)$$

$$\varphi_{\text{en}, i} = \frac{4\tilde{i}_{\text{en}}}{\sqrt{2\eta_{\text{het}} \bar{i}_1 \bar{i}_2}} \quad (7.9)$$

$$\tilde{\varphi}_{1f\text{-RIN } i} = \sqrt{\frac{\bar{i}_1^2 \tilde{r}_1^2 + \bar{i}_2^2 \tilde{r}_2^2}{2\eta_{\text{het}} \bar{i}_1 \bar{i}_2}} \quad (7.10)$$

$$\tilde{\varphi}_{2f\text{-RIN } i} = \sqrt{\frac{\tilde{r}_1^2 + \tilde{r}_2^2}{8}}. \quad (7.11)$$

The combined phase noises for one QPD channel is

$$\tilde{\varphi}_i = \sqrt{\frac{8q(\bar{i}_1 + \bar{i}_2) + 16\tilde{i}_{\text{en}}^2 + \bar{i}_1^2 \tilde{r}_1^2 + \bar{i}_2^2 \tilde{r}_2^2}{2\eta_{\text{het}} \bar{i}_1 \bar{i}_2} + \frac{\tilde{r}_1^2 + \tilde{r}_2^2}{8}}. \quad (7.12)$$

The phase noise of one segment $\tilde{\varphi}_i$ is also the noise affecting one error signal of the DPLL E_i , hence $\tilde{E}_i = \tilde{\varphi}_i$. This for instance holds for all the four DPLLs in the old architecture.

In the new architecture the error signals are combined by the matrix \hat{M} to calculate the error signals of the DWS signals. In this process uncorrelated noises as shot noise and electronic noise add quadratically, while correlated noises as RIN add linearly. The signal also adds linearly.

For the LPS (or x) signal, $E_x = \frac{1}{4}(E_A + E_B + E_C + E_D)$. The factor $\frac{1}{4}$ is not relevant for the C/N₀ and will be neglected. The resulting RMS is four times that of the single segment, hence $\text{RMS}_x = \sqrt{2\eta_{\text{het}} \bar{i}_1 \bar{i}_2}$. This leads to the noise contributions

$$\tilde{\varphi}_{\text{shot}, x} = \sqrt{\frac{q(\bar{i}_1 + \bar{i}_2)}{\eta_{\text{het}} \bar{i}_1 \bar{i}_2}} \quad (7.13)$$

$$\varphi_{\text{en}, x} = \frac{2\tilde{i}_{\text{en}}}{\sqrt{2\eta_{\text{het}} \bar{i}_1 \bar{i}_2}} \quad (7.14)$$

$$\tilde{\varphi}_{1f\text{-RIN } x} = \sqrt{\frac{\bar{i}_1^2 \tilde{r}_1^2 + \bar{i}_2^2 \tilde{r}_2^2}{2\eta_{\text{het}} \bar{i}_1 \bar{i}_2}} \quad (7.15)$$

$$\tilde{\varphi}_{2f\text{-RIN } x} = \sqrt{\frac{\tilde{r}_1^2 + \tilde{r}_2^2}{8}}. \quad (7.16)$$

These give a total x phase noise of

$$\tilde{E}_x = \sqrt{\frac{2q(\bar{i}_1 + \bar{i}_2) + 4\tilde{i}_{\text{en}}^2 + \bar{i}_1^2 \tilde{r}_1^2 + \bar{i}_2^2 \tilde{r}_2^2}{2\eta_{\text{het}} \bar{i}_1 \bar{i}_2} + \frac{\tilde{r}_1^2 + \tilde{r}_2^2}{8}}. \quad (7.17)$$

This signal has the same level of RIN as a single channel, but half of the shot noise and electronic noise. The improvement factor depends on the exact contribution of each noise source. In the inter-satellite interferometer (ISI), which is dominated by electronic and shot noise, this improvement is very close to a factor 2.

This advantage is even bigger for the angular signals α , β and ε , as RIN partially cancels out in the combination of the error signals. Focusing for simplicity only on the case of DWSv (or β), the phase contributions of 1f-RIN and 2f-RIN are described in equations (5.23, 5.24),

The noise contributions are hence

$$\tilde{\varphi}_{\text{shot, } \beta} = \sqrt{\frac{q(\bar{i}_1 + \bar{i}_2)}{\eta_{\text{het}} \bar{i}_1 \bar{i}_2}} \quad (7.18)$$

$$\varphi_{\text{en, } \beta} = \frac{2 \tilde{i}_{\text{en}}}{\sqrt{2 \eta_{\text{het}} \bar{i}_1 \bar{i}_2}} \quad (7.19)$$

$$\tilde{\varphi}_{1f\text{-RIN } \beta} = \sqrt{\frac{2(\bar{i}_1^2 \tilde{r}_1^2 + \bar{i}_2^2 \tilde{r}_2^2)}{\eta_{\text{het}} \bar{i}_1 \bar{i}_2}} \left| \sin\left(\frac{1}{2} \kappa_1 \theta\right) \right| \quad (7.20)$$

$$\tilde{\varphi}_{2f\text{-RIN } \beta} = \sqrt{\frac{\tilde{r}_1^2 + \tilde{r}_2^2}{8}} |\sin(\kappa_1 \theta)|, \quad (7.21)$$

and the error signal's noise is

$$\tilde{E}_\beta = \sqrt{\frac{2q(\bar{i}_1 + \bar{i}_2) + 4\tilde{i}_{\text{en}}^2 + 4(\bar{i}_1^2 \tilde{r}_1^2 + \bar{i}_2^2 \tilde{r}_2^2) \sin^2(\frac{1}{2} \kappa_1 \theta)}{2 \eta_{\text{het}} \bar{i}_1 \bar{i}_2} + \frac{\tilde{r}_1^2 + \tilde{r}_2^2}{8} \sin^2(\kappa_1 \theta)}. \quad (7.22)$$

The same holds *mutatis mutandis* for the horizontal DWS. Regarding E_ε , for this peculiar signal combination RIN vanishes independently on the angle, giving an error signal noise of

$$\tilde{E}_\varepsilon = \sqrt{\frac{2q(\bar{i}_1 + \bar{i}_2) + 4\tilde{i}_{\text{en}}^2}{2 \eta_{\text{het}} \bar{i}_1 \bar{i}_2}}. \quad (7.23)$$

Signal	Shot noise	Elec. noise	1fRIN	2fRIN	Total	Impr.
Segment	2.52×10^{-4}	2.80×10^{-4}	4.25×10^{-5}	1.50×10^{-8}	3.79×10^{-4}	-
x	1.26×10^{-4}	1.40×10^{-4}	4.25×10^{-5}	1.50×10^{-8}	1.93×10^{-4}	1.96
α & β	1.26×10^{-4}	1.40×10^{-4}	1.31×10^{-9}	4.61×10^{-13}	1.88×10^{-4}	2.01
ε	1.26×10^{-4}	1.40×10^{-4}	0	0	1.88×10^{-4}	2.01

Table 7.1: Estimation of the individual noise sources and total noise in rad/ $\sqrt{\text{Hz}}$ for a single channel in a QPR in the ISI, representing the old architecture and for the longitudinal x and angular signals α , β , ε representing the new architecture. The old architecture estimation is based on equations (7.8, 7.9, 7.10, 7.11, 7.12). The estimations for x are based on equations (7.13, 7.14, 7.15, 7.16, 7.17). The estimations for α and β are based on equations (7.18, 7.19, 7.20, 7.21, 7.22). The estimations for ε are based on equations (7.18, 7.19, 7.23). The following values are assumed: power values for the RX and TX beam from Table 6.1, $\tilde{i}_{\text{en}} = 2 \text{ pA}/\sqrt{\text{Hz}}$, $\kappa_1 = 2842 \text{ rad/rad}$ from Table 5.4, $\tilde{r}_1 = \tilde{r}_2 = 3 \times 10^{-8}$. These values are taken from [30]. θ is assumed to have an exaggerated value of 10 nrad.

It is important to stress that the output LPS and DWS signals of the old architecture and new architecture have the same SNR. The advantage of the new architecture is that the improved SNR of the error signals makes the DPLL more robust locks and gives a lower probability of cycle slips. These slips occur when the phase error between input signal and NCO exceeds ± 0.5 cycles, driving the PI servo

Signal	Shot noise	Elec. noise	$1fRIN$	$2fRIN$	Total	Impr.
Segment	1.89×10^{-8}	1.90×10^{-6}	3.50×10^{-7}	1.50×10^{-8}	2.70×10^{-6}	-
x	9.45×10^{-7}	9.52×10^{-7}	3.50×10^{-5}	1.50×10^{-8}	1.39×10^{-6}	1.95
α & β	1.26×10^{-4}	1.40×10^{-4}	8.04×10^{-12}	3.45×10^{-13}	1.34×10^{-6}	2.02
ε	1.26×10^{-4}	1.40×10^{-4}	0	0	1.34×10^{-6}	2.02

Table 7.2: Estimation of the individual noise sources and total noise in $\text{rad}/\sqrt{\text{Hz}}$ for a single channel in a QPR in the TMI, representing the old architecture and for the longitudinal x and angular signals α , β , ε representing the new architecture. The old architecture estimation is based on equations (7.8, 7.9, 7.10, 7.11, 7.12). The estimations for x are based on equations (7.13, 7.14, 7.15, 7.16, 7.17). The estimations for α and β are based on equations (7.18, 7.19, 7.20, 7.21, 7.22). The estimations for ε are based on equations (7.18, 7.19, 7.23). The following values are assumed: power values for the LO and TX beam are $1.34 \mu\text{W}$ and $40.1 \mu\text{W}$ respectively, $\tilde{i}_{\text{en}} = 2 \text{ pA}/\sqrt{\text{Hz}}$, $\kappa_1 = 2268 \text{ rad}/\text{rad}$ from Table 5.4, $\tilde{r}_1 = \tilde{r}_2 = 3 \times 10^{-8}$. These values are taken from [30]. θ is assumed to have an exaggerated value of 10 nrad.

to find stability one or more cycles apart. This concept is explained in more detail in [38, section 4.1]. One of the main cause is a low C/N density ratio, which leads to higher phase error and higher likelihood that such a process takes place. Therefore the improved C/N density ratio given by the new architecture would reduce the frequency of such events.

The current baseline for LISA is to implement the new architecture, which is still awaiting testing in a LISA representative setup. This architecture has been implemented on the FMC PM parallelly to the old architecture by Pascal Grafe and it has been successfully tested to work on a split test using electric input signals in [9, section 4.7]. During this chapter I will describe the first testing of the new architecture done with input optical signals.

7.2 Experimental Testing with Optical Signals

TDOBS is the best available facility at AEI to test the new architecture, as the other experiments like the Hexagon (see [68, 83]) lack the possibility of actively tilting the laser beams. A similar measurements was performed by [9, Section 4.7] by inputting electrical signals to the PM.

7.2.1 Setup

The measurement setup is as when measuring the performance of TDOBS in Subsection 5.4. The RX-GB & LO beam interference was measured using the REFQPDs, as the SCIQPDs are affected by straylight. This measurement was performed when the REFQPDs were still featuring the OpAmp-based TIA #1 and the PM temperature conditions are that of the Feedback AC circuit in Figure 5.17. The used beam powers are of the order few μW per segment per beam, which is the highest power that the QPR can handle. The used heterodyne is 5 MHz. A further test at a higher frequency as 25 MHz makes little sense given the performance of TDOBS at such frequency (see Figure 5.25).

During the measurement the RX-GB beam was aligned to its nominal position

and the actuators were still. A null measurement was synthesized by taking the difference the measurements by REFQPD1 and REFQPD2. In [9, Section 4.7] two separate measurements were done: one with no input signal and one with a 10 mHz phase modulation injected into β . In TDOBS such modulation is not possible as it would require to continuously move the step actuators. However, the phase stability of each beat note in TDOBS is much lower than that of an electrical signal. The used loop gains are reported in Table 7.3. The gain value for the x signal is kept the same as in the old architecture. The gain values for the angular signals was chosen as the highest gain for which the loops were locking.

Architecture	P	I
old	15	5
new, x	15	5
new, $\alpha, \beta, \varepsilon$	14	4

Table 7.3: Proportional and Integral gains used for the new architecture measurement

7.2.2 Results

The plots use the same notation as in Subsection 5.4, where REFQPD 1-2 indicate the differential DWS and LPS measurements, plus "Old" and "New" indicate if the old or new architecture was used.

Figure 7.4 shows the PT corrected LPS measured by REFQPD1. Its noise level is dominated by the OPD loop's performance. The measurement by the new architecture matches that of the old architecture. This result is expected as the x loop in the new architecture is identical to any loop in the old architecture.

Figure 7.5 shows the PT corrected and not PT corrected LPS measured by REFQPD 1-2. The PT correction in the old architecture gives a moderate improvement of the LPS performance around 100 mHz. The non PT-corrected differential LPS signal from the new architecture gives the same spectrum as that from the old architecture. On the other hand, the PT corrected differential LPS signal almost sees no improvement if not around 1 Hz.

The performance reached by the old architecture is limited by thermoelectronic phase noise up to ~ 70 mHz and electronic and shot noise after 100 mHz. The measurement by the new architecture matches that of the old architecture. This result for the non PT-corrected LPS is expected as the x loop works in the same way as the old architecture. The lack of improvement for the PT corrected differential LPS is not expected and will be the target of further investigation.

Figure 7.6 shows the measured DWS noise from REFQPD1 with and without PT correction. For frequencies lower than 100 mHz the DWSv and DWSh curves agree, stating that the new architecture is capable of tracking the beam's angular motion. For frequencies higher than that an additional white looking noise contribution at a $\sim 5 \mu\text{rad}/\sqrt{\text{Hz}}$ appears exclusively in the new architecture's outputs.

Figure 7.7 shows the measured differential DWS noise with and without PT correction. The same holds as for Figure 7.6, as the DWS outputs from the new architecture are limited by a white looking noise contribution at a $\sim 5 \mu\text{rad}/\sqrt{\text{Hz}}$.

This is highlighted better in Figure 7.8, which shows the differential DWSv noise from the old and new architectures with and without PT correction. For both the

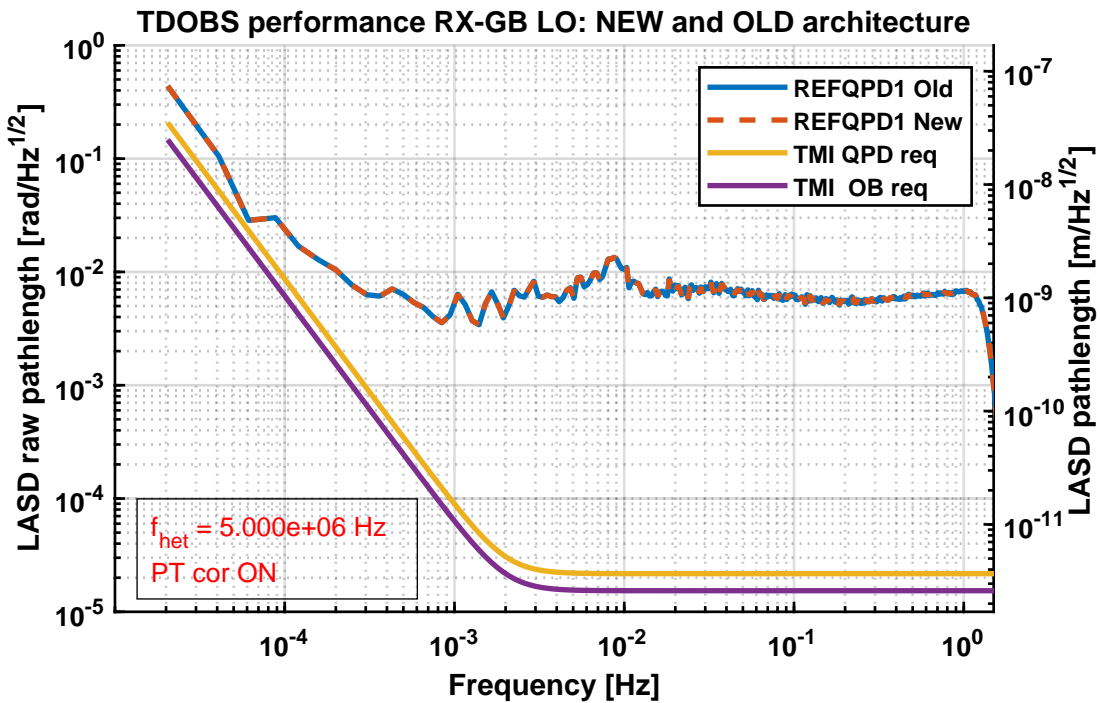


Figure 7.4: Plot of the LPS noise measured by REFQPD1 with both old and new architecture.

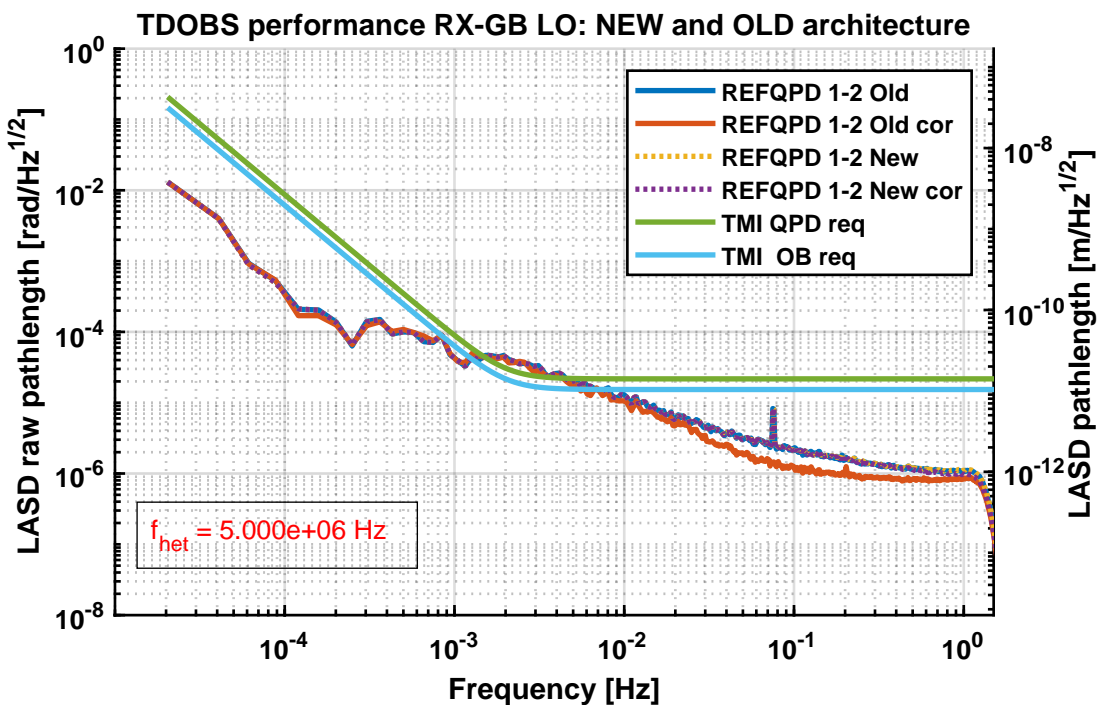


Figure 7.5: Plot of the differential LPS noise, with and without PT correction.

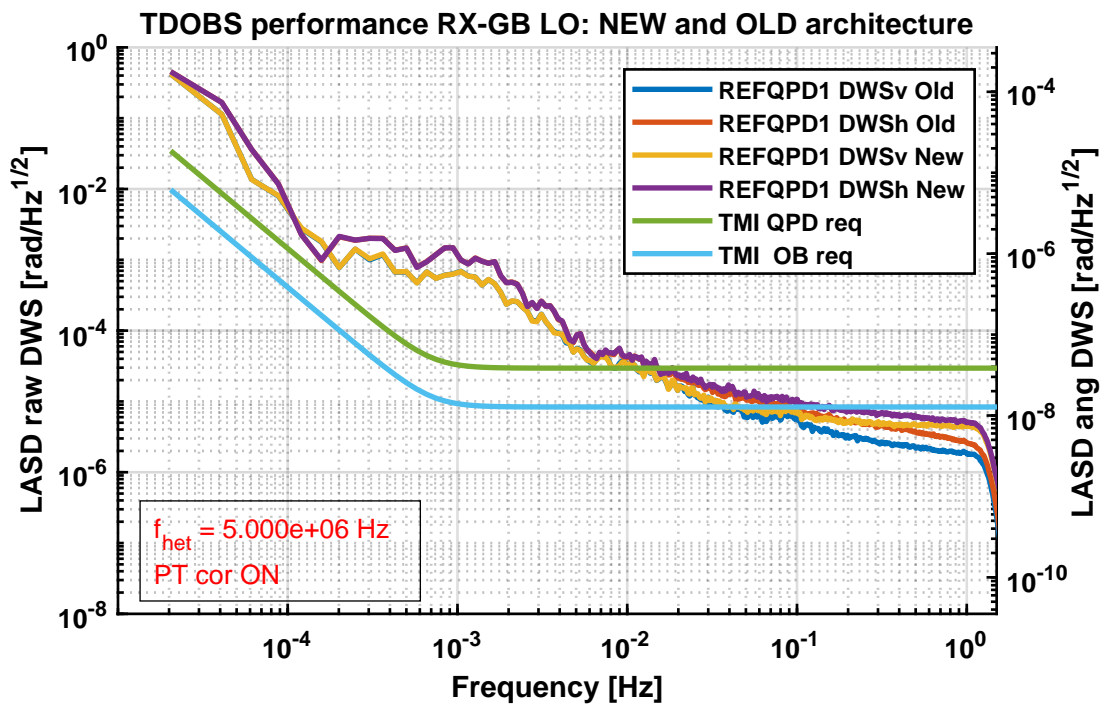


Figure 7.6: Plot of the DWS noise from REFQPD1 with and without PT correction.

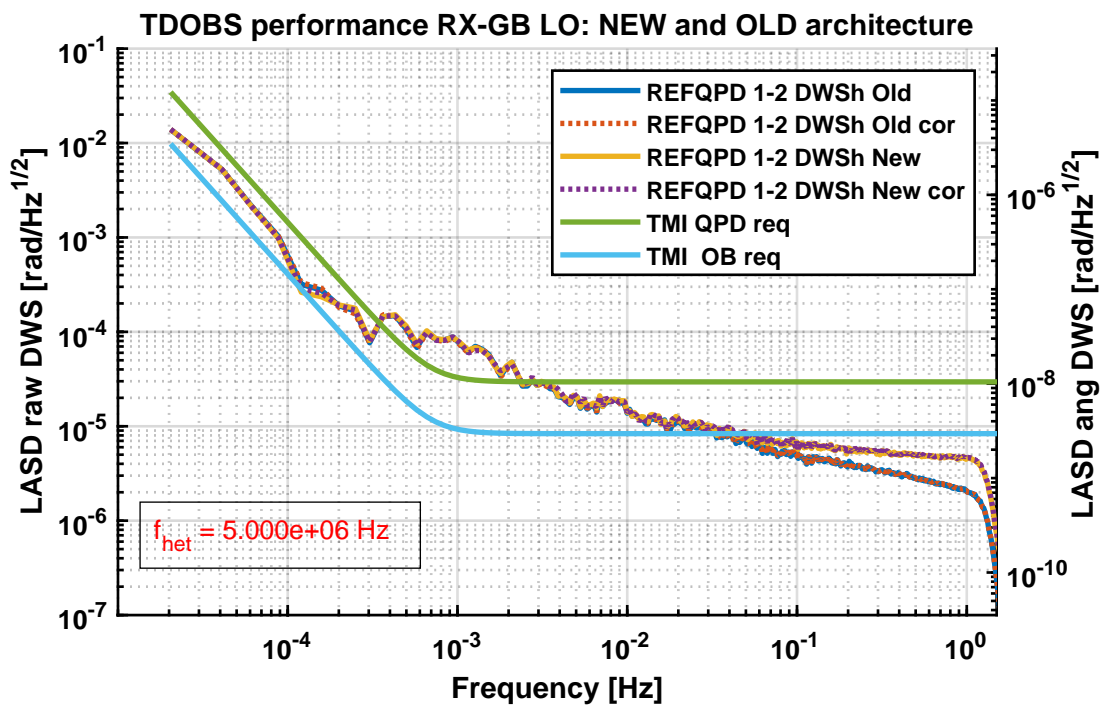


Figure 7.7: Plot of the differential DWS noise with and without PT correction.

old and new architecture the PT induces almost no change in the performance. The new architecture's output manifests a white noise contribution visible from ~ 70 mHz, which is independent of the PT correction.

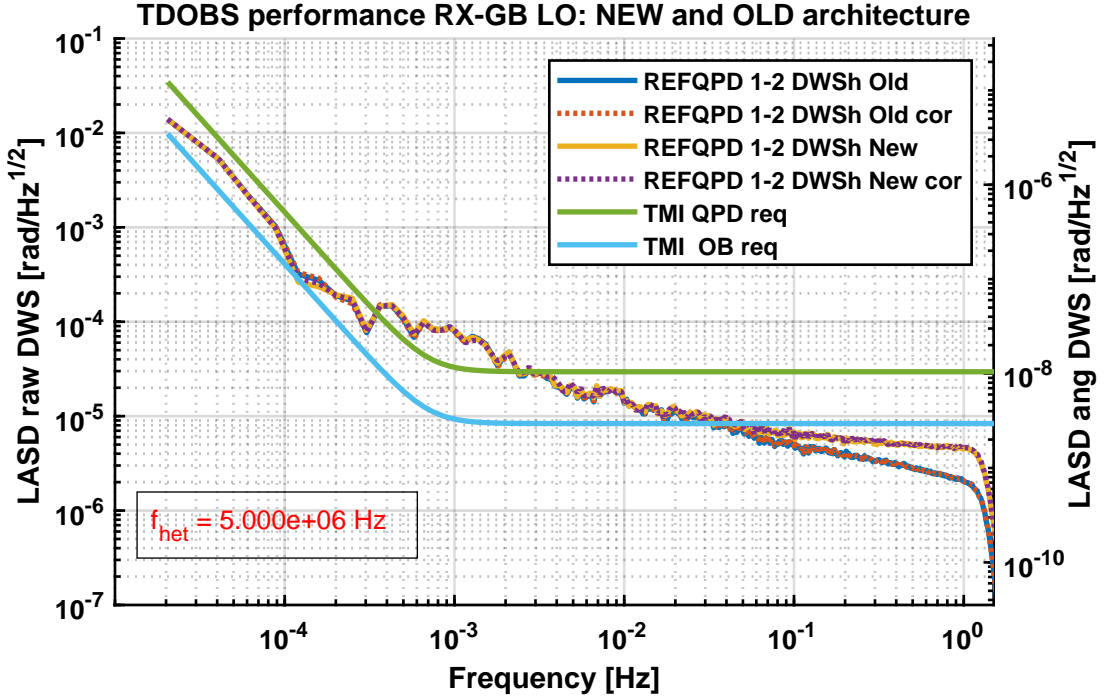


Figure 7.8: Plot of the differential DWSv noise from the old and new architectures with and without PT correction.

These results are in line with what found in [9, Section 4.7], where the output of the new architecture is affected by a white noise at high frequencies. The suspected cause is a flawed implementation in the FPGA. Such noise is still well within the requirements for LISA.

7.3 Conclusion

A new concept of DWS tracking from a QPD was tested for the first time with optical input signals representative of the TMI in LISA. The obtained DWS and LPS performance is limited by experimental noise for frequencies lower than 100 mHz. For higher frequencies, the performance is limited by a white noise which is suspected to come from a faulty implementation of the architecture itself in the FPGA. Overall, this architecture not only is able to readout the same signals as the old architecture, but also reaches a performance which is very well within the requirements for the TMI.

Chapter 8

Summary, Future Improvements and Conclusions

8.1 Summary

LISA will be the first space-based GW observatory, aiming to detect GW in the 10^{-4} – 10^{-1} Hz band. The detection principle is to measure the displacement between free-falling test masses (TMs) separated by millions of kilometers using heterodyne interferometry. The required displacement sensitivity for detecting GWs is of the order of $\text{pm}/\sqrt{\text{Hz}}$. To reach such sensitivity, many technical challenges have to be solved, such as the weak-light condition and the coupling of the angular jitter of the spacecraft and TMs to the interferometrically-measured longitudinal displacement, or tilt-to-length (TTL).

The weak-light condition, due to a combination of limited power of the laser, limited size of the telescope and separation between the spacecraft, causes the detected signal to be very small in amplitude. An extremely low-noise heterodyne readout is needed to maximize the signal-to-noise ratio. The pivotal elements in the detection chain are a low capacitance QPD and the trans-impedance amplifier (TIA). LISA’s quadrant photoreceivers (QPRs) are planned to use a transistor-based TIA with a noise level lower than $2 \text{ pA}/\sqrt{\text{Hz}}$ developed at AEI.

A key feature for the mitigation of TTL is the use of differential wavefront-sensing (DWS), which allows the estimation of the occurring tilt angles with a sensitivity of $\text{nrad}/\sqrt{\text{Hz}}$. This information is used both in the drag-free attitude control system (DFACS) to maintain the alignment of the constellation and of the moving optical subassemblies (MOSAs) and of the test mass (TM), and in post-processing for the subtraction of TTL.

The first chapter of this thesis provides an overview of general relativity, gravitational waves and the key features of the Laser Interferometer Space Antenna (LISA) mission that are relevant to the scope of this work.

The second chapter describes Gaussian beams, heterodyne interferometry, imaging systems (ISs), and the relevant QPR signals. A detailed model of DWS was developed, allowing the DWS signal of an interferometer to be derived analytically under specific conditions or numerically in a general case. This model was successfully verified with the calibration of TDOBS and was used during the thesis to predict the DWS signals in the ISI and TMI in LISA. Furthermore, the model also provides the heterodyne efficiency of each QPD segment as a function of the tilt

angle, which is a relevant parameter entering the calculations of the LPS and DWS noises.

The third chapter, after a short introduction about TTL and its mitigation strategies in LISA, describes the TDOBS experiment, an ultra-stable Zerodur® testbed representative of LISA’s optical bench (OB). This testbed consists of two main baseplates, the LISA-OB simulating an OB in LISA and the TS, providing beams representative of either the ISI (the RX Flat-Top beam) or the TMI (the RX-Gaussian Beam). This experiment was upgraded from a kHz heterodyne interferometer - which was already successful in testing TTL mitigation via imaging systems - to a LISA-representative MHz heterodyne interferometer. The upgrade consisted of

- Upgrading the modulation bench (MB) to generate three beams with variable \sim MHz frequency differences between them.
- Upgrading REFQPD2 and the REFSEPD.
- Designing new and dedicated mechanical mounts to hold the TIAs, which must be placed as close as possible to the PDs.
- Upgrading the TIAs of the QPRs to amplify beat notes up to 30 MHz. This was done using low-noise TIA designs; among these is a transistor-based TIAs model based on the design of LISA’s QPR with equivalent input current noise lower than $2 \text{ pA}/\sqrt{\text{Hz}}$ below 15 MHz.
- Installing a MHz compatible DPLL-based phasemeter (PM). This PM implements the classical architecture of DWS signal tracking together with a novel architecture.
- Realizing additional second-stage amplifiers to taylor the beat note’s amplitude to the ADC range.
- Installation of a thermal shield around the two baseplates.

The `tdobs-control` software was upgraded with new actuation routines to perform the beam motions necessary for the calibration procedures.

The fourth chapter describes the calibration procedure followed in TDOBS. This can be summarized as

- Calibration of the DPS signal of the RX beams on an externally added QPD, the AUXQPD. The DPS signal is a one beam DC signal used to recover the beam’s position. This QPD can be shifted laterally to calibrate the DPS. This step allows to measure the RX beam’s angles using an *optical lever*.
- Calibration of the DPS signal of the RX beams on the fixed QPD in TDOBS. The RX beam can be tilted using the actuators on the telescope simulator (TS).
- Calibration of the DWS signal of the RX beams interfered with the LO beam. The DWS is a 2-beam interferometric signal representative of the beam’s angle.

A novel calibration technique was developed for the DWS signals involving the RX-FT beam. This was necessary due to the fact that the 1 mm diameter REFQPDs are insensitive to the DPS signal of the RX-FT beam, making the control of its position unfeasible. This technique exploits the fact that the rotation of a flat beam is independent of the rotation pivot. A data analysis pipeline was developed in MATLAB to be able to ingest, process, and analyze TDOBS data.

The fifth chapter is split into three parts. The first part derives the requirements to be tested on ground in order to validate LISA's planned performance. As LISA uses four QPRs per interferometer, the requirements are broken down into

- QPD-level requirements, i.e. the performance which each QPD has to achieve, and
- OB-level requirements, i.e. the performance that the four combined QPDs have to achieve, with this last one being more stringent.

Equivalent requirements for TDOBS are derived by comparing the DWS gains of LISA and TDOBS. The second part focuses on the noise sources in TDOBS, and provides a noise budget of the experiment. The third part reports the achieved sensitivity in three different test configurations which simulate the sensitivity of DWS to either TM or spacecraft rotations in LISA:

1. RX-GB & LO beams on the REFQPDs
2. RX-FT & LO beams on the REFQPDs
3. RX-GB & LO beams on the SCIQPDs

Due to the motion of the RX beam caused by the thermal drift of the actuators, the performance measurements require the use of two QPDs placed in optical copies. This allows to synthesize a virtual null measurement. The sensitivity limitations of the TDOBS are heterodyne frequency dependent. These noise limitations are understood for low heterodyne frequencies in the LISA heterodyne band, and are *thermoelectronic phase noise* for frequencies lower than 100 mHz, and a combination of shot noise and electronic noise for frequencies higher than 100 mHz. The DWS noise at higher heterodyne frequencies in the LISA heterodyne band is higher than the noise budget predicts and not fully understood.

Chapter Six reports on two investigations that were conducted using the upgraded TDOBS testbed and that are highly relevant to the LISA mission. The results of these investigations address and fill two significant gaps in the current understanding of the DWS performance. The first is a test of the DWS sensitivity of the interferometric detection system (IDS) at various light-power levels, including and going beyond the weak-light conditions - roughly 100 pW of RX beam power at the QPD - of the ISI. The DWS requirement was successfully achieved in terms of DWS sensitivity at the QPD ($\widetilde{D}_{\text{WS}} < 150 \text{ nrad}/\sqrt{\text{Hz}}$) and in terms of additive phase noise due to the PM ($\widetilde{\varphi}_{\text{PM}} < 23.6 \mu\text{rad}/\sqrt{\text{Hz}}$) in the frequency band 1mHz-1Hz. Crucial for this goal was the development of the low-noise transistor-based TIA.

The second investigation is the analysis of DWS noise as a function of the tilt angle of the measurement beam, which is meant to validate that the required DWS sensitivity is also achieved when the interferometer configuration departs from the

ideal case. The current requirement in LISA is that the QPD-level requirement of $\widetilde{DWS} < 150 \text{ nrad}/\sqrt{\text{Hz}}$ has to be reached in an angular range of $\pm 405 \mu\text{rad}$. The DWS performance was verified to comply with this requirement in the significantly larger tilt range of $\pm 1.5 \text{ mrad}$.

Finally, chapter Seven reports the motivation and the experimental results of the use of a novel architecture for tracking the heterodyne signals from a QPD. This architecture tracks combinations of the error signals from the QPD, outputting the DWS signals directly. The equivalence of the two architectures is discussed and verified in a simulation. Analytical estimations are performed, showing the partial noise cancellation of common-mode noises as RIN, and reduction of the signal's dynamics due to cancellation of frequency noise. Therefore, such a scheme is expected to be more robust and less prone to cycle slips, as the tracked error signals have a higher SNR. Last, this architecture was successfully tested with the use of optically-generated input signals.

8.2 Improvements and Future Projects

Future improvements of TDOBS include first the mitigation of the DWS noise at high heterodyne frequencies. This would allow to perform the investigations carried out in this thesis in the whole LISA heterodyne band. This requires the mitigation of thermoelectronic phase noise, which is currently the limiting noise source for frequencies below 100 mHz at low heterodyne frequencies. The current measurement chain uses QPR located inside the vacuum chamber (VC), while the AC-DC splitters and the PM are placed in air. If this configuration is maintained, a better thermal isolation of the PM and AC-DC splitters is needed. Alternatively, the AC-DC splitters dedicated to the REFQPDs could be moved to the inside the vacuum chamber (VC), partially solving the problem. A further improvement would be to place the whole electronics in vacuum. A project recently started by Pascal Grafe plans to place a technology readiness level (TRL) 6 PM in a second VC, located in the vicinity of TDOBS. Such PM already includes a variable gain controller for signal pre-conditioning, requiring no use of the AC-DC splitters. The use of such PM in TDOBS could possibly extend the performance of a few $\text{nrad}/\sqrt{\text{Hz}}$, currently reached by TDOBS at the high frequency, down to mHz. Furthermore, the higher number of channels would allow the simultaneous use of REFQPDs and SCIQPDs.

Another significant issue which is affecting mostly the measurement procedure is the thermal drift of the piezo step actuators. Their drift, due to mostly temperature variations, requires to measure DWS using two QPDs placed in *optical copies*. This drift was never a limitation to the DWS sensitivity in all measurements, except when using the Flat-Top beam. A direct noise impact of reducing the drift is hard to compute, but this could be done relatively easily by replacing the piezo step actuators with simple piezo actuators, allowing the use of a feedback loop using e.g. REFQPD2 to keep the RX beam centered on REFQPD1, and hence measuring the DWS stability using REFQPD1 or the SCIQPDs.

A further issue that can be improved is the lack of a QPD capable of measuring the DPS signal of the RX-FT beam on the TS, which limits the control on its position. This is needed to perform any kind of measurement using the RX-FT beam, starting from a precise calibration. The calibration method used during this thesis, which relied on rotating the RX-FT beam not around the RX-clip, was sufficient,

but could be improved. This issue can be solved by adding a large silicon QPD. Such a QPR was already been designed by the Author, but was not installed yet.

The current implementation of the new architecture on the PM, which is affected by an ununderstood white noise at a level of a few nrad/ $\sqrt{\text{Hz}}$, has to be improved. The removal of such issue would allow a full test of the new architecture, validating it as the only architecture to be used in LISA.

Last, the use of the SCIQPDs is still not possible due to a yet unidentified source of straylight. To ease its identification, Gerhard Heinzel recently developed a circuit that converts the PM's output into an audio signal. This can be used to 'listen' to the output of the interferometer while softly hitting the optical components of the interferometer. As the straylight culprit is hit, it is expected to cause a considerable audio signal, whereas all other optical components should have a minor influence on the audio output. Once this issue will be solved, it will make sense to upgrade the SCIQPDs to the better performing transistor-based TIA and perform the noise investigations using the SCIQPDs. Furthermore, within a short timeframe, the AEI will receive a few models of the LISA-QPDs from SRON. The current plan is to use them as SCIQPDs.

8.3 Takeaways for LISA

Two key insights emerge from this thesis. First, TDOBS has proved that the telescope simulator (TS) is an excellent OGSE for the calibration of DPS and DWS signals in an interferometer. A similar device, or a similar method, could potentially be used to calibrate the DWS signals in the three LISA spacecraft before they are sent to space. For such a task, an OGSE delivering tiltable flat-top and Gaussian beams would be needed to inject a) a plane wave, either at the telescope or at the RX-clip for the ISI and b) of a Gaussian beam for the TMI. Such calibration would be a pre-test of the calibration that LISA would undergo once in space. The comparison of the two calibrations could give vital information about the effects of the launch's vibrations on the spacecraft.

Second, the numerical simulations of the heterodyne efficiency (see paragraph 2.3.3) suggest it might be preferable to minimize the wavefront mismatch between the beams in LISA. In the current beam parameter range, the maximum relative-wavefront-mismatch is $|\rho| = 0.469$. Such a mismatch would imply, together with a reduction of the maximum heterodyne efficiency, the disadvantage that the heterodyne efficiencies of the IFMs at individual quadrants of a QPDs would be maximum at grossly different beam tilt angles. For $|\rho| = 0.469$, the deviation would be 800 μrad . In such a configuration, the segments would have significantly different SNRs, and the angular dependence of DWS noise is expected to worsen, as the noise would be dominated by that of the segment with lowest SNR. The recommendation is to have an as small as possible wavefront mismatch.

Apart from this potential issue, the work presented in this thesis has demonstrated that LISA's interferometric detection system (IDS) can utilize DWS to achieve the required angular measurement sensitivity, even under the expected conditions during flight of weak received light and misaligned measurement beams. Consequently, DWS is validated as a method to both provide the error signals for the spacecraft's active control and enabling post-processing subtraction of TTL.

Acronyms

AEI	Albert Einstein Institute
ESA	European Space Agency
NASA	National Aeronautics and Space Administration
SRON	Netherlands Institute for Space Research
Nikhef	Nationaal Instituut voor subatomaire fysica
GR	general relativity
GW	gravitational wave
TT	traceless transverse
TDOBS	tilt-to-length coupling and DWS Optical Bench Simulator
TS	telescope simulator
LISA-OB	LISA-Optical Bench
MB	modulation bench
FIOS	fiber injector optical sub-assembly
CQP	calibrated quadrant photodiode pair
IS	imaging system
TTL	tilt-to-length
OS	optical system
VC	vacuum chamber
REFQPD	reference QPD
SCIQPD	science QPD
AUXQPD	auxiliary QPD
REFSEPD	reference SEPD
TRL	technology readiness level
LISA	Laser Interferometer Space Antenna
IDS	interferometric detection system
DFACS	drag-free attitude control system
OB	optical bench
MOSA	moving optical subassembly

OATM	optical assembly tracking mechanism
GRS	gravity reference sensor
PAAM	point-ahead angle mechanism
BAM	beam alignment mechanism
TM	test mass
ISI	inter-satellite interferometer
TMI	test mass interferometer
RFI	reference interferometer
TDI	time delayed interferometry
OGSE	optical ground support equipment
PMS	phase measurement sub-system
MOFPA	master oscillator fiber power amplifier
NPRO	non-planar ring oscillator
IFM	interferometer
BS	beam splitter
PBS	polarizing beam splitter
HWP	half waveplate
QWP	quarter waveplate
PD	photodiode
SEPD	single element photodiode
QPD	quadrant photodiode
QPR	quadrant photoreceiver
PR	photoreceiver
EOM	electro-optical modulator
AOM	acousto-optical modulator
TEM₀₀	transverse electromagnetic ₀₀
RoC	radius of curvature
DWS	differential wavefront-sensing
LPS	longitudinal pathlength sensing

DPS	differential power sensing
OPD	optical pathlength difference
RIN	relative intensity noise
InGaAs	indium gallium arsenide
TIA	trans-impedance amplifier
TF	transfer function
SG	signal generator
ADC	analog to digital converter
PM	phasemeter
OpAmp	operational amplifier
PCB	printed circuit board
FEE	front-end Electronics
BEE	back-end electronics
LPF	low-pass filter
MELF	metal electrode leadless face
SPICE	simulation program with integrated circuit emphasis
SVN	small vector noise
DPLL	digital phase-locked loop
NCO	numerically controller oscillator
PA	phase accumulator
PI	proportional-integral
PIR	phase increment register
LUT	look up table
FPGA	field-programmable gate array
FMC	FPGA mezzanine card
PT	pilot tone
RF	reference frame
FIR	finite impulse response
PSD	power spectral density

ASD	amplitude spectral density
LASD	logarithmic amplitude spectral density
FFT	fast fourier transform
C/N	carrier-to-noise
C/N₀	C/N density ratio
SNR	signal-to-noise ratio
RMS	root mean square

Appendices

Appendix A

Small Vector Noise

Small vector noise (SVN) occurs when a signal is contaminated by another much smaller signal. This is for instance the case of straylight interfering with the measurement beams or crosstalk in electronics. Let the beat note signal and the parasitic signal be described by the phasors

$$A_{\text{signal}}(t) = A_s e^{i(\omega_s t + \varphi_s)} \quad (\text{A.1})$$

$$A_{\text{parasitic}}(t) = A_p e^{i(\omega_p t + \varphi_p)}. \quad (\text{A.2})$$

The measured phasor is

$$\begin{aligned} A_{\text{meas}}(t) &= A_{\text{signal}}(t) + A_{\text{parasitic}}(t) \\ &= A_s e^{i(\omega_s t + \varphi_s)} + A_p e^{i(\omega_p t + \varphi_p)} \\ &= e^{i(\omega_s t + \varphi_s)} (A_s + A_p e^{i(\varphi_p - \varphi_s)}). \end{aligned} \quad (\text{A.3})$$

The time component $e^{i\omega_s t}$ will from now on be omitted. The amplitude of the parasitic signal will be assumed to be much smaller than the amplitude of the signal, $A_p \ll A_s$. The amplitude and phase of the new signal are

$$|A_{\text{meas}}| = \sqrt{A_p^2 + A_s^2 + 2A_p A_s \cos(\varphi_s - \varphi_p)} \quad (\text{A.4})$$

$$\arg(A_{\text{meas}}) = \varphi_s + \text{atan2} \left(\frac{A_p \sin(\varphi_p - \varphi_s)}{A_s + A_p \cos(\varphi_p - \varphi_s)} \right). \quad (\text{A.5})$$

By assuming $A_p \ll A_s$, this then becomes

$$\arg(A_{\text{meas}}) = \varphi_s + \frac{A_p}{A_s} (\varphi_p - \varphi_s). \quad (\text{A.6})$$

The phase error is hence

$$\Delta\varphi_{\text{err, SVN}} = \arg(A_{\text{meas}}) - \arg(A_{\text{signal}}) = \frac{A_p}{A_s} (\varphi_p - \varphi_s). \quad (\text{A.7})$$

In the case of electrical crosstalk between two beat notes the parasitic signal is going to be one beat note multiplied by a crosstalk coefficient c . In DWS such two beat notes could be provided by a QPD and have very similar amplitudes $A_A = A_B = A_C$ and having strongly correlated phases, as $\varphi_A = \varphi_B = -\varphi_C$ for

vertical DWS. A and B would produce no cross coupling as the phase difference is zero, while between A and C the coupling is

$$A_{\text{signal}}(t) = A_A e^{i(\omega_s t + \varphi_A)} \quad (\text{A.8})$$

$$A_{\text{parasitic}}(t) = c \cdot A_C e^{i(\omega_s t + \varphi_C)} \quad (\text{A.9})$$

$$\Delta\varphi_{\text{err, SVN}} = -2c \varphi_A, \quad (\text{A.10})$$

which would in principle allow to correct the phase error, if the constant c is known, as

$$\varphi_A = (1 + 2c)^{-1} \varphi_{\text{meas}}. \quad (\text{A.11})$$

In the case of straylight, the phase dynamics of the parasitic signal can be totally unrelated from that of the signal. What is sometimes observed is an oscillating value of φ_p , as $\varphi_p = k \cdot \sin(\omega_p t + \varphi_{p,0})$. This causes small sinusoidal phase oscillations around the signal's phase and well describes the plot in Figure 5.8, left.

$$\Delta\varphi_{\text{err, SVN}} = \text{atan2} \left(\frac{A_p}{A_s} (k \cdot \sin(\omega_p t + \varphi_{p,0}) - \varphi_s) \right) \quad (\text{A.12})$$

Depending on the specific values of k and ω_p this might relatively be strong enough or in the detection bandwidth to be seen in frequency domain.

Appendix B

Electronics' Schematics

This Appendix contains the design of the TIA circuits mentioned in Section 3.3.2 and Paragraph 3.3.2, as well as the schematics of the AC-DC splitters mentioned in Section 3.3.3.

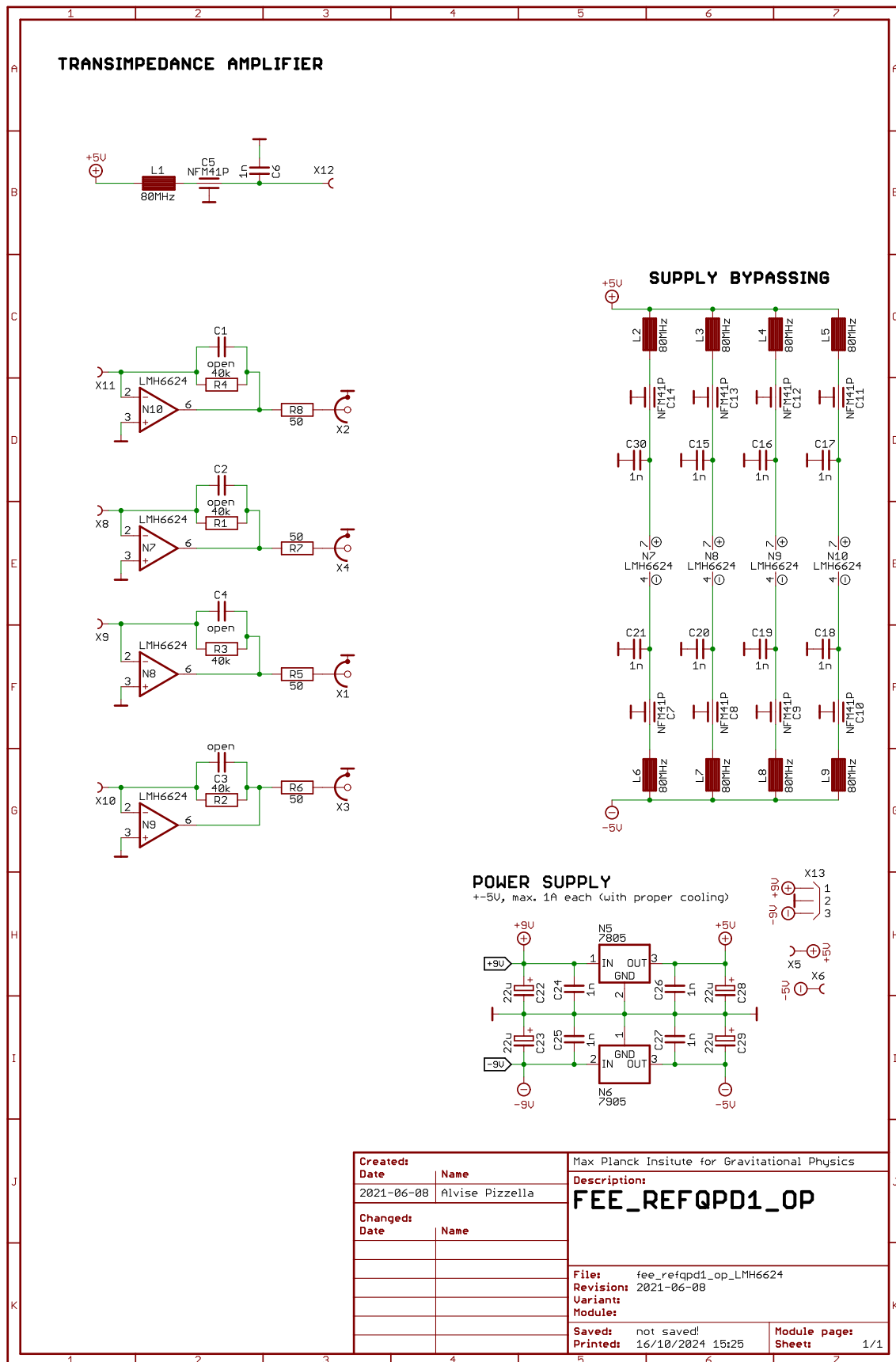


Figure B.1: Schematics of the OpAmp based TIA, labeled #1.

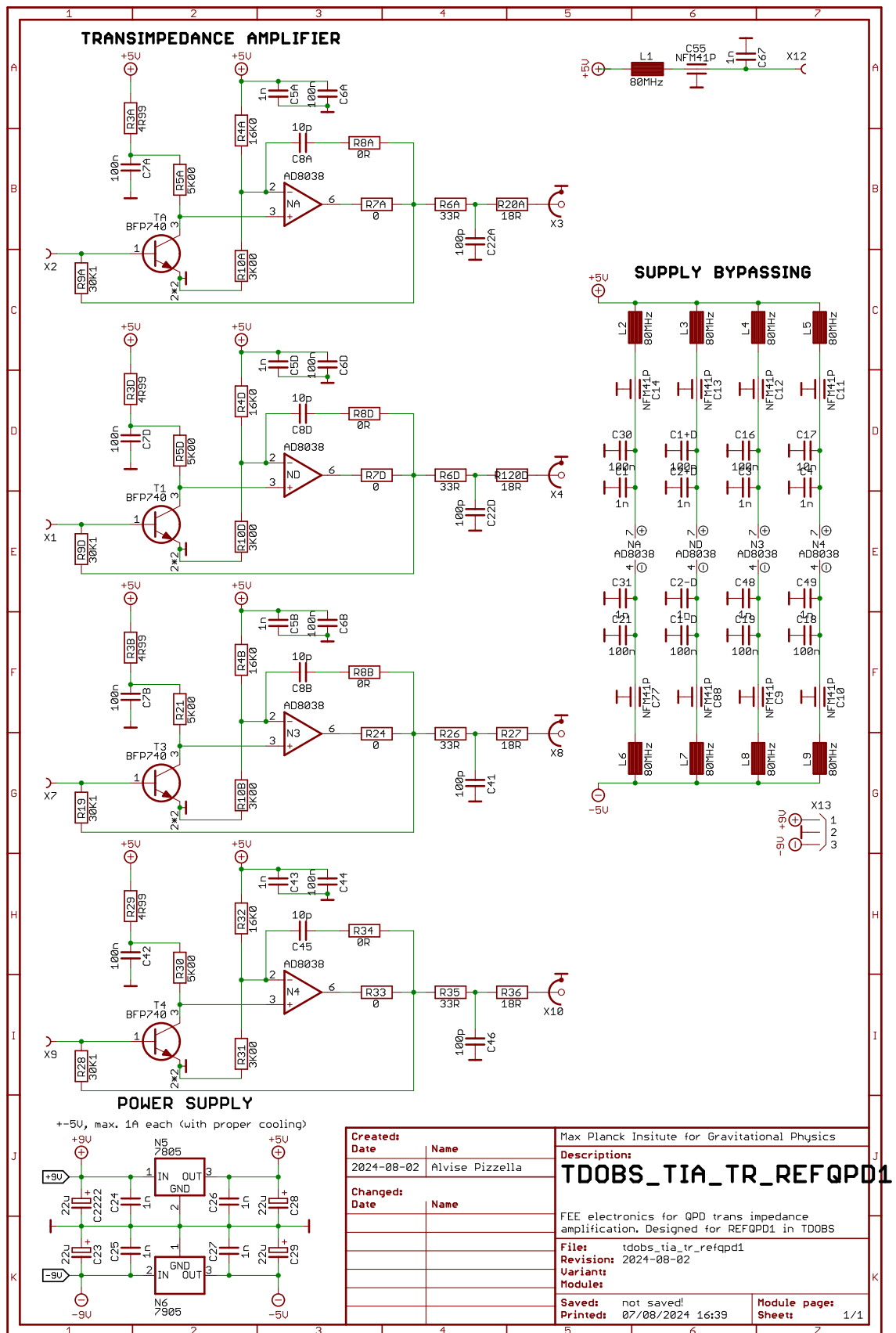


Figure B.2: Schematics of the transistor based TIA, labeled #2.

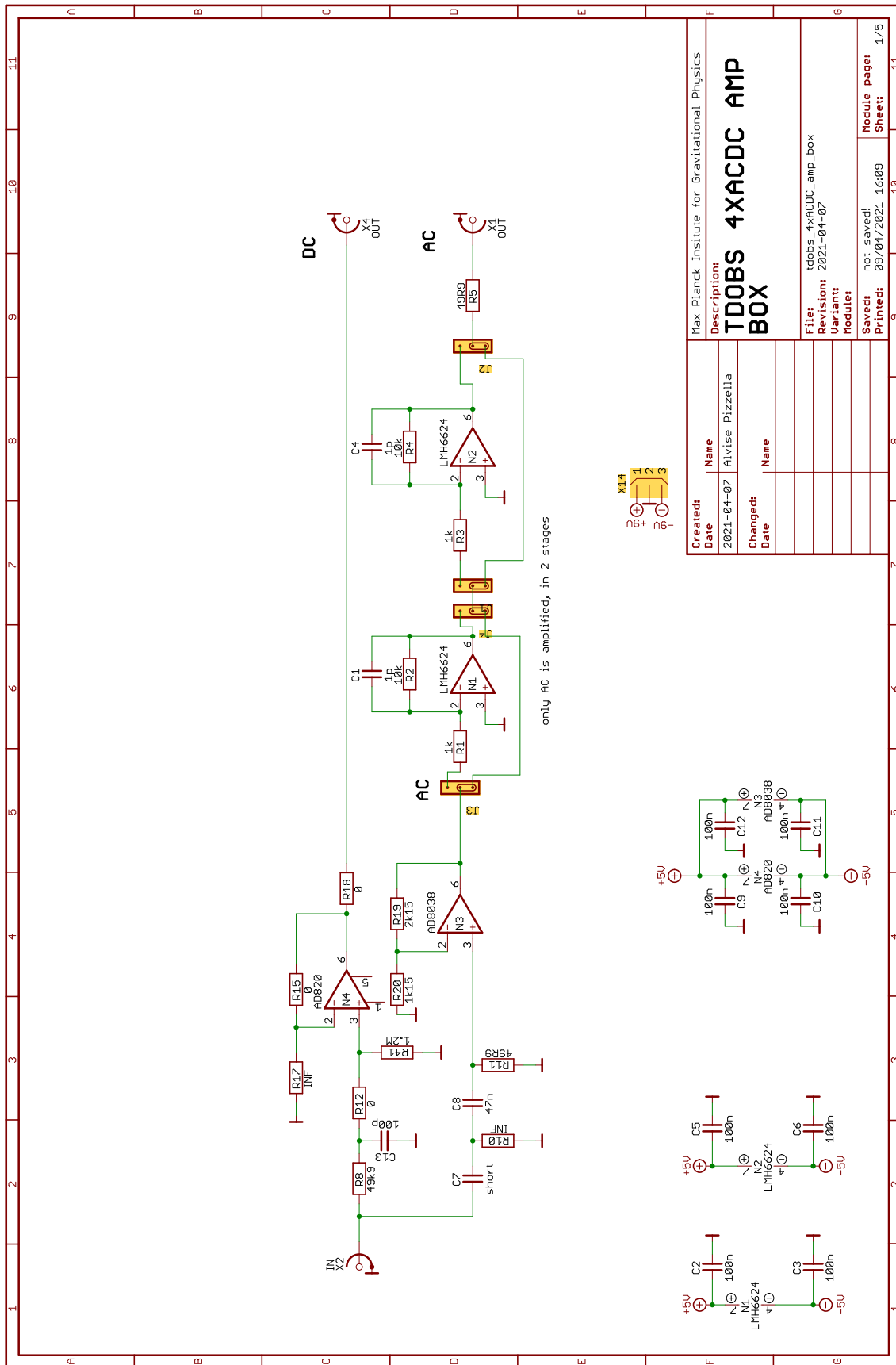


Figure B.3: Schematics of one channel of one AC-DC splitter.

Appendix C

DPS calibrations from TDOBS

The here shown curves are all fit with polynomials of some order n

$$y(x) = \sum_{i=0}^n p_i x^i. \quad (\text{C.1})$$

The obtained parameters p_i and the relative errors are reported in the associated tables. This Appendix report, in order, the DPS calibrations of the

- AUXQPD, RX-GB and RX-FT beams,
- REFQPD1, RX-GB,
- REFQPD2, RX-GB,
- CQPD2, RX-GB and RX-FT beams.

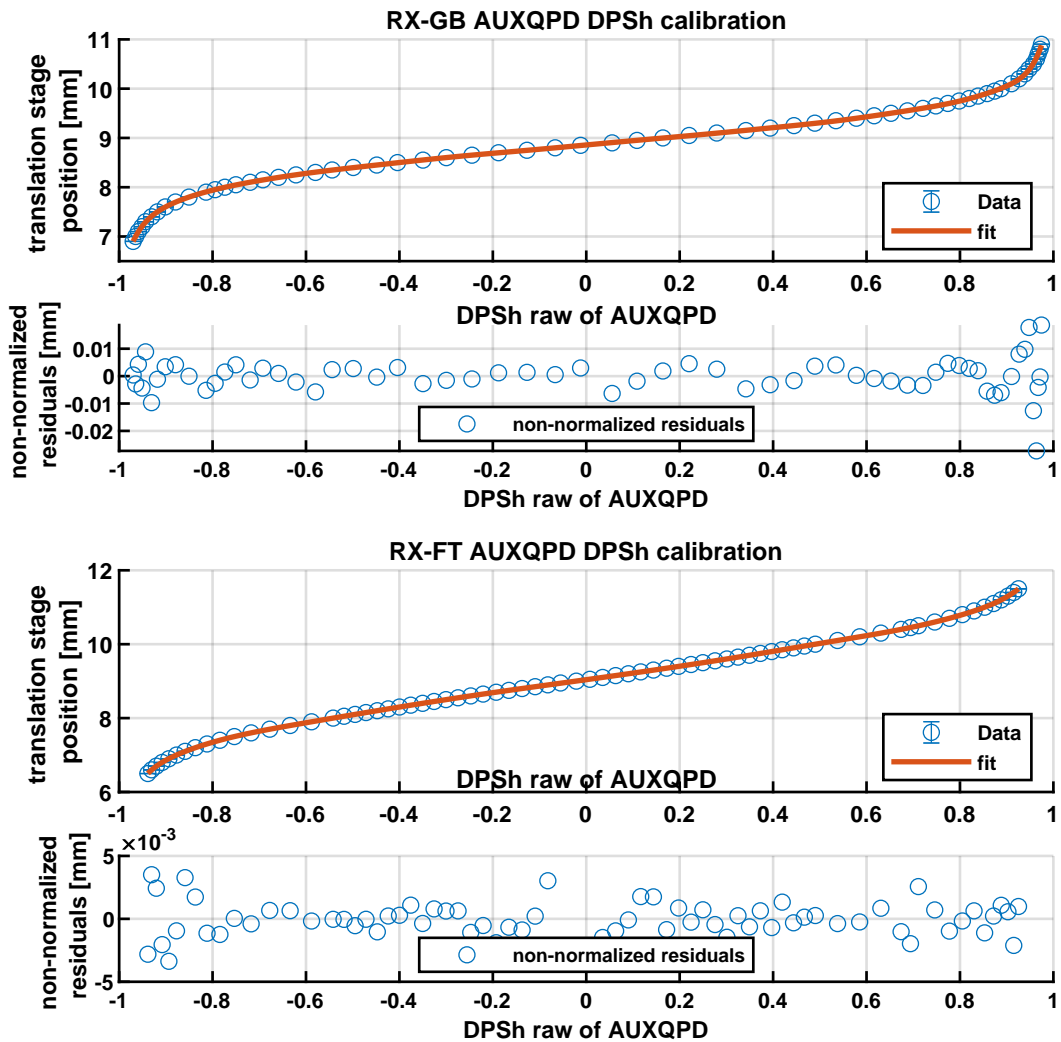


Figure C.1: Calibration plot of the DPS signal of the RX-GB (above) and RX-FT (below) on the AUXQPD. The fit parameters are reported in C.1 and C.2.

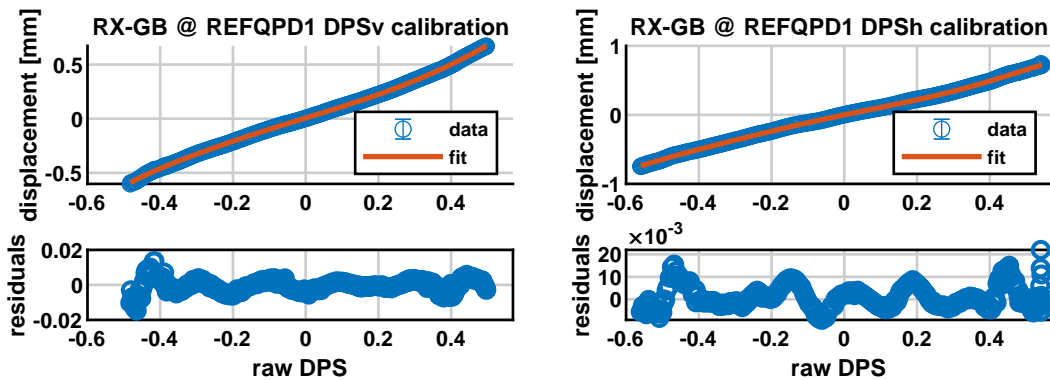


Figure C.2: Calibration plot of the DPS signal of the RX-GB on REFQPD1. The fit parameters are in table C.3.

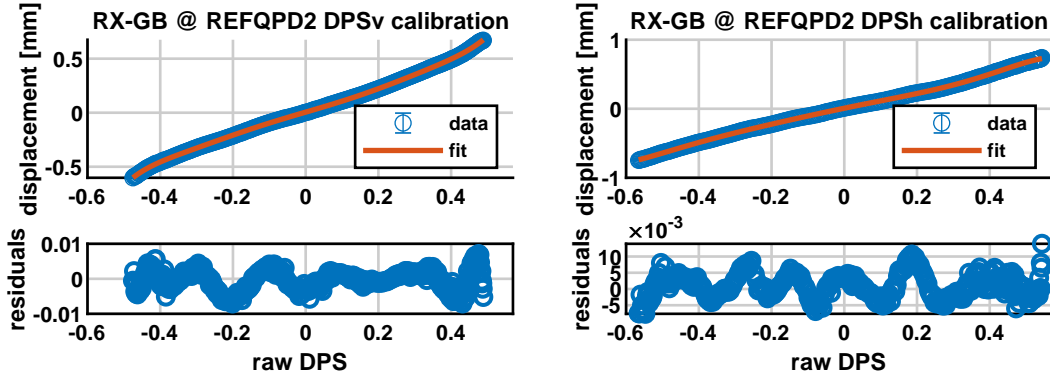
Parameter [mm]	Vertical		Horizontal	
p_0	7.4691	\pm 0.0006	8.8583	\pm 0.0001
p_1	0.840	\pm 0.006	0.883e	\pm 0.006
p_2	-1.92	\pm 0.04	0	\pm 0.04
p_3	-1.2	\pm 0.2	-1.8	\pm 0.2
p_4	3.4	\pm 0.7	1.4	\pm 0.7
p_5	25	\pm 3	30	\pm 3
p_6	-29	\pm 5	-23	\pm 5
p_7	-200	\pm 18	-218	\pm 20
p_8	130	\pm 21	130	\pm 20
p_9	800	\pm 60	840	\pm 60
p_{10}	-300	\pm 50	-360	\pm 45
p_{11}	-1830	\pm 120	-1860	\pm 120
p_{12}	390	\pm 60	525	\pm 55
p_{13}	2400	\pm 140	2350	\pm 130
p_{14}	-265	\pm 40	-390	\pm 35
p_{15}	-1600	\pm 80	-1580	\pm 80
p_{16}	72	\pm 10	110	\pm 93
p_{17}	450	\pm 20	440	\pm 19

Table C.1: Calibration parameters of the DPS signal of the RX-GB beam on the AUXQPD.

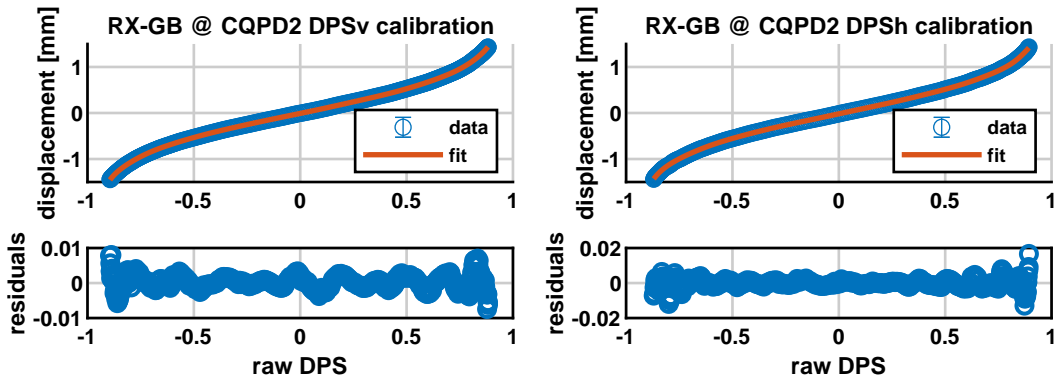
Parameter [mm]	Vertical		Horizontal	
p_0	10.401	\pm 0.001	9.040	\pm 0.001
p_1	1.797	\pm 0.004	1.750	\pm 0.005
p_2	0	\pm 0.03	0.025	\pm 0.03
p_3	2.8	\pm 0.2	0.9	\pm 0.2
p_4	1.1	\pm 0.6	-3.3	\pm 0.6
p_5	-36	\pm 3	0	\pm 3
p_6	-10	\pm 5	28	\pm 6
p_7	220	\pm 20	-10	\pm 20
p_8	39	\pm 23	-137	\pm 25
p_9	-717	\pm 72	22	\pm 75
p_{10}	-87	\pm 60	355	\pm 60
p_{11}	1350	\pm 160	-30	\pm 160
p_{12}	100	\pm 80	-500	\pm 80
p_{13}	-1500	\pm 200	48	\pm 20
p_{14}	-70	\pm 55	370	\pm 60
p_{15}	850	\pm 130	-64	\pm 130
p_{16}	19	\pm 16	-110	\pm 17
p_{17}	-200	\pm 35	3.1	\pm 40

Table C.2: Calibration parameters of the DPS signal of the RX-FT beam on the AUXQPD.

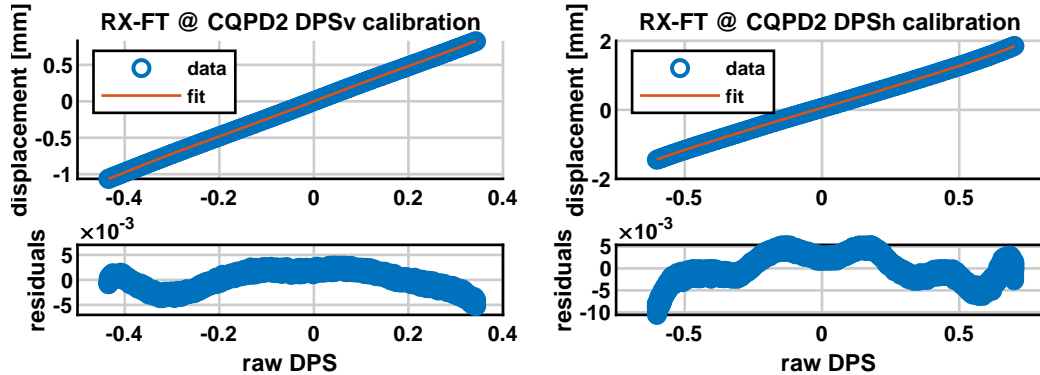
Parameter [mm]	Vertical			Horizontal		
p_0	0.00673	\pm	0.00001	-0.00012	\pm	0.00001
p_1	1.0374	\pm	0.0001	1.098	\pm	0.0001
p_2	-0.0185	\pm	0.0001	-0.3197	\pm	0.0006
p_3	1.155	\pm	0.005	0.977	\pm	0.003
p_4	1.10	\pm	0.01	2.534	\pm	0.006
p_5	-1.58	\pm	0.05	-0.51	\pm	0.02
p_6	-2.80	\pm	0.04	-4.71	\pm	0.02
p_7	4.91	\pm	0.15	-0.77	\pm	0.06

Table C.3: Calibration parameters of the DPS signal of the RX-GB beam on REFQPD1.**Figure C.3:** Calibration plot of the DPS signal of the RX-GB on REFQPD2. The fit parameters are in table C.4.

Parameter [mm]	Vertical			Horizontal		
p_0	0.00527	\pm	0.00001	0.007671	\pm	0.000001
p_1	0.9877	\pm	0.0001	1.09142	\pm	0.00001
p_2	0.0048	\pm	0.0009	-0.3406	\pm	0.0005
p_3	2.836	\pm	0.005	0.284	\pm	0.003
p_4	1.24	\pm	0.01	3.119	\pm	0.006
p_5	-18.35	\pm	0.05	6.61	\pm	0.02
p_6	-4.36	\pm	0.04	-6.59	\pm	0.01
p_7	53.48	\pm	0.16	-16.72	\pm	0.06

Table C.4: Calibration parameters of the DPS signal of the RX-GB beam on REFQPD2.**Figure C.4:** Calibration plot of the DPS signal of the RX-GB on CQPD2. The fit parameters are in table C.5.

Parameter [mm]	Vertical			Horizontal		
p_0	-0.009293	\pm	0.00004	-0.01815	\pm	0.00001
p_1	0.9543	\pm	0.0001	0.9945	\pm	0.0001
p_2	0.1305	\pm	0.0003	-0.0050	\pm	0.0004
p_3	0.987	\pm	0.002	-0.610	\pm	0.003
p_4	-1.262	\pm	0.006	0.93	\pm	0.01
p_5	-1.02	\pm	0.02	12.7	\pm	0.04
p_6	5.13	\pm	0.05	-9.918	\pm	0.07
p_7	68.0	\pm	0.2	-76.3	\pm	0.2
p_8	-7.3	\pm	0.2	42.0	\pm	0.3
p_9	-221.4	\pm	0.6	244.0	\pm	0.9
p_{10}	-2.4	\pm	0.5	-88.9	\pm	0.6
p_{11}	383	\pm	1	-415	\pm	2
p_{12}	13.9	\pm	0.5	92.4	\pm	0.7
p_{13}	-336	\pm	1	355	\pm	1
p_{14}	-8.3	\pm	0.2	-37.5	\pm	0.3
p_{15}	118.3	\pm	0.4	-119.0	\pm	0.6

Table C.5: Calibration parameters of the DPS signal of the RX-GB beam on CQPD2.**Figure C.5:** Calibration plot of the DPS signal of the RX-FT on CQPD2. The fit parameters are in table C.6.

Parameter [mm]	Vertical			Horizontal		
p_0	0.000088	\pm	0.00001	0.05551	\pm	0.00002
p_1	2.477	\pm	0.001	2.3182	\pm	0.0008
p_3	-3.05	\pm	0.07	1.52	\pm	0.02
p_5	45	\pm	2	-11.64	\pm	.03
p_7	-320	\pm	24	49	\pm	1
p_9	1350	\pm	140	-93	\pm	3
p_{11}	-2500	\pm	270	68	\pm	2

Table C.6: Calibration parameters of the DPS signal of the RX-GB beam on CQPD2.

Appendix D

DWS calibrations from TDOBS

This Appendix report, in order, the DWS calibrations of the

- RX-GB & LO beams on REFQPD2.
- RX-FT & LO beams on REFQPD2.

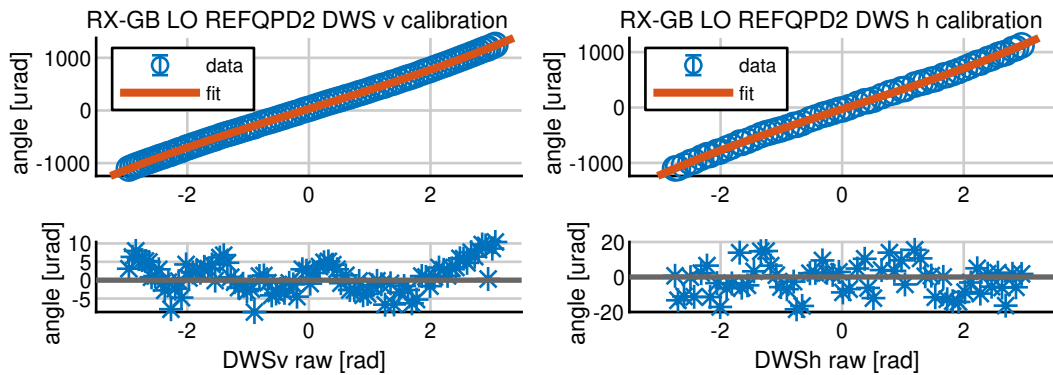


Figure D.1: Calibration plot of the DWS signal of the RX-GB & LO beam pair on REFQPD2. This calibration was realized using phase measurements from the FMC PM at a heterodyne frequency of 156.25 kHz.

Parameter	Vertical			Horizontal		
p_1 [$\mu\text{rad}\text{rad}^{-1}$]	350	\pm	0.6	352	\pm	2
p_3 [$\mu\text{rad}\text{rad}^{-3}$]	3.66	\pm	0.15	4.6	\pm	0.4
x_0 [rad]	-0.088	\pm	0.001	0.081	\pm	0.003

Table D.1: Calibration parameters of the DWS signal of the RX-GB & LO beam pair on REFQPD2 in figure D.1.

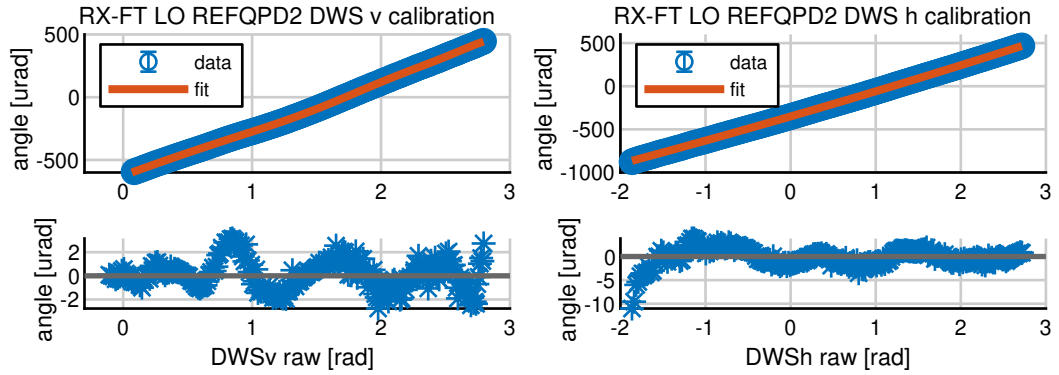


Figure D.2: Calibration plot of the DWS signal of the RX-FT & LO beam pair on REFQPD2. This calibration was realized using phase measurements from the FMC PM at a heterodyne frequency of 5 MHz.

Parameter	Vertical			Horizontal		
	p_0 [urad]	p_1 [uradrad $^{-1}$]	p_2 [uradrad $^{-2}$]	p_3 [uradrad $^{-3}$]	p_4 [uradrad $^{-4}$]	p_5 [uradrad $^{-5}$]
p_0 [urad]	-625.7 \pm 0.1	381 \pm 1	9 \pm 10	-300 \pm 50	860 \pm 120	-1230 \pm 140
p_1 [uradrad $^{-1}$]		285.82 \pm 0.08				
p_2 [uradrad $^{-2}$]		5.37 \pm 0.07				
p_3 [uradrad $^{-3}$]		0.03 \pm 0.03				
p_4 [uradrad $^{-4}$]					-	
p_5 [uradrad $^{-5}$]						-
p_6 [uradrad $^{-6}$]						-
p_7 [uradrad $^{-7}$]						-
p_8 [uradrad $^{-8}$]						-
p_9 [uradrad $^{-9}$]						-

Table D.2: Calibration parameters of the DWS signal of the RX-FT & LO beam pair on REFQPD2 in figure D.2.

Appendix E

Imaging System calculations

This Appendix reports some calculations realized using the ray transfer matrix formalism in Section 2.2.

E.1 Propagation of a generic beam through a generic optical system

This is a totally general calculation for the propagation of a beam with q parameter $q_0 = iz_R + z_0$ through an ABCD matrix.

$$\begin{aligned}
q_1 &= \frac{Aq_0 + B}{Cq_0 + D} \\
&= \frac{A(iz_R + z_0) + B}{C(iz_R + z_0) + D} \\
&= \frac{Az_0 + B + iAz_R}{Cz_0 + D + iCz_R} \\
&= \frac{Az_0 + B + iAz_R}{Cz_0 + D + iCz_R} \frac{Cz_0 + D - iCz_R}{Cz_0 + D - iCz_R} \\
&= \frac{ACz_0^2 + ADz_0 - iACz_0z_R + BCz_0 + BD - iBCz_R + iACz_Rz_0 + iADz_R + ACz_R^2}{(Cz_0 + D)^2 + C^2z_R^2} \\
&\quad + i \frac{z_R(AD - BC)}{(Cz_0 + D)^2 + C^2z_R^2} + \frac{AC(z_0^2 + z_R^2) + (AD + BC)z_0 + BD}{(Cz_0 + D)^2 + C^2z_R^2} \\
&= iz'_R + z'_0
\end{aligned} \tag{E.1}$$

The new beam parameters are hence

$$z'_R = \frac{z_R(AD - BC)}{(Cz_0 + D)^2 + C^2z_R^2} \tag{E.2}$$

$$z'_0 = \frac{AC(z_0^2 + z_R^2) + (AD + BC)z_0 + BD}{(Cz_0 + D)^2 + C^2z_R^2}. \tag{E.3}$$

E.2 Propagation through a generic Imaging System

In case of an Imaging System $B=0$ and $AD=1$, and hence equations (E.2) and (E.3) become

$$z'_R = \frac{z_R}{(Cz_0 + D)^2 + C^2z_R^2} \quad (E.4)$$

$$z'_0 = \frac{AC(z_0^2 + z_R^2) + z_0}{(Cz_0 + D)^2 + C^2z_R^2} \quad (E.5)$$

It is interesting to calculate from here the spot size of new beam at the exit pupil of the IS. The waist of the new beam is $w'_0 = \sqrt{\frac{\lambda}{\pi} z'_R}$. The spot size of the beam at the exit pupil of the imaging system is

$$\begin{aligned} w'_0(z'_0) &= w'_0 \sqrt{1 + \left(\frac{z'_0}{z'_R}\right)^2} \\ &= \sqrt{\frac{\lambda}{\pi} z'_R} \sqrt{1 + \left(\frac{z'_0}{z'_R}\right)^2} \\ &= \sqrt{\frac{\lambda}{\pi}} \sqrt{\frac{z_R}{(Cz_0 + D)^2 + C^2z_R^2}} \sqrt{1 + \left(\frac{AC(z_0^2 + z_R^2) + z_0}{z_R}\right)^2} \\ &= \sqrt{\frac{\lambda}{\pi}} \sqrt{\frac{z_R}{(Cz_0 + D)^2 + C^2z_R^2}} \sqrt{\frac{(Dz_R)^2 + (C(z_0^2 + z_R^2) + z_0D)^2}{(z_R D)^2}} \\ &= \sqrt{\frac{\lambda}{\pi}} \sqrt{\frac{A}{(Cz_0 + D)^2 + C^2z_R^2}} \sqrt{\frac{(Dz_R)^2 + C^2(z_0^2 + z_R^2)^2 + (z_0D)^2 + 2DCz_0(z_0^2 + z_R^2)}{z_R D}} \\ &= \sqrt{\frac{\lambda}{\pi}} \sqrt{\frac{A}{C^2(z_0^2 + z_R^2) + 2DCz_0 + D^2}} \sqrt{\frac{(z_0^2 + z_R^2)(C^2(z_0^2 + z_R^2) + 2DCz_0 + D^2)}{z_R D}} \\ &= \sqrt{\frac{\lambda}{\pi}} \sqrt{\frac{(z_0^2 + z_R^2)A}{z_R D}} \\ &= \sqrt{\frac{\lambda}{\pi} z_R} \sqrt{\frac{(z_0^2 + z_R^2)A}{z_R^2 D}} \\ &= w_0 A \sqrt{1 + \left(\frac{z_0}{z_R}\right)^2}, \end{aligned} \quad (E.6)$$

meaning that the spot size of a Gaussian beam at the exit pupil of an IS is that at the entrance multiplied by a scaling factor A . In similar fashion a calculation for the RoC at the exit pupil gives

$$\begin{aligned} R'(z'_0) &= z'_0 \left(1 + \left(\frac{z'_R}{z'_0}\right)^2\right) \\ &= A^3(C(z_0^2 + z_R^2) + A^{-1}z_0) \left(1 + \left(\frac{z_R}{z_0}\right)^2\right). \end{aligned} \quad (E.7)$$

This is not a function of the RoC at the entrance pupil. It would be if the IS featured also $C=0$, being a 'collimating IS'. For such a system

$$\begin{aligned} R'(z'_0) &= A^2 z_0 \left(1 + \left(\frac{z_R}{z_0} \right)^2 \right) \\ &= A^2 R(z_0). \end{aligned} \quad (\text{E.8})$$

For such an IS the ABCD matrix takes the form

$$M = \begin{pmatrix} A & 0 \\ 0 & A^{-1} \end{pmatrix} = \begin{pmatrix} \frac{1}{m} & 0 \\ 0 & m \end{pmatrix} \quad (\text{E.9})$$

which is for convenience expressed using the *angular magnification*. The propagation through such a system yields

$$z'_R = A^2 z_R = \frac{1}{m^2} z_R \quad (\text{E.10})$$

$$z'_0 = A^2 z_0 = \frac{1}{m^2} z_0 \quad (\text{E.11})$$

and

$$w'(z'_0) = A w(z_0) = \frac{1}{m} w(z_0) \quad (\text{E.12})$$

$$R'(z'_0) = A^2 w(z_0) = \frac{1}{m^2} R(z_0). \quad (\text{E.13})$$

E.2.1 AOM double-pass imaging systems

For the realization of the three AOM double-pass reported in Subsection 3.3.1 we implemented three ISs using a curved mirror placed at a RoC distance from the AOM. Such topology quickly proved to be better than the alternative using a lens and a flat mirror. In this way the output beam from the AOM is reflected back into the AOM itself. The output light is separated from the incoming light by means of a quarter waveplate (QWP) and a PBS. This concept is illustrated in figure E.1.

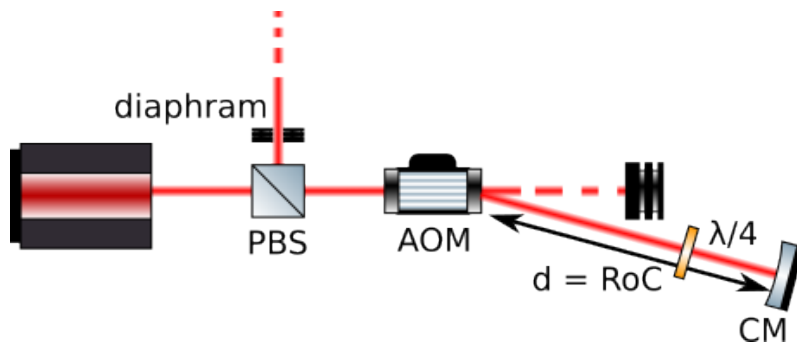


Figure E.1: Illustration of an AOM double-pass system using a curved mirror (CM). The exit beam is separated from the input beam with a QWP and a PBS. The zero order beam is dumped in the first pass with a beam dump and in the second pass by an diaphragm because of space constrains, as the beam should be fiber coupled in as little space as possible minimize the effect of the IS's imperfections.

The ray transfer matrix to describe this is

$$\begin{aligned}
M &= \text{Propagation}(RoC) \cdot \text{CurvedMirror}(RoC) \cdot \text{Propagation}(RoC) \\
&= \begin{pmatrix} 1 & RoC \\ 0 & 1 \end{pmatrix} \cdot \begin{pmatrix} 1 & 0 \\ -\frac{2}{RoC} & 1 \end{pmatrix} \cdot \begin{pmatrix} 1 & RoC \\ 0 & 1 \end{pmatrix} \\
&= \begin{pmatrix} -1 & 0 \\ -\frac{2}{RoC} & -1 \end{pmatrix}.
\end{aligned} \tag{E.14}$$

Besides this, in the realization of such systems one has to also take care of the beam profile. AOMs happen to be more efficient for wider beams and when positioned close to the beam's waist (so the beam is not opening up too quickly), as I personally characterized. Provided that the AOM is positioned at the beam's waist, by propagating a generic beam of waist w_0 (and hence Rayleigh-range z_R) and waist position z_0 one gets, using equation (2.97):

$$z'_0(z_R, RoC) = \frac{2z_R^2 RoC}{4z_R^2 + RoC^2} \tag{E.15}$$

$$z'_R(z_R, RoC) = \frac{z_R RoC^2}{4z_R^2 + RoC^2}. \tag{E.16}$$

For the second pass, equation (E.6) states that the beam spot size at the second pass will be the same as in the first pass, although the second pass will not be at the beam's waist position. This is relieving, as the beam will make it through the small aperture of the AOM. To minimize the separation between the return beam's waist and the second pass, one has to minimize z'_0 . This happens if either if $z_R \rightarrow \infty$ or $RoC \rightarrow \infty$. As the first option is in conflict with the AOM's efficiency, to minimize this parameter one has to pick a big RoC. Because of this, the largest curved mirror fittable on the MB was chosen, with a RoC of 1.5 m (see figure E.2). Implementations where the AOM first pass is not at the waist have not been investigated because the gain would be negligible in comparison to the effort.

E.3 DWS and Imaging Systems

This section supposes the use of a collimating IS described by equation (E.9). Imaging systems only apparently increase the sensitivity of DWS by their magnification. Let two beams, a measurement and a reference beam, have waist $w_{0,r}$ and $w_{0,m}$ and waist positions $z_{0,r}$ and $z_{0,m}$. The measurement beam is free to rotate around a pivot located at $z = z_P$. Their DWS signal is measured at $z = z_P$ with an infinite radius QPD. The DWS gain at null angle is given by equations (2.133, 2.134).

$$\text{DWS}(\theta) = \arg \left(\frac{1 + i\alpha}{1 - i\alpha} \right) \quad \alpha = \text{erfi} \left(\frac{w_{\text{eff}} k \theta}{2} \sqrt{\frac{1 + i\rho}{1 + \rho^2}} \right) \quad \rho = \frac{w_{\text{eff}}^2 k}{2R_{\text{rel}}} \tag{E.17}$$

w_{eff} and R_{rel} are the known quantities from equation (2.25).

$$\frac{1}{w_{\text{eff}}^2} = \frac{1}{w_m^2(z_P)} + \frac{1}{w_r^2(z_P)} \quad \frac{1}{R_{\text{rel}}} = \frac{1}{R_m(z_P)} - \frac{1}{R_r(z_P)} \tag{E.18}$$

If instead of the QPD an IS with angular magnification m is placed with entrance pupil at z and the QPD is positioned at the exit pupil of the IS, then

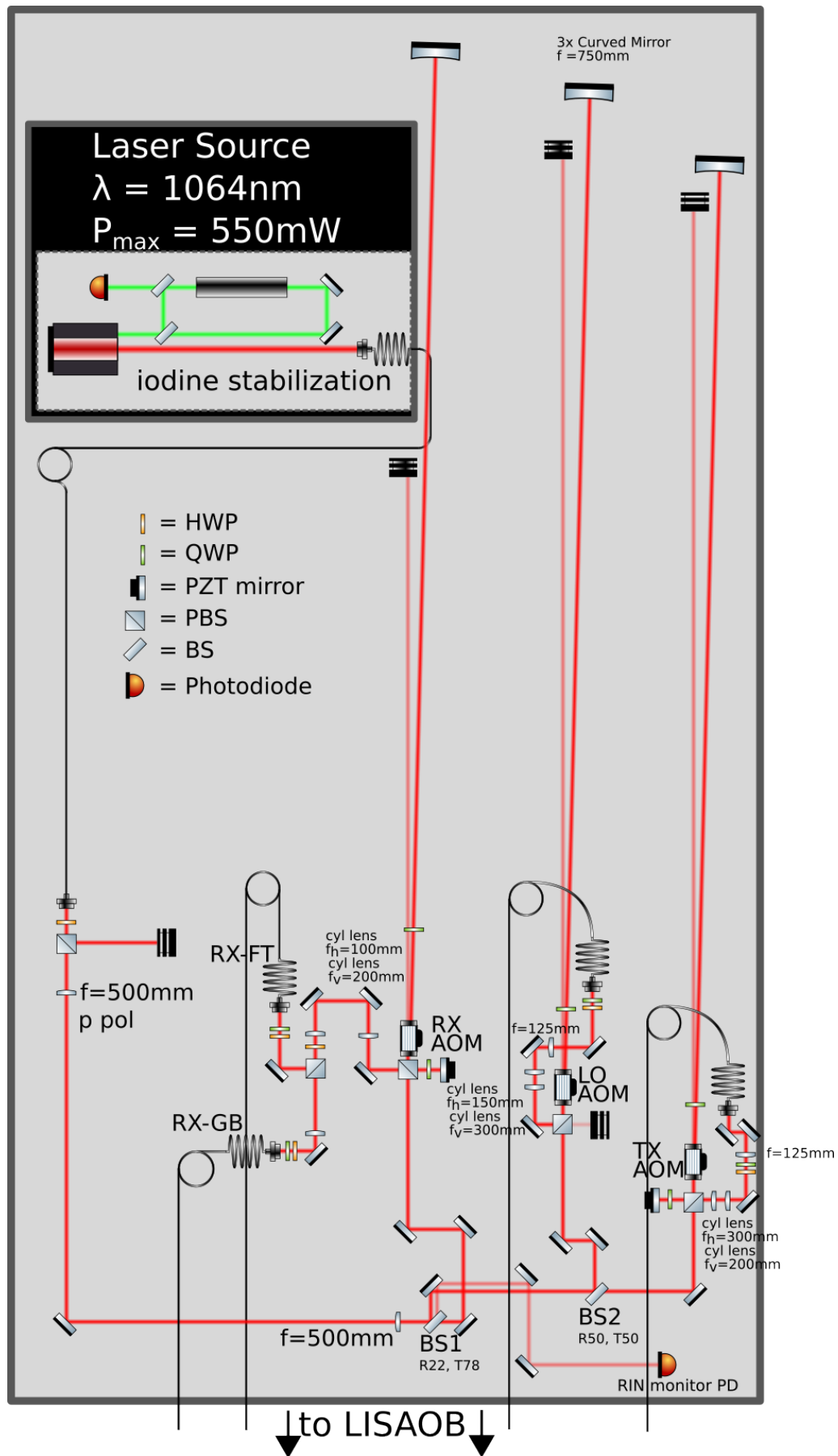


Figure E.2: Layout of the MB.

- the angle of the measurement beam is magnified $\theta' = m\theta$. In this step it is assumed that the resulting angle θ' is still reasonably small in order to perform a linear expansion as in equations (2.120, 2.121).
- the new DWS signal DWS' can be calculated by applying equations (E.12, E.13)

$$\frac{1}{w'_{\text{eff}}^2} = \frac{m^2}{w_m^2(z_P)} + \frac{m^2}{w_r^2(z_P)} = \frac{m^2}{w_{\text{eff}}^2} \quad (\text{E.19})$$

$$\frac{1}{R'_{\text{rel}}} = \frac{m^2}{R_m(z_P)} - \frac{m^2}{R_r(z_P)} = \frac{m^2}{R_{\text{rel}}} \quad (\text{E.20})$$

$$\rho' = \frac{w_{\text{eff}}^2}{m^2} \frac{m^2}{R_{\text{rel}}} \frac{k}{2} = \rho \quad (\text{E.21})$$

$$\alpha' = \text{erfi} \left(\frac{w'_{\text{eff}} k \theta'}{2} \sqrt{\frac{1 + i \rho'}{1 + \rho'^2}} \right) = \alpha \quad (\text{E.22})$$

$$\text{DWS}'(\theta') = \text{DWS}(\theta) \quad (\text{E.23})$$

This argument does not hold anymore if the QPD has a size comparable to that of the beam. Placing an IS is advantageous for other reasons, as compressing the beam allows to use a smaller QPD, which has lower capacitance (see equation (3.4)) and hence the QPR has lower electronic noise (see equation (3.5)).

Bibliography

- [1] B. P. Abbott et al. “GW170817: Observation of Gravitational Waves from a Binary Neutron Star Inspiral”. In: *Phys. Rev. Lett.* 119 (16 Oct. 2017), p. 161101. DOI: 10.1103/PhysRevLett.119.161101. URL: <https://link.aps.org/doi/10.1103/PhysRevLett.119.161101> (cit. on p. 5).
- [2] B. P. Abbott et al. “Observation of Gravitational Waves from a Binary Black Hole Merger”. In: *Phys. Rev. Lett.* 116 (6 Feb. 2016), p. 061102. DOI: 10.1103/PhysRevLett.116.061102. URL: <https://link.aps.org/doi/10.1103/PhysRevLett.116.061102> (cit. on pp. 5, 6).
- [3] L. d’Arcio et al. “Optical Bench Developement for LISA”. In: *International Conference on Space Optics 2010* (2010). URL: https://pure.mpg.de/rest/items/item_1660150/component/file_1660149/content (cit. on pp. 12, 60).
- [4] Pau Amaro-Seoane et al. *Laser Interferometer Space Antenna*. 2017. arXiv: 1702.00786 [astro-ph.IM]. URL: <https://arxiv.org/abs/1702.00786> (cit. on p. 18).
- [5] F Antonucci et al. “LISA Pathfinder: mission and status”. In: *Classical and Quantum Gravity* 28.9 (Apr. 2011), p. 094001. DOI: 10.1088/0264-9381/28/9/094001. URL: <https://dx.doi.org/10.1088/0264-9381/28/9/094001> (cit. on p. 38).
- [6] M. Armano et al. “LISA Pathfinder platform stability and drag-free performance”. In: *Physical Review D* 99.8 (Apr. 2019). ISSN: 2470-0029. DOI: 10.1103/physrevd.99.082001. URL: <http://dx.doi.org/10.1103/PhysRevD.99.082001> (cit. on p. 169).
- [7] M. Armano et al. “Sensor noise in *LISA Pathfinder*: Laser frequency noise and its coupling to the optical test mass readout”. In: *Phys. Rev. D* 109 (4 Feb. 2024), p. 042003. DOI: 10.1103/PhysRevD.109.042003. URL: <https://link.aps.org/doi/10.1103/PhysRevD.109.042003> (cit. on pp. 130, 136).
- [8] Simon Barke et al. “ESA ITT AO/1-6238/10/NL/HB LISA Metrology System Final Report”. In: (2014) (cit. on pp. 15, 17).
- [9] Christoph Bode. “Noise in the LISA phasemeter”. PhD thesis. Leibniz Universität Hannover, 2024 (cit. on pp. 16, 86, 87, 131, 136, 137, 165, 177, 180, 184, 185, 188).
- [10] J Bogenstahl et al. “LTP fibre injector qualification and status”. In: *Journal of Physics: Conference Series* 154.1 (Mar. 2009), p. 012011. DOI: 10.1088/1742-6596/154/1/012011. URL: <https://dx.doi.org/10.1088/1742-6596/154/1/012011> (cit. on p. 64).

- [11] Nils Christopher Brause. “Auxiliary function development for the LISA metrology system”. PhD thesis. Leibniz Universität Hannover, 2018 (cit. on p. 177).
- [12] William Brzozowski et al. “The LISA optical bench: an overview and engineering challenges”. In: *Space Telescopes and Instrumentation 2022: Optical, Infrared, and Millimeter Wave*. Ed. by Laura E. Coyle, Shuji Matsuura, and Marshall D. Perrin. Vol. 12180. International Society for Optics and Photonics. SPIE, 2022, 121800O. DOI: 10.1117/12.2627465. URL: <https://doi.org/10.1117/12.2627465> (cit. on pp. 9, 61).
- [13] J Camp, K Numata, and M Krainak. “Progress and Plans for a US Laser System for LISA”. In: *Journal of Physics: Conference Series* 840.1 (May 2017), p. 012013. DOI: 10.1088/1742-6596/840/1/012013. URL: <https://dx.doi.org/10.1088/1742-6596/840/1/012013> (cit. on p. 14).
- [14] Eleonora Capocasa. “Optical and noise studies for Advanced Virgo and filter cavities for quantum noise reduction in gravitational-wave interferometric detectors”. PhD thesis. Université Paris Diderot, 2017 (cit. on p. 5).
- [15] M Chwalla et al. “Design and construction of an optical test bed for LISA imaging systems and tilt-to-length coupling”. In: *Classical and Quantum Gravity* 33.24 (Nov. 2016), p. 245015. DOI: 10.1088/0264-9381/33/24/245015. URL: <https://dx.doi.org/10.1088/0264-9381/33/24/245015> (cit. on pp. 62, 64, 65, 66, 77).
- [16] M. Chwalla et al. “Optical Suppression of Tilt-to-Length Coupling in the LISA Long-Arm Interferometer”. In: *Physical Review Applied* 14.1 (July 2020). DOI: 10.1103/physrevapplied.14.014030. URL: <https://doi.org/10.1103/2Fphysrevapplied.14.014030> (cit. on pp. 61, 62, 70, 71, 85, 132).
- [17] Monica Colpi et al. *LISA Definition Study Report*. 2024. arXiv: 2402.07571 [astro-ph.CO]. URL: <https://arxiv.org/abs/2402.07571> (cit. on pp. 8, 10, 12, 15, 60).
- [18] OptoElectronic Components. *OEC*. URL: <https://optoecomponents.com/> (cit. on pp. 75, 76).
- [19] LISA Consortium. *Home page of the LISA Consortium*. URL: <https://www.elisascience.org/> (cit. on pp. 7, 8, 10, 11, 13, 14, 15, 18).
- [20] Karsten Danzmann, T Prince, and the Lisa internatinal science team. “Assessment study report (Yellow Book)”. In: *Tech. rep. ESA* (Feb. 2011). URL: https://sci.esa.int/documents/35005/36499/1567258681608-LISA_YellowBook_ESA-SRE-2011-3_Feb2011.pdf (cit. on pp. 7, 8, 9, 10, 11, 13, 14, 15, 17).
- [21] N. Darbeheshti et al. “Instrument data simulations for GRACE Follow-on: observation and noise models”. In: *Earth System Science Data* 9.2 (2017), pp. 833–848. DOI: 10.5194/essd-9-833-2017. URL: <https://essd.copernicus.org/articles/9/833/2017/> (cit. on p. 60).
- [22] *Dizionario Etimologico Online*. URL: <https://www.etimo.it/?term=misura> (cit. on p. ii).
- [24] Albert Einstein. “Erklärung der Perihelbewegung des Merkur aus der allgemeinen Relativitätstheorie”. In: *Preussische Akademie der Wissenschaften, Sitzungsberichte* (Nov. 1915), pp. 831–839 (cit. on p. 3).

- [25] Albert Einstein. “Feldgleichungen der Gravitation”. In: *Preussische Akademie der Wissenschaften, Sitzungsberichte* (Nov. 1915), pp. 844–847 (cit. on p. 3).
- [26] Albert Einstein. “Grundgedanken der allgemeinen Relativitätstheorie und Anwendung dieser Theorie in der Astronomie”. In: *Preussische Akademie der Wissenschaften, Sitzungsberichte* (Nov. 1915), p. 315 (cit. on p. 3).
- [27] Albert Einstein. “Zur allgemeinen Relativitätstheorie”. In: *Preussische Akademie der Wissenschaften, Sitzungsberichte* (Nov. 1915), pp. 778–786, 799–801 (cit. on p. 3).
- [28] ESA. *The European Space Agency home webpage*. URL: <https://www.esa.int/> (cit. on p. 7).
- [32] German Fernandez Barranco. “Photodetection in intersatellite laser interferometers”. PhD thesis. Leibniz Universität Hannover, 2017 (cit. on pp. 74, 77, 81, 82, 83).
- [36] Ewan D. Fitzsimons et al. “Precision absolute positional measurement of laser beams”. In: *Appl. Opt.* 52.12 (Apr. 2013), pp. 2527–2530. DOI: 10.1364/AO.52.002527. URL: <https://opg.optica.org/ao/abstract.cfm?URI=ao-52-12-2527> (cit. on p. 65).
- [37] Ewan et al Fitzsimons. *LISA Optical Bench*. July 2024. URL: <https://www.youtube.com/channel/UCjQT50o21xDigkUxL-W0aqQ/about> (cit. on p. 61).
- [38] Samuel Peter Francis. “Multi-link laser interferometer architecture for a next generation GRACE”. PhD thesis. Australian National University, 2017 (cit. on p. 184).
- [39] Oliver Gerberding. “Phase readout for satellite interferometry”. PhD thesis. Leibniz Universität Hannover, 2014 (cit. on p. 131).
- [40] Marie-Sophie Hartig. “Tilt-To-Length Coupling in LISA Pathfinder: Model, Data Analysis and Take-Away-Messages for LISA”. PhD thesis. Leibniz Universität Hannover, 2022 (cit. on pp. 59, 60).
- [41] Gerald Hechenblaikner. “Measurement of the absolute wavefront curvature radius in a heterodyne interferometer”. In: *J. Opt. Soc. Am. A* 27.9 (Sept. 2010), pp. 2078–2083. DOI: 10.1364/JOSAA.27.002078. URL: <https://opg.optica.org/josaa/abstract.cfm?URI=josaa-27-9-2078> (cit. on pp. 40, 45, 100, 103).
- [43] Gerhard Heinzel et al. “Tracking Length and Differential-Wavefront-Sensing Signals from Quadrant Photodiodes in Heterodyne Interferometers with Digital Phase-Locked-Loop Readout”. In: *Phys. Rev. Appl.* 14 (5 Nov. 2020), p. 054013. DOI: 10.1103/PhysRevApplied.14.054013. URL: <https://link.aps.org/doi/10.1103/PhysRevApplied.14.054013> (cit. on pp. 177, 178, 180).
- [44] Victor Huarcaya et al. “ 2×10^{-13} Fractional Laser-Frequency Stability with a 7-cm Unequal-Arm Mach-Zehnder Interferometer”. In: *Phys. Rev. Appl.* 20 (2 Aug. 2023), p. 024078. DOI: 10.1103/PhysRevApplied.20.024078. URL: <https://link.aps.org/doi/10.1103/PhysRevApplied.20.024078> (cit. on pp. 71, 130).

- [45] Infineon. *BFP740, SiGe:C NPN RF bipolar transistor*. 2018. URL: https://www.infineon.com/dgdl/Infineon-BFP740-DS-v02_00-EN.pdf?fileId=5546d46265f064ff0166389680a24ea4 (cit. on p. 83).
- [46] Texas Instruments. *ADS6445-EP, Quad-Channel, 14-Bit, 125-MSPS Analog-to-Digital Converter (ADC) - Enhanced-Product*. URL: <https://www.ti.com/product/ADS6445-EP> (cit. on p. 86).
- [47] Texas Instruments. *LMH6624 and LMH6626 Single/Dual Ultra Low Noise Wideband Operational Amplifier*. 2014. URL: <https://www.ti.com/lit/ds/symlink/lmh6624.pdf> (cit. on p. 83).
- [48] R V Jones. “Some developments and applications of the optical lever”. In: *Journal of Scientific Instruments* 38.2 (Feb. 1961), p. 37. DOI: 10.1088/0950-7671/38/2/301. URL: <https://dx.doi.org/10.1088/0950-7671/38/2/301> (cit. on p. 100).
- [49] Germany LPF Team. “LISA Pathfinder Mission Extension Report for the German Contribution”. In: (Feb. 2020) (cit. on p. 60).
- [50] Jun Luo et al. “TianQin: a space-borne gravitational wave detector”. In: *Classical and Quantum Gravity* 33.3 (Jan. 2016), p. 035010. DOI: 10.1088/0264-9381/33/3/035010. URL: <https://dx.doi.org/10.1088/0264-9381/33/3/035010> (cit. on pp. 6, 7).
- [51] Michele Maggiore. *Gravitational Waves. Vol. 1: Theory and Experiments*. Oxford University Press, 2007. ISBN: 978-0-19-171766-6, 978-0-19-852074-0. DOI: 10.1093/acprof:oso/9780198570745.001.0001 (cit. on pp. 3, 6, 19, 24, 30, 34).
- [52] Riccardo Maggiore et al. *Angular control noise in Advanced Virgo and implications for the Einstein Telescope*. 2024. arXiv: 2401.13013 [astro-ph.IM]. URL: <https://arxiv.org/abs/2401.13013> (cit. on p. 59).
- [53] Waldemar Martens and Eric Joffre. “Trajectory Design for the ESA LISA Mission”. In: *The Journal of the Astronautical Sciences* (June 2021). DOI: <https://doi.org/10.1007/s40295-021-00263-2>. URL: <https://link.springer.com/article/10.1007/s40295-021-00263-2> (cit. on p. 7).
- [54] Timesh et al Mistry. *The Eyes of LISA*. July 2024 (cit. on pp. 74, 75, 76, 122).
- [55] Euan Morrison et al. “Automatic alignment of optical interferometers”. In: *Appl. Opt.* 33.22 (Aug. 1994), pp. 5041–5049. DOI: 10.1364/AO.33.005041. URL: <https://opg.optica.org/ao/abstract.cfm?URI=ao-33-22-5041> (cit. on p. 39).
- [56] Euan Morrison et al. “Experimental demonstration of an automatic alignment system for optical interferometers”. In: *Appl. Opt.* 33.22 (Aug. 1994), pp. 5037–5040. DOI: 10.1364/AO.33.005037. URL: <https://opg.optica.org/ao/abstract.cfm?URI=ao-33-22-5037> (cit. on p. 39).
- [57] Newport. *Agilis AG-M050 and AG-M100 mirror mounts* (cit. on p. 143).
- [58] S. Paczkowski et al. “Postprocessing subtraction of tilt-to-length noise in LISA”. In: *Phys. Rev. D* 106 (4 Aug. 2022), p. 042005. DOI: 10.1103/PhysRevD.106.042005. URL: <https://link.aps.org/doi/10.1103/PhysRevD.106.042005> (cit. on pp. 60, 63, 119).

- [59] Sarah Katharina Paczkowski. “Laser Frequency Stabilisation and Interferometer Path Length Differences during the LISA Pathfinder Satellite Mission”. PhD thesis. Leibniz Universität Hannover, 2017 (cit. on p. 34).
- [60] Rüdiger Paschotta. *RP Photonics*. URL: <https://www.rp-photonics.com> (cit. on p. 28).
- [61] Michael Perreir-Lloyd. *Opto-mechanical design for space science*. Oct. 2014. URL: https://www.gla.ac.uk/media/Media_374991_smxx.pdf (cit. on p. 77).
- [62] Guido Pizzella. *Fisica Sperimentale del Campo Gravitazionale*. Jan. 1993, p. 320 (cit. on p. 6).
- [63] Dong Qiao et al. “A Review of Orbital Mechanics for Space-Based Gravitational Wave Observatories”. In: *Space: Science & Technology* 3 (2023), p. 0015. DOI: 10.34133/space.0015. eprint: <https://spj.science.org/doi/pdf/10.34133/space.0015>. URL: <https://spj.science.org/doi/abs/10.34133/space.0015> (cit. on p. 7).
- [64] D I Robertson et al. “Construction and testing of the optical bench for LISA Pathfinder”. In: *Classical and Quantum Gravity* 30.8 (Mar. 2013), p. 085006. DOI: 10.1088/0264-9381/30/8/085006. URL: <https://dx.doi.org/10.1088/0264-9381/30/8/085006> (cit. on p. 77).
- [65] Shannon R Sankar and Jeffrey Livas. “Optical alignment and wavefront error demonstration of a prototype LISA telescope”. In: *Classical and Quantum Gravity* 37.6 (Feb. 2020), p. 065005. DOI: 10.1088/1361-6382/ab6adf. URL: <https://dx.doi.org/10.1088/1361-6382/ab6adf> (cit. on p. 10).
- [66] Peter R. Saulson. *Interferometric Gravitational Wave Detectors*. 2017 (cit. on pp. 5, 6).
- [67] Sönke Schuster. “Tilt-to-length coupling and diffraction aspects in satellite interferometry”. PhD thesis. Leibniz Universität Hannover, 2017 (cit. on pp. 28, 59, 60, 61, 62, 69, 74, 99).
- [68] Thomas S. Schwarze. “Phase Extraction for laser interferometry in space: phase readout schemes and optical testing”. PhD thesis. Leibniz Universität Hannover, 2018 (cit. on p. 184).
- [69] A.E. Siegman. *Lasers*. University Science Books, 1986. ISBN: 9780685055953. URL: <https://books.google.de/books?id=qBBaDQEACAAJ> (cit. on pp. 19, 35, 36, 37).
- [70] Andrew Sutton et al. “Laser ranging and communications for LISA”. In: *Opt. Express* 18.20 (Sept. 2010), pp. 20759–20773. DOI: 10.1364/OE.18.020759. URL: <https://opg.optica.org/oe/abstract.cfm?URI=oe-18-20-20759> (cit. on p. 13).
- [71] Massimo Tinto et al. “Implementation of time-delay interferometry for LISA”. In: *Phys. Rev. D* 67 (12 June 2003), p. 122003. DOI: 10.1103/PhysRevD.67.122003. URL: <https://link.aps.org/doi/10.1103/PhysRevD.67.122003> (cit. on p. 13).

[72] M Tröbs et al. “Reducing tilt-to-length coupling for the LISA test mass interferometer”. In: *Classical and Quantum Gravity* 35.10 (Apr. 2018), p. 105001. DOI: 10.1088/1361-6382/aab86c. URL: <https://dx.doi.org/10.1088/1361-6382/aab86c> (cit. on pp. 61, 62, 70, 71, 85, 132).

[74] Lucia Trozzo and Francesca Badaracco. “Seismic and Newtonian Noise in the GW Detectors”. In: *Galaxies* 10.1 (2022). ISSN: 2075-4434. DOI: 10.3390/galaxies10010020. URL: <https://www.mdpi.com/2075-4434/10/1/20> (cit. on p. 7).

[75] Vishay. *Surface Mount Multilayer Ceramic Chip Capacitors MIL Qualified, Type CDR data sheet*. 2024. URL: <https://www.vishay.com/docs/45026/cdrmilprf55681.pdf> (cit. on p. 130).

[76] Vishay. *Thin film Mini-MELF resistors SMM0204 data sheet*. 2024. URL: <https://www.vishay.com/docs/20004/smm0204.pdf> (cit. on p. 130).

[77] Gudrun Wanner. “Complex optical systems in space : numerical modelling of the heterodyne interferometry of LISA Pathfinder and LISA”. PhD thesis. Leibniz Universität Hannover, 2010 (cit. on p. 60).

[78] Gudrun Wanner and Gerhard Heinzel. “Analytical description of interference between two misaligned and mismatched complete Gaussian beams”. In: *Appl. Opt.* 53.14 (May 2014), pp. 3043–3048. DOI: 10.1364/AO.53.003043. URL: <https://opg.optica.org/ao/abstract.cfm?URI=ao-53-14-3043> (cit. on p. 23).

[79] John Arcibald Wheeler. *Geons, Black Holes, and Quantum Foam*. 1998 (cit. on p. 3).

[81] Lennart Wissel et al. “Relative-Intensity-Noise Coupling in Heterodyne Interferometers”. In: *Phys. Rev. Appl.* 17 (2 Feb. 2022), p. 024025. DOI: 10.1103/PhysRevApplied.17.024025. URL: <https://link.aps.org/doi/10.1103/PhysRevApplied.17.024025> (cit. on pp. 32, 33).

[82] Yue-Liang Wu et al. “China’s first step towards probing the expanding universe and the nature of gravity using a space borne gravitational wave antenna”. In: *Communications Physics* 4.1 (Feb. 2021), p. 34. ISSN: 2399-3650. DOI: 10.1038/s42005-021-00529-z. URL: <https://doi.org/10.1038/s42005-021-00529-z> (cit. on pp. 6, 7).

[83] Kohei Yamamoto. “Intersatellite Clock Syncronization and Absolute Ranging for Gravitational Wave Detection in Space”. PhD thesis. Leibniz Universität Hannover, 2023 (cit. on p. 184).

Project Documents

- [23] Miguel Dovale et al. “LISA-AEI-IDS-RS-0010 IPU Requirements Document”. In: (2024) (cit. on p. 125).
- [29] “ESA-LISA-EST-IDS-RS-0002 LISA IDS System and Interface Requirement Document (IDS-IRD)”. In: (2024) (cit. on pp. 119, 120, 121).
- [30] German F. Barranco. “LISA-AEI-IDS-AN-005 Readout Chain Budget”. In: (2024) (cit. on pp. 10, 35, 83, 121, 157, 158, 183, 184).
- [31] German Fernandez Barranco. “LISA-AEI-IDS-AN-005 Readout Chain Budget”. In: (2024) (cit. on p. 121).
- [33] Ewan Fitzsimons and Martin Hewitson. “Concept for Balanced Detection in LISA”. In: (2021) (cit. on pp. 9, 121).
- [34] Ewan Fitzsimons, Joseph Martino, and Daniele Vetrugno. “LISA-LCST-INST-TN-003 LISA Performance Model and Error Budget”. In: (2021) (cit. on pp. 11, 12, 13, 14, 17, 59, 60, 108).
- [35] Ewan Fitzsimons et al. “IDS Performance Budgets”. In: (2024) (cit. on p. 121).
- [42] Gerhard Heinzel. “LISA-AEI-INST-TN-002 LISA frequency planning”. In: (2021) (cit. on pp. 11, 15).
- [73] Michael Tröbs et al. “LOB-AEI-TN-005.1 Test of interferometry concept”. In: (2011) (cit. on p. 70).
- [80] Lennart Wissel, Christoph Bode, and Thomas Schwarze. “RIN requirements for LISA-LISA-AEI-TN-xxxx”. In: (2020) (cit. on p. 23).

Acknowledgements

A long list of people deserves a heartfelt and profound thank you for making this PhD thesis possible. First and foremost, I want to express my deep gratitude to Professor Gerhard Heinzel. The acceptance itself to become his PhD student had an immensely positive impact on my life. Not only did it allow me to conduct decent research in a field that interests me very much, but it also led to the incredible fortune of meeting my fantastic wife, with whom I have now a wonderful daughter. I am grateful to him for being such an inspiring person in every possible aspect, from scientific excellence to kindness and his view on different cultures. I was particularly impressed by his thoughtful offer of support during my forced quarantine following my return from Italy during the coronavirus pandemic.

Secondly, I would like to extend my sincere thanks to Professor Karsten Danzmann for founding and leading the Albert Einstein Institute, making it an incredibly nurturing workplace that attracts outstanding people from around the world. This gave me the chance to get to know so many people from many diverse cultural backgrounds, allowing me to grow as a person.

I am also very grateful to Professor Oliver Gerberding. His participation in the advisory committee meetings and his general online presence provided me with thoughtful and highly valuable insights and advice.

A big thank you goes to Miguel Dovale for supervising my work during these five years, providing timely support and guidance. Special thanks to German, who taught me how to construct a crucial photoreceiver during the most intense phase of the measurement campaign. Furthermore, I would like to thank Birgit Ohlendorf for her invaluable assistance in navigating the bewildering bureaucracy of applying to the university and submitting the thesis.

Beyond this, I want to acknowledge all the colleagues working ad AEI, who contribute every day to one of humanity's most challenging endeavors: the measurement of gravitational waves! With many of these people, also due to similarity in personalities, I was able to develop close friendships that I hope will last forever. To these belong Matteo, Stefano, Rodrigo, Pablo, Angela, Jonathan, Martin, Niklas, Mariia, Roberta, Luis and Simone. Special thanks to all of those who joined me for the craziest and northeast trips of my life, giving me the right breaks to reflect during my PhD work.

I would also like to thank all the proofreaders of my thesis who dedicated their time to ensure I submitted a polished document. These are Jonathan, Rodrigo, Stefano, Yongho, Christoph, Matteo, Miguel and my wife Stefanie. I especially admire Stefanie's humbleness in reading through the entire text and "doing her best despite understanding nothing of the content".

I thank Stefanie for being my beloved partner over the past four years. I am grateful for her care of our daughter, especially during the final, most demanding phase of my PhD.

Finally, I thank my family, who have always given me the best support, even as I am living abroad. I am profoundly thankful to my father Alessandro and my grandfather Guido, both of whom inspired me as physicists since I am a kid. Guido not only pioneered the gravitational wave detection research in Italy, but also provided me with the right book for any of my physics- and non-physics question during my visits. Every sentence you say motivates me more to pursue this career!

Special mentions also go to Bechstein, for having provided me with an excellent grand piano to relax me every afternoon and to the Hannover Basketball Dragons, who have accepted me as a team member and with which I had lots of fun playing in the Landesliga Hannover. On top of that, we even managed to be promoted to Oberliga in 2022! I will think about you during my defence, defence, defence! Thanks also to Andronaco and Vicofoodbox, without which I would not have survived as an Italian expat in Germany.

Curriculum Vitae

Leibniz Universität Hannover Max Planck Institute for Gravitational Physics (Albert Einstein Institute) PhD studies, Physics	06/2019 - 01/2025
Università degli Studi di Padova Dipartimento di Fisica e Astronomia Galileo Galilei Master Degree, Experimental Physics	10/2016 - 10/2018
Università degli Studi di Padova Dipartimento di Fisica e Astronomia Galileo Galilei Bachelor Degree, Physics	10/2013 - 10/2016
Liceo Scientifico Enrico Fermi High school degree	09/2008 - 07/2013